ANALYSIS OF STRUCTURE ON GALACTIC AND EXTRAGALACTIC SCALES

By

Qingqing Mao

Dissertation

Submitted to the Faculty of the

Graduate School of Vanderbilt University

in partial fulfillment of the requirements

for the degree of

DOCTOR OF PHILOSOPHY

in

PHYSICS

August, 2015

Nashville, Tennessee

Approved:

Dr. Andreas A. Berlind

Dr. Robert J. Scherrer

Dr. Kelly Holley-Bockelmann

Dr. Thomas J. Weiler

Dr. M. Shane Hutson

ACKNOWLEDGMENTS

I am most thankful for the supervision of my advisor Dr. Andreas Berlind. This dissertation would not be possible without his mentorship and guidance. I am grateful to the members of my committee for taking time from their busy schedules to help me along this journey. They have all played critical roles in my development as a scientist.

I am extremely grateful to my collaborators for all of their helpful suggestions, vibrant discussions and insightful advice on my research projects. I am also grateful to the SDSS collaboration for providing a fertile environment to conduct my research.

I would like to thank my fellow graduate students and friends, especially the crew on the 9th floor. Without their support and friendship, my Ph.D. life would not have been so enjoyable, and I would have never made it this far.

Finally, I would like to thank my mother Ziqiang Xu and father Lei Mao. They have always been a constant source of support and love throughout all of my pursuits in life. Thanks to Luxi Wang, whose patience, encouragement, and companionship has kept me going.

TABLE OF CONTENTS

LIST OF TABLES

LIST OF FIGURES

CHAPTER I

Introduction

The Universe is full of structures on all scales, from stars and planets to galaxies and, on much larger scales, a web-like structure built with galaxy clusters, superclusters, filaments and walls, and enormous cosmic voids between galaxies. Theoretical and observational research over the last three decades has led to the view that the present-day rich structures developed through gravitational amplification of tiny density fluctuations generated in the very early stage of the Universe. Recent observations of the cosmic microwave background (CMB) and large-scale structure (LSS) determined the energy content of the Universe and the basic statistics of the initial density field with great accuracy. Modern astronomical surveys, such as the Sloan Digital Sky Survey (SDSS), have provided us a huge amount of observational data and have allowed us to investigate structures on all different scales. New generation of observations will surely keep providing more and better data, which will give us great opportunities to fuel our knowledge of the Universe.

What can we learn from all these observed structures? How can we connect observations to theoretical models? How can we relate the present-day rich structures to the origin and the evolution of the Universe? In this dissertation, I present some different statistical analyses of structures on both Galactic and extragalactic scales, ranging from the very early universe to the present-day Milky Way structure. These analyses are facets in the broad field of structure formation and cosmology. As I will elaborate on in this document, these analyses can help us understand the cosmology, the formation and the evolution of the large-scale structure of the Universe, and the spatial structure and the dynamics of our Milky Way.

I.1 The Expanding Universe and ΛCDM Model

The standard theory of cosmology is the *Hot Big Bang*, according to which the Universe began in a hot, dense, nearly uniform state approximately 13.8 billion years ago, and it has been expanding ever since. In the 1920's, from Einstein's field equations, Alexander Friedmann derived his *Friedmann equations*, which show that the universe might expand at a rate calculable by the equations (Friedman 1922). Observationally, in 1929, Edwin Hubble found the famous linear relation (Hubble 1929), now known as *Hubble's Law*, between galaxies' redshift and distance:

$$z = \frac{H_0}{c} d \tag{I.1}$$

where H_0 is a constant called the Hubble constant. This shows the fact that the universe is expanding. In 1998, the observations of Type Ia supernovae (SNe Ia) suggested that the expansion of the universe is actually accelerating (Riess et al. 1998; Perlmutter et al. 1999).

Observational facts in the last couple of decades have led us to an established concordance cosmological model known as the ΛCDM model. The model states that, except for the normal baryonic matter, there are two components pertaining to the dark sector of the Universe: *Cold Dark Matter* (CDM), one or more species of undetermined non-relativistic particles which most likely only interact with baryonic matter through gravity, and *Dark Energy* (Λ), the negative pressure causing the accelerating expansion of the Universe.

While people are still trying to find the nature of dark matter and dark energy, the ΛCDM model has gained a lot of success. In the past few years, several independent observations have corroborated the ΛCDM model, including the cosmic microwave background (CMB), the baryon acoustic oscillations (BAO) in large-scale structure, the distance measurements from the Type Ia supernovae (SN), the gravitational lensing signals, and the properties of galaxy clusters. We have now determined that the total energy density in the universe today consists of about 4% baryonic matter, 26% dark matter and 70% dark

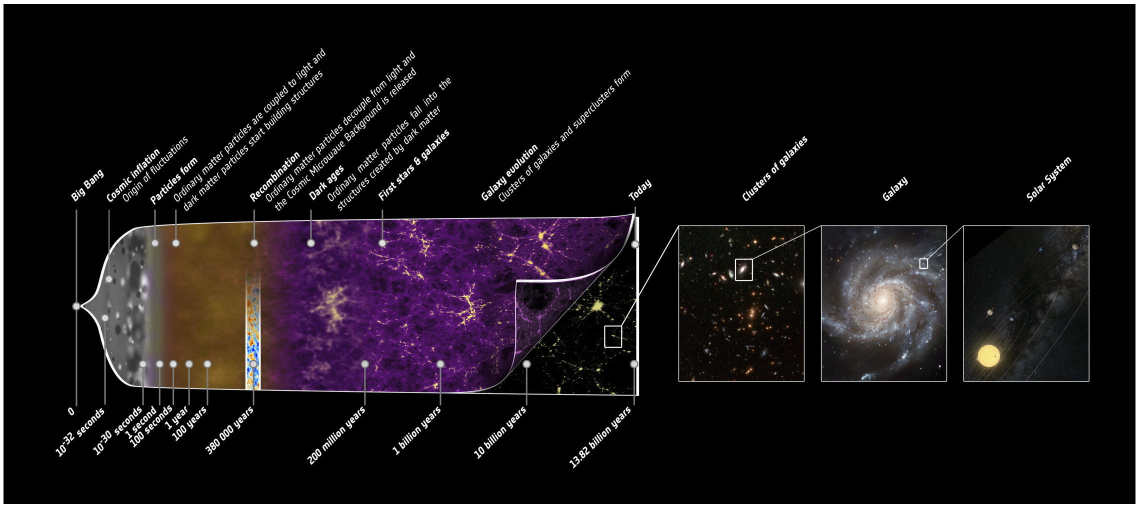

Figure I.1 A brief timeline of the evolution of the universe over 13.8 billion years. The far left depicts the earliest moment we can now probe, when a period of "inflation" produced a burst of exponential growth in the universe. Credit: ESA C. Carreau

energy with great accuracy (Planck Collaboration et al. 2015).

Based on these observations, we can now assemble the detailed history of our universe. Figure I.1 shows a brief timeline of our universe. Right after the Big Bang, the Universe very likely experienced a rapid exponential expansion called inflation, during which tiny density fluctuations caused by quantum fluctuations were generated. These fluctuations were the "seeds" for the growth of structures, and they left imprints on the CMB which we observe today. After inflation, the Universe continued to expand and decrease in density and fall in temperature, and nucleosynthesis took place. Billions of years of gravitational evolution caused the formation of the stars, galaxies, and the large-scale structure we see today.

I.2 The Very Early Universe and Inflation

The earliest phases of the Universe are subject to much speculation. Research on the very early universe is always an active area, and recently it has attracted more attention due to new observational discoveries which make it possible to probe the very early universe much more quantitatively. There are many theories about the very early universe. And a very promising paradigm is that the very early universe experienced an extremely rapid epoch of exponential expansion, called *inflation*.

Inflation was originally motivated by several problems in the Big Bang cosmology pointed out in the 1970's. These are the flatness problem, the horizon problem, and magnetic-monopole problem (Peebles 1993; Liddle & Lyth 2000). In 1980, Alan Guth found an exponential expansion of space can be driven by a negative-pressure vacuum energy density, and he proposed the hypothesis of inflation (Guth 1981). Inflation can flatten the space, cause the horizon size to grow exponentially, and dilute the abundance of magnetic-monopoles. It can naturally solve the above problems all together and explain the origin of the large-scale structure. If inflation did happen, it lasted from 10^{-36} seconds after the Big Bang to sometime between 10^{-33} and 10^{-32} seconds, and the universe expanded by a factor of at least 60 *e*-folds in volume in such a short period (Guth 1997).

The standard inflationary paradigm predicts a nearly Gaussian and scale invariant primordial density fluctuations, which is consistent with the observations in CMB and LSS in the last few decades. However, even the simplest inflation model predicts some small deviation from Gaussianity. Recently, *primordial non-Gaussianity*, i.e., the study of non-Gaussian contributions to the primordial density fluctuations, has grabbed more and more attention and has become a very important probe of the very early universe. There are currently many viable inflationary models, but it is hard to discriminate between different models. Probing primordial non-Gaussianity provides a powerful tool to put constraints on different inflationary models, since different models can predict slightly different deviations from Gaussian fluctuations. Constraining non-Gaussianity to high precision can help revealing the mysterious secrets of the very early universe.

I.3 Large-Scale Structure of the Universe

Over 13.8 billion years of evolution, primordial tiny density ripples have been amplified to enormous proportions by gravitational forces, producing ever-growing concentrations of dark matter in which ordinary gases cool, condense and fragment to make galaxies. Galaxies, groups and clusters are linked together in an intricate web-like pattern of filaments, sheets, and voids, that is commonly known as the "cosmic web" (Bond et al. 1996).

Galaxy redshift surveys, such as Center for Astrophysics (CfA) galaxy redshift survey (Geller & Huchra 1989), the 2-degree Field Galaxy Redshift Survey (2dFGRS; Colless et al. 2001), and the Sloan Digital Sky Survey (SDSS; York et al. 2000), have observed and quantified this web-like extragalactic structure. Figure I.2 illustrates subregions of the CfA, 2dFGRS, and SDSS survey data, which reveal a tremendous richness of structure. It also shows mock galaxy surveys constructed from the Millennium Simulation, the result of a simulation of the growth of structure and of the formation of galaxies in the current standard model of cosmology. The similarity between theory and observation is striking, and is supported by a quantitative comparison of clustering of galaxies.

While most of the study of large-scale structure is focused on the clustering of galaxies and the distribution of clusters, filaments and sheets, cosmic voids are another dominant feature present in the hierarchical structure of the Universe. Cosmic voids are large underdense regions living between filaments and sheets, which contain very few galaxies. More than half of the volume in the universe is taken by these nearly empty regions. They were first discovered in some of the early galaxy redshift surveys (Gregory & Thompson 1978; Kirshner et al. 1981; de Lapparent et al. 1986) over thirty years ago. Ever since their discovery, voids have been recognized as very interesting cosmological laboratories for studying galaxy evolution, structure formation and cosmology. The low-density environment of voids provides an ideal place to study the influence of environment on the formation and evolution of galaxies. The size and shape distribution of voids and their intrinsic structure and dynamics can provide insights into the growth of structure and dark

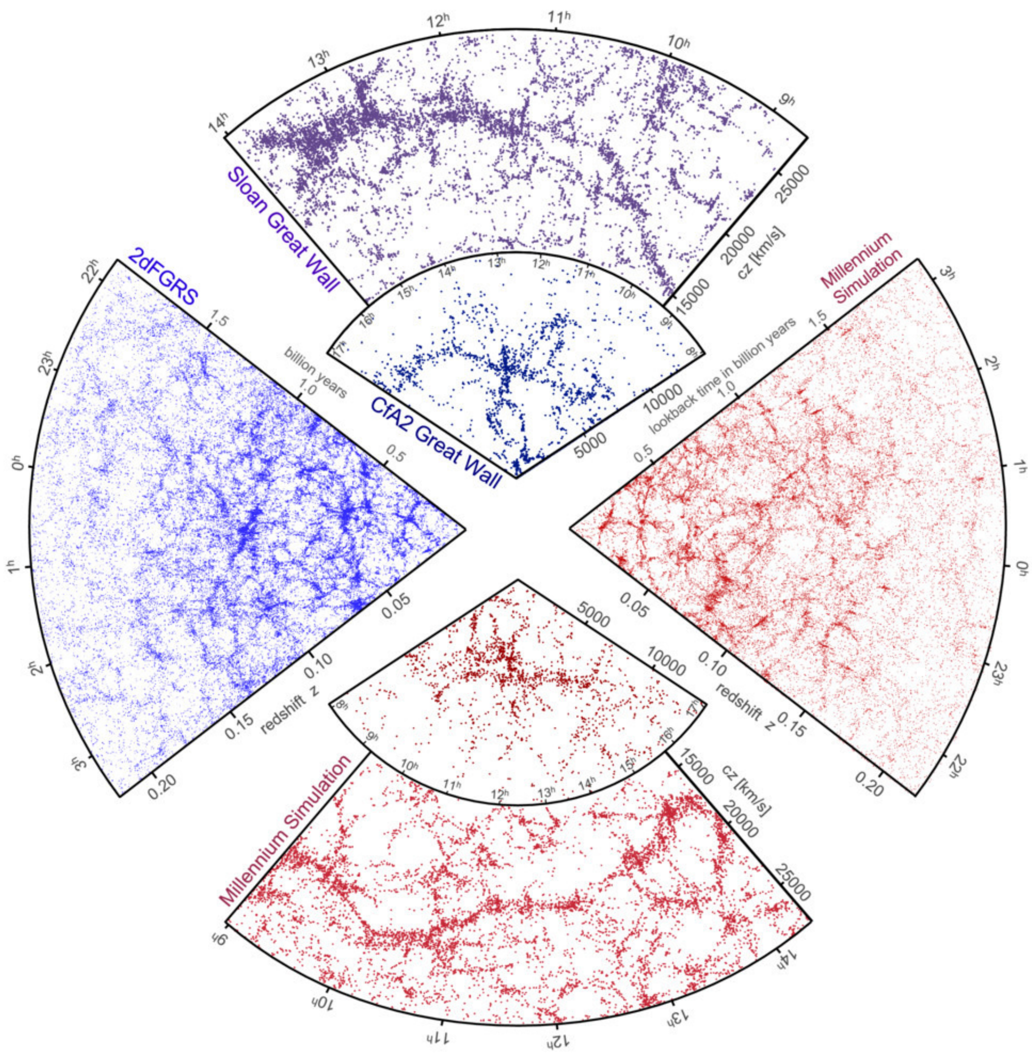

Figure I.2 An illustration showing structures observed by CfA, 2dFGRS, and SDSS, comparing with mock catalogs constructed from Millennium Simulation. The up-down and left-right quadrants have the same redshift depth and angular sky coverage. Image from Springel et al. 2006.

energy.

Though cosmic voids are intriguing objects, identifying voids and studying them statistically is very challenging. Galaxy redshift surveys with sufficient volume is necessary. Not until recently, galaxy redshift surveys, such as the Baryon Oscillation Spectroscopic Survey (BOSS; Dawson et al. 2013) in SDSS-III, have produced much bigger data sets. Recent development of void finding algorithm, such as the ZOBOV algorithm (Neyrinck 2008), allows us to identify voids and explore their natural extension accurately. These provide great opportunities to study void properties systematically and in detail.

I.4 Milky Way Structure

On the galactic scales, matter collapsed around high density regions in the density fluctuations and formed galaxies. Galaxy formation and evolution is one of the most active fields in modern astrophysics. Our own Galaxy, the Milky Way, provides a unique opportunity to study a galaxy in detail.

Observations have provided us with a comprehensive picture of our Milky Way. We now know that the Milky Way is a barred spiral galaxy. At the center of the Milky way exists a supermassive black hole, surrounded by a bar-shaped bulge. The majority of the gas, dust and stars are concentrated in a thin disk, in which there are roughly logarithmic spiral arm structures. In addition to the thin disk, there is a diffuse thick disk population. The disk components are surrounded by a spheroidal halo of old stars and globular clusters, and satellite galaxies farther out. All the components are encased in a massive dark matter halo.

Although it is elaborate, this picture is still evolving. The desire to understand the structure and the formation and evolutionary history of the Milky Way is the driving factor for much on-going research today. Mapping the different components of the Milky Way is only the first step to create a complete understanding of galaxy formation and evolution. Recent surveys, such as SDSS, the Two-Micron All Sky Survey (2MASS; Skrutskie et al.

2006), the Radial Velocity Experiment (RAVE; Kordopatis et al. 2013), and others show significant spatial substructure in the Milky Way. With more and more observational data becoming available, information about the density, kinematics, and chemistry of stars and their preferred locations within the Galaxy introduces new possibilities for understanding the galaxy formation and evolution (Freeman & Bland-Hawthorn 2002). To fully utilize observational data, testing and exploring different statistical tools is essential.

I.5 Sloan Digital Sky Survey

Many of the analyses in this dissertation are based on the data collected by the *Sloan Digital Sky Survey* (SDSS; York et al. 2000). SDSS is one of the most ambitious and influential surveys in the history of astronomy. SDSS began in 2000, followed by SDSS-II in 2005, SDSS-III in 2008 (Eisenstein et al. 2011), and SDSS-IV in 2014. It is a multi-filter imaging and spectroscopic survey using a dedicated 2.5-meter wide-field optical telescope at Apache Point Observatory in New Mexico. After years of observation, the final data set from SDSS-III, Data Release 12 (DR12), was released in 2015, containing over 14,000 square degrees of imaging and more than 4 million spectra in total (Alam et al. 2015). Spectroscopic data include spectra of around 2.5 million galaxies, 480,000 quasars, and 850,000 stars.

SDSS-III consists of four surveys. BOSS, the Baryon Oscillation Spectroscopic Survey, measured redshifts of around 1.5 million massive galaxies and 300,000 quasars to map the large-scale structure. SEGUE-2, the continuation of the SDSS-II Sloan Extension for Galactic Understanding and Exploration (SEGUE), measured medium-resolution optical spectra of stars in a variety of target categories, totaling 380,000 stars in the catalog (Rockosi et al. 2009), to probe chemical evolution, stellar kinematics and substructure in our Milky Way. APOGEE, the Apache Point Observatory Galactic Evolution Experiment, obtained high-resolution, high signal-to-noise infrared spectra of 10,000 evolved late-type stars to create the first high-precision spectroscopic survey of all Galactic stellar populations with a uniform set of stellar tracers and spectral diagnostics. The Multi-object APO Radial Velocity Exoplanet Large-area Survey (MARVELS) monitored radial velocities of more than 8000 FGK stars to detect giant planets with periods up to two years.

The tremendous size and the richness of the SDSS data allow us to study structures on both Galactic and extragalactic scales. In this dissertation, I largely use data from BOSS and SEGUE to do my analyses.

I.5.1 BOSS

Galaxy redshift surveys are surveys that attempt to map the galaxy distribution to trace the large-scale structure in 3-dimensional space. A complete 3D map allows for the precision study of large-scale structure and cosmology. In order to make precise measurements, surveys need to have accurate position measurements in huge volumes, which means both covering larger areas of the sky and going deep in space. Key steps in this development have included the Center for Astrophysics redshift surveys (Geller & Huchra 1989), the Las Campanas Redshift Survey (Shectman et al. 1996), and the Two Degree Field Galaxy Redshift Survey (Colless et al. 2001). The largest and most powerful redshift surveys to date have been those from the SDSS, which measured redshifts of nearly one million galaxies in spectroscopic observations during SDSS-I and SDSS-II between 2000 and 2008 (Abazajian et al. 2009).

The Baryon Oscillation Spectroscopic Survey is the largest of the four surveys that comprise SDSS-III. It is designed to measure the scale of baryon acoustic oscillations (BAO) in the clustering of matter over a larger volume than the combined efforts of all previous spectroscopic surveys of large-scale structure. BOSS surveyed galaxies and quasars over two large contiguous regions of sky in the Northern and Southern Galactic Caps. It measured 1.5 million luminous galaxies as faint as $i = 19.9$ over 10,400 deg^2. The majority of the galaxies were uniformly targeted for large-scale structure studies in a sample focused on relatively low redshifts ("LOWZ", with $z < 0.4$) and a sample with $0.4 < z < 0.7$ de-

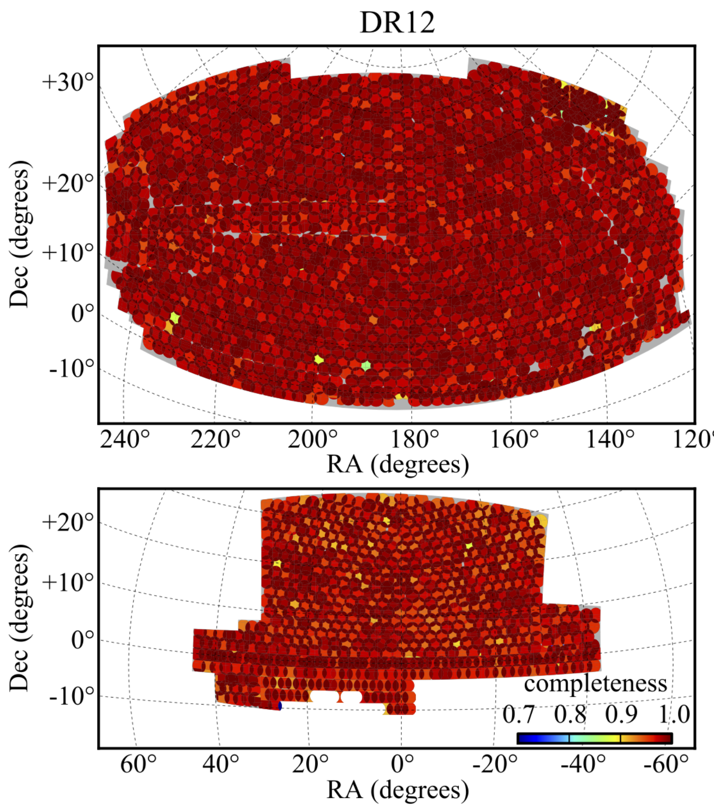

Figure I.3 BOSS DR12 spectroscopic sky coverage in the Northern Galactic Cap (top) and Southern Galactic Cap (bottom). The color coding indicates the survey completeness of the CMASS galaxies. The total coverage is 10,400 deg^2, with an average completeness of 94%. Image from Alam et al. 2015.

signed to give a sample approximately volume-limited in stellar mass ("CMASS"; Reid et al. in prep.). The total volume covered by LOWZ and CMASS is more than 6 h^{-3}Gpc^3. Figure I.3 shows the sky coverage of the BOSS DR12 and the survey completeness of the CMASS galaxy catalog.

BOSS also observed a large set of quasar spectra to map the density distribution and constrain BAO at high redshift through quasar clustering and Lyα forest, but this is beyond the scope of this dissertation.

The larger than ever galaxy survey volume of BOSS provides a ideal data set to study cosmic voids and voids related science. In this dissertation, I use the BOSS galaxy data in the SDSS Data Release 12 (DR12), which is the most recent data release and the final data release of SDSS-III, to identify and analyze cosmic voids.

I.5.2 SEGUE

The Sloan Extension for Galactic Understanding and Exploration (SEGUE; Yanny et al. 2009) is a spectroscopic sub-survey of the SDSS, focused on Galactic science. SEGUE provides the largest spectroscopic sample available, and it covers a much more extensive volume of the Milky Way than all previous studies. It provides stellar parameters, kinematics, and metallicities of stellar populations from the disk all the way to the outer stellar halo. Thus the complete SEGUE survey provides a great opportunity to study the structure of the Milky Way.

SEGUE combines the extensive and uniform photometry from SDSS with medium-resolution ($R \sim 1800$) spectroscopy over a broad spectral range ($3800-9200$Å) for $\sim$ 240,000 stars over a range of spectral types. SEGUE was designed to sample the Galactic structure at a variety of distances in ~ 200 "pencil beam" volumes spread out over the sky. Each pencil beam covers a circular region of 7 square degrees, probing the sky with 640 spectroscopic fibers (Yanny et al. 2009).

Among all the stellar populations, the G-dwarf sample represents SEGUE's largest sin-

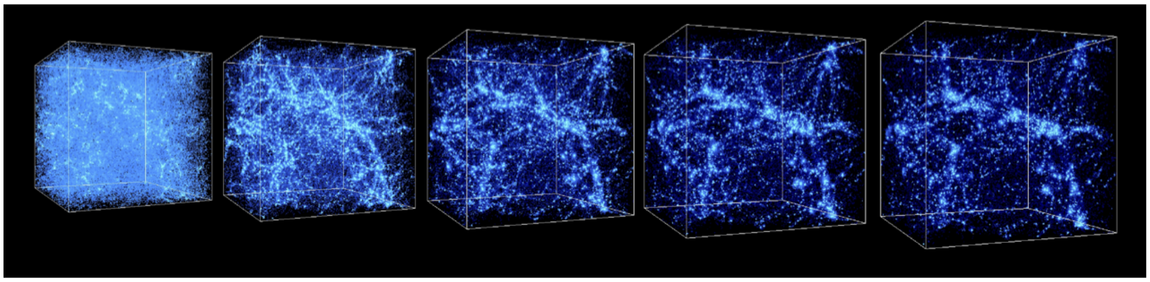

Figure I.4 N-body simulations show the evolution of structures. Performed at the National Center for Supercomputer Applications by Andrey Kravtsov (The University of Chicago) and Anatoly Klypin (New Mexico State University). Visualizations by Andrey Kravtsov.

gle homogeneous stellar spectral category. The SEGUE G dwarfs are defined as having magnitudes and colors in the range $14.0 < r_0 < 20.2$ and $0.48 < (g-r)_0 < 0.55$. This simple target selection makes the selection biases very small (Yanny et al. 2009), though not nonexistent, and the selection bias can be corrected by various weights. In this dissertation, I apply the spatial correlation function statistics to this G-dwarf sample to constrain the structure of the Milky Way.

I.6 N-body Simulations and Mock Catalogs

I.6.1 N-body Simulations in General

The equations of motion for a gravitationally collapsing system can only be analytically solved in the linear regime. To study the processes of non-linear structure formation, numerical N-body simulations are a very powerful and necessary tool. N-body simulations can reproduce the history of structure growth, which allows us to trace back the evolution of the density field at different redshifts. However, N-body simulations are highly time consuming and limited by computational capabilities. With the development of supercomputers and better algorithms, today we are able to run simulations with billions of particles. Figure I.4 shows an example of N-body simulations performed at the National Center for Supercomputer Applications. A series of snapshots show the evolution of structures in a 43 Mpc simulation box from redshift 10 to present.

The basic steps for running cosmological N-body simulation are as follows. Dark matter "particles" are laid down smoothly in a simulation box of some desired size. Each "particle" is not a real physical particle but is corresponding to certain amount of mass. Then the positions of the particles are perturbed and initial velocities are given based on perturbation theory from a particular choice of cosmology. This gives us the initial conditions at a very high staring redshift. After that, in steps of time, the gravitational forces between particles are calculated and each particle is moved based on its velocity and the total force applied to it. This step is repeated over and over until the desired redshift. By tuning the initial bispectrum and trispectrum in the initial perturbation setting, we can also make simulations containing different kinds of primordial non-Gaussianity.

When the simulations are done, dark matter halos can be identified by halo finding algorithms such as the *friends-of-friends* (FoF) method (Davis et al. 1985). The identified dark matter halos are then populated with mock galaxies by using the *Halo Occupation Distribution* (HOD) model (Berlind & Weinberg 2002), which describes the number, spatial and velocity distributions of galaxies within a dark matter halo. Mock galaxy catalogs provide the way to compare theoretical models to observed galaxy distributions.

I.6.2 Redshift Space Distortions

In galaxy redshift surveys, distances to galaxies are measured from their redshift assuming they all move with the Hubble flow. However, the local mass distribution also affects the motion of galaxies due to gravity, causing relative motions in addition to the Hubble flow, i.e. the peculiar motion. This relative motion causes additional redshift, and the actual measured redshift is from the combination of the Hubble flow and the additional peculiar velocity. Because of this, the positions of galaxies are displaced in redshift space, which is called *Redshift Space Distortions* (RSD).

Figure I.5 is an illustration of the RSD effects. On relatively small scales, velocities of collapsing objects caused by gravity in galaxy clusters are big compared to the scale, which

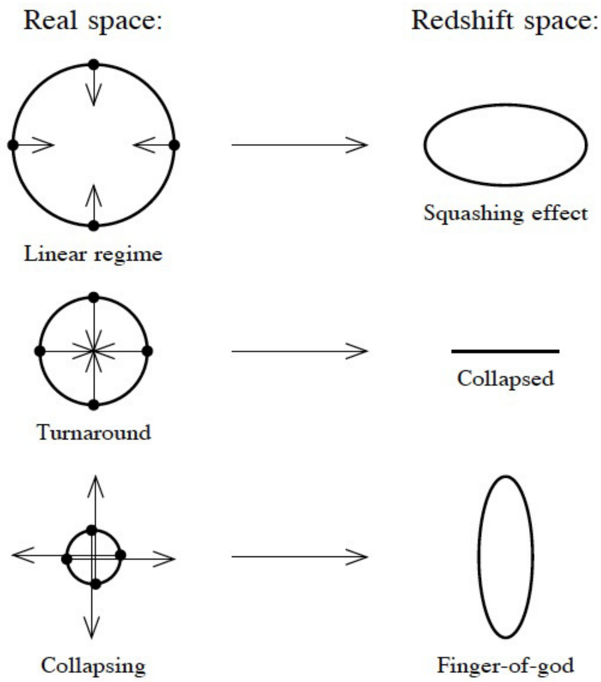

Figure I.5 An illustration presenting how peculiar velocities lead to the redshift distortions (Hamilton 1997).

can make closer galaxies looks far away and vice versa. This forms elongated shapes in redshift space known as “Fingers-of-God” (FoG). But on very large scales, the peculiar velocity of in-falling motion of clusters is small compared to the scale, which causes squashing effects.

RSD is one of the biggest systematics we need to consider in many of the structure analyses. It is essential to carefully model the RSD. Because simulations contain the full dynamical information, we can generate redshift distortions according to the velocities of the particles in the simulation boxes. This allows us to investigate the RSD effects for different statistics in detail and compare the theoretical models to the observed data in redshift space. Thus, N-body simulations and mock galaxy catalogs are a key component in our analyses.

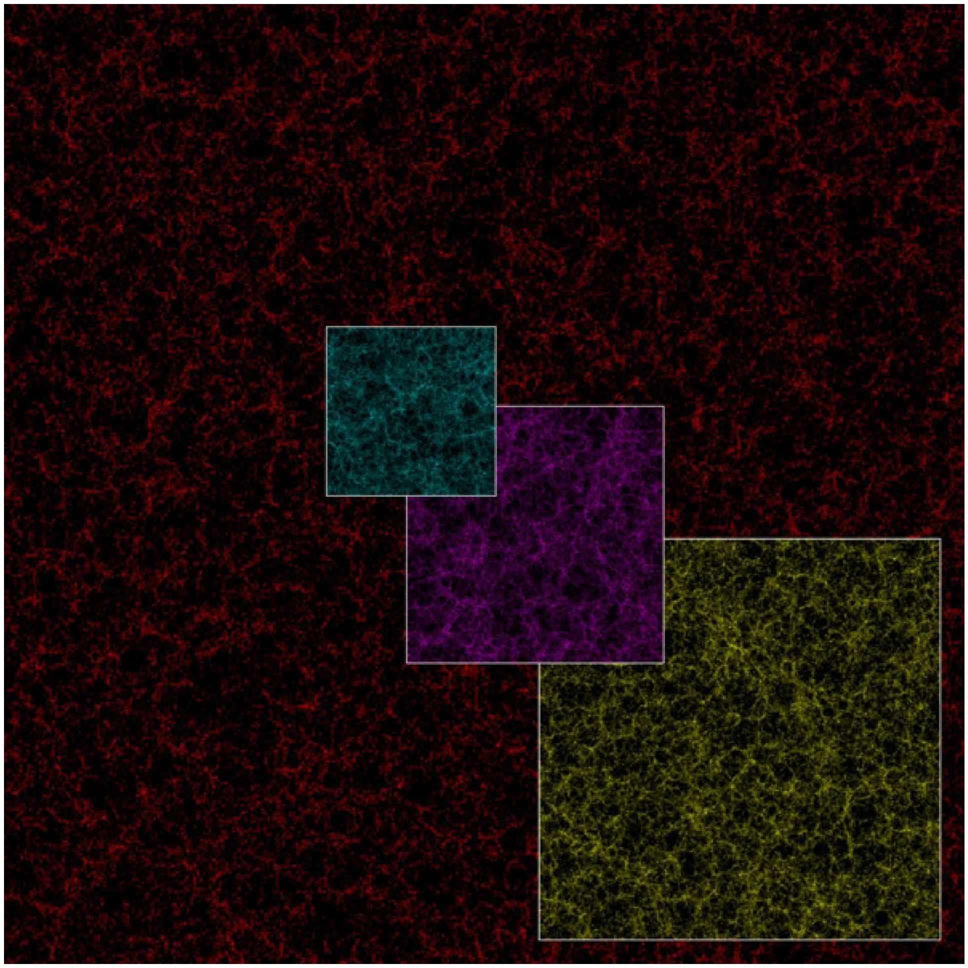

Figure I.6 Smoothed distribution of halos (mass-weighted) of a 40 h^{-1}Mpc thick slice of the four LasDamas simulation boxes. Descending in size: Oriana, Carmen, Esmeralda, and Consuelo. Credit: LasDamas Team.

I.6.3 LasDamas Simulations

One set of the simulations I am using is the *Large Suite of Dark Matter Simulations* (LasDamas) (McBride et al. 2011). LasDamas is a project that runs many cosmological N-body simulations with same cosmological model but different initial phases, i.e. different random seeds when generating the initial conditions. Instead of a single simulation, many realizations together can provide an enormous volume and still have adequate resolution, which is appropriate for statistical studies. All simulations use the following cosmological model: $\Omega_{\rm m} = 0.25$, $\Omega_\Lambda = 0.75$, $\Omega_b = 0.04$, $h = 0.7$, $\sigma_8 = 0.8$, $n_s = 1.0$.

There are four different LasDamas simulation boxes with different box sizes and resolutions for different study purposes, showing in figure I.6. We would like to focus on the *Oriana* simulations, since they have the biggest box size among the four LasDamas boxes and are suitable for doing statistics on very large scales. Each Oriana box has a volume of $(2.4Gpc/h)^3$ and contains 1280^3 particles. The mass of each particle is $45.73 \times 10^{10} h^{-1} M_\odot$, and the softening of the gravitational potential is $53h^{-1}$kpc. CMBfast (Seljak & Zaldarriaga 1996) is used to compute the power spectrum of density fluctuations. The initial density field, started at $z = 49$, is generated and initial positions and velocities are computed for the particles using the 2LPT code (Crocce et al. 2006). The gravitational evolution is then performed using the publicly available Gadget-2 code (Springel 2005). For each realization, i.e. each initial phase, a simulation using Gaussian initial condition is run, as well as a couple of simulations using three different non-Gaussian initial conditions. This allows us to directly compare Gaussian and non-Gaussian models.

Dark matter halos are identified by the FoF method with a linking length $b = 0.2$ in units of the mean inter-particle separation. These halos are populated with mock galaxies using HOD parameters which are adjusted to ensure that the mocks have the same number density and projected correlation functions as observed SDSS samples. These mock galaxy catalogs are created from both Gaussian and non-Gaussian simulations, which allows us to test the effect of primordial non-Gaussianity.

I.6.4 Quick Particle-Mesh Simulations and Mocks

I also use a set of 1,000 mock galaxy catalogs generated using the "quick particle mesh" (QPM) methodology described by White et al. (2014). These QPM mocks were based on a set of rapid but low-resolution particle mesh simulations which accurately reproduce the large-scale dark matter density field. The time steps are set to be quite large and the mesh scale and mean inter-particle spacing exceed the size of all but the largest dark matter halos. In this manner, it can generate enough volume to fit the whole BOSS survey in one simulation box, but still keeps both the run time and the memory requirements modest.

Each QPM simulation contained 1280^3 particles in box of side length 2,560 h^{-1}Mpc. The chosen cosmology has $\Omega_\mathrm{m} = 0.29$, $h = 0.7$, $n_s = 0.97$ and $\sigma_8 = 0.8$. Mock halos were selected based on the local density of each particle. These halos were then populated using the halo occupation distribution method to create galaxy mocks. The HOD was chosen such that the clustering amplitude of mock galaxies matches the observed measurements. The survey masks were then applied so that the mock catalogs have the same survey geometry as the BOSS data. Finally, the mock catalogs were randomly down-sampled to have the same angular sky completeness and the same radial mean $n(z)$ as the data. This set of mocks enables us to characterize the uncertainties and correct for the redshift space distortions for our cosmic voids analysis.

I.7 Summary

Equipped with the tremendous SDSS data and large sets of simulations and mock catalogs, I perform clustering analyses on both extragalactic and Galactic scales. This document is organized as follows. In chapter II, I investigate whether measurements of the moments of large-scale structure can yield constraints on primordial non-Gaussianity. In chapter III, I present a public cosmic void catalog using the most recent large-scale structure galaxy catalog from the BOSS survey data. In chapter IV, I apply the Alcock-Paczyński test to the voids identified in the BOSS data to obtain a constrain on the standard cosmology. In chapter V, I adopt the two-point correlation function statistics, which is widely used in galaxy clustering analysis, and apply it to the SEGUE G-dwarf stars to constrain the structure of the Milky Way. A short conclusion is in chapter VI.

CHAPTER II

Constraining Primordial Non-Gaussianity with Moments of the Large Scale Density Field

Abstract

We use cosmological N-body simulations to investigate whether measurements of the moments of large-scale structure can yield constraints on primordial non-Gaussianity. We measure the variance, skewness, and kurtosis of the evolved density field from simulations with Gaussian and three different non-Gaussian initial conditions: a local model with $f_{\rm NL} = 100$, an equilateral model with $f_{\rm NL} = -400$, and an orthogonal model with $f_{\rm NL} = -400$. We show that the moments of the dark matter density field differ significantly between Gaussian and non-Gaussian models. We also make the measurements on mock galaxy catalogs that contain galaxies with clustering properties similar to those of luminous red galaxies (LRGs). We find that, in the case of skewness and kurtosis, galaxy bias reduces the detectability of non-Gaussianity. However, in the case of the variance, galaxy bias greatly amplifies the detectability of non-Gaussianity. In all cases we find that redshift distortions do not significantly affect the detectability. When we restrict our measurements to volumes equivalent to the Sloan Digital Sky Survey II (SDSS-II) or Baryon Oscillation Spectroscopic Survey (BOSS) samples, the probability of detecting a departure from the Gaussian model is high by using measurements of the variance, but very low by using only skewness and kurtosis. We estimate that in order to detect an amount of non-Gaussianity that is consistent with recent CMB constraints using skewness or kurtosis, we would need a galaxy survey that is much larger than any planned future survey. However, future surveys should be large enough to place meaningful constraints using galaxy variance measurements.

II.1 Introduction

Inflation is the most promising paradigm for the early universe (Guth 1981). The standard inflationary paradigm predicts nearly Gaussian and scale invariant primordial density fluctuations, which are consistent with the observations of the Cosmic Microwave Background (CMB) and Large-Scale Structure (LSS) in the last few decades. However, even the simplest inflation model predicts some small deviation from Gaussianity (Falk et al. 1993; Gangui et al. 1994; Maldacena 2003; Bartolo et al. 2004). Within the standard inflationary paradigm, there are currently many viable inflationary models, but it is difficult to discriminate between them. While most of the popular inflation models predict slight deviations from Gaussian fluctuations, different models predict different amounts and flavors of non-Gaussianity, which makes it a very powerful tool for constraining inflationary models (e.g., see Chen 2010 for a review). Detecting primordial non-Gaussianity is thus an important goal of modern cosmology and it has recently garnered much attention.

The primordial density fluctuations are both the direct cause of CMB anisotropy, and the seeds of large scale structure (LSS) formation. Deviations from primordial Gaussianity can thus leave signals on both the CMB and LSS. To date, observations of the CMB have been playing the central role in constraining the amplitudes of various types of primordial non-Gaussianity, with tight constraints coming from both WMAP (Bennett et al. 2013) and, most recently, Planck (Planck Collaboration et al. 2013, paper XXIV). However, ongoing and future high quality redshift surveys raise hope for detecting non-Gaussianity in LSS. The Sloan Digital Sky Survey (SDSS; York et al. 2000) has provided redshifts of over 100,000 luminous red galaxies (LRGs) in a large volume (Eisenstein et al. 2001), and the ongoing Baryon Oscillation Spectroscopic Survey (BOSS; Dawson et al. 2013), which is part of the SDSS-III project (Eisenstein et al. 2011), is mapping 1.5 million luminous galaxies to redshift $z \sim 0.7$. Future redshift surveys like eBOSS, DESI, and Euclid will map even larger volumes. These surveys provide great opportunities of constraining primordial non-Gaussianity with large-scale structure.

There are several avenues for constraining primordial non-Gaussianity with galaxy surveys, including the galaxy power spectrum, higher order correlations of the density field, e.g., the bispectrum, and statistics of rare peaks, i.e., the abundance of massive clusters. There have been many studies attempting to detect non-Gaussianity using the galaxy power spectrum (e.g., Slosar et al. 2008; Afshordi & Tolley 2008; Ross et al. 2013; Giannantonio et al. 2014). The galaxy bispectrum is much more difficult to measure and there has only been one attempt to use it for the purpose of constraining non-gaussianity (Scoccimarro et al. 2004). However, it provides a highly sensitive probe of non-Gaussianity and is likely to yield the best constraints from LSS with future surveys (Sefusatti & Komatsu 2007; Sefusatti 2009; Baldauf et al. 2011; Scoccimarro et al. 2012)

A much simpler set of statistics for quantifying departures from Gaussianity are the higher order moments of the density field, of which the most frequently used are the third order normalized moment *skewness* and fourth order normalized moment *kurtosis*. Though gravitational evolution contributes most of the signal in these moments in the present day density field, small departures from Gaussianity in the primordial density field may still cause slightly different skewness and kurtosis today, which may be detectable in sufficiently large galaxy redshift surveys.

The evolution of skewness, and kurtosis for Gaussian initial conditions has been studied both analytically and numerically in many published works (Peebles 1980; Fry 1985; Coles & Frenk 1991; Juszkiewicz & Bouchet 1992; Weinberg & Cole 1992; Bouchet et al. 1992; Lahav et al. 1993; Luo & Schramm 1993; Coles et al. 1993; Juszkiewicz et al. 1993; Lucchin et al. 1994; Frieman & Gaztanaga 1994; Bernardeau 1994; Hui & Gaztañaga 1999; Bernardeau et al. 2002). For arbitrary non-Gaussian initial conditions, Fry & Scherrer (1994) computed the evolution of skewness in second-order perturbation theory, and Chodorowski & Bouchet (1996) computed the kurtosis case. Observationally, skewness and kurtosis have been measured for many galaxy redshift surveys (Bernardeau et al. 2002), such as QDOT (Saunders et al. 1991), 1.2Jy IRAS (Bouchet et al. 1992, 1993; Kim & Strauss 1998), CfA-SRSS (Gaztanaga 1992), 1.9Jy IRAS (Fry & Gaztanaga 1994), PPS (Ghigna et al. 1996), SRSS2 (Benoist et al. 1999), PSCz (Szapudi et al. 2000), Durham/UKST (Hoyle et al. 2000), Stromlo/APM (Hoyle et al. 2000), 2dFGRS (Croton et al. 2004), VVDS (Marinoni et al. 2005), and SDSS (Szapudi et al. 2002; Ross et al. 2008; Pápai & Szapudi 2010). So far all results are consistent with Gaussian initial conditions, but these surveys have not had sufficient volume to detect plausible amounts of primordial non-Gaussianity.

With much larger redshift surveys coming out in the next decade, we think this is a good time to revisit this question. Though the skewness and kurtosis contain less information than their corresponding non-zero separation correlations, the 3 and 4-point correlation functions (and their Fourier transforms, the bispectrum and trispectrum), they are conceptually simpler and much easier to measure. In this chapter, we use N-body simulations to investigate the detectability of inflationary-motivated primordial non-Gaussianity from skewness and kurtosis measurements of the present day galaxy distribution. We also investigate the second order moment of the density field, *variance*, which contains similar information to the power spectrum. In §II.2, we review the background theory and some related definitions. In §II.3 we present the details of our simulations, which include both Gaussian and non-Gaussian initial conditions, and we describe how we measure the density field moments from these simulations. We show our results in §II.4, including measurements on both dark matter particles and mock galaxy catalogs constructed to model the distribution of SDSS LRGs. We also make measurements on subsets of the simulations that have volumes equivalent to the SDSS-II and BOSS surveys, and we calculate the likelihood of detecting departures from the Gaussian model with variance, skewness or kurtosis measurements from these surveys. We present our conclusions and some discussion in §II.5.

II.2 Background Theory

II.2.1 Skewness and Kurtosis

The smoothed density fluctuation δ_R with smoothing scale R can be written as

$$\delta_R = \frac{\rho_R}{\langle \rho_R \rangle} - 1, \tag{II.1}$$

where ρ_R is the smoothed density. The *variance* of the density field is $\langle \delta_R^2 \rangle$. Higher order moments are typically normalized by the variance so that the normalized moment of order n is defined as

$$s_n \equiv \frac{\langle \delta_R^n \rangle_c}{\langle \delta_R^2 \rangle^{n/2}}, \tag{II.2}$$

while $\langle \delta_R^n \rangle_c$ is the nth order connected moment. The third and fourth order normalized moments are called *skewness* and *kurtosis* respectively. Another definition commonly used is the *hierarchical amplitude*:

$$S_n \equiv \frac{\langle \delta_R^n \rangle_c}{\langle \delta_R^2 \rangle_c^{n-1}}. \tag{II.3}$$

In the literature of large-scale structure, the third and fourth hierarchical amplitudes S_3 and S_4 are often referred to as the skewness and kurtosis parameters, respectively. Hereafter in this dissertation, we also use this definition:

$$S_3 = \frac{\langle \delta_R^3 \rangle_c}{\langle \delta_R^2 \rangle_c^2} = \frac{\langle \delta_R^3 \rangle}{\langle \delta_R^2 \rangle^2}, \tag{II.4}$$

$$S_4 = \frac{\langle \delta_R^4 \rangle_c}{\langle \delta_R^2 \rangle_c^3} = \frac{\langle \delta_R^4 \rangle - 3\langle \delta_R^2 \rangle^2}{\langle \delta_R^2 \rangle^3}. \tag{II.5}$$

For a Gaussian initial distribution, second-order perturbation theory predicts constant values for these parameters, with $S_3 = 34/7$ (Peebles 1980) and $S_4 = 60712/1323$ (Bernardeau 1992), if smoothing is not considered. Including the effect of top-hat smoothing, S_3 and S_4

can also be derived and have the form (Bernardeau 1994)

$$S_3 = \frac{34}{7} + \gamma_1, \tag{II.6}$$

$$S_4 = \frac{60712}{1323} + \frac{62\gamma_1}{3} + \frac{7\gamma_1^2}{3} + \frac{2\gamma_2}{3}, \tag{II.7}$$

where

$$\gamma_p = \frac{d^p \log \sigma^2(R)}{d \log^p R}, \tag{II.8}$$

and $\sigma^2(R)$ is another way of denoting the variance of the density field smoothed on a scale R.

II.2.2 Non-Gaussian Initial Distribution

To describe primordial non-Gaussianity generated during inflation, the initial conditions are commonly written as the sum of a linear Gaussian term and a non-linear quadratic term that contains the deviation from Gaussianity:

$$\Phi = \phi + \frac{f_{\rm NL}}{c^2}(\phi^2 - \langle \phi^2 \rangle). \tag{II.9}$$

Here Φ is Bardeen's gauge-invariant potential (Salopek & Bond 1990), and ϕ denotes a Gaussian random field. In general, the dimensional parameter $f_{\rm NL}$ is scale and configuration dependent. When $f_{\rm NL}$ is simply a constant, it yields the so called *local* model. In Fourier space, the bispectrum of the local model can be written as (Gangui et al. 1994; Verde et al. 2000; Komatsu & Spergel 2001)

$$B_{local}(k_1, k_2, k_3) = 2 f_{\rm NL}[P(k_1)P(k_2) + 2cyc.]. \tag{II.10}$$

Here $P(k)$ is the power spectrum and $cyc.$ denotes the cyclic terms over k_1, k_2, k_3. The bispectrum for the local type non-Gaussianity peaks when $k_1 \approxeq k_2 \ll k_3$ (the so-called "squeezed" configuration; Babich et al. 2004).

While beyond single-field models of inflation generically predict the local type, single-field models generate predominantly other forms. One is the *equilateral* type, for which the bispectrum peaks when $k_1 \simeq k_2 \simeq k_3$, and can be written as (Creminelli et al. 2006)

$$\begin{aligned} B_{equil}(k_1,k_2,k_3) = 6f_{\rm NL}[&-P(k_1)P(k_2)+2cyc. \\ &-2[P(k_1)P(k_2)P(k_3)]^{2/3} \\ &+P^{1/3}(k_1)P^{2/3}(k_2)P(k_3)+5cyc.]. \end{aligned} \tag{II.11}$$

Senatore et al. (2010) constructed another distinct shape of non-Gaussianity called *orthogonal*, for which the bispectrum can be approximately given by this template:

$$\begin{aligned} B_{orthog}(k_1,k_2,k_3) = 6f_{\rm NL}[&-3P(k_1)P(k_2)+2cyc. \\ &-8[P(k_1)P(k_2)P(k_3)]^{2/3} \\ &+3P^{1/3}(k_1)P^{2/3}(k_2)P(k_3)+5cyc.]. \end{aligned} \tag{II.12}$$

More precisely, this template is only a good approximation to the orthogonal shape away from the squeezed limit ($k_3 \to 0$). This is relevant to the calculation of the large-scale bias, as the more accurate template does not lead to a scale-dependent bias at low-k whereas the simpler template in equation (II.12) leads to a $1/k$ correction to the bias. On the other hand, such a behavior is interesting from a phenomenological point of view as it is in between scale independence and the $1/k^2$ of local PNG. In this chapter, we use N-body simulations that are generated with all three of the above types of non-Gaussian initial conditions, and are described in detail by Scoccimarro et al. (2012).

The evolution of skewness for non-Gaussian initial conditions was first investigated by Fry & Scherrer (1994); this was extended to the kurtosis by Chodorowski & Bouchet (1996). Although general expressions for S_3 and S_4 can be derived for arbitrary non-Gaussian initial conditions, these generally involve complicated integrals over the initial density field correlators and are not easily generalized to the smoothed density field. For S_3, for example, the general expression consists of a term encoding the initial (non-Gaussian) value for S_3, which decays as $1/a$, where a is the scale factor, a second "Gaussian" term which is constant and equal to the Gaussian value for S_3, and a third set of terms that are also constant and depend on the initial 3-point and 4-point correlations in the initial density field.

For the local non-Gaussian model, Scoccimarro et al. (2004) derived an expression for the evolved bispectrum. Similar to the derivation in Fry & Scherrer (1994), the evolved bispectrum contains a "Gaussian" piece identical to the bispectrum for Gaussian initial conditions, a "non-Gaussian" piece corresponding to the non-Gaussian initial value of S_3, and a third piece arising from the trispectrum. Scoccimarro et al. (2004) noted that the second term scales as $f_{\rm NL}$, while the third scales as $f_{\rm NL}^2$. Thus, in the limit of small $f_{\rm NL}$, it is sufficient to consider only the contributions from the Gaussian term and the term arising from the initial skewness. These terms can be integrated with the appropriate window functions to give a reasonable estimate for S_3 for non-Gaussian initial conditions (Scoccimarro et al. 2004; Lam & Sheth 2009; Lam et al. 2009). The value of S_3 in the evolved density field then involves a competition between the intrinsic initial value for S_3, which dominates on large scales, and the evolved Gaussian piece, which dominates on small scales. Of course, in either case the expressions derived from quasi-linear perturbation theory become progressively less accurate on smaller (more nonlinear) scales. In this chapter, we only compare our results to the analytic expressions for S_3 and S_4 in the case of Gaussian initial conditions, i.e., equations (II.6) and (II.7). We only mention the non-Gaussian analytic expressions for the insight that they offer into our numerical results.

II.2.3 Galaxy Bias

In redshift surveys we observe galaxies, and their distribution is "biased" relative to the underlying mass distribution. We assume that the smoothed galaxy density fluctuation is a local function of the smoothed mass density fluctuation and can be expressed as a Taylor series:

$$\delta_R^{gal} = \sum_{k=0}^{\infty} \frac{b_k}{k!} \delta_R^k. \tag{II.13}$$

Here b_0 is fixed to be $b_0 = -\sum_{k=2}^{\infty} b_k \langle \delta_R^k \rangle / k!$ to make sure $\langle \delta_R^{gal} \rangle = 0$. The b_1 term corresponds to the usual linear bias factor b, and b_2 is the nonlinear quadratic bias. These bias factors are scale dependent on small scales, but they become scale independent on large scales (Manera & Gaztañaga 2011). By using the hierarchical relation equation (II.3), the relation between the skewness and kurtosis parameters for galaxies and mass can be derived as (Fry & Gaztanaga 1993):

$$S_3^{gal} = b^{-1}(S_3 + 3c_2), \tag{II.14}$$

$$S_4^{gal} = b^{-2}(S_4 + 12c_2 S_3 + 4c_3 + 12c_2^2), \tag{II.15}$$

where $c_k = b_k / b$ for $k \geq 2$.

Now let us consider the effect of biasing on the measurement of the variance and S_3 for non-Gaussian initial conditions. The total linear bias can be written as the usual (Gaussian) bias b_G plus a non-Gaussian correction:

$$b_{NG} = b_G + \Delta b_{f_{\rm NL}}. \tag{II.16}$$

In general, the non-Gaussian correction of bias depends not only on $f_{\rm NL}$, but also on scale. Dalal et al. (2008) showed that for the local non-Gaussian model the linear bias correction depends on scale k as

$$\Delta b_{f_{\rm NL}}(k) = 2(b_G - 1) f_{\rm NL} \delta_c \frac{3\Omega_m}{2ag(a) r_H^2 k^2}, \tag{II.17}$$

where Ω_m is the matter density parameter, a is the scale factor, r_H is the Hubble radius, δ_c is the critical threshold for collapse, and $g(a)$ is the growth suppression rate defined as

$D(a)/a$, where $D(a)$ is the growth factor. A similar scale dependence due to $f_{\rm NL}$ holds for the quadratic bias factor b_2 (Giannantonio & Porciani 2010; Scoccimarro et al. 2012), which must be considered when discussing S_3. These results give corrections to the bias in Fourier space that are scale (k) dependent and they can be used to calculate the bispectrum for the local non-Gaussian case. One can then integrate the resulting bispectrum numerically to obtain the skewness at a scale R.

II.2.4 Discrete Distribution

Whether we measure density using dark matter particles or galaxies, in a simulation we always deal with discrete numbers of points. Specifically, we measure density by counting the number of dark matter particles or galaxies within top-hat spheres. The density fluctuation with smoothing radius R is then

$$\delta_R = \frac{N}{\langle N \rangle} - 1, \tag{II.18}$$

where N is the number of particles in a given sphere and $\langle N \rangle$ is the mean over all spheres. Since counts are discrete numbers, we cannot directly use equations (II.4) and (II.5) to calculate S_3 and S_4. Here we apply a Poisson correction (Peebles 1980) using the Lahav et al. (1993) notation. The moments of the density fluctuation δ_R can be expressed in terms of the n-point correlation functions and Poisson terms involving $\langle N \rangle$:

$$\langle \delta_R^2 \rangle = \frac{1}{\langle N \rangle} + \Psi_2, \tag{II.19}$$

$$\langle \delta_R^3 \rangle = \frac{1}{\langle N \rangle^2} + \frac{3}{\langle N \rangle}\Psi_2 + \Psi_3, \tag{II.20}$$

$$\langle \delta_R^4 \rangle = \frac{1}{\langle N \rangle^3} + \frac{1}{\langle N \rangle^2}(3+7\Psi_2) + \frac{6}{\langle N \rangle}(\Psi_2+\Psi_3) + 3\Psi_2^2 + \Psi_4, \tag{II.21}$$

where

$$\Psi_2 = \frac{1}{V^2}\int \xi_{12} dV_1 dV_2, \tag{II.22}$$

$$\Psi_3 = \frac{1}{V^3} \int \zeta_{123} dV_1 dV_2 dV_3, \tag{II.23}$$

$$\Psi_4 = \frac{1}{V^4} \int \eta_{1234} dV_1 dV_2 dV_3 dV_4. \tag{II.24}$$

ξ_{12}, ζ_{123}, η_{1234} denote two-, three- and four-point correlation functions, and V is the volume of the smoothing sphere.

We can measure the moments of δ_R and the mean counts $\langle N \rangle$ directly from the simulations, solve for Ψ_2, Ψ_3 and Ψ_4 using equations II.19–II.21, and then evaluate S_3 and S_4 as

$$S_3 = \frac{\Psi_3}{\Psi_2^2}, \tag{II.25}$$

$$S_4 = \frac{\Psi_4}{\Psi_2^3}. \tag{II.26}$$

These are the main equations we use to measure the variance, skewness, and kurtosis parameters in this dissertation.

II.3 Simulated Data

II.3.1 LasDamas Simulations

We use simulated data from the Large Suite of Dark Matter Simulations project (LasDamas; McBride et al. 2009). The LasDamas project has focused on running many independent N-body realizations with the same cosmology but different initial phases. The simulation data we analyze have WMAP5 motivated cosmological parameters, specifically $\Omega_m = 0.25, \Omega_\Lambda = 0.75, \Omega_b = 0.04, h = 0.7, \sigma_8 = 0.8, n_s = 1.0$. The LasDamas simulations are designed to model SDSS galaxies and contain four different volume and resolution configurations that were chosen to match different luminosity samples. In this chapter we focus on the the largest volume “Oriana” realizations, which are designed to model SDSS LRGs. Each Oriana simulation evolves 1280^3 dark matter particles in a cubic volume of $2.4h^{-1}$Gpc on a side, resulting in a particle mass of $45.7 \times 10^{10} h^{-1} M_\odot$. The simulations are seeded with second-order Lagrangian perturbation theory (2LPT) initial conditions (Scoccimarro 1998; Crocce et al. 2006) and evolved from a starting redshift of $z_{init} = 49$ to $z = 0$ using the Gadget-2 code (Springel 2005), with a gravitational force softening of $53h^{-1}$kpc.

The initial density field for the LasDamas simulations is Gaussian, and here we analyze 40 Oriana realizations (over $550h^{-3}$Gpc^3 total volume). To complement these simulations, we also have sets of simulations seeded with three different models of primordial non-Gaussianity: local, equilateral and orthogonal. These simulations are described in detail by Scoccimarro et al. (2012). Specifically, we have 12 realizations of each non-Gaussian model, and these are constrained to have the same box size, resolution and initial phases as 12 of the Gaussian Oriana realizations. We can thus compare the Gaussian and three non-Gaussian models in 12 boxes ($165h^{-3}$Gpc^3 total volume per model) without having to worry about cosmic variance differences.

The non-Gaussian models we use have $f_{\rm NL}$ amplitudes of 100 for the local model, and -400 for each of the equilateral and orthogonal models. These values were marginally consistent with constraints from WMAP at the time that the simulations were run. However, the recent Planck constraints have ruled these models out definitively, since they constrain $f_{\rm NL}$ to be consistent with zero with 1σ errors of 5.8, 75, and 39 for the local, equilateral, and orthogonal models, respectively (Planck Collaboration et al. 2013). It is thus important to emphasize that the results that we present in this dissertation apply to our specific models and are exaggerated with respect to realistic models. In § II.4.4, we discuss how some of our conclusions might scale to much lower amplitude non-Gaussian models that are still allowed by the Planck constraints.

II.3.2 Mock Galaxy Catalogs

To include the effects of galaxy bias, we analyze mock galaxy catalogs that model SDSS-II LRG galaxies. Specifically, we use two sets of mock catalogs from LasDamas that correspond to LRG samples with g-band absolute magnitudes of $M_g < -21.2$ and LRG $M_g < -21.8$. The average comoving number density of these samples is $9.7 \times 10^{-5}\ h^3$Mpc^{-3}

and $2.4 \times 10^{-5}\ h^3\mathrm{Mpc}^{-3}$, respectively (Zehavi et al. 2005; Kazin et al. 2010). The mock catalogs were constructed by first identifying friends-of-friends halos in the dark matter distribution at $z = 0.34$ (roughly the median redshift of the brighter LRG sample), and then populating these halos with galaxies using a halo occupation distribution (HOD; Berlind & Weinberg 2002). The parameters of the HOD were determined by fitting to the observed small-scale clustering of LRGs, as described by McBride et al. (2009). In each halo, a central galaxy was placed at the halo center and given the halo's mean velocity, and satellite galaxies were given the positions and velocities of randomly selected dark matter particles within the halo. We do not apply realistic observational sky footprints to our mock catalogs within the analysis we present here, but rather use the whole simulation cubes. To include the effects of redshift space distortions, we make use of the distant-observer approximation in the mock galaxy catalogs. In other words, we add distortions using the peculiar velocity component along a single coordinate axis of the simulation cubes. The linear bias of galaxies in our mock catalogs is approximately $b \sim 2.2$ and 2.6 for the lower and higher luminosity samples, respectively. This range of bias is roughly consistent with both SDSS LRGs (Marín 2011), and BOSS galaxies (Parejko et al. 2013; Nuza et al. 2013; Guo et al. 2013), so results from our mock samples are relevant to both survey data sets.

II.3.3 Survey Equivalent Volumes

We wish to estimate the observational constraints from measurements of variance, S_3 and S_4 using realistic sized surveys. For this reason, we create subsets of our total simulation volume to match the volumes of the SDSS-II LRG and BOSS samples (in both cases, however, we use the SDSS II LRG mock galaxies described above). SDSS-II has a sky coverage of about $8000\mathrm{deg}^2$ and the brightest LRG sample can reach a redshift $z \sim 0.45$ (Eisenstein et al. 2001), which results in a comoving volume of approximately $1h^{-3}\mathrm{Gpc}^3$. BOSS covers about $10000\mathrm{deg}^2$ area and includes galaxies out to $z \sim 0.7$ (Eisenstein et al. 2011), corresponding to a comoving volume of approximately $4h^{-3}\mathrm{Gpc}^3$. Each of the

Oriana simulation boxes has a comoving volume of $2.4^3 h^{-3}\mathrm{Gpc}^3 = 13.8 h^{-3}\mathrm{Gpc}^3$, which we trim to make many realizations of each survey volume. To do this, we cut each box into slices that have volumes equivalent to SDSS-II or BOSS. We leave gaps between subsets to ensure that there are no overlaps between subsets for our density estimates, even with the largest smoothing scale that we employ ($100h^{-1}$Mpc). For the 12 simulations of 3 non-Gaussian models, this results in 144 SDSS-II like surveys ($1h^{-3}\mathrm{Gpc}^3$) and 36 BOSS like surveys ($4h^{-3}\mathrm{Gpc}^3$) for each model. We apply the same method to our Gaussian simulations, but since we start with 40 Gaussian realizations, we end up with 480 SDSS-II volume subsets and 120 BOSS volume subsets.

II.4 Results

In each simulation box we estimate densities δ_R within top-hat smoothing spheres that are arranged on a grid of positions. Since the total volume covered by these spheres will vary with smoothing scale, we add more spheres on small scales and discard some spheres on large scales to ensure that the total volume covered by spheres is always roughly the same on every scale. We then calculate Ψ_2 from equation (II.19), and S_3 and S_4 from equations (II.25) and (II.26). In all the results that follow, we use a set of ten smoothing scales ranging from $10h^{-1}$Mpc to $100h^{-1}$Mpc.

II.4.1 Dark Matter

We first focus on the moments measured from the full dark matter particle distribution. We use all 12 simulation boxes for each non-Gaussian model, as well as the 12 Gaussian boxes with matching initial phases. Figure II.1 shows the variance (top panels), skewness (middle panels), and kurtosis (bottom panels) parameters as a function of scale for these different models. The points in the left three panels represent the mean Ψ_2, S_3, and S_4 from the 12 realizations and the error bars show the uncertainty of the mean estimated from their standard deviation. In the case of skewness and kurtosis, we also show the the perturbation theory prediction of the Gaussian model, which we calculate for each realization using

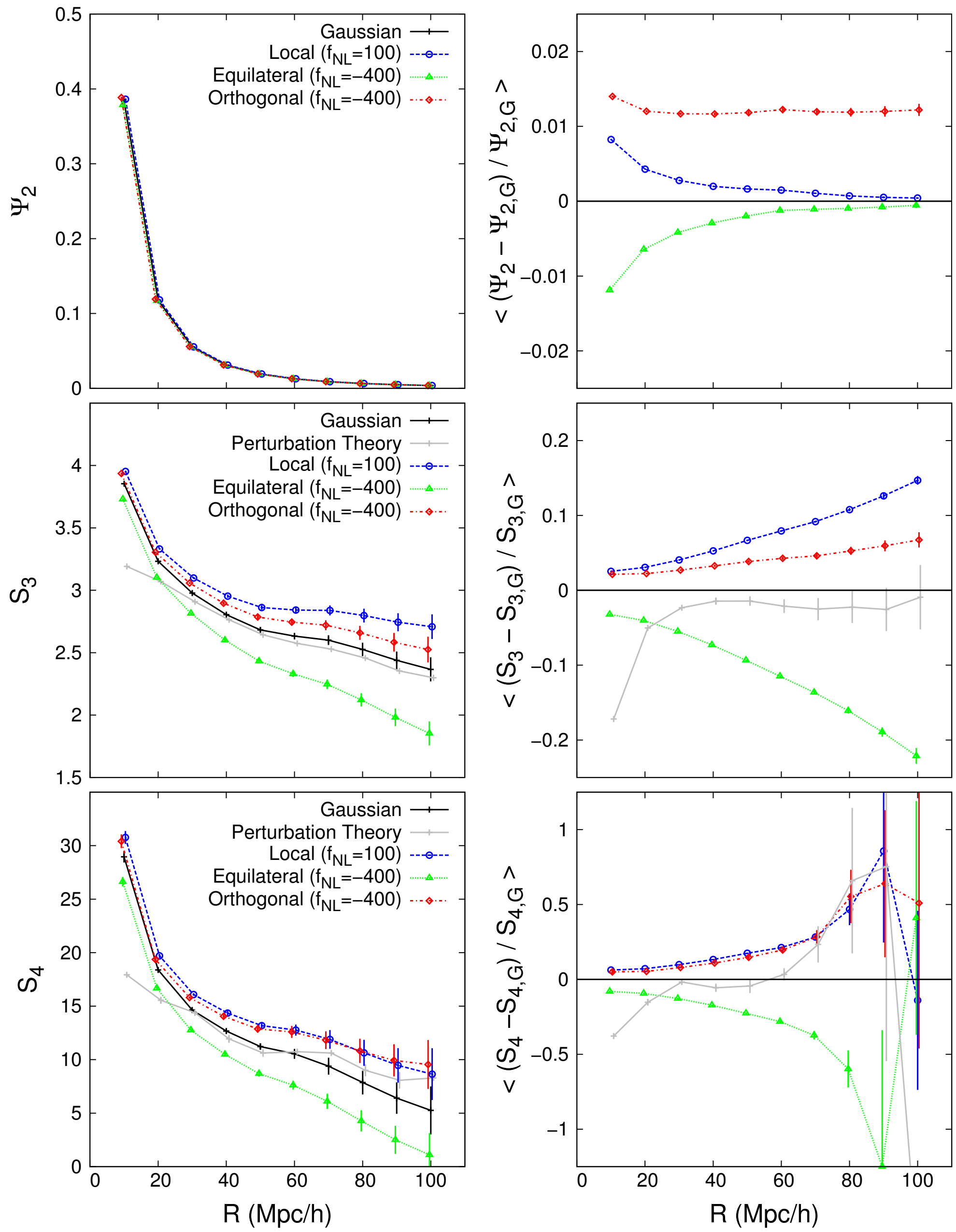

Figure II.1 Ψ_2 (top left panel), S_3 (middle left panel), and S_4 (bottom left panel) measurements as a function of smoothing scale for the dark matter distribution in the Gaussian and non-Gaussian simulations. Also shown are the theoretical predictions for S_3 and S_4 in the Gaussian case from perturbation theory, which are numerically calculated using equations (II.6) and (II.7). Right hand panels show the corresponding residuals of all models with respect to the Gaussian model. In all cases, points show the mean of 12 simulation realizations and error bars show the uncertainty in the mean calculated from their standard deviation. Residuals are likewise calculated separately for each realization and then averaged.

equations (II.6), (II.7), and (II.8). We evaluate the derivatives in equation (II.8) by spline fitting σ^2 as a function of smoothing scale and then taking the numerical derivatives. For each realization, we also calculate the residuals between each non-Gaussian model and the Gaussian model, and we show the mean residuals over the 12 realizations along with their errors in the three right panels of Figure II.1. Since each realization of the non-Gaussian models and the Gaussian model have the same initial phases, the residuals calculated in this way are not sensitive to cosmic variance.

Let us first focus on results for the variance Ψ_2, shown in the top two panels. The variance in the non-Gaussian models is almost identical to that of the Gaussian case. The residuals show that the local and equilateral models have a $\sim 1\%$ deviation from the Gaussian variance on the smallest scale we consider, but this deviation vanishes at larger scales. In contrast, the orthogonal model has a roughly constant $\sim 1\%$ deviation from the Gaussian variance at all scales. We now move on to the skewness S_3, shown in the middle two panels. The residuals clearly show that different non-Gaussian models have different skewness, and the discrepancy increases with scale. For example, the local non-Gaussian model has a skewness that is 3% higher than the Gaussian model at a scale of $10h^{-1}$Mpc, but climbs to 15% when measured using $100h^{-1}$Mpc smoothing. The difference in sign of the residuals with respect to the Gaussian case is not determined by $f_{\rm NL}$ alone, e.g. local and orthogonal have positive residuals (despite having opposite signs of $f_{\rm NL}$) and equilateral has negative residuals (despite having the same $f_{\rm NL}$ as orthogonal). This is a result of integrating over the non-trivial configuration dependence of the bispectrum in each case (see Eqs. II.10$-$II.12). Note that though the departure from the Gaussian model grows with scale, so do the skewness error bars. It is thus not obvious from this result which scales can yield the tightest constraints on models. We investigate this further below. Lastly, we turn to the kurtosis parameter S_4, shown in the bottom two panels. The difference between the kurtosis of the Gaussian and non-Gaussian models is clear to see and is actually larger than it was for the skewness, reaching as high as 50% at large scales. However, the error bars for our kurtosis measurements are substantially larger than they were for the skewness, such that the signal-to-noise of the measurement actually worsens.

Figure II.1 also shows that the perturbation theory prediction for S_3 in the Gaussian case, as given by equation II.6, is fairly accurate on scales larger than $30h^{-1}$Mpc. We detect a 2% offset that is consistent with loop corrections in perturbation theory (Scoccimarro & Frieman 1996; Fosalba & Gaztanaga 1998), which are not included in equation (II.6). On smaller scales, the accuracy of the prediction drops dramatically, which is expected since perturbation theory breaks down on those scales. The perturbation theory prediction for S_4, which we calculate using equation (II.7), is fairly accurate on scales larger than $30h^{-1}$Mpc, but fails substantially on smaller scales, as expected. The discrepancy seen for scales larger than $70h^{-1}$Mpc is not statistically significant.

II.4.2 Mock Galaxy Catalogs

We next investigate the role of galaxy bias on the moments of the density field by measuring them on mock galaxy catalogs instead of the full dark matter distribution. The two catalogs we use correspond to two SDSS LRG samples with absolute magnitude thresholds of $M_g < -21.8$ and $M_g < -21.2$. We measure Ψ_2, S_3, and S_4 for all the mock catalogs (12 simulation realizations $\times$ 4 sets of initial conditions $\times$ 2 galaxy samples) using the same method we applied to the dark matter particles. Figure II.2 shows Ψ_2 (top panel) S_3 (middle panel), and S_4 (bottom panel) measurements on dark matter particles and the two mock galaxy catalogs in the Gaussian case. Mock galaxy results are shown both with and without redshift distortions.

Galaxy bias boosts the variance on all scales, as expected. This is because the variance of the galaxy density field is equal to the variance of the mass field times the linear bias factor squared. Since SDSS LRGs have a bias factor of ~ 2, we expect their variance to be roughly four times higher than that of the mass field. Moreover, we expect the more luminous (and thus highly biased) LRG sample to have a higher variance than the lower

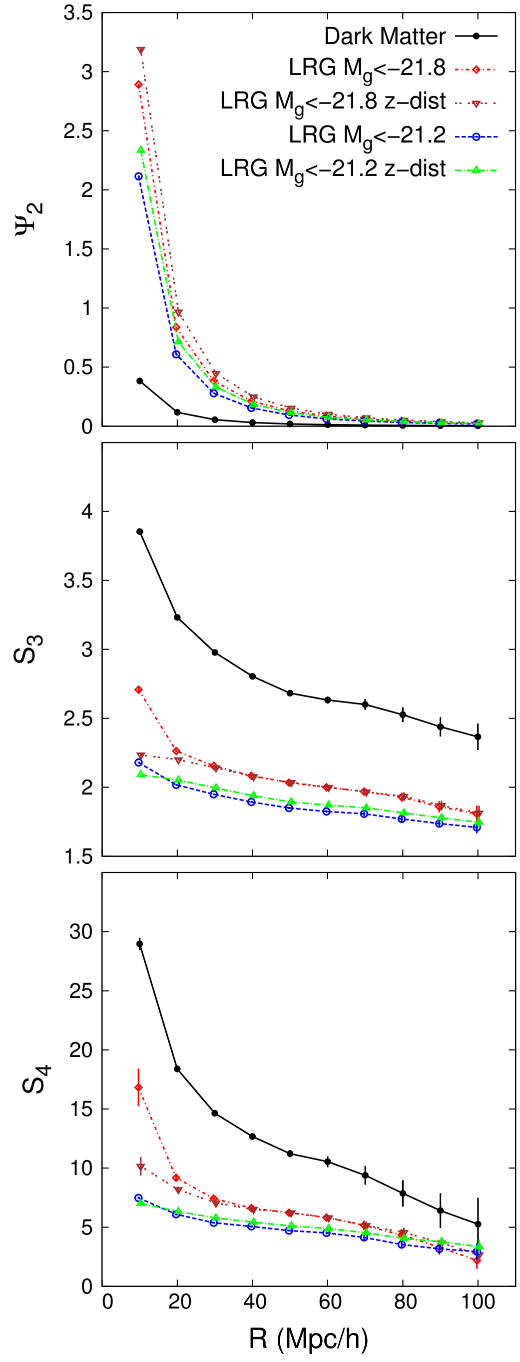

Figure II.2 Ψ_2 (top panel), S_3 (middle panel), and S_4 (bottom panel) measurements as a function of smoothing scale on Gaussian simulations for dark matter particles and two mock galaxy catalogs corresponding to SDSS LRGs with $M_g < -21.8$ and $M_g < -21.2$. For each galaxy sample, results are shown both with and without redshift distortions. As in Fig.II.1, points show the mean of 12 simulation realizations and error bars show the uncertainty in the mean.

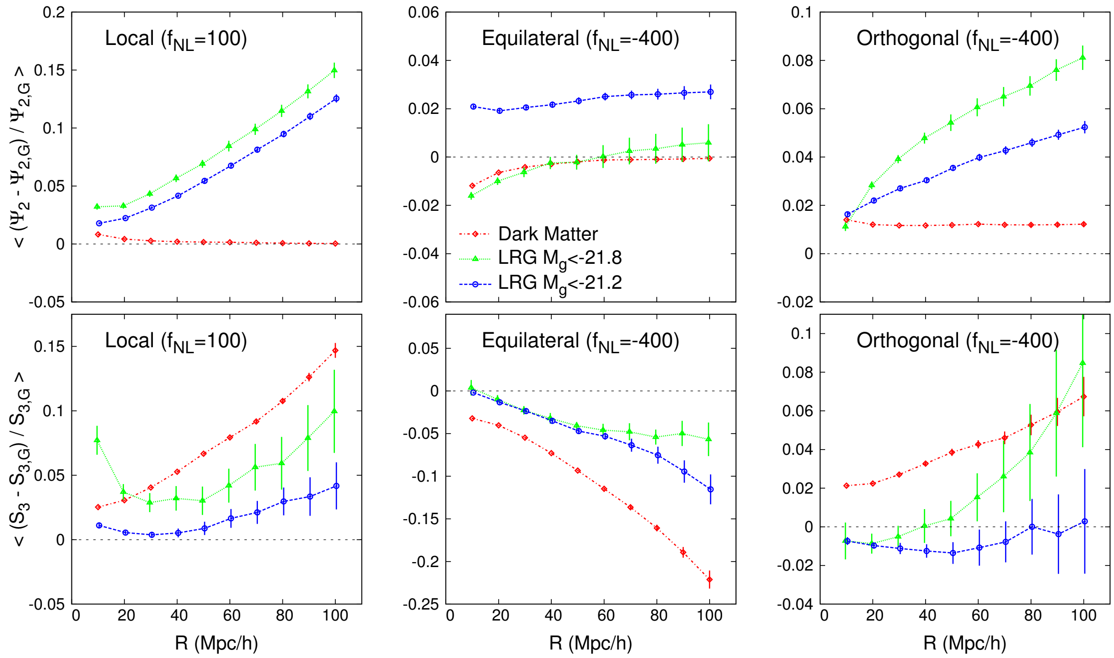

Figure II.3 The effect of galaxy bias on the Ψ_2 (top panels) and S_3 (bottom panels) residuals of non-Gaussian models with respect to the Gaussian model. Each column of panels shows a different non-Gaussian model and the three different lines show residuals for dark matter (red dot-dashed lines), mock LRGs with $M_g < -21.8$ (green dotted lines) and mock LRGs with $M_g < -21.2$ (blue dashed lines). The residuals are averaged over 12 simulation realizations and error bars show the uncertainty of the mean.

luminosity sample, which is also clear in the top panel of Figure II.2. Redshift distortions lead to a small increase in the variance on all the scales that we consider. This is because our scales are all in the quasilinear regime where distortions boost the clustering.

Galaxy bias also has a large effect on S_3, decreasing its amplitude by $\sim 30-40\%$. This is because the skewness generally scales with the inverse of the linear bias factor, as seen in equation (II.14). It is interesting that the more luminous (and highly biased) sample has a higher skewness than the lower bias sample. This is due to the nonlinear quadratic bias term in the same equation, which is larger for the more luminous sample. Redshift distortions generally reduce the skewness on small scales and boost it on large scales; however the exact effect depends on the galaxy sample. In the more luminous of our two samples redshift distortions do not affect the skewness on scales larger than $30h^{-1}$Mpc, whereas in

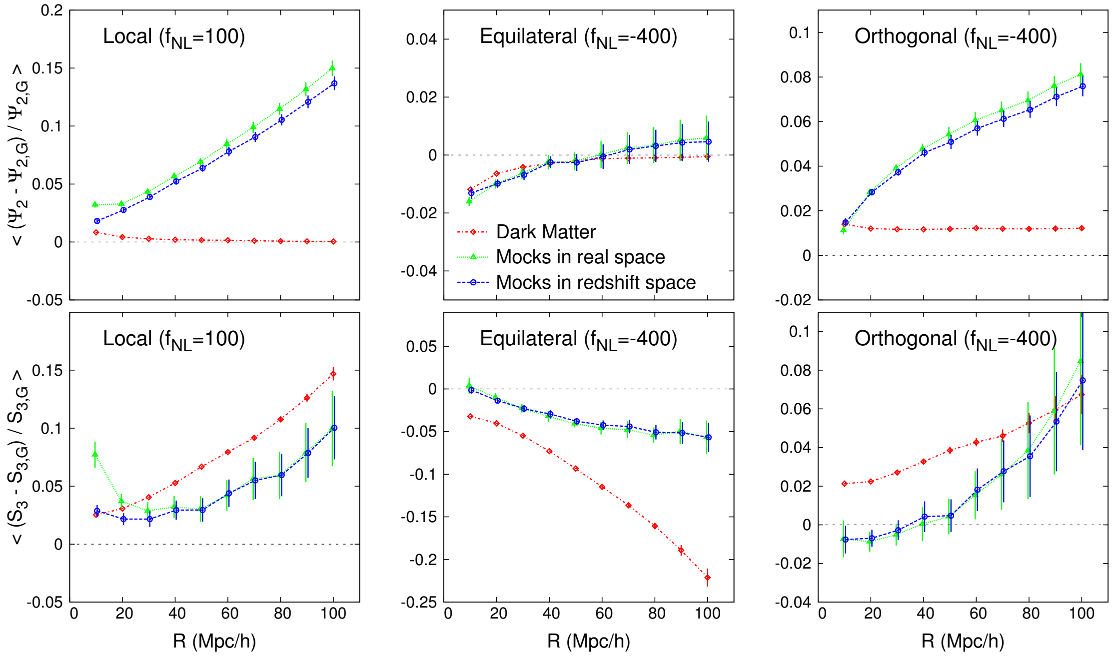

Figure II.4 The effect of redshift distortions on the Ψ_2 (top panels) and S_3 (bottom panels) residuals of non-Gaussian models with respect to the Gaussian model. Each column of panels shows a different non-Gaussian model and the three different lines show residuals for dark matter (red dot-dash lines), mock galaxies in real space (green dot lines) and mock galaxies in redshift space (blue dash lines). The mock galaxies in both cases represent LRGs with $M_g < -21.8$. The residuals are averaged over 12 simulation realizations and error bars show the uncertainty of the mean.

the less luminous sample redshift distortions boost the skewness by $\sim$2% on large scales. Similar results for galaxy bias and redshift distortions hold for the kurtosis S_4.

We next focus on the effect of galaxy bias and redshift distortions on non-Gaussian models and, in particular, on the detectability of the models. In other words, we investigate to what extent bias and redshift distortions affect non-Gaussian models differently from Gaussian models. In this discussion, we only show results for Ψ_2 and S_3 because S_4 is substantially noisier than S_3. Figure II.3 shows the Ψ_2 (top panels) and S_3 (bottom panels) residuals between the three non-Gaussian models (each in a different panel) and the Gaussian model for dark matter and the two mock galaxy catalogs. As before, residuals are first calculated for each realization and then averaged.

Galaxy bias has a dramatic effect on the detectability of non-Gaussianity using the variance, particularly for the local case, as expected from power spectrum results (Dalal et al. 2008). While the deviation from the Gaussian model in the dark matter density field is minimal, it becomes significant in the galaxy mock catalogs. This is because non-Gaussianity leads to corrections in the linear bias factor. In the case of the local non-Gaussian model (top left panel), the fractional difference of the galaxy variance relative to the Gaussian model climbs steadily with scale and reaches as high as 15% at the largest scale we consider. In addition, the more luminous sample shows a larger deviation than the lower luminosity sample. This behavior is consistent with the bias correction term given by equation (II.17), which shows that the correction grows with both scale and the bias itself. We see similar qualitative behavior for the orthogonal non-Gaussian model (top right panel), though the overall amplitude of the effect is smaller. This is understood from the squeezed limit of the orthogonal template used here, which generates a $1/k$ bias, as discussed after equation (II.12). In the equilateral non-Gaussian model, however, results are different, with the more luminous sample showing a negligible deviation from the Gaussian case, and the less luminous sample showing a $\sim 2\%$ higher variance at all scales.

Looking at the skewness, the residuals for the mock galaxies have much larger uncertainties than for the dark matter because the galaxy catalogs have much lower number densities. Nevertheless, it is clear that for all three non-Gaussian models galaxy bias significantly reduces the deviation of the skewness parameter from the Gaussian case. Moreover, this reduction is scale dependent, indicating that scale dependent bias affects the detectability of non-Gaussian models. The precise relationship between the amount of galaxy bias and the residual skewness is complex and depends on both scale and choice of non-Gaussian model. For example, in the local and orthogonal non-Gaussian models the more luminous mock galaxy sample yields a larger residual than the lower luminosity mock sample. However, in the equilateral non-Gaussian model the opposite is true. Though we do not show results for the kurtosis, we find similar results as we did for skewness: galaxy bias generally degrades the discrepancy (and hence detectability) between non-Gaussian and Gaussian models.

Figure II.4 shows the effect of redshift distortions on the Ψ_2 (top panels) and S_3 (bottom panels) residuals. Each panel shows a different non-Gaussian model and shows results for the more luminous $M_g < -21.8$ mock galaxy sample. In almost all cases, the difference between the results on mock galaxy catalogs with and without redshift distortions is negligible. The only exception to this is a $\sim 1\%$ deviation for the variance of the local non-Gaussian model. Redshift distortions thus affect Ψ_2 and S_3 similarly in the Gaussian and non-Gaussian cases, and therefore do not affect the detectability of non-Gaussianity from these measurements. We find the same qualitative result when investigating the kurtosis.

II.4.3 SDSS-II and BOSS Equivalent Volumes

We have shown that non-Gaussian initial conditions leave signatures in the skewness of the evolved dark matter density field and that these signatures remain (though diminished) in the galaxy density field as measured in redshift space. In the case of the variance, non-Gaussian initial conditions leave their strongest signatures in the galaxy density field. However, in most cases we have investigated, the differences from the Gaussian model are fairly small and they tend to be strongest at the largest scales, where cosmic variance errors are also large. In order to quantify whether moments of the density field can be used to constrain non-Gaussian models with measurements from current galaxy surveys, we now use the subsets of our mock catalogs that have volumes equivalent to those of SDSS-II and BOSS, as described in §II.3.3.

Figure II.5 shows the distribution of Ψ_2 and S_3 measurements over these subsets of the local non-Gaussian simulations, for the case of mock LRGs with $M_g < -21.8$ in redshift space. Solid black curves show the mean over all subsets and the shaded grey regions show their standard deviation. The shaded regions thus span the range of skewness values that we would likely measure from SDSS-II (left panels) or BOSS (right panels) if the local

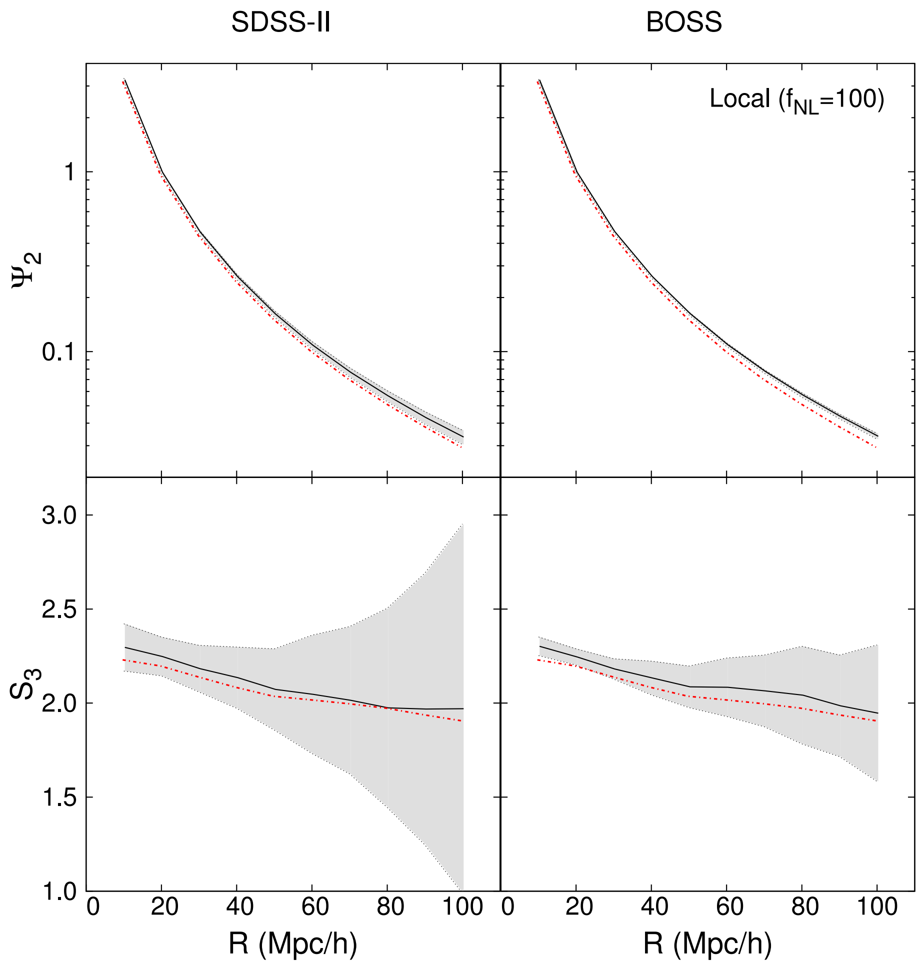

Figure II.5 Ψ_2 (top panels) and S_3 (bottom panels) measurements on SDSS-II (left panels) and BOSS (right panels) equivalent volumes. Each panel shows the mean (solid black curve) and standard deviation (shaded grey region) of the variance or skewness for the local non-Gaussian model, as measured from many independent samples of volume equal to the SDSS-II LRG or BOSS survey. In all cases, the measurements are made on mock LRGs with $M_g < -21.8$ in redshift space. For comparison, the red dot-dashed curves show the result for the Gaussian case, averaged over all our Gaussian simulations.

non-Gaussian model studied here correctly described the universe. For comparison, the red dot-dashed curves show the Gaussian case, which is averaged over all 40 of our Gaussian simulation boxes. The moments of the Gaussian model are thus very well defined and we can ignore their uncertainties. Comparing the red dot-dashed curves with the shaded regions gives us a sense of how well we can discriminate between the local non-Gaussian model and the Gaussian model by measuring Ψ_2 or S_3 from one of the surveys. Since the skewness of the Gaussian model lies within the 1σ range of measurements on all scales and for both survey volumes, it is clear that these surveys will not have the power to detect local non-Gaussianity using skewness measurements, even at the unrealistically large $f_{\rm NL}$ value of our simulations. However, the variance of the Gaussian model lies well outside the shaded region - especially for the BOSS equivalent volumes. This means that a measurement of the variance from the BOSS survey could in principle be used to detect local non-Gaussianity with our adopted $f_{\rm NL}$ value.

To quantify this result, we calculate the likelihood that a given survey will detect the departure from primordial Gaussianity using a Ψ_2, S_3, or S_4 measurement on each scale. For each non-Gaussian model (e.g., local model), mock galaxy luminosity (e.g., LRGs with $M_g < -21.8$), survey volume (e.g., BOSS), choice of moment (e.g., skewness), and scale (e.g., $20h^{-1}$Mpc), we calculate the χ^2 value between the measurement of each non-Gaussian subset and the "true" Gaussian measurement. For example, in the case of the skewness, this is

$$\chi_i^2 = \frac{(S_{3NG,i} - S_{3G})^2}{(\sigma_{S_{3G}})^2}, \tag{II.27}$$

where $S_{3NG,i}$ is the skewness of the ith non-Gaussian subset (we have 144 subsets for SDSS-II and 36 for BOSS), S_{3G} is the "true" skewness of the Gaussian model measured from all 40 Gaussian simulation boxes, and $\sigma_{S_{3G}}$ is the standard deviation of skewness values measured from all the Gaussian subsets (we have 480 subsets for SDSS-II and 120 for BOSS). Note that $\sigma_{S_{3G}}$ is not the standard deviation of the non-Gaussian subsets as shown in Figure II.5. We choose to use the Gaussian subsets because we have many more Gaussian

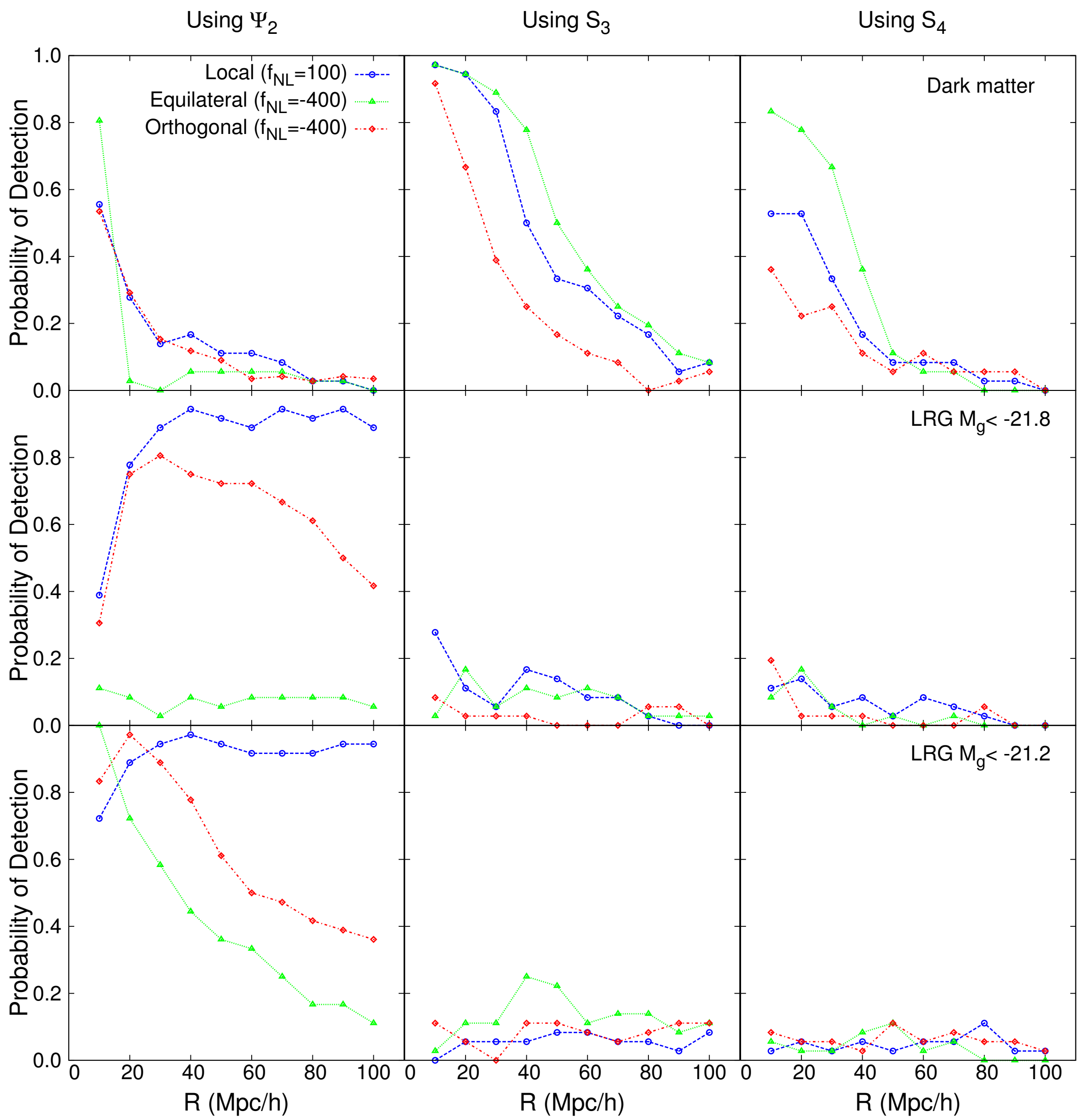

Figure II.6 The probability that a measurement of Ψ_2 (left panels), S_3 (middle panels), or S_4 (right panels) in the BOSS galaxy survey can be used to detect a deviation from the Gaussian model at the 2σ level. Results are shown for the idealized case of dark matter (top panels), as well as mock LRGs with $M_g < -21.8$ (middle panels) and $M_g < -21.2$ (bottom panels). The three curves in each panel represent the three non-Gaussian models that we explore in this dissertation: local (blue dashed curves), equilateral (green dotted curves), and orthogonal (red dot-dashed curves). The probabilities are given by the percentage of BOSS survey equivalent volumes that have a χ^2 value higher than the value corresponding to the 2σ level, where each χ^2 value is calculated from comparing the measurement from a single non-Gaussian sample volume to the mean of all Gaussian realizations. See §II.4.3 for details.

simulations and so the standard deviation can be more accurately estimated than from the non-Gaussian subsets. Moreover, the standard deviation is dominated by shot noise and cosmic variance and we do not expect it to vary significantly between the Gaussian and non-Gaussian models. Once we have a χ^2 value for each realization of a survey volume, we estimate the fraction of these values that exceed the value corresponding to a 2σ detection. For one degree of freedom, this value is 4. The fraction of realizations that have $\chi^2 > 4$ is thus the probability that a measurement from such a survey would be able to provide 2σ evidence for $f_{\rm NL}$.

Figure II.6 shows these probabilities as a function of smoothing scale for a BOSS equivalent volume. Each panel shows results for one combination of density field moment and density field tracer and the three curves in each panel show results for the three non-Gaussian models. The results are somewhat noisy because we only have a limited number of BOSS survey volume subsets, but the main conclusions are clear. Skewness measurements at small scales ($10-20h^{-1}$Mpc) using the full dark matter distribution would be able to provide evidence for $f_{\rm NL}$ in the BOSS survey. However, the probabilities drop dramatically when galaxies are used instead of dark matter. The probability of detecting non-Gaussianity by measuring the galaxy skewness in BOSS is at best $\sim 25\%$, and closer to 10% in most cases, even for our unrealistically high $f_{\rm NL}$ models. Kurtosis measurements are noisier and thus even less likely to yield a detection of non-Gaussianity. Figure II.6 shows that the likelihood of detecting the non-Gaussian models with a kurtosis measurement of the BOSS galaxy density field is below the 10% level for almost all galaxy samples, scales and non-Gaussian models.

The story is different, however, in the case of the variance. Figure II.6 shows that measurements of Ψ_2 from a galaxy survey like BOSS would in principle be able to detect our non-Gaussian models if they correctly described the universe. The optimal galaxy sample and smoothing scale depends on the specific non-Gaussian model. For example, if the universe were described by the local non-Gaussian model, we would have a more

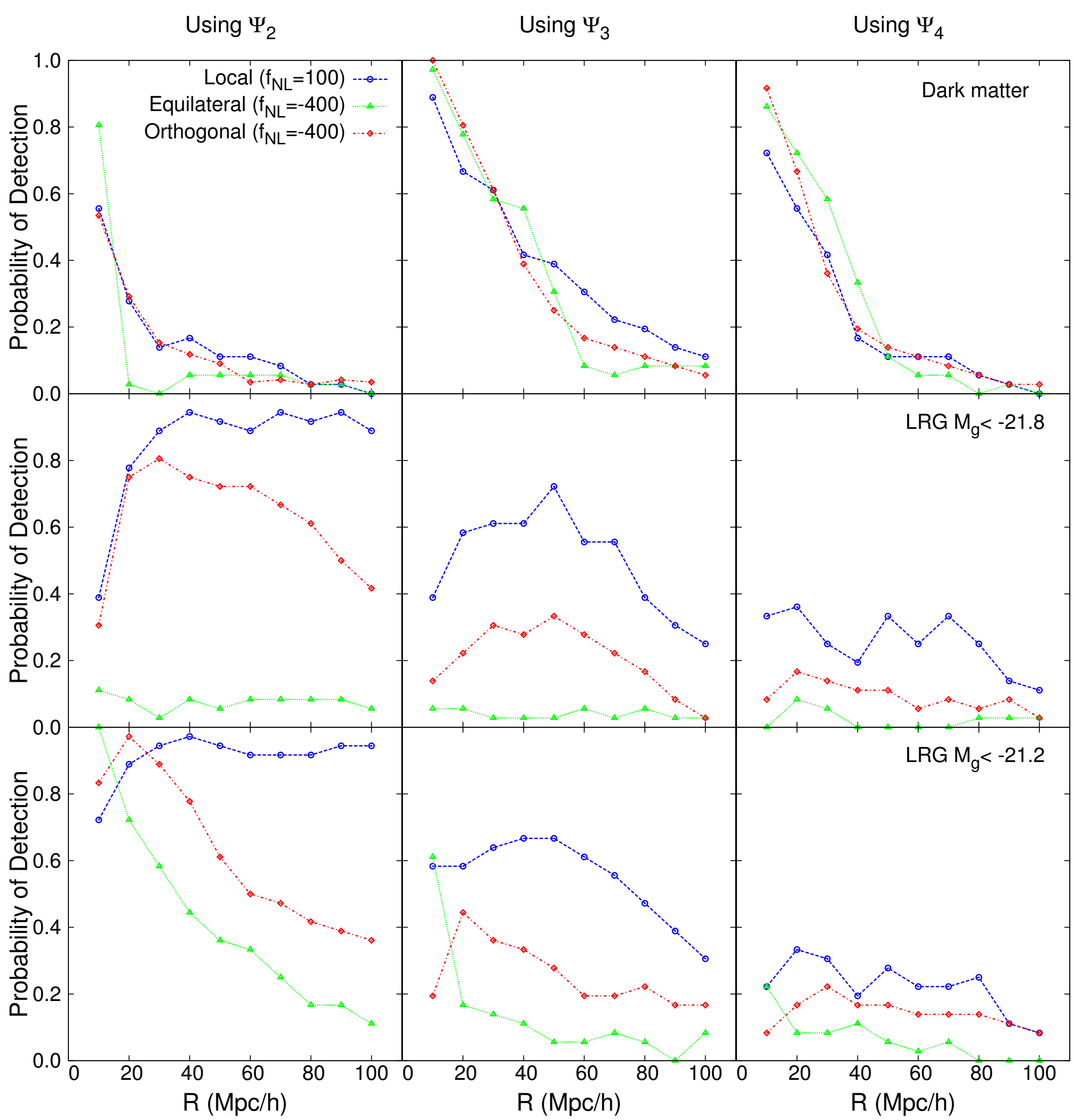

Figure II.7 Similar in every respect to Fig II.6, except that the skewness and kurtosis are replaced by the third and fourth moments, Ψ_3 and Ψ_4.

than 90% chance of detecting the departure from Gaussianity at the 2σ level with either of our galaxy samples and on any scale larger than $30h^{-1}$Mpc. In the case of the orthogonal model, we would need to measure the variance on scales of $20-30h^{-1}$Mpc with either sample. On the other hand, the equilateral model would only be detected with a small scale measurement at $10h^{-1}$Mpc, and only using our less luminous LRG sample. The more luminous sample would yield no detection at all.

The success of the variance raises the question of whether the higher order moments would provide more constraining power if they were not normalized by the variance. In other words, what happens when we use Ψ_3 and Ψ_4, instead of S_3 and S_4? We show results for this in Figure II.7, which is exactly the same as Figure II.6 in every respect except that S_3 and S_4 are replaced by Ψ_3 and Ψ_4. The figure shows that the raw moments perform much better than their normalized versions when galaxy samples are used. However, they do not perform as well as the variance, and they are expected to be more covariant with Ψ_2 than S_3 and S_4 given what is known from the bispectrum versus reduced bispectrum (Sefusatti et al. 2006). For all non-gaussian models, Ψ_2 shows the most promise, followed by Ψ_3 and then Ψ_4. S_3 and S_4 come last, showing the least constraining power in detecting $f_{\rm NL}$. We thus conclude that the constraining power of the higher order moments essentially comes from the variance and that any additional information that exists in the higher moments provides minimal constraint.

In summary, the N-body simulations clearly show that Gaussian and different non-Gaussian initial conditions lead to different moments in the evolved density field. However, the probability of detecting this inconsistency with the Gaussian model by measuring the moments on a galaxy survey like SDSS-II or BOSS is in most cases low, even for the unrealistically large amplitude non-Gaussian models that we consider here. The variance of the galaxy density field is the only measurement that could in principle detect evidence for the $f_{\rm NL}$ models we use.

II.4.4 Scaling Down to Realistic $f_{\rm NL}$ Values

It would be useful to know how much survey volume is needed to reliably detect a deviation from the Gaussian model using the skewness. We estimate the volume needed by rescaling the standard deviation of skewness in equation (II.27). On large scales, the standard deviation of the skewness is dominated by cosmic variance and we simply assume that it scales as $1/\sqrt{V}$, where V is the survey volume. We rescale the standard deviation of the skewness in this way and recalculate the probability that a skewness measurement from a survey with a given volume can provide 2σ evidence for $f_{\rm NL}$, following the methodology described in § II.4.3. We find that if the local non-Gaussian model ($f_{\rm NL} = 100$) correctly described the universe, we would need a survey volume that is 1.5 times the BOSS volume to have a 50% likelihood of detecting non-Gaussianity by measuring the skewness of LRGs with $M_g < -21.8$ on a $10h^{-1}$Mpc scale. If instead the equilateral non-Gaussian model ($f_{\rm NL} = -400$) correctly described the universe, we would need a survey volume that is 2.3 times the BOSS volume to have a 50% likelihood of detecting non-Gaussianity by measuring the skewness of LRGs with $M_g < -21.2$ on a $40h^{-1}$Mpc scale. Note that while we have considered here a single scale R in deriving constraints, including more scales in the analysis is not expected to qualitatively change the conclusions, since different smoothing scales are significantly covariant.

These results apply to the specific non-Gaussian models that we consider in this dissertation, which have large non-Gaussian amplitudes compared to what is allowed from recent Planck constraints. Any realistic departures from Gaussianity (if they exist) in the universe are thus far smaller than what we have studied and will require even larger survey volumes to detect them. We can estimate how much larger a survey volume is needed for a realistic model, by scaling the volume by $1/f_{\rm NL}^2$, since the primordial skewness is directly proportional to $f_{\rm NL}$ (keeping shot noise and galaxy bias fixed). For example, adopting the Planck 1σ constraints, a local non-Gaussian model with $f_{\rm NL} = 6$ would require a volume that is ~ 280 times larger than the one needed to detect the $f_{\rm NL} = 100$ model. This is much larger than the future Euclid survey, which will have approximately 30 times more volume than BOSS. An equilateral non-Gaussian model with $f_{\rm NL} = -75$ would require a volume that is approximately 30 times larger than the one needed to detect the $f_{\rm NL} = -400$ model. This is also larger than what Euclid will provide. We can therefore conclude that skewness and kurtosis measurements are never likely to yield a detection of primordial non-Gaussianity of inflationary type. In principle, there could be other types of non-Gaussianities for which this conclusion may not hold, e.g. non-Gaussianity that is the result of nonlinearities in the density rather than the potential (Scherrer & Schaefer 1995; Verde et al. 2001).

In the case of the variance, we can also find the survey volume that would be needed to detect non-Gaussian models with realistic $f_{\rm NL}$ amplitudes. First let us find the volume that would be needed to yield a 50% likelihood of detecting our unrealistically high $f_{\rm NL}$ models. We can do that by scaling the denominator in equation (II.27) when rewritten for Ψ_2 (i.e., the standard deviation of the variance) by $1/\sqrt{V}$. Then we can recalculate the probability that a variance measurement from a survey with a given volume can provide 2σ evidence for $f_{\rm NL}$. We find that we would need a survey volume that is 0.37 times that of BOSS to have a 50% likelihood of detecting our local non-Gaussian model by measuring the variance of LRGs with $M_g < -21.2$ on a $40h^{-1}$Mpc scale. In the case of the equilateral model, we would need a volume that is 0.33 times that of BOSS when using a variance measurement on the same galaxy sample on a $10h^{-1}$Mpc scale. Now we can estimate what survey volumes are necessary to detect more realistic $f_{\rm NL}$ amplitudes. As before, detecting a local non-Gaussian model with $f_{\rm NL} = 6$ requires 280 times more volume, while detecting an equilateral non-Gaussian model with $f_{\rm NL} = -75$ requires 30 times more volume. For our best case sets of galaxy sample and scales, this translates to survey volumes that are 100 and 9.4 times larger than BOSS, respectively. The first is larger than any planned future survey, but the second will be achieved by Euclid.

We list the volumes needed to have a 50% likelihood of detecting different non-Gaussian models by measuring the variance or the skewness in Table II.1. We note that these numbers

Model		Using Ψ_2	Using S_3
Local	$f_{\rm NL} = 100$	0.37	1.5
	$f_{\rm NL} = 6$	100	420
Equilateral	$f_{\rm NL} = -400$	0.33	2.3
	$f_{\rm NL} = -75$	9.4	65
Orthogonal	$f_{\rm NL} = -400$	0.46	4.9
	$f_{\rm NL} = -39$	48	520

Table II.1 The estimated survey volumes needed to have a 50% likelihood of detecting each non-Gaussian model by measuring the variance or the skewness. The volumes are in units of the BOSS volume. In each case, we pick the best scale and galaxy sample available in our analysis, then rescale on volume and $f_{\rm NL}$. We describe the rescaling method in detail in §II.4.4.

could potentially be improved using cosmic variance cancellation techniques such as Seljak (2009) and Hamaus et al. (2011). However, we have not explored this in this dissertation.

II.4.5 Comparison With Existing Measurements

We have demonstrated that measurements of moments of the galaxy density field in existing survey data are unlikely to provide meaningful constraints on primordial non-Gaussianity anytime soon. Nevertheless, these measurements are very easy to make and it is thus still worth making a quick measurement of variance, skewness, and kurtosis in the SDSS-II and BOSS survey data and comparing it to the Gaussian model.

Pápai & Szapudi (2010) measured Ψ_2, S_3 and S_4 in the SDSS-II DR7 spectroscopic LRG sample. They selected their LRG sample with k-corrected absolute magnitudes between -22.3 and -24.3 in the r band, which is close to our $M_g < -21.2$ sample. Their measurements range from $30-90h^{-1}$Mpc. However, they used a CIC method with cubic cells so their scales roughly correspond to 1.6 times our scales, i.e. the range of scales in their work corresponds to the range $19-56h^{-1}$Mpc in our work. In Figure II.8, we plot their measurements along with their 1σ uncertainties, compared with our measurements from the Gaussian model using mock LRGs with $M_g < -21.2$ in redshift space. Our measurements represent the mean of 120 mocks with SDSS-II equivalent volumes. We should be cautious about making a direct comparison between these two results because there are

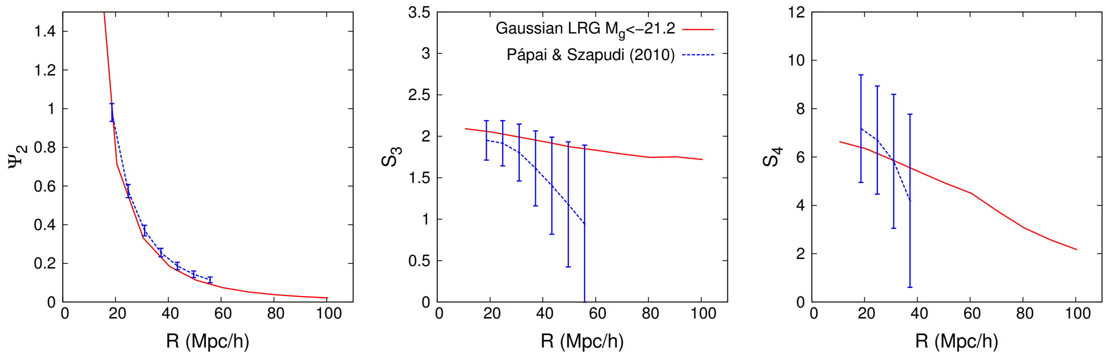

Figure II.8 A comparison of the Pápai & Szapudi (2010) measurements of Ψ_2 (left panel), S_3 (middle panel) and S_4 (right panel) from SDSS-II data with the measurements from our Gaussian simulations. The dashed blue curves show the Pápai & Szapudi (2010) measurements on a SDSS-II LRG sample using CIC smoothing in cubic cells, along with their 1σ uncertainties. The solid red curves show measurements from our Gaussian simulations, using mock LRGs with $M_g < -21.2$ in redshift space. The Gaussian results represent an average over 120 SDSS-II equivalent volumes and the error bars show their standard deviation. Note that we have shifted the scales of the Pápai & Szapudi (2010) measure ments to account for the different definition of smoothing filter between their and our work.

differences in the methods used, including the choice of smoothing filter, estimator and sample selection. Nevertheless, we see that the Pápai & Szapudi (2010) measurements are consistent with the Gaussian model. Their variance measurements are slightly larger than ours and their skewness measurements are lower than ours, but these differences are not significant given their error bars.

II.5 Summary and Discussion

In this chapter, we have measured the variance Ψ_2, skewness parameter S_3, and kurtosis parameter S_4 on N-body simulations that are seeded with local ($f_{\rm NL} = 100$), equilateral ($f_{\rm NL} = -400$), and orthogonal ($f_{\rm NL} = -400$) non-Gaussian initial conditions, as well as with Gaussian initial conditions. We have made measurements on the evolved dark matter density field and on two different sets of mock galaxy catalogs that were designed to simulate two different luminosity samples. Finally, we have investigated the detectability of non-Gaussianity for different galaxy survey volumes. Our main conclusions are as follows.

- Simulations seeded with Gaussian and different non-Gaussian initial conditions show different variance, skewness, and kurtosis in the evolved density field. The differences are clear in both the dark matter distribution and mock galaxy catalogs.

- Galaxy bias, for the LRG-type galaxies that we consider, significantly reduces the detectability of primordial non-Gaussianity using skewness and kurtosis measurements, but dramatically increases the detectability using measurements of the variance. Since different non-Gaussian models provide different scale-dependent bias corrections, the deviation of non-Gaussian models from the Gaussian case depends on the amount of bias and the scale, as well as the nature of the non-Gaussian model.

- Redshift distortions shift the variance, skewness, and kurtosis in the same way for Gaussian and non-Gaussian initial conditions. As a result, they do not affect the detectability of primordial non-Gaussianity.

- Skewness and kurtosis measurements made in current galaxy survey volumes will not have sufficient signal-to-noise to detect primordial non-Gaussianity. The likelihood of finding 2σ evidence for $f_{\rm NL}$ by making a skewness measurement in a volume equivalent to the BOSS survey is less than $\sim 25\%$ for the galaxy samples and scales and $f_{\rm NL}$ values we consider. Kurtosis measurements provide even worse constraining power. Measurements of the galaxy variance however, have a high probability of detecting our $f_{\rm NL}$ values in a volume equivalent to BOSS. However, our $f_{\rm NL}$ values are high and have been ruled out at high significance by current studies.

- The unnormalized higher order moments Ψ_3 and Ψ_4 provide more constraining power than their normalized versions S_3 and S_4. However, these moments do not perform as well as the variance, and they are expected to be more covariant with Ψ_2.

- Using simple arguments to scale our results to more realistic $f_{\rm NL}$ values (for example, $f_{\rm NL} = 6$ for the local model and $f_{\rm NL} = -75$ for the equilateral model), we find that skewness and kurtosis measurements will likely never have sufficient signal-to-noise to detect non-Gaussianity of inflationary type, since the required survey volumes exceed those of the largest planned future surveys. Measurements of the galaxy variance, however, should be able to probe interesting values of $f_{\rm NL}$ for some non-Gaussian models in a survey like Euclid.

These results are not surprising because the skewness and kurtosis only contain reduced information about the density field. They are not nearly as sensitive as the bispectrum and trispectrum when used as a probe of primordial non-Gaussianity. On the other hand, the variance contains very similar information to the power spectrum, which many studies have shown will be able to provide competitive constraints on non-Gaussianity (e.g., Giannantonio et al. 2012). Measurements of the skewness and kurtosis from larger future redshift surveys, such as eBOSS, DESI, and Euclid will have much larger signal-to-noise and will provide tighter constraints on non-Gaussian models. However, as we discussed above, these constraints will not be competitive with already existing constraints from Planck. Only the bispectrum and trispectrum have sufficient constraining power to have a chance at detecting primordial non-Gaussianity. Their higher constraining power results from the shape dependence of these correlators that is lost when integrating it out with spherical top-hat filters to get the skewness and kurtosis parameters. To take advantage of such dependencies, however, nontrivial effects due to bias and redshift-space distortions must be fully accounted for. We hope to report on this soon.

CHAPTER III

A Cosmic Void Catalog of SDSS DR12 BOSS Galaxies

Abstract

We present a cosmic void catalog using the large-scale structure galaxy catalog from the Baryon Oscillation Spectroscopic Survey (BOSS). This galaxy catalog is part of the Sloan Digital Sky Survey (SDSS) Data Release 12 and is the final catalog of SDSS-III. We take into account the survey boundaries, masks, and angular and radial selection functions, and apply the ZOBOV void finding algorithm to the galaxy catalog. We identify 1228 voids with effective radii spanning the range 20-100h^{-1}Mpc and with central densities that are, on average, 30% of the mean sample density. We discuss the basic statistics of voids, such as their size and redshift distributions, and measure the radial density profile of the voids via a stacking technique. In addition, we construct mock void catalogs from 1000 mock galaxy catalogs, and find that the properties of BOSS voids are in good agreement with those in the mock catalogs. We compare the stellar mass distribution of galaxies living inside and outside of the voids, and find no significant difference. These BOSS and mock void catalogs are useful for a number of cosmological and galaxy environment studies.

III.1 Introduction

Cosmic voids are large underdense regions present in the hierarchical structure of the Universe. Surrounded by filaments, walls and clusters, voids are an essential component of the cosmic web. They were first discovered in early galaxy redshift surveys (Gregory & Thompson 1978; Kirshner et al. 1981; de Lapparent et al. 1986) over thirty years ago. More recent redshift surveys such as the 2dF Galaxy Redshift Survey (2dFGRS; Colless et al. 2001) and the Sloan Digital Sky Survey (SDSS; York et al. 2000), have greatly expanded our view of the large-scale structure, and provide much larger data sets to study void properties systematically and in detail.

Cosmic voids have been recognized as interesting cosmological laboratories for investigating galaxy evolution, structure formation and cosmology. The low-density environment of voids provides an ideal place to examine the influence of environment on the formation and evolution of galaxies (Peebles 2001; Gottlöber et al. 2003; Rojas et al. 2004, 2005; Hoyle et al. 2005, 2012). Voids also contain information on the structure formation history and cosmological scenario. The size and shape distribution of voids and their intrinsic structure can provide insights into the growth of structure (Jennings et al. 2013) and dark energy (Lee & Park 2009; Biswas et al. 2010; Bos et al. 2012). Moreover, the Alcock-Paczyński test (Alcock & Paczynski 1979) can be applied to “stacked” voids to probe the expansion history of the universe (Ryden 1995; Lavaux & Wandelt 2012; Sutter et al. 2012a). Voids can also be correlated with the cosmic microwave background (Bennett et al. 2013) to study the integrated Sachs-Wolfe effect (Thompson & Vishniac 1987; Granett et al. 2008; Planck Collaboration et al. 2014). Since voids are nearly empty, the dynamics in their interior are dominated by dark energy (Goldberg & Vogeley 2004), making them potentially important probes for studying the nature of dark energy and testing exotic physics such as modified gravity or a fifth force (Li et al. 2012; Spolyar et al. 2013; Clampitt et al. 2013; Zivick et al. 2014).

To unleash the power of these cosmological applications, it is important to first find voids robustly from simulations, mock galaxy catalogs and galaxy surveys. Although voids occupy most of the volume in the Universe, they are not straightforward to define and identify, especially in surveys where the density field is traced by a set of sparsely sampled galaxies and the survey geometry is complicated. There exist a number of quite different void-finding algorithms (Colberg et al. 2008). While each algorithm has different advantages and disadvantages, Colberg et al. (2008) found that their basic results agree with each other when applied to the dark matter distributions of N-body simulations. One popular algorithm among these is ZOBOV (Neyrinck 2008), which is based on Voronoi tessellations and the watershed method (Platen et al. 2007). One of the advantages of ZOBOV is that it does not assume anything about void shape, thus allowing us a full exploration of the natural shape of voids and their hierarchical structure. ZOBOV in general is parameter free, but additional restrictions can be introduced as needed.

In this chapter we present a catalog of voids by applying the ZOBOV algorithm to SDSS data. There have been previous void catalogs produced from the SDSS data. Pan et al. (2012) identified voids in the SDSS Data Release 7 (DR7; Abazajian et al. 2009) main galaxy sample (Strauss et al. 2002) using a nearest neighbor algorithm. Recently, Sutter et al. (2012b) successfully applied ZOBOV to the SDSS DR7 main galaxy sample and the luminous red galaxy sample (Eisenstein et al. 2001), and Sutter et al. (2014) applied ZOBOV to the SDSS Data Release 9 (DR9; Ahn et al. 2012) CMASS sample. We apply ZOBOV to the most recent SDSS Data Release 12 (DR12; Alam et al. 2015) CMASS and LOWZ galaxy samples, which comprise the largest spectroscopic galaxy redshift samples available to date. We take into account the survey geometry and completeness. The void catalogs will be useful for many void-based studies in cosmology and galaxy formation and evolution.

In §III.2, we describe the galaxy and mock catalogs used in this study. In §III.3, we present the void finding methodology in detail. We describe the resulting void catalogs in §III.4 and show statistics of the identified voids in §III.5. Conclusions and discussion follow in §III.6.

III.2 LSS catalog and QPM mocks

The galaxy sample used in this study is from the Baryon Oscillation Spectroscopic Survey (BOSS; Dawson et al. 2013), which is part of the third generation of the Sloan Digital Sky Survey (SDSS-III; Eisenstein et al. 2011). BOSS made use of the dedicated SDSS telescope (Gunn et al. 2006), multi-object spectrograph (Smee et al. 2013), and software pipeline (Bolton et al. 2012), to obtain the spectra of over 1.37 million galaxies over two large contiguous regions of sky in the Northern and Southern Galactic Caps, covering over

10,000 deg^2 in total. DR12 is the final data release of SDSS-III and contains all six years of BOSS data.

We use the large-scale structure (LSS) galaxy catalogs for DR12 produced by the BOSS collaboration. BOSS galaxies were uniformly targeted in two samples: a relatively low-redshift sample with $z < 0.45$ (LOWZ) and a sample with $0.4 < z < 0.7$ that was designed to be approximately volume-limited in stellar mass (CMASS). A full description of the targeting criteria can be found in Dawson et al. (2013). We place the redshift cuts $0.2 < z < 0.43$ on the LOWZ sample and $0.43 < z < 0.7$ on the CMASS sample to ensure clear geometric boundaries and no overlap between samples. Our study has four large areas of data, CMASS North and South, and LOWZ North and South.

Due to hardware constraints and pipeline failures, not all targeted galaxies result in a good redshift measurement. Each galaxy is weighted to correct for the effects of redshift failures and fiber collisions (no two targets in a spectroscopic observation can be separated by less than 62″ on the sky). In addition, there are weights to account for the systematic relationships between the number density of observed galaxies and stellar density and seeing. These weights are all included in the LSS catalogs and their detailed description can be found in Reid et al. (in preparation).

The LSS catalogs use the MANGLE software (Swanson et al. 2008) to account for the survey geometry and angular completeness. For each distinct region, we up-weight all the galaxies in the region according the its completeness to correct for the angular selection function. The LOWZ and CMASS samples are not strictly volume-limited and their number densities depend on redshift. This redshift dependence of density does not strongly impact void properties because most voids do not span a wide enough redshift range to be sensitive to changes in the underlying density. However, anytime we need to compare a local density measurement to the mean density of the sample, we always compare it to the observed radial density distribution $n(z)$, measured at the corresponding redshift.

To test our void finding algorithm, we also use a set of 1,000 mock galaxy catalogs generated using the "quick particle mesh" (QPM) methodology described by White et al. (2014). These QPM mocks were based on a set of low-resolution particle mesh simulations that accurately reproduce the large-scale dark matter density field on few Mpc scales. Each simulation contained 1280^3 particles in a box of side length 2,560 h^{-1}Mpc. The chosen cosmology has $\Omega_\mathrm{m} = 0.29$, $h = 0.7$, $n_s = 0.97$ and $\sigma_8 = 0.8$. Mock halos were selected based on the local density of each particle, and populated using the halo occupation distribution (HOD; e.g., Berlind & Weinberg 2002) method to create galaxy mocks. The HOD was chosen such that the clustering amplitude of mock galaxies matches the observed measurements. The survey masks were then applied so that the mock catalogs have the same survey geometry as the BOSS data. Finally, the mock catalogs were randomly down-sampled to have the same angular sky completeness and the same radial mean $n(z)$ as the data. We have mock catalogs for the CMASS North and South samples, but not the LOWZ samples.

III.3 Void finding algorithm

We use the ZOBOV algorithm to find voids in the BOSS LSS catalog and QPM mock catalogs. The first step of ZOBOV is to perform a Voronoi tessellation on a given set of particles. The tessellation assigns each particle a Voronoi cell defined as the set of all points in space that are closer to that particle than to any other. The volume of the Voronoi cell provides a density estimate for each particle. The tessellation also provides a natural adjacency measurement for each particle. ZOBOV then applies the watershed transform algorithm to group neighboring Voronoi cells into zones and eventually subvoids and voids. Each void is like a basin composed of a set of attached Voronoi cells, surrounding a local density minimum. ZOBOV also measures the statistical significance of a void by comparing its density contrast, which is the ratio the density measured at the void ridge to the minimum density, to the distribution of density contrasts that can arise from Poisson fluctuations. For a more detailed discussion of this analysis package, see Neyrinck (2008).

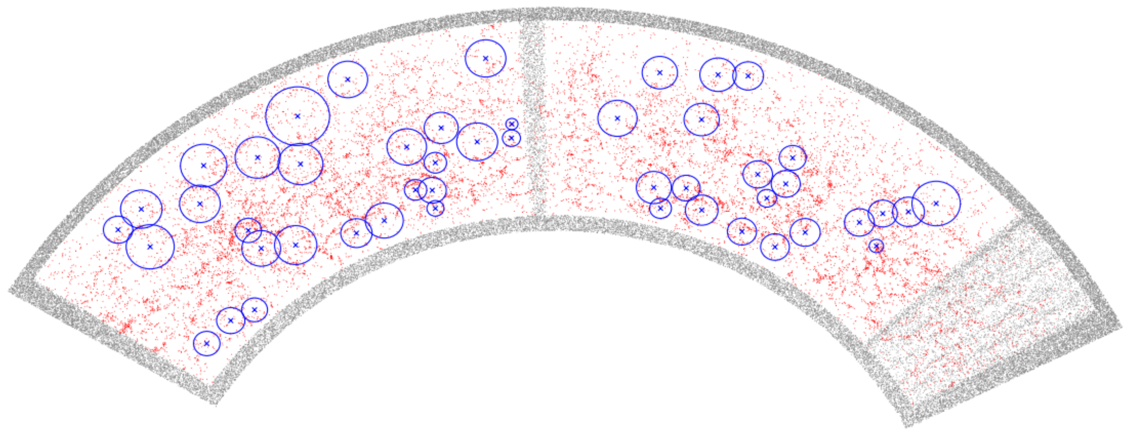

Figure III.1 A thin slice of CMASS North galaxies (red) and random buffer particles (gray). The slice is centered on the celestial equator and is 2° thick in declination. Blue crosses show the central positions of the identified voids whose weighted centers are also located in the slice; the sizes of the blue circles indicate the effective radii of the voids.

To run the Voronoi tessellation, we first convert galaxy redshifts to line-of-sight distances assuming a flat ΛCDM universe with $\Omega_\mathrm{m} = 0.3$. We then prepare the LSS catalog to take into account the survey geometry. The survey masks are used to generate a high number density of randomly distributed buffer particles and place them just outside and all around the survey boundaries. The purpose of these buffer particles is to ensure the tessellation process works even for galaxies close to the survey boundaries. However, the buffer particles and the galaxies adjacent to buffer particles are not included in the watershed transform step. Figure III.1 displays a thin slice of the galaxies from the CMASS North sample together with the buffer particles that surround the survey geometry and fill the holes.

All the weights are applied immediately after the tessellation step by directly modifying the corresponding number density of each galaxy as $n_i = w_i/V_i$, where w_i is the total weight of the galaxy and V_i is the volume of the Voronoi cell. However, all the adjacency information is retained untouched. This is an easy way to include the systematic weights and apply the angular selection function. The watershed method can then be run smoothly with no additional modification.

In general, ZOBOV can be parameter free, but some restrictions produce catalogs better-suited to typical void analysis. For example, ZOBOV zones and voids are grouped around all local minima, including those sitting in high density environments, in which case an identified void may actually have a high mean density. Since we are interested in low density regions, we set some density criteria during the void finding process. First, there is a density threshold parameter that limits ZOBOV to only group zones with mean density less than a certain level during the watershed transform step. This value is set to 0.5, which means that only zones with mean density lower than half the mean density of the whole sample can be joined to voids. In sparsely sampled catalogs, most physical voids only contain one zone, in which case this density threshold parameter has no effect. We also exclude voids where the minimum Voronoi density is higher than the mean density of the sample. Finally, only voids with significance larger than 2σ are included, which is calculated based on the depth of a void (see the next section for the detailed description).

III.4 Void catalogs

We apply the ZOBOV algorithm to four separate regions of BOSS galaxies: CMASS North, CMASS South, LOWZ North, and LOWZ South. In these regions we find 584, 190, 319, and 135 voids, respectively. We parse the ZOBOV outputs and calculate the essential properties for all the voids. For each void, we find the weighted center of the void, which is the average position of the void galaxies weighted by the inverse of their Voronoi density,

$$\mathbf{X} = \frac{\sum_i \mathbf{x}_i/n_i}{\sum_i 1/n_i}, \tag{III.1}$$

where $\mathbf{x}_i$ are the positions of the galaxies in the void and n_i are their corresponding Voronoi densities. The Voronoi density of each galaxy is defined as $n_i = w_i/V_i$, where w_i is the weight of the galaxy and V_i is the Voronoi volume from the tessellation. The effective

Table III.1 Part of the void catalog from the BOSS CMASS North sample.

ID	RA	DEC	z	$N_{\rm gal}$	V	$R_{\rm eff}$	$n_{\rm min}$	$\delta_{\rm min}$	r	P	$D_{boundary}$
	(deg)	(deg)			(h^{-3}Mpc^3)	(h^{-1}Mpc)	(h^3Mpc^{-3})				(h^{-1}Mpc)
(1)	(2)	(3)	(4)	(5)	(6)	(7)	(8)	(9)	(10)	(11)	(12)
60	114.782	37.641	0.648	35	1.411e+05	32.298	2.486e-05	-0.717	3.922	3.220e-14	52.504
10020	184.261	1.326	0.500	25	1.704e+04	15.964	1.364e-04	-0.652	3.441	2.200e-10	28.489
11496	124.855	3.090	0.648	117	6.052e+05	52.473	1.872e-05	-0.778	3.372	6.630e-10	54.891
15935	230.976	13.239	0.459	83	2.425e+05	38.683	3.120e-05	-0.876	3.328	1.330e-09	57.265
4407	237.406	16.985	0.463	372	1.071e+06	63.467	2.934e-05	-0.884	3.001	1.330e-07	73.644

Notes—The columns are described in the text. Table 1 is available in its entirety in the electronic edition of the Astrophysical Journal Supplement.

radius of a void is defined as

$$R_{\text{eff}} \equiv \left(\frac{3}{4\pi}V\right)^{1/3}, \tag{III.2}$$

where V is the total Voronoi volume of the void, which is equal to the sum of Voronoi volumes of all the member galaxies in the void. We also provide the density minimum of the void, as well as its density contrast compared to the mean density at that redshift. ZOBOV calculates the ratio between the minimum density particle on a ridge to the minimum density particle of the whole void. This ratio, r, is used to determine the statistical significance of the void by comparing it to those arising from Poisson fluctuations. Both these measurements are given in our catalogs. Finally, we calculate the distance from each void's weighted center to its nearest survey boundary by finding the nearest buffer particle to the void center.

In Table III.1, we present a few of the most significant voids in the CMASS North sample. We list the void ID (col. [1]); the (J2000.0) right ascension and declination of the void weighted center (cols. [2] and [3]); the redshift of the weighted center (col. [4]); the number of galaxies in the void, N_{gal} (col. [5]); the total Voronoi volume of the void, V (col. [6]); the effective radius, R_{eff} (col. [7]); the number density of the minimum density Voronoi cell in the void, n_{min} (col. [8]); the density contrast of the minimum density cell comparing to the mean density at that redshift, δ_{min} (col. [9]); the ratio r between the minimum density particle on a ridge to the minimum density particle of the void (col. [10]); the probability that the void arises from Poisson fluctuations (col. [11]); the distance from the weighted center to the nearest survey boundary (col. [12]). The voids are ranked in decreasing order of the probability. The complete void catalogs for all four galaxy samples are published in the electronic version of this article. These catalogs, along with the void catalogs from the 1,000 mock catalogs are also available for download on an external site [1].

To visualize the voids, their positions are displayed in the slice in Figure III.1, with their

[1] http://lss.vanderblt.edu/voids

effective radii indicated by the circles. Although the circles indicating the effective radii appear to overlap in some cases, the voids found by ZOBOV do not actually overlap with each other. A ZOBOV void either stands alone, or is fully embedded in a larger void as a subvoid. All the voids that satisfy our criteria in this catalog are stand-alone voids. Some of the voids identified in Figure III.1 appear to contain high density regions. This effect is partly due to projection and partly due to the fact that ZOBOV voids are not actually spherical and so not all the region inside the effective radius is necessarily part of the void. We show that the voids in our catalogs actually represent underdense regions when we investigate their stacked density profiles in the next section.

III.5 Void statistics and properties

III.5.1 Size and redshift distributions

The distributions of void sizes are presented in Figure III.2 and the void center redshifts in Figure III.3. The measurements from the 1000 QPM CMASS mock catalogs are also plotted for comparison. In general, the measurements from the BOSS LSS catalogs agree with those from the QPM mocks. There is an overall amplitude difference between the BOSS and mock histograms such that there are 10-20% fewer voids found in the BOSS CMASS sample than in the mean of the mocks; however, this difference is not highly significant.

The majority of the voids in this catalog have sizes ranging from $30h^{-1}$Mpc to $80h^{-1}$Mpc. This is relatively large compared to the previous catalogs using the SDSS main galaxy sample (Pan et al. 2012; Sutter et al. 2012b), but is comparable to the previous catalogs using CMASS galaxies (Sutter et al. 2014). The deficit of small voids is due to the sparse sampling of the galaxies in our samples. The mean galaxy separation in the CMASS sample is about $30h^{-1}$Mpc, thus it is difficult to identify reliable voids smaller than that size. The void catalogs are not volume complete since the number density of galaxies depends on redshift. We naturally find relatively fewer small voids at the low and high redshift ends of

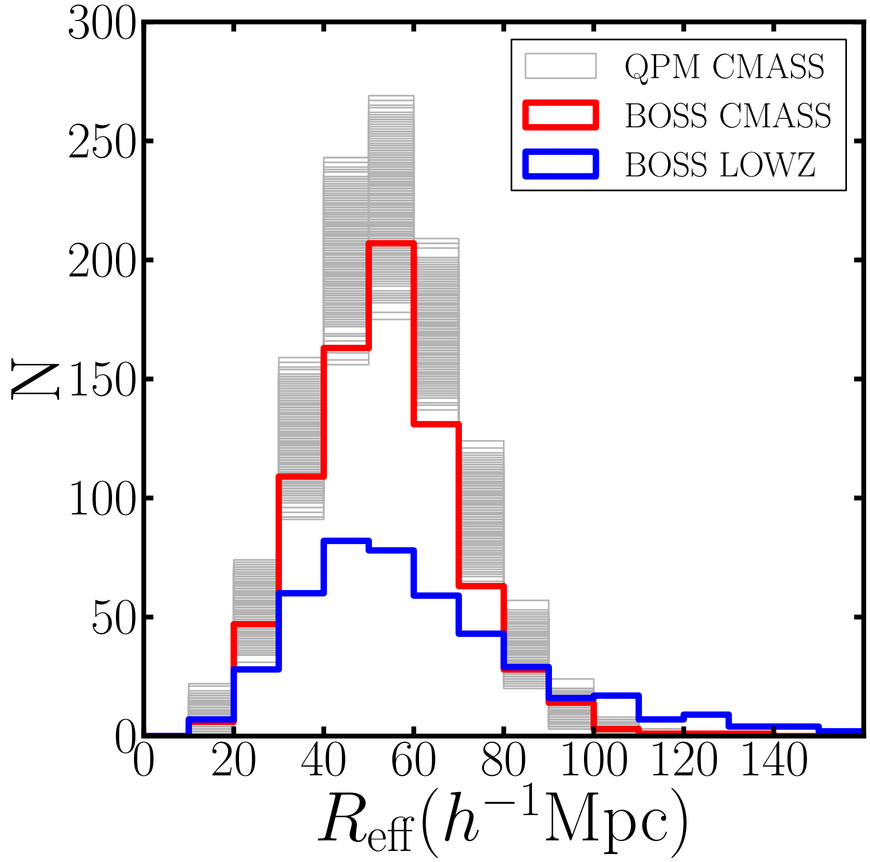

Figure III.2 Distribution of void sizes. Each gray line represents the void effective radius distribution for one of the 1000 QPM CMASS (North + South) mock catalogs. Results for the CMASS (North + South) and LOWZ (North + South) samples are shown by the red and blue lines, respectively. Most voids have effective radii between 30 and $80h^{-1}$Mpc. The mock catalogs contain, on average, 10-20% more voids than found in the CMASS sample.

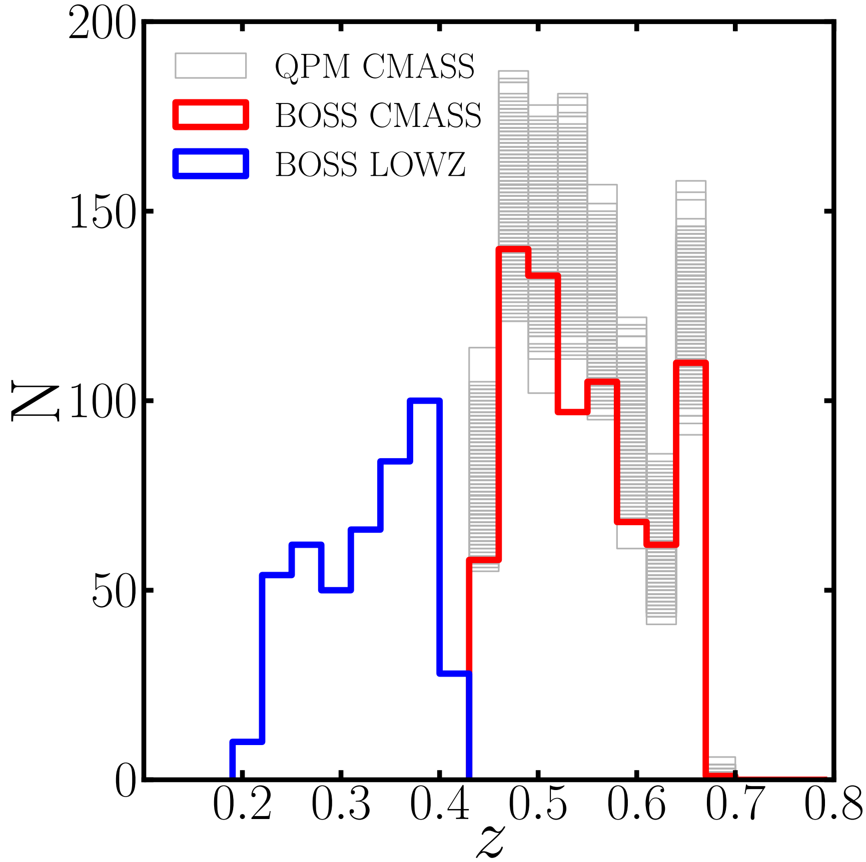

Figure III.3 Distribution of void redshifts. Each gray line represents the redshift distribution of void centers from one of the 1000 QPM CMASS (North + South) mock catalogs. Results for the CMASS (North + South) and LOWZ (North + South) samples are shown by the red and blue lines, respectively.

each sample, where the galaxy number density is lower.

The void catalogs include the distance from each void center to its nearest survey boundary, which is calculated by finding the nearest buffer particle to the void center. Figure III.4 presents these boundary distances compared to the void sizes for the voids in the CMASS North and South samples. There is a clear correlation between the void size and the distance to the boundary for voids that are within $100h^{-1}$Mpc of the boundaries. This result suggests that many voids in this region are truncated by the survey boundaries. For science applications that require an unbiased void size distribution, it may be prudent to restrict the void samples to regions that are sufficiently far from the boundaries.

III.5.2 Density profiles

Individual voids contain few galaxies and have all kinds of shapes and orientations. However, when one "stacks" the individual voids, the composite is stable and reveals the average density structure of voids. We stack all the voids from the BOSS CMASS sample and include all the galaxies around their weighted centers (not just void member galaxies). Each void is rescaled to its effective radius before stacking. Figure III.5 shows a slice through this stacked void. The dots show all the galaxies in a slice of the stacked void whose thickness is 0.25 times the effective radius. The stacked void looks spherical, and its central region has a low density, as expected.

We measure the 1-dimensional density profiles of the stacked voids by measuring the number densities n in a set of shells around each void center and then scaling the number densities to the mean number density $\bar{n}$, as measured at the redshift of the void center. We then scale the radii in each void's density profile by its effective radius, and calculate the mean $n/\bar{n}$ of all the voids in our catalog. Figure III.6 presents the resulting stacked profile of the BOSS CMASS sample compared to the profiles of the QPM CMASS mocks. Since we measure the number densities for individual voids before stacking, the presence of a single galaxy in an inner shell of a small void can generate a high $n/\bar{n}$ in that shell, which

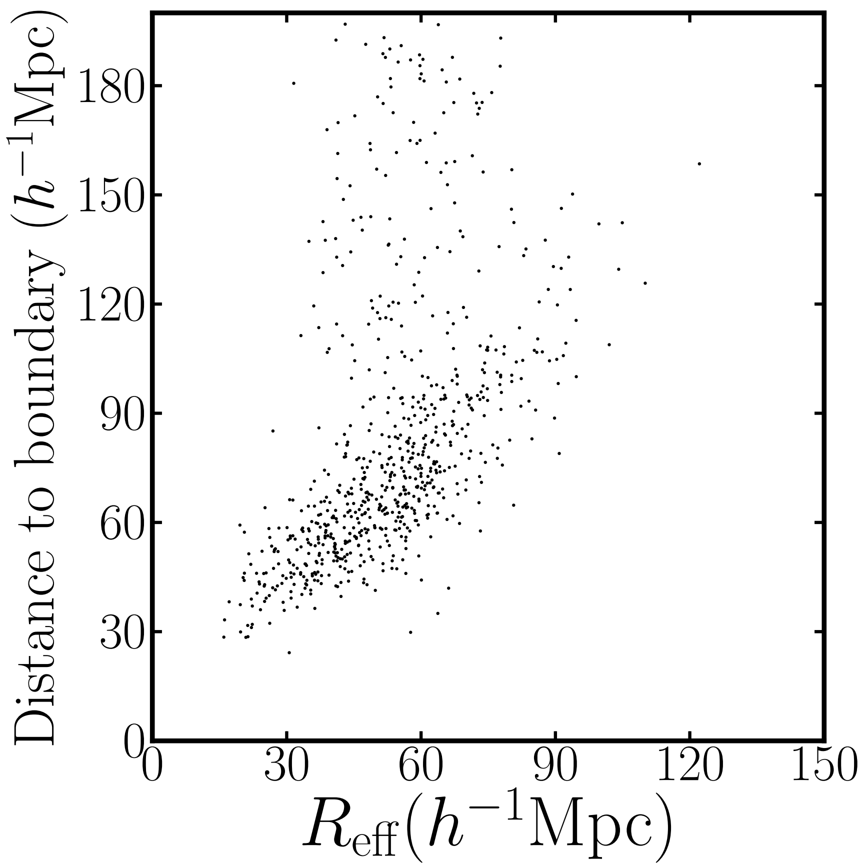

Figure III.4 Distance from void center to the nearest survey boundary compared to void effective radius for the voids in the CMASS North and South samples. There is a clear correlation for voids within $100h^{-1}$Mpc of the survey boundary, suggesting that many voids are truncated by the boundaries.

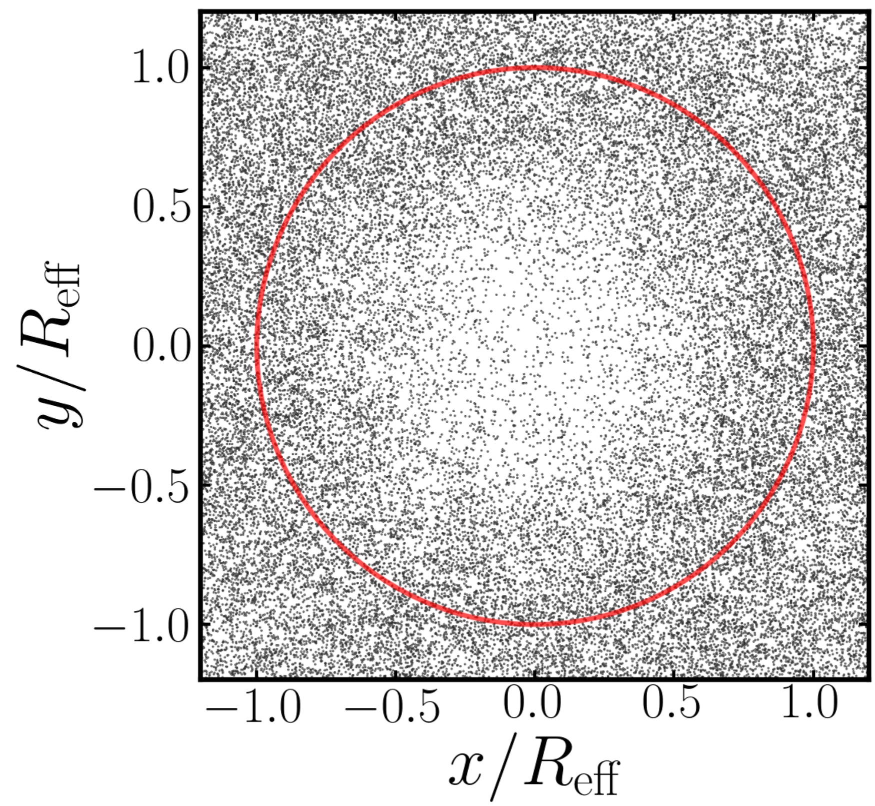

Figure III.5 A slice through the stacked void using all the voids identified in the BOSS CMASS sample. Each void was rescaled by its effective radius before stacking. The slice includes all galaxies around each void center and not just the void member galaxies. The red circle shows the unit radius for reference. The central region of the stacked void is clearly underdense and roughly spherical in shape.

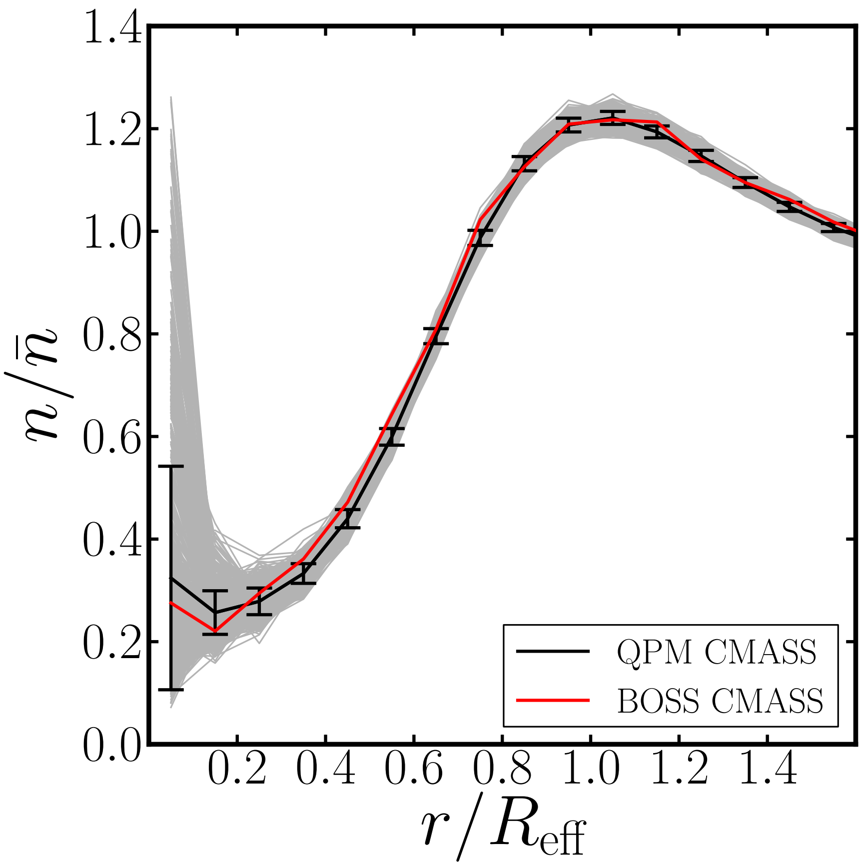

Figure III.6 1-Dimensional stacked density profile from the CMASS sample. The profile is measured by calculating the density profiles for each void individually in a set of shells around each void center, scaling the densities to the mean sample density and the radii to the void effective radii, and averaging over all the voids. Each gray line represents the result for one of the 1000 QPM mock catalogs. The peak at the center is an artifact due to the way we measure the profile. The black line indicates the mean of all the mocks and error bars show the standard deviation among the mocks. The red line is the measurement from the BOSS LSS catalog. CMASS voids have central densities that are $\sim 30\%$ of the mean sample density. Moreover, the density profiles of CMASS and mock galaxies are in excellent agreement with each other.

produces the artificial peaks at the center. This procedure, however, ensures that the stacked density profile has the correct physical meaning. The BOSS profile agrees with the mock profiles extremely well. The density profile reveals that our ZOBOV voids have central regions with a density that is on average $\sim 30\%$ of the mean. The density peaks at a value that is 20% higher than the mean at about one effective radius from the void center. This peak represents the walls and filaments that surround each void. The overall shape of the stacked void profile agrees with that found by previous studies, such as Sutter et al. (2014), Ceccarelli et al. (2013), and Hamaus et al. (2014).

III.5.3 Stellar mass distributions

It is interesting to investigate whether galaxies living inside voids have different properties compared with galaxies living outside voids. To this end, we measure the stellar mass distributions of BOSS CMASS galaxies in different environments. The stellar masses of the galaxies are taken from the 'Portsmouth SED-fit Stellar Masses' catalog, which is a value-added catalog in the SDSS data release. These stellar masses are obtained by fitting model spectral energy distributions to the observed u, g, r, i, z magnitudes (Fukugita et al. 1996) of BOSS galaxies with the spectroscopic redshift determined by the BOSS pipeline, as in Maraston et al. (2013). There are two sets of templates available, a passive template and a star-forming template, each for both the Salpeter (1955) and Kroupa (2001) initial mass functions (IMF). Here we adopt the stellar masses derived from the passive template with Kroupa IMF.

Figure III.7 presents the stellar mass distributions of all galaxies, the void galaxies, and all low-density galaxies, which we define as having Voronoi densities lower than 0.3 of the mean density. Void galaxies have stellar mass distributions that are indistinguishable from that of all galaxies. Low-density region galaxies have a distribution that is slightly shifted to lower masses, but the difference is quite small. The similarity in stellar masses is somewhat surprising as we expect low density regions to contain lower mass halos and

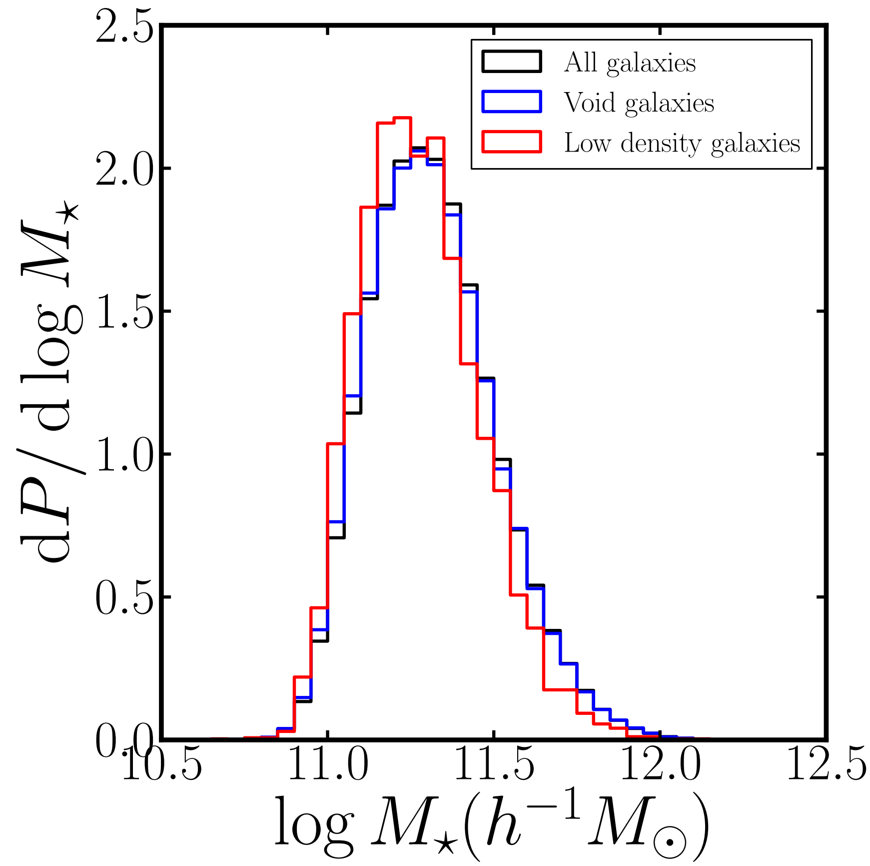

Figure III.7 The stellar mass probability distribution of all BOSS CMASS galaxies (black), the void member galaxies (blue), and all galaxies with very low Voronoi density ($< 0.3\bar{n}$) (red). The stellar masses of void galaxies are not appreciably different from those of all galaxies, while galaxies in low density regions are slightly less massive than all galaxies.

thus less massive galaxies than high density regions. However, the BOSS CMASS sample has a fairly narrow range of stellar masses, since it only probes the high mass end of the galaxy distribution. Differences between low and high density regions can therefore not be too large. We investigate this issue further by examining the dark matter halo mass distributions of void and non-void galaxies in our QPM mocks. We find that the halo mass distributions are very similar for these different environments, which explains why we do not see a difference in the stellar mass distributions.

III.6 Conclusions

We have applied the ZOBOV algorithm to the BOSS DR12 CMASS and LOWZ large-scale structure catalogs, taking into account survey boundaries, masks, and incompleteness, to construct cosmic void catalogs. These catalogs contain voids across a redshift range from $z = 0.2$ to 0.7, and with effective radii spanning the range from 15 to $130h^{-1}$Mpc. The general properties of these voids, including their size and redshift distributions, as well as their stacked density profiles, are in agreement with earlier works. We have also constructed void catalogs from 1000 mock catalogs of the CMASS sample. The statistics of mock voids agree well with those of the BOSS galaxies. Finally, we have measured the stellar mass distributions of galaxies in different environments and find no significant difference between the stellar masses of void galaxies compared to all galaxies, but galaxies with very low Voronoi densities have stellar masses that are slightly lower than all galaxies.

The cosmic void catalogs presented here are useful for many void related studies, including, but not limited to, the study of massive galaxy environments, the formation of structure on large scales, and cosmological applications such as the integrated Sachs-Wolfe effect and the Alcock-Paczyński test. The void catalogs from the mock galaxy catalogs can provide information on systematic effects such as redshift distortions, and can characterize the statistical uncertainties in measured void statistics. The mock void catalogs are also useful for estimating theoretical expectations for future surveys. Galaxy redshift surveys such as eBOSS (K. Dawson et al. 2015, in preparation), DESI (Levi et al. 2013), Euclid (Laureijs et al. 2011) and WFIRST (Spergel et al. 2013) will produce galaxy samples in even larger volumes in the next decade, which will also greatly advance void related science.

CHAPTER IV

Alcock-Paczyński Test Using Cosmic Voids in BOSS DR12

Abstract

We apply the Alcock-Paczyński (AP) test to the voids identified in the most recent large-scale structure galaxy catalog from the Baryon Oscillation Spectroscopic Survey (BOSS). This galaxy catalog is part of the Sloan Digital Sky Survey (SDSS) Data Release 12. We also use 1000 mock galaxy catalogs to characterize the uncertainties of the measurements and correct for the redshift space distortions. We use the ZOBOV algorithm to find voids in both BOSS data and mock catalogs, and we accurately measure the shape of the stacked voids. We find that the stacked voids in redshift space are slightly squashed, which is consistent with previous studies. Assuming a flat ΛCDM cosmology, we obtain a measurement of $\Omega_{\rm m} = 0.38^{+0.18}_{-0.15}$ at 68% confidence level from the AP test.

IV.1 Introduction

Cosmic acceleration (Riess et al. 1998; Perlmutter et al. 1999) is the most surprising cosmological discovery in many decades, which implies that today's Universe is dominated by some form of dark energy. Probing the expansion history of the Universe and revealing the nature of dark energy is one of the greatest challenges in today's observational cosmology. There exist a wide variety of dark energy models. To constrain these theories, it is important to apply a variety of statistical methods to available observational data (Weinberg et al. 2013).

In order to test the expansion history of the universe, Alcock and Paczyński (Alcock & Paczynski 1979) proposed a purely geometric test (AP test) based on the ratio of observed angular size to radial size of objects which are known to be intrinsically isotropic. Most applications of the AP test have focused on measuring the anisotropic clustering of galaxies using the correlation function or power spectrum. However this method is inevitably limited by redshift space distortions (RSD). Another interesting approach is to measure the symmetry properties of close galaxy pairs (Marinoni & Buzzi 2010). Unfortunately this method is seriously affected by dynamics at small scales (Jennings et al. 2012).

First proposed by Ryden (1995) and extensively discussed by Lavaux & Wandelt (2012), cosmic voids provide an attractive alternative for applying the AP test. Voids are large underdense regions present in the hierarchical structure of the Universe. Ever since their discovery more than 30 years ago (Gregory & Thompson 1978; Kirshner et al. 1981; de Lapparent et al. 1986), voids have been recognized as very interesting laboratories for studying cosmology. The low-density nature of voids places them in the quasi-linear regime, which means it is relatively easier to model the systematics such as RSD effects. Though the shape of individual voids can be very noisy, the AP test can be applied to stacked voids to significantly reduce the Poisson noise.

To successfully apply the AP test to voids, a large volume spectroscopic galaxy redshift survey is essential. The Sloan Digital Sky Survey (SDSS; Eisenstein et al. 2011) provides the largest spectroscopic survey volume to date, and it is the ideal data set to make this measurement. The AP test using cosmic voids has been explored by using galaxy catalogs in SDSS Data Release 7 (DR7) (Sutter et al. 2012a) and SDSS Data Release 10 (Sutter et al. 2014). Here we use the galaxy catalogs in the SDSS Data Release 12 (DR12), which is the most recent and the final data release of SDSS-III. We identify voids using the ZOBOV void-finding algorithm (Neyrinck 2008), and we measure the shape of the stacked voids. In addition, we also use 1000 galaxy mock catalogs to characterize the uncertainties and correct for the systematics such as RSD effects.

In this chapter, we first briefly introduce the AP test in §IV.2. In §IV.3, we describe the galaxy and mock catalogs we use in this study. In §IV.4, we describe the method and the steps we take to identify the voids. We then discuss how to stack the voids in §IV.5 and how to accurately measure the shape of stacked voids in §IV.6. In §IV.7 we show our AP test results and the constraint of cosmological parameters. Conclusion and discussion follow in §IV.8.

IV.2 Alcock-Paczyński Test

Consider an intrinsically spherical object at redshift z with an extension of Δz in the line-of-sight direction and $\Delta\theta$ across the sky. In comoving coordinates, it has size Δl in the line-of-sight direction and Δr in the projected direction. Then Δl is related to Δz by

$$\Delta l = \frac{c}{H(z)}\Delta z, \tag{IV.1}$$

where H is the Hubble parameter. In a flat ΛCDM universe,

$$H(z) = H_0\sqrt{\Omega_{\rm m}(1+z)^3 + \Omega_\Lambda}, \tag{IV.2}$$

where H_0 is the present value of the Hubble parameter. The transverse comoving size Δr is related to $\Delta\theta$ by

$$\Delta r = D_M(z)\Delta\theta = (1+z)D_A(z)\Delta\theta, \tag{IV.3}$$

where D_M is the transverse comoving distance and D_A is the angular diameter distance (Hogg 1999). In a flat universe with no curvature, the transverse comoving distance is simply the line-of-sight comoving distance,

$$D_M(z) = D_C(z) = c\int_0^z \frac{{\rm d}z'}{H(z')}. \tag{IV.4}$$

Since Δl and Δr are equal for a spherical object, combining equation IV.1 and IV.3 gives us the ratio

$$\frac{\Delta z}{z\Delta\theta} = \frac{(1+z)}{cz}D_A(z)H(z). \tag{IV.5}$$

This is the original form of the AP test, and one can directly compare the observables to a cosmological model.

Another way to look at the AP test is that we will only recover the spherical symmetry of the object if we assume the true cosmology. If we convert redshift to comoving distance by assuming a fiducial cosmology, we can measure the ratio

$$e(z) = \frac{\Delta l'/\Delta r'}{\Delta l/\Delta r} = \frac{\Delta l'}{\Delta r'} = \frac{D_A(z)H(z)}{D'_A(z)H'(z)}, \tag{IV.6}$$

where primes indicate quantities calculated using the assumed cosmology and D_A and H are the values of the true cosmology. This means we can test the ratio $e(z)$ with a set of different fiducial cosmologies, and getting $e(z) = 1$ means we have adopted the correct cosmology.

In this study, we always assume a flat ΛCDM with a cosmological constant. We use a set of fiducial cosmologies with different Ω_m values, and for each Ω_m we convert redshifts to comoving distances and identify voids in both BOSS galaxy catalog and mock galaxy catalogs, then measure the ratio $e(z)$ of the stacked voids.

IV.3 Data and mocks

We use the galaxy catalog from the Baryon Oscillation Spectroscopic Survey (BOSS; Dawson et al. 2013), which is part of the third generation of the Sloan Digital Sky Survey (SDSS-III; Eisenstein et al. 2011). BOSS obtained the spectra of over 1.37 million galaxies over two large contiguous regions of sky in the Northern and Southern Galactic Caps, covering over 10,000 deg^2 in total. DR12 is the final data release of SDSS-III and contains all the data BOSS has collected over the last 6 years.

BOSS galaxies were uniformly targeted in two samples, a relatively low redshift sample with $z < 0.45$ (LOWZ) and a high redshift sample with approximately $0.4 < z < 0.7$ (CMASS). A full description for the targeting criteria can be found in Dawson et al. (2013). We only include the CMASS sample in this analysis, and we place a redshift cut of $0.43 < z < 0.7$ on the CMASS sample to ensure clear geometrical boundaries. The median redshift of the sample is 0.57. The CMASS sample is not volume-limited and the number densities depend on redshift. Any time we need to compare the density to the mean density of the sample, we always compare it to the observed radial density distribution $n(z)$.

The large-scale structure (LSS) galaxy catalogs are produced by the BOSS collaboration as a value-added catalog. The catalogs include weights to correct for the effects of redshift failures and fiber collisions. In addition to that, there are also systematic weights to account for the systematic relationships between the number density of observed galaxies and stellar density and seeing. The detailed description of the weights can be found in Reid et al. (in prep.). The LSS catalogs use the MANGLE software (Swanson et al. 2008) to take into account the survey geometry and the angular completeness. For each distinct region, we also upweight all the galaxies in the region based on the completeness to correct for the angular selection effect.

A set of 1000 mock galaxy catalogs generated using the "quick particle mesh" (QPM) methodology (White et al. 2014) is used to estimate the uncertainties and study the systematics. These QPM mocks are based on a set of rapid but low-resolution particle mesh simulations which accurately reproduce the large-scale dark matter density field. Each simulation uses 1280^3 particles in box of side length 2560 h^{-1}Mpc. The chosen cosmology has $\Omega_\mathrm{m} = 0.29$, $h = 0.7$, $n_s = 0.97$ and $\sigma_8 = 0.8$. Mock halos are selected based on the local density of each particle. These halos are then populated using the halo occupation distribution (HOD, Berlind et al. 2003) method to create galaxy mocks. The HOD was chosen such that the clustering amplitude should correspond to observed measurements. The survey masks are applied so that the mocks have the same survey geometry as the data. The mocks are also randomly downsampled to have the same angular sky completeness and the same radial density distribtion $n(z)$ as the data. Redshift space distortions are generated based on the velocity of the simulation particles.

IV.4 Finding voids

We use the ZOBOV algorithm to find voids in the BOSS data and QPM mock catalogs. ZOBOV first uses Voronoi tessellation to assign a Voronoi cell and get a density estimate for each galaxy, and then uses the watershed transform to group neighboring Voronoi cells into zones and eventually subvoids and voids. ZOBOV also provides the statistical significance of a void. One of the advantages of ZOBOV is that it does not assume anything about shape; thus, it allows us to explore the natural shape of voids. The detailed description of the algorithm can be found in Neyrinck (2008).

We prepare the LSS catalog to take into account the survey geometry by putting high number density and randomly distributed buffer particles around the survey boundaries. The purpose of these buffer particles is to ensure the tessellation process even for galaxies close to the survey boundaries, and they are not included in the watershed transform step. We apply all the weights right after the tessellation step by directly modifying the corresponding density of each galaxy as $\rho_i = w_i/V_i$, where w_i is the total weight of the galaxy and V_i is the volume of the Voronoi cell. But we keep all the adjacency information untouched. This is a very easy way to include the systematic weights and angular selection, and next the watershed method can be run smoothly with no additional modification.

In general ZOBOV is parameter free, but some restrictions can be applied as needed. We decide to set the density threshold parameter to 0.5, which limits ZOBOV to only group zones with mean density lower than 0.5 of the mean density of the whole sample during the watershed transform step. We also check the minimum Voronoi density of each void and compare it to the mean density $n(z)$ at the void center's redshift, and exclude the voids with minimum density higher than 0.5 of the mean density. Finally, we only include voids with significance higher than 2σ.

We directly run the algorithm on the data in redshift space and we do not attempt to remove the redshift distortions in the data. But for QPM mocks, we find voids in both the real space catalogs and the redshift space catalogs.

The void finding procedure is basically the same as our recent void catalog release in Mao et al. (2015). The only difference is that in the public catalog we assume a fixed fiducial cosmology of $\Omega_{\rm m} = 0.3$, but here for the AP test, we assume a series of different

Ω_m's. For each cosmology, we convert galaxy redshifts to line-of-sight distances using that cosmology before we apply the ZOBOV algorithm.

IV.5 Stacking voids

The weighted center of each void is defined as the average position of the void galaxies weighted by the inverse density, calculated as

$$\mathbf{X} = \frac{\sum_i \mathbf{x}_i / n_i}{\sum_i 1/n_i}, \tag{IV.7}$$

where $\mathbf{x}_i$ is the position of each galaxy in the void and n_i is the corresponding weighted density of the Voronoi cell. The size of a void is defined by its effective radius:

$$R_{\text{eff}} \equiv (\frac{3}{4\pi} V)^{1/3}, \tag{IV.8}$$

where V is the sum of all the Voronoi volumes in the void.

We take the voids with effective radius ranging from 30 h^{-1}Mpc to 100 h^{-1}Mpc, which contain most of the identified voids, and stack them on their weighted centers. Voids are rescaled to their effective radius and rotated to align to a common line-of-sight direction before stacking. The stacking can be done by only using void galaxies or by using all the galaxies around each void center. Our tests show that both methods give very similar results, but the shape measurements are more stable when using all the galaxies. In figure IV.1, we show an example of a slice of the stack using all galaxies around void centers. It clearly shows a low density central region, and the density rises when you move towards the outer part of the stacked void. The red circle in the plot has a radius of 0.7, which refers to the region we use to measure the shape of the stacked voids.

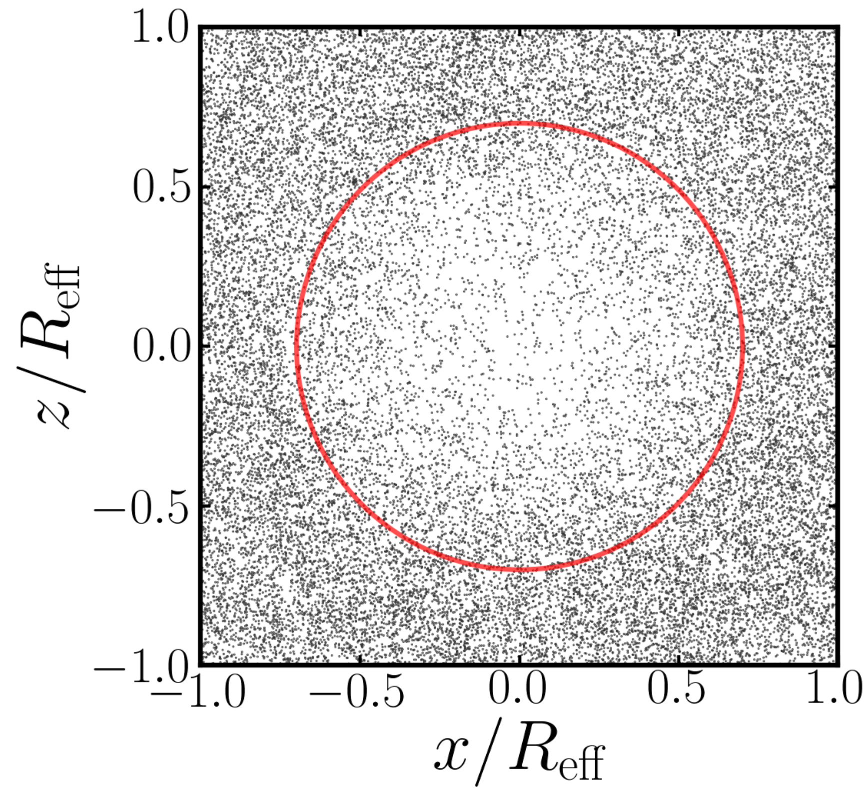

Figure IV.1 A slice of the stacked void using the voids with effective radius ranging from 30 h^{-1}Mpc to 120 h^{-1}Mpc. Each void is rescaled to its effective radius before stacking. We include all the galaxies around each void center. The red circle has a radius of 0.7 for reference.

IV.6 Shape measurements

Whether using only void galaxies or all galaxies around void centers, stacked voids do not have a clear outside boundary, and the outer part of stacked voids may be strongly affected by the high density structures surrounding voids. To measure the internal shape of stacked voids, we develop a method and the steps are stated as follows. We put a spheroidal cut with a given ellipticity e_{cut} centered on the stacked void center and gather all the galaxies within the spheroid. We then use these galaxies to measure the axis ratio e as

$$e = \sqrt{\frac{2\sum_i w_i z_i^2}{\sum_i w_i (x_i^2 + y_i^2)}}, \tag{IV.9}$$

where x_i, y_i and z_i are the galaxy's Cartesian coordinates in the stacked voids and z is in the aligned line-of-sight direction, w_i is the galaxy weight, and the summation is taken over all the galaxies within the spheroidal cut. If the selected $e_{\rm cut}$ matches the actual shape of the stacked void, the measured axis ratio e is expected to be equal to the selected $e_{\rm cut}$. By varying $e_{\rm cut}$, we can find the point where the measured e converges to the $e_{\rm cut}$ and take that measurement as the internal shape of the stacked voids.

For certain density distributions, this method can be proved analytically by integrating over the spheroid. In figure IV.2 we analytically test density distributions with different power law profiles, all stretched by 15 percent. Figure IV.2 shows that for different assumed spheroidal shapes $e_{\rm cut}$, the measured e converges with $e_{\rm cut}$ where the assumption matches the true 15 percent stretch, which is indicated by the black vertical dashed line. Numerical tests using randomly generated points following the same density profiles give exactly the same results. This method works for density distributions with a density gradient, but not for the uniform distribution. Since we are dealing with stacked voids with a clear density gradient from center to edge, we can use this method to measure the shape.

Using this method, we first measure the shape of the stacked voids in our 1000 QPM mock catalogs in real space. We assume the same fiducial cosmology as the one used for

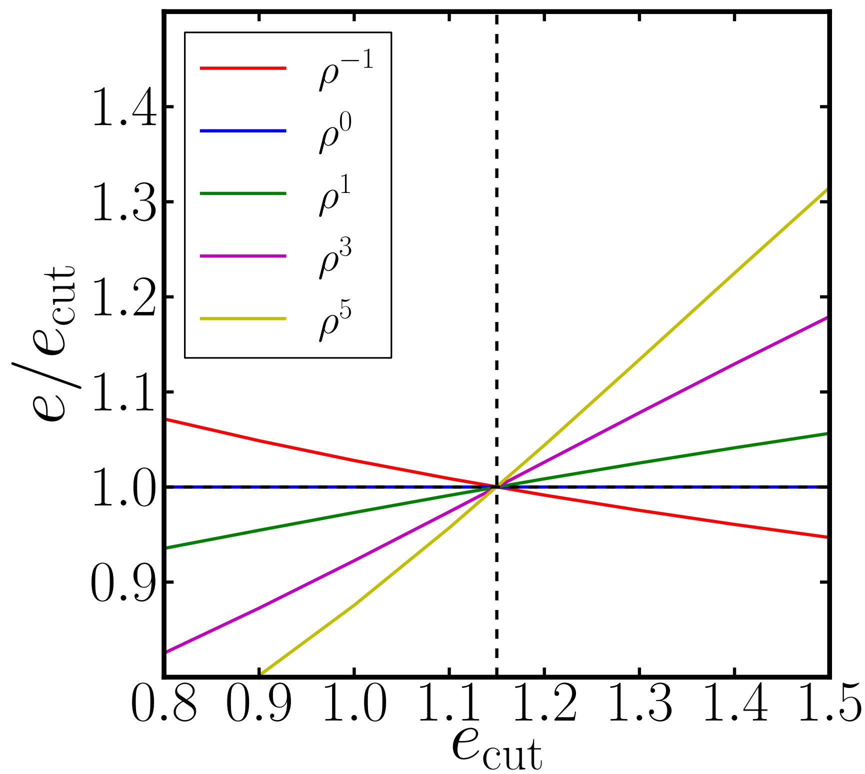

Figure IV.2 An analytical test of our method of shape measurement. For different assumed spheroidal shapes $e_{\rm cut}$, the measured e converges to $e_{\rm cut}$ where the assumption matches the true stretch, which is indicated by the black vertical dashed line. The method works for all kinds of density distributions with different power law profiles, except for the uniform distribution.

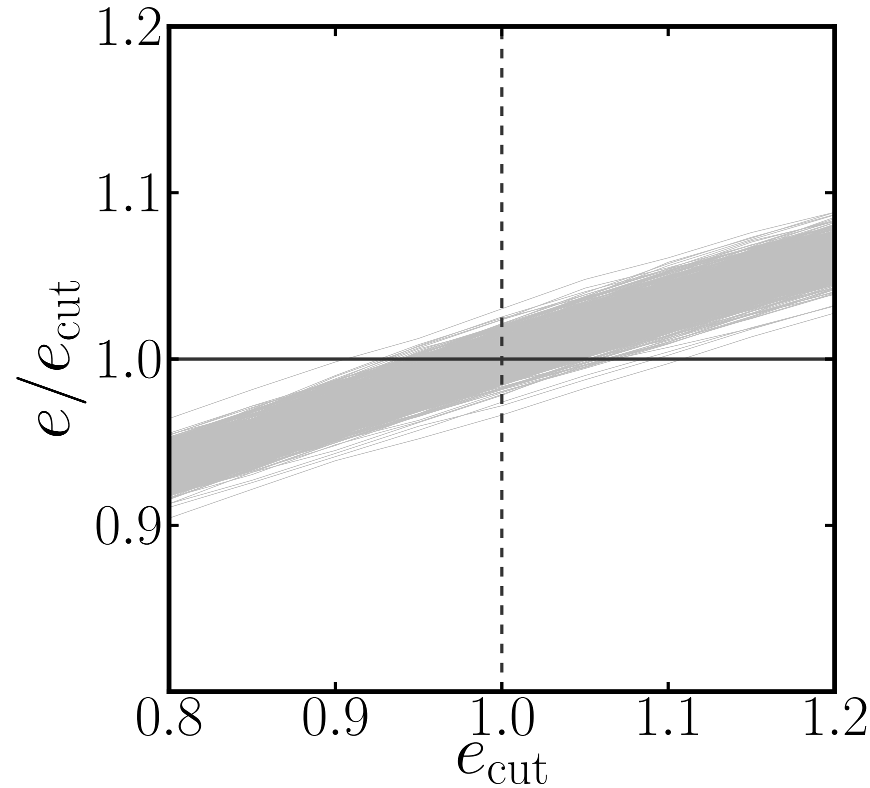

Figure IV.3 Ratio between the measured axis ratio and the assumed axis ratio versus the assumption. Each gray line is measured from one of the 1000 mock catalogs in real space, assuming the same cosmology as the fiducial cosmology for generating the mocks.

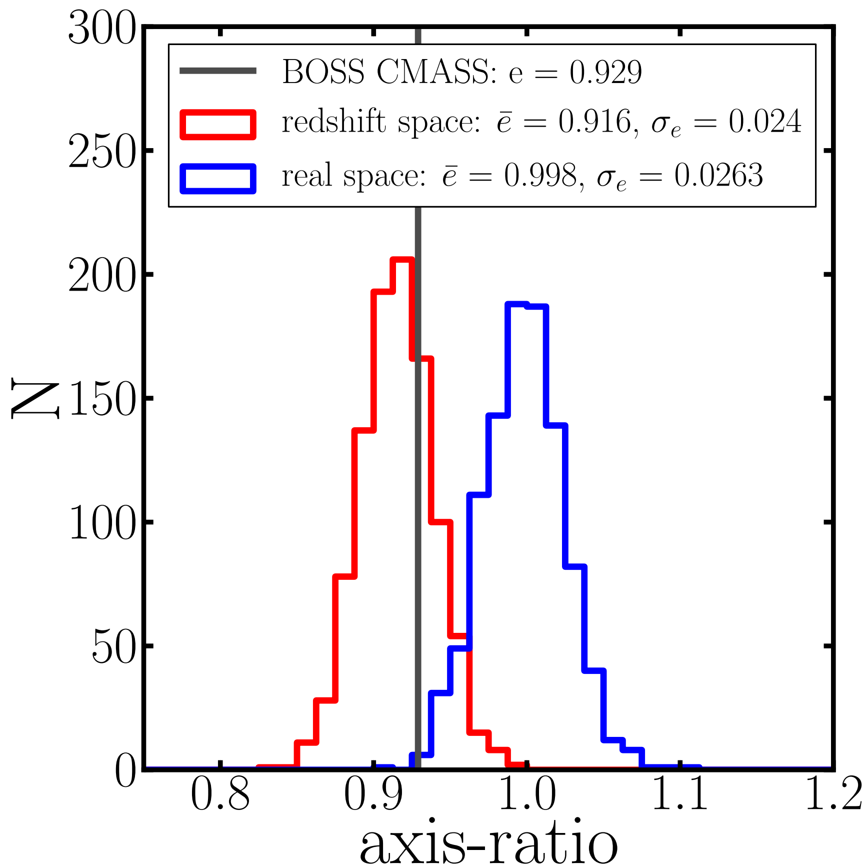

Figure IV.4 The distribution of the shape of the stacked voids measured from our 1000 QPM mock catalogs in real space (blue) and redshift space (red), assuming the same cosmology as the fiducial cosmology for generating the mocks. In real space we retrieve the spherical shape, and in redshift space we measure a slightly squashed shape with axis ratio of 0.92. The measurement from the BOSS CMASS data is indicated as the black vertical line, which is consistent with the mocks in redshift space.

running the simulations and generating the mocks. We run ZOBOV on each mock and stack voids as we described. We then apply a spheroidal cut with changing ellipticity e_{cut} but fixed volume equal to a $R = 0.7$ sphere. In figure IV.3, each gray line represents a measurement from one of the 1000 mocks. We do a spline fit to each gray line to find out where the measured e and the assumed e_{cut} converge, i.e. where the gray line crosses the line of $e/e_{\mathrm{cut}} = 1$, and the e_{cut} at the cross point is the measurement of the shape of the stacked void.

Since we assume the true cosmology for the mocks, we should be able to retrieve the spherical shape in real space. In figure IV.4 the blue line shows the distribution of the shape measurements from our 1000 mocks. It shows that in real space we do get an axis ratio of 1 on average, with a 1σ error of about 2.6%.

We also measure the shape of the stacked voids in the 1000 mocks in redshift space, using the same cosmology. This can show the effect of the redshift space distortions. The result is also in figure IV.4, shown in red. In redshift space, the stacked voids show a slightly squashed shape. This is consistent with other recent studies using the same kind of void finding algorithm (Lavaux & Wandelt 2012). We then also measure the shape of the stack void in the BOSS CMASS galaxy catalog with the same fiducial cosmology and indicate the result in the figure IV.4 with the black vertical line. The measurement from the CMASS galaxies is consistent with the shape distribution measured from the mocks in redshift space.

IV.7 Cosmological constraints

We have shown that we can accurately measure the shape of the stacked voids. To apply the AP test, we then need to repeat the steps for different cosmologies. Here we always assume a flat ΛCDM universe with a cosmological constant, and we repeat the measurements for a set of different Ω_{m} values. For each Ω_{m}, we reconvert galaxy redshifts to line-of-sight distances and rerun the void finding algorithm, then measure the shape of stacked voids based on the new set of voids. We do this for both the QPM mocks and the BOSS data.

Figure IV.5 shows the shape measurements of the stacked voids assuming different Ω_m. The blue line shows the mean shape measurements from the 1000 QPM mocks in real space, with the error bars showing the standard deviation of the 1000 measurements for each Ω_m. At the true cosmology which the mocks are based on, we successfully retrieve the spherical shape. The dashed line shows the theoretical prediction given by equation IV.6, using the median CMASS redshift 0.57. Ideally the blue line should follow the trend of the dashed line, but due to the sparse sampling and the nature of the void finding algorithm, this is not the case. We discuss this issue more in §IV.8.

The red line shows the same kind of measurements as the blue line, but in redshift space. We find that the redshift distortions give an almost constant shift across all the range of Ω_m. The solid black line shows the measurement from the BOSS CMASS galaxy catalog, and it is consistent with the measurements of mocks in redshift space.

Since we can only measure the BOSS data in redshift space, we need to compare the data measurement with the measurement from the mocks in redshift space. The point at $\Omega_m = 0.29$ is highlighted with a red star, because this is the shape of the stacked void when assuming the right cosmology and including the RSD effects; thus we treat the value and the uncertainty at the star point as the expected axis ratio. For each Ω_m we have measured an axis ratio from the data, we then compare this measured axis ratio to the rank ordered 1000 shape measurements from the mocks at $\Omega_m = 0.29$, which gives us an estimate on the probability of each Ω_m. The result probability distribution is shown as the red curve in figure IV.6. We then obtain a measurement of $\Omega_m = 0.38^{+0.18}_{-0.15}$ at 68% confidence level from the probability distribution of Ω_m.

Though we cannot obtain the same slope as the theoretical prediction due to the sparse sampling, it is interesting to see what we can get in an ideal case. We compare the theoretical prediction (dash-dot curve in figure IV.5) also to the expected value at the red star point, and the result is shown as the blue dashed line in figure IV.6. We find that ideally

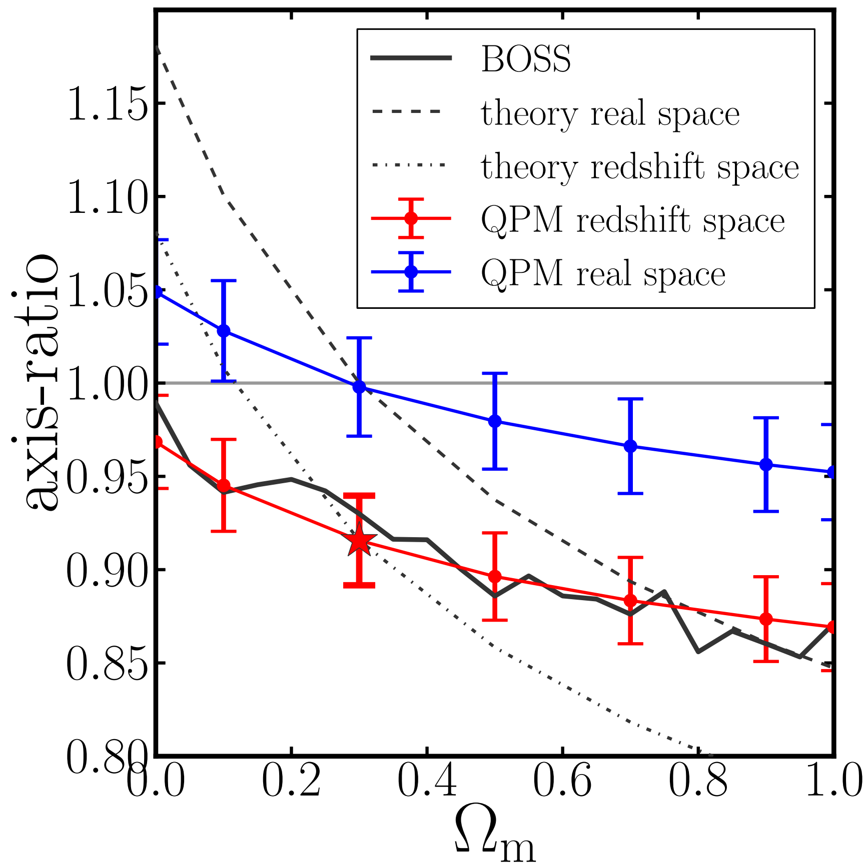

Figure IV.5 Shape measurements of the stacked voids assuming different Ω_m. Blue and red lines show the mean measurements from 1000 QPM mock catalogs in real space and redshift space, with the error bars showing the standard deviation of the 1000 measurements. The black line shows the measurement from the BOSS CMASS galaxy catalog. The red point at $\Omega_m = 0.29$ is highlighted with a star to show that this is the shape of the stacked void when assuming the right cosmology and including the RSD effects. The dashed line shows the ideal theoretical prediction in real space given by equation IV.6, and the dash-dot line is the theoretical prediction in redshift space by simply shifting the dashed line by the value of the red star point.

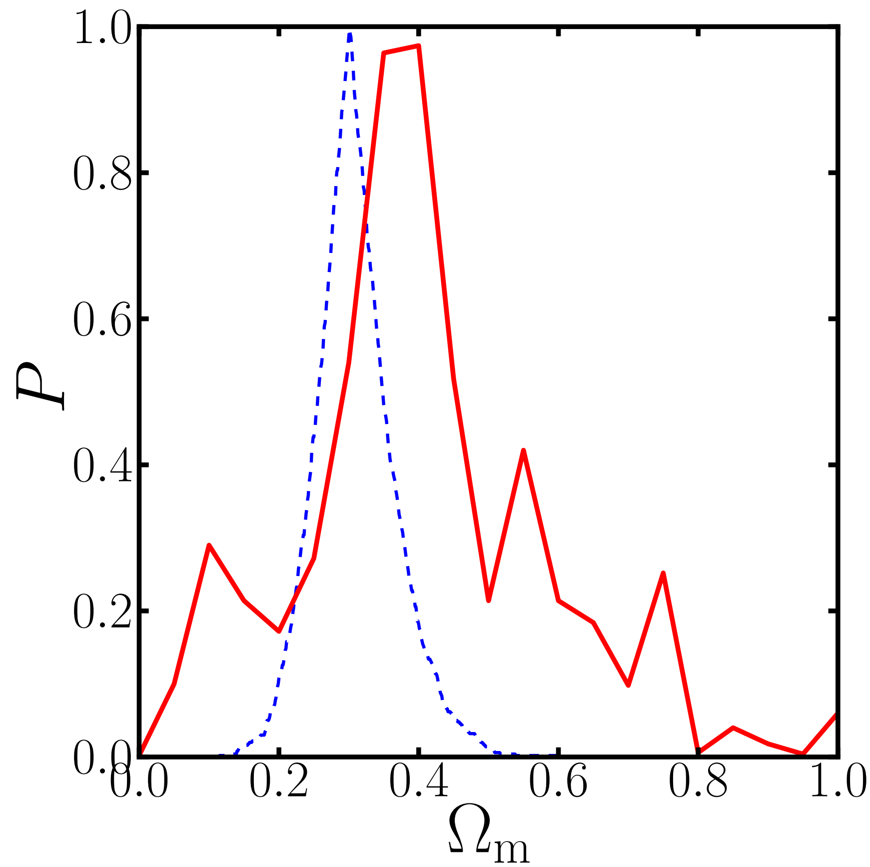

Figure IV.6 The probability distribution of Ω_m (red curve) calculated by comparing the shape measurements of the CMASS data to the expected value (red star point in figure IV.5) measured from the mock catalogs. The blue dashed curve indicates the ideal constraint by comparing the theoretical prediction (dash-dot curve in figure IV.5) to the expected value.

this would give us a constraint of $\Omega_{\mathrm{m}} = 0.30 \pm 0.05$.

IV.8 Discussion and conclusion

We identify the cosmic voids in the most recent BOSS galaxy catalog and a set of 1000 QPM mock galaxy catalogs with the ZOBOV void finding algorithm, and we accurately measure the shape of the stacked voids. By repeating the steps for different cosmology, we apply the Alcock-Paczyński test on the stacked voids and put a constraint on the parameter Ω_{m}.

Sutter et al. (2012a) suggested that it is important to avoid using the voids that may be intersected by the survey boundaries. We argue that voids which align along different parts of the boundaries may still cancel out each other. Using a large set of mocks, we find that we can still reliably retrieve the correct shape without considering whether the voids are intersected by the boundaries. Our tests show that if we only use the voids which are not intersected by any of the boundaries, the shape of the stacked voids is always consistent with the shape of the stacked voids made of all the voids. However, the uncertainties are larger because the number of the voids which are far away from any boundaries is limited.

Using all galaxies around void centers gives us many more points in the stack, which improves the Poisson noise and traces the full shape of the voids better. But it is also more likely to include some nearby clusters, which can affect the accuracy of the shape measurements. We compare the shape measurements of the stacked voids using all galaxies around void centers and using only void galaxies, and find that while both methods retrieve the consistent shape measurements, using all galaxies gives us around 30% better accuracy in the shape measurements.

When we measure the shape using the central part of the stacked voids, choosing a smaller spheroid can result in too few points and increase the Poisson noise. But if the spheroid is too large, it is more likely to be affected by the high density regions surrounding the voids. We test the shape measurements using different spheroid sizes, and we find

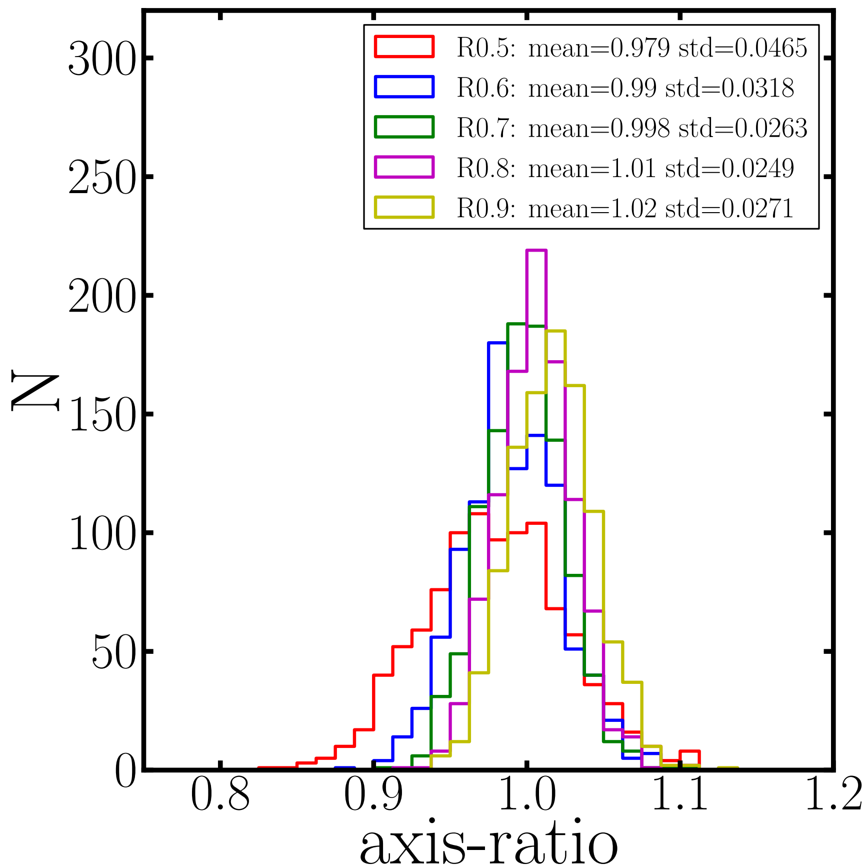

Figure IV.7 Shape measurements using different size of spheroids, with the volume equal to spheres of radius ranging from 0.5 to 0.9 of the effective radius of the stacked voids. This test is done on QPM mocks in real space.

that a spheroid with the volume equal to a sphere of radius R around 0.7 to 0.8 of the effective radius of the stacked voids provides the most stable results and the optimized uncertainties. Figure IV.7 shows the effect of using different size of spheroids. Though all measurements are consistent with the intrinsic spherical shape, there is a slight trend in the shape measurement when varying the spheroidal size, of which the reason is unclear. We decide to choose $R = 0.7$ because it recover the intrinsic shape best and its uncertainty is among the smallest.

We measure the shape of the stacked voids with an accuracy of 2.6%. To understand how much of the uncertainties comes from the Poisson process, we generate mock spheres filled with random points with the same number density and a similar density profile as the stacked voids from the CMASS sample, and we measure their shape. We find that Poisson noise contributes around 0.6% out of the 2.6%. The remainder is due to the limited number of voids in the survey volume and the variance of the shape of individual voids. So a future survey with higher density of tracers will only slightly improve the Poisson noise, but a much larger volume may provide more accurate shape measurements.

Redshift space distortion is the biggest concern in applying the AP test. In this analysis, we find that the shape of the stacked voids in redshift space is squashed by a factor of 0.92. While people may expect the stacked voids to be elongated in redshift space, recent studies using the same ZOBOV void finding algorithm all show similar squashing. For example, Lavaux & Wandelt (2012) found that the squashing effect is almost universal and constant, though they only used high density N-body simulation particles as the tracers and the voids they used were much smaller. Sutter et al. (2014) used mock catalogs to show the squashing appears universal for all void sizes at all redshifts and for all tracer densities. In this study, we find that in all cases RSD effects show a nearly constant and stable squashing in the shape of the stacked voids. The exact mechanism of this squashing is unclear and requires further investigation, but our tests show that it is not just caused by small-scale redshift space distortions. Using the halo catalogs from the 40 Carmen simulations, we remove

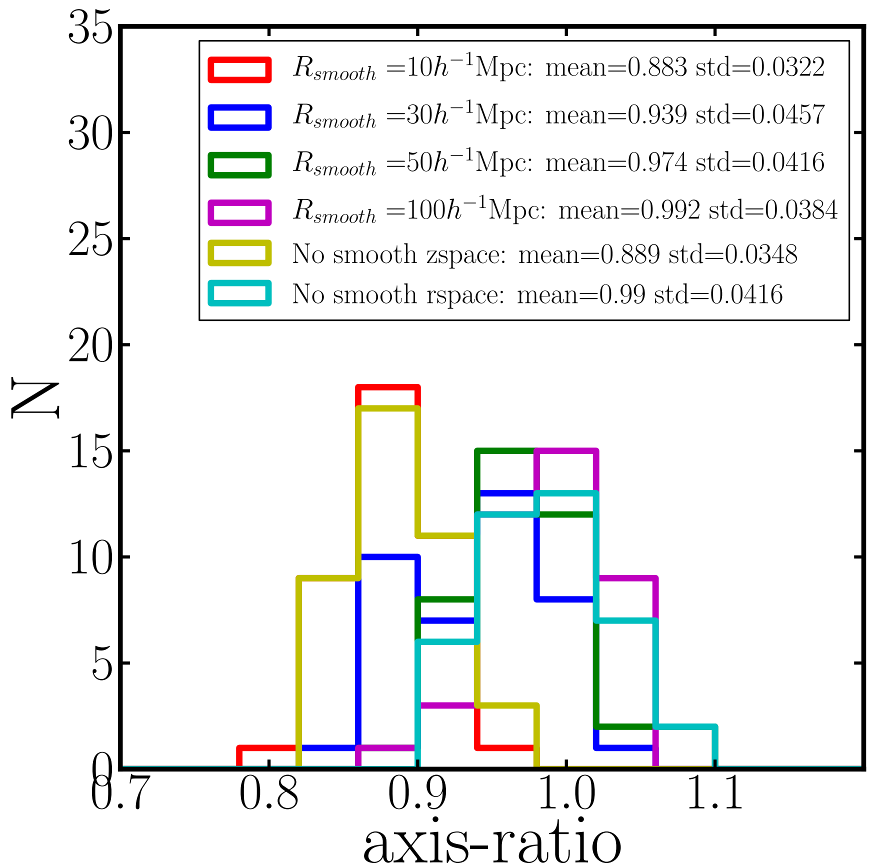

Figure IV.8 Testing the effect of squashing in redshift space by smoothing the velocity field. We smooth the velocity field in the 40 Carmen halo catalogs with different scales and redo the procedure in redshift space. The result shows that larger smoothing scales will decrease the redshift distortion effect as expected, but the squashing effect is still noticeable even on the scales as large as 50 h^{-1}Mpc.

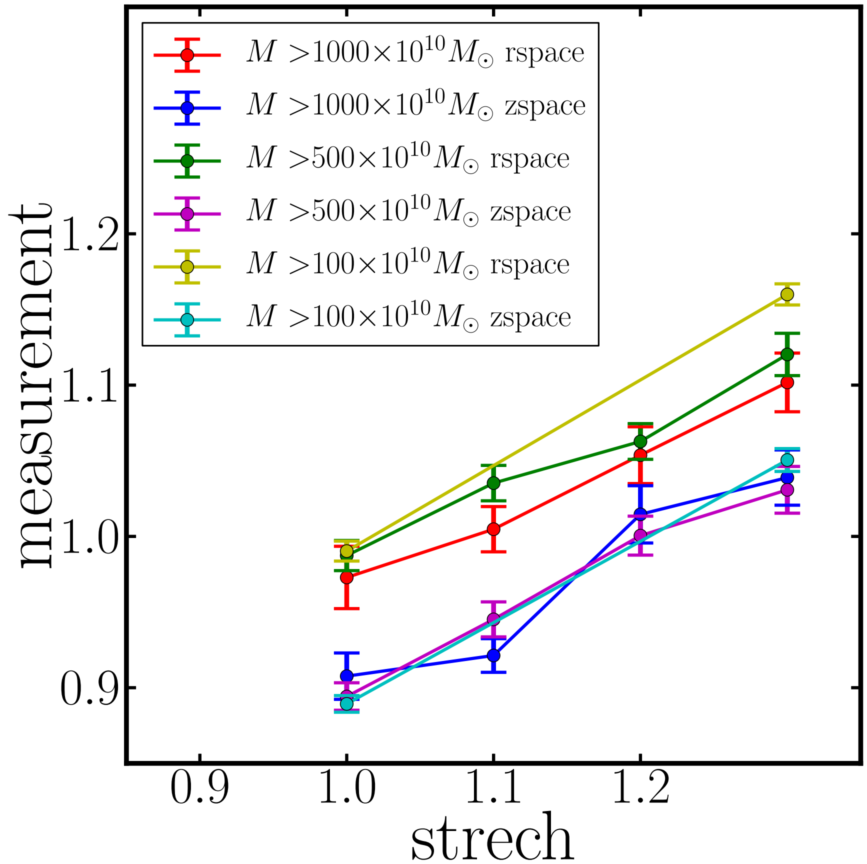

Figure IV.9 Testing the effect of the tracer density on the shaped of the stacked void using different halo catalogs from the LasDamas simulations. Lower halo mass cut (higher tracer density) leads to a slightly steeper trend, which is closer to the actual stretch.

the small-scale fingers-of-god effects by assigning satellite galaxies the same velocities as their central galaxies, and then redo the whole procedure in the redshift space. We find that removing fingers-of-god has nearly no effect on the shape measurements in redshift space. We also smooth the velocity field in the Carmen halo catalogs using different sizes of smoothing spheres. In figure IV.8, the result shows that the larger the smoothing scale, the smaller the redshift distortion effect on the shape of the stacked voids. But even on the scale of 50 h^{-1}Mpc, the squashing is still noticeable. We thus correct for the redshift space distortions empirically, and we leave more sophisticated RSD effects modeling to future studies.

One may expect that the average shape measurements of the mocks in real space should match the theoretical prediction as shown in equation IV.6, but this is not the case. Due to the sparse sampling, we can never find all the voids in their natural extension. For example, in a very sparse sample, an elongated void may be recognized as two separate voids, which both don't have the expected elongation. To test how sparse sampling may affect the result, we use a set of halo catalogs from the LasDamas simulation (McBride et al. 2009) and we make different halo mass cuts to generate samples with different sparseness. We manually stretch the simulation box and run our method on the halo catalogs. Figure IV.9 shows that the denser the sample, the closer we can recover the actual stretch, though it is still far away from recovering the actual stretch. This means that a future survey with higher number density of the tracers will provide a stronger constraint not only by slightly improving the Poisson error but also by bringing the shape measurements closer to the theoretical prediction.

To estimate how the uncertainty scales with the survey volume, we combine the mocks and stack the voids from multiple mocks to mimic a larger volume survey. For example, we combine every 5 mocks to mimic a survey of 5 times the volume of the BOSS CMASS sample, which leaves us 200 samples in total. We then get a new uncertainty of the shape of the stacked void in such volume. Using this uncertainty, we can recalculate the probability distribution of Ω_m and measure the uncertainty in Ω_m. We calculate the percent uncertainty in Ω_m for different survey volumes, and the result is shown in figureIV.10. The realistic case in the plot is calculated by comparing the polynomial fit of the black data curve in figure IV.5 to the red star reference point with updated uncertainties for different volumes, and the optimal case is calculated by comparing the theoretical prediction (dash-dot line in figure IV.5) to the reference point. We find that the uncertainty roughly scales with square root of the survey volume. For a future survey of 10 times the BOSS CMASS sample, we can expect to measure the Ω_m with 12% accuracy using the same technique and procedure we present in this chapter. In the most optimal case where we can perfectly

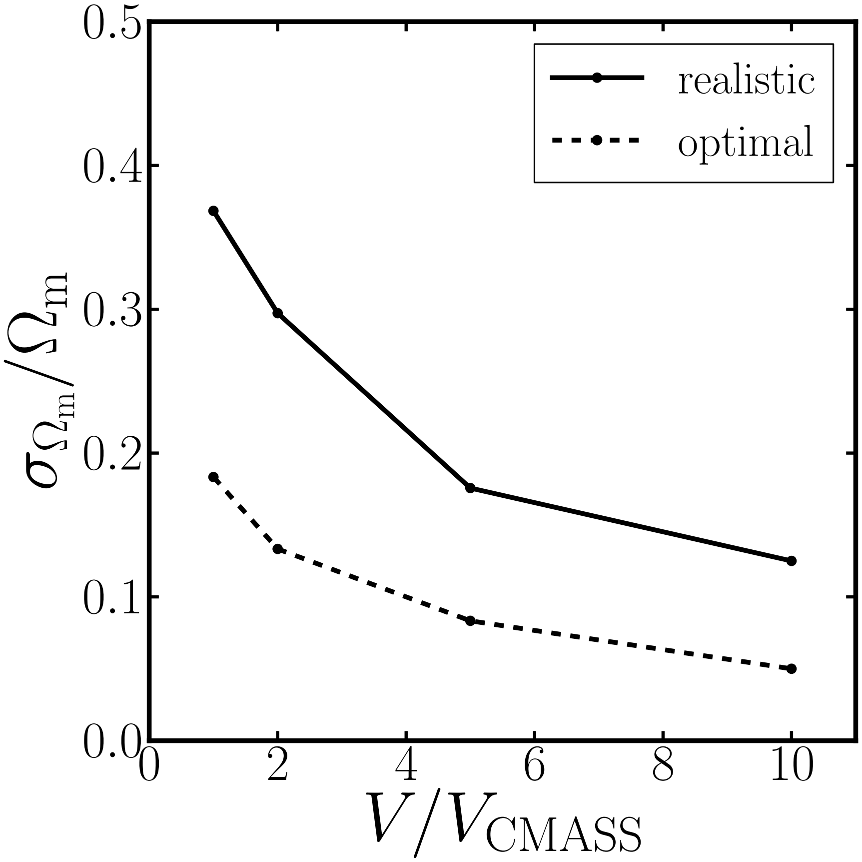

Figure IV.10 Predictions of how the uncertainty in Ω_m scales with the survey volume. The predictions are made by combining multiple mocks to mimic a larger survey volume. The realistic case (solid curve) shows how the uncertainty will scale if we apply the same procedure to a larger volume. The optimal case (dashed curve) shows the lower limits of the uncertainties assuming we can perfectly retrieve each void in their natural extension and fully recover the AP signal.

retrieve the natural extension of every void and fully recover the AP signal, we can expect an accuracy of 5% via the AP test on the stacked voids. Note that this prediction assumes larger surveys with the same number density and redshift range as the BOSS survey. Future galaxy redshift surveys will extend to higher redshift regions and the sample may be much denser, which can all benefit the AP test.

Many steps in this study can still be improved, including but not limited to better RSD modeling, optimizing the method of shape measurement, and testing the constraining power of different size and redshift binning. Future galaxy redshift surveys such as eBOSS (Dawson et al. 2015, in preparation), DESI (Levi et al. 2013), Euclid (Laureijs et al. 2011) and WFIRST (Spergel et al. 2013) will produce larger than ever maps of galaxies in the next decade, which can potentially make cosmic voids a very powerful tool to constrain cosmology.

CHAPTER V

Probing Galactic Structure with the Spatial Correlation Function of SEGUE G-dwarf Stars

Abstract

We measure the two-point correlation function of G-dwarf stars within $1-3$ kpc of the Sun in multiple lines-of-sight using the Schlesinger et al. G-dwarf sample from the SDSS SEGUE survey. The shapes of the correlation functions along individual SEGUE lines-of-sight depend sensitively on both the stellar-density gradients and the survey geometry. We fit smooth disk galaxy models to our SEGUE clustering measurements, and obtain strong constraints on the thin- and thick-disk components of the Milky Way. Specifically, we constrain the values of the thin- and thick-disk scale heights with 3% and 2% precision, respectively, and the values of the thin- and thick-disk scale lengths with 20% and 8% precision, respectively. Moreover, we find that a two-disk model is unable to fully explain our clustering measurements, which exhibit an excess of clustering at small scales ($\lesssim 50$ pc). This suggests the presence of small-scale substructure in the disk system of the Milky Way.

V.1 Introduction

The Milky Way provides a unique laboratory for studying the structure of a galaxy in detail, by allowing us to measure and analyze the properties of large samples of individual stars (see reviews by Ivezić et al. 2012 and Rix & Bovy 2013). Recent surveys, such as the Sloan Digital Sky Survey (SDSS I-III; York et al. 2000; Eisenstein et al. 2011), the Two-Micron All Sky Survey (2MASS; Skrutskie et al. 2006), the Radial Velocity Experiment (RAVE; Kordopatis et al. 2013), and others have placed strong constraints on the smooth components of the Milky Way (e.g., Carollo et al. 2010; Bovy et al. 2012b), and have discovered significant spatial substructure in the Milky Way, such as stellar streams (e.g., Belokurov et al. 2006) and stellar overdensities (e.g., Jurić et al. 2008). Investigating the structure of the Milky Way provides clues about galaxy formation and evolution that cannot be extracted from observations of distant galaxies.

The Sloan Extension for Galactic Understanding and Exploration (SEGUE; Yanny et al. 2009) is a spectroscopic sub-survey of the SDSS that focused on Galactic science. SEGUE data provides the largest spectroscopic sample of Galactic stars currently available, and covers a more extensive volume of the Milky Way than previous studies, probing from the local disk all the way to the outer stellar halo. The full SEGUE survey provides an unprecedented opportunity to investigate the structure of the Milky Way (e.g., Carollo et al. 2010; de Jong et al. 2010; Cheng et al. 2012).

The spatial two-point correlation function is one of the simplest and most effective statistical tools for studying clustering in general, and it is widely used in studies of the large-scale structure of the Universe (Peebles 1973; see Anderson et al. 2014 for a recent example). However, it has rarely been used in Galactic structure studies, mainly due to the lack of large and homogeneous spectroscopic stellar samples. There have only been a few applications of the correlation function applied to Galactic halo stars, especially giants and blue horizontal-branch (BHB) stars, but the sample sizes were limited. Doinidis & Beers (1989) analyzed over 4,400 BHB stars, and found an excess correlation with separations $r \leq$ 25 pc. Starkenburg et al. (2009) developed a phase-space correlation function, and applied it to 101 giants in the Spaghetti project (Morrison et al. 2000) to search for substructures in the halo. The phase-space correlation function has also been applied to various BHB samples to quantify the amount of spatial and kinematic substructure in the Milky Way's stellar halo (De Propris et al. 2010; Xue et al. 2011; Cooper et al. 2011). In addition to these spatial studies, the angular two-point correlation function has been used to study the stellar cluster distribution (Lopez-Corredoira et al. 1998) and to search for wide binaries (see Longhitano & Binggeli 2010 as an example).

With the advent of large stellar samples provided by the SEGUE survey, it is time to explore Galactic structure by applying the correlation function to stars. In this article,

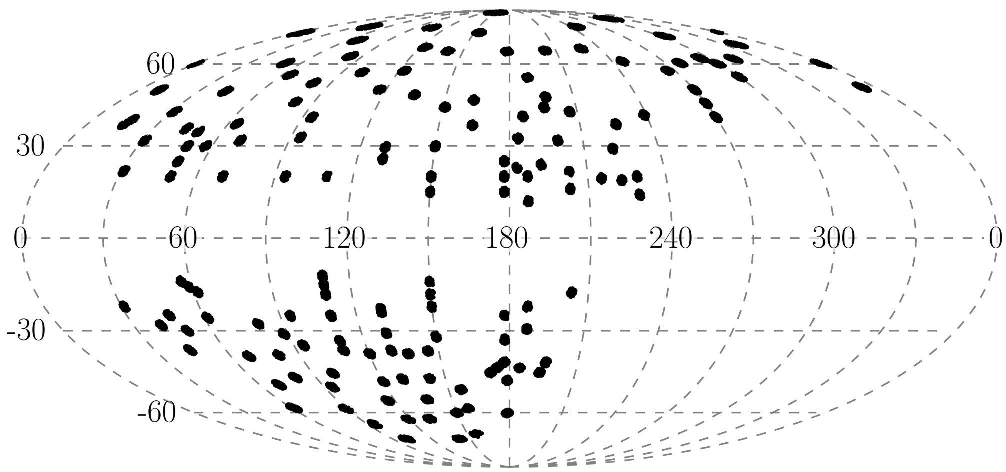

Figure V.1 Sky map of the 152 SEGUE fields used in this study, shown in a Mollweide projection in Galactic coordinates. Each point indicates the location of a single pencil-beam volume that is probed by a SEGUE spectroscopic plate covering 7 deg^2 on the sky.

we measure the full 3-D spatial two-point correlation function of the SEGUE G-dwarf sample, which is the largest stellar category in the survey. In §V.2 we describe the basics of the SEGUE survey and the G-dwarf sample we use. In §V.3 we present our correlation function measurements and build intuition about its shape by investigating how it depends on the underlying stellar-density gradient and survey geometry. In §V.4 we fit a smooth Galactic model to our measurements and in §V.5 we study residuals with respect to this model. Finally, we summarize our results and discuss possible future work in §V.6.

V.2 SEGUE G-dwarf Sample

The SEGUE survey makes use of the dedicated SDSS telescope (Gunn et al. 2006) and multi-object spectrograph (Smee et al. 2013). SEGUE combines the extensive and uniform photometry from the SDSS with medium-resolution ($R \sim 1800$) spectroscopy over a broad spectral range ($3800-9200$Å) for $\sim 240{,}000$ stars spanning a range of spectral types. SEGUE was designed to sample Galactic structure at a variety of distances in ~ 200 pencil-beam' volumes spread over the sky available from Apache Point. Each pencil beam

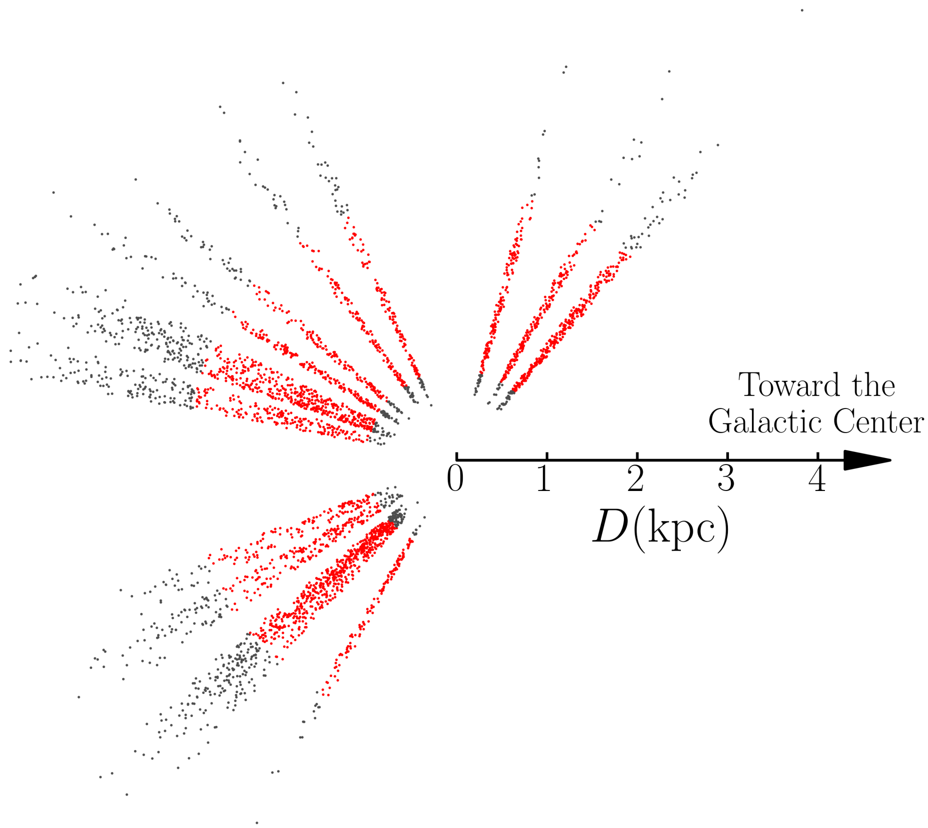

Figure V.2 A selection of SEGUE pencil-beam fields in a slice perpendicular to the Galactic plane, including the Galactic center. Specifically, the slice shows fields with Galactic longitudes within ten degrees of 0° or 180° Galactic longitude. Each dot shows the location of a SEGUE G-dwarf, with red points indicating stars with distances between $1-3$ kpc, which are used in this study.

corresponds to a single SDSS spectroscopic plate covering a circular region of 7 square degrees and probes a selection of stars in that line-of-sight with up to 640 spectroscopic fibers (Yanny et al. 2009). Figure V.1 displays the sky positions of the pencil beams included in this study using a Mollweide projection in Galactic coordinates. Figure V.2 presents an edge-on view of the pencil beams with Galactic longitudes near the Galactic center and the Galactic anticenter.

The G-dwarf sample represents SEGUE's largest single homogeneous stellar spectral target category. The SEGUE G dwarfs are defined as having magnitudes and colors in the range $14.0 < r_0 < 20.2$ and $0.48 < (g-r)_0 < 0.55$, where g_0 and r_0 are the extinction-corrected g- and r-band magnitudes (the extinction correction uses the Schlegel et al. 1998 dust map). This simple target selection makes the selection biases relatively straightforward to understand (Yanny et al. 2009). Here we use the G-dwarf catalog with distances and weights derived by Schlesinger et al. (2012). Distances are estimated with an isochrone-matching technique that is accurate to $\sim 8\%$ for metal-poor and $\sim 18\%$ for metal-rich stars (An et al. 2009).

We also apply the target-type weights and the r-magnitude weights in the catalog described by Schlesinger et al. (2012) to correct for various selection biases. SEGUE categories often focus on specific ranges in parameter space, and targets that fulfill multiple target-type criteria have multiple opportunities to be assigned a spectroscopic fiber. This approach leads to a slightly biased G-dwarf selection, which can be corrected for by the target-type weights. SEGUE assigns roughly the same number, ~ 300, of spectroscopic fibers to G-dwarf targets on each plug-plate, but this is far less than the actual number of available G-dwarfs, which also varies from field-to-field. As the stellar number density changes over the SEGUE footprint, we must use r-magnitude weights to correct for this variable sampling, in order to better represent the true underlying stellar distribution in the Milky Way. For more details about the survey completeness and weights, we refer readers to Schlesinger et al. (2012,§4.7). Figure V.3 presents the distribution of G-dwarf stars with

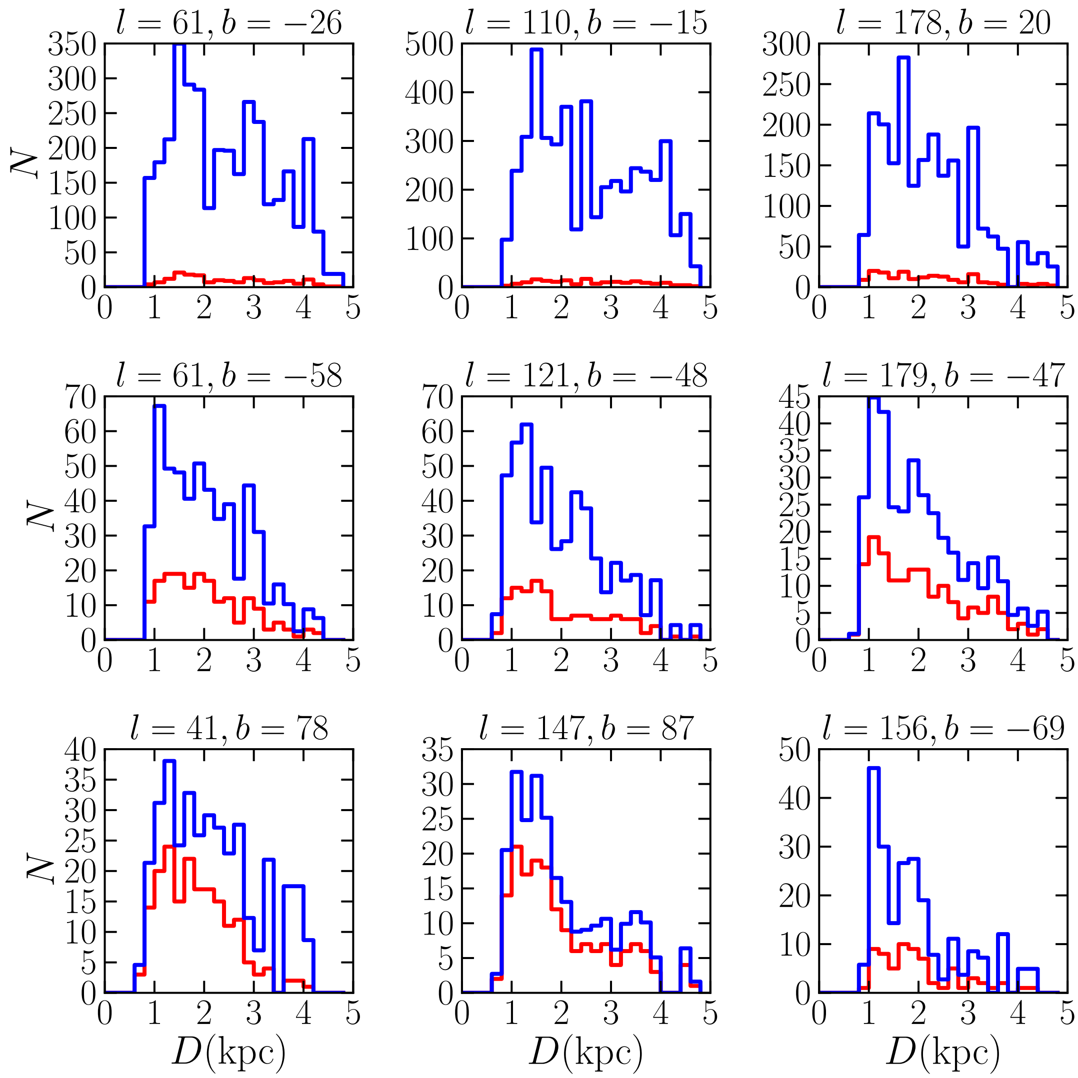

Figure V.3 Distribution of G-dwarf stars with distance, along a selection of nine SEGUE lines-of-sight. Each panel shows a particular SEGUE field, with panels arranged so that, going from top to bottom, fields point farther away from the Galactic plane in latitude, and, going from left to right, fields point farther away from the Galactic center in longitude. The Galactic coordinates of each field are listed at the top of each panel. The unweighted distributions are shown in red, while the weighted distributions, which are corrected for incompleteness, are shown in blue (see Schlesinger et al. 2012 for more details on the weighting scheme employed).

distance for a selection of nine SEGUE fields of varying Galactic latitude and longitude. The figure shows both the raw and weighted stellar distributions. Although the different lines-of-sight contain similar numbers of G-dwarf stars (as seen from the unweighted distributions), it is clear that there are large differences in the weighted distributions. Fields near the Galactic disk and the Galactic center have larger r-weights to account for the denser stellar distributions in those directions.

To achieve a sufficiently high number density of stars throughout our sample volume, and to avoid unrealistically large weights at the near and far ends of the pencil beams, we restrict the sample to stars with distances from $1-3$ kpc, and ignore pencil beams containing less than 50 G dwarfs. These selection criteria produce a sample of 18,067 G dwarfs in 152 pencil beams that we use in our analysis.

V.3 Two-point Correlation Function Measurements

In galaxy surveys, a common method to estimate the correlation function of a given sample is to construct a denser and uniform random sample with the same survey geometry, and then, in each distance separation bin $[r, r+\Delta r]$, count the number of pairs in both the survey data and the random sample. The correlation function can then be estimated by the so-called natural estimator,

$$\xi(r) = \frac{DD(r)}{RR(r)} - 1, \tag{V.1}$$

where DD are the weighted and normalized pair counts of objects found in each separation bin, and RR are the normalized pair counts of random points. The two terms are normalized by dividing by the square of the total number of data and random points, respectively. When estimating the correlation function of galaxies, it makes sense to use a uniformly distributed random sample because the universe is intrinsically homogeneous and isotropic on large scales. However, this is not the case for stars within the Galaxy, which are distributed in disk and halo structures that exhibit strong global density gradients.

If we know the global spatial-density distribution of stars in the Galaxy, we can construct a substitute for the random sample that instead follows the same global distribution as the stars. The measured correlation function will then mostly cancel on all scales, and reveal whatever excess clustering remains. If we do not fully know the underlying density distribution of stars, we can still compare the observed data to a uniform random sample, but then the measured correlation function will have a shape that encodes this information. The pencil-beam survey geometry can also add complications. The interplay between the survey geometry and the non-uniform density distribution of stars can create additional signals in the correlation function.

Before computing the correlation function of the SEGUE stars, we first investigate how stellar-density gradients and the pencil-beam survey geometry can affect the shape of the correlation function in general, by creating different mock star samples and measuring their correlation function. First, we set the mock survey geometry to be the same as that in one of our SEGUE lines-of-sight, i.e., a pencil beam with an angular diameter of $3°$ and distances between $1-3$ kpc. We generate mock star samples within this geometry, each containing 1000 mock stars, using different power-law density profiles. Specifically, the density gradients we adopt are $n \sim d^{-4}$, d^{-3}, d^{-2}, d^{-1}, d^{1}, and d^{2}, where n is the number density of stars and d is the distance from the observer. We then construct a uniformly distributed random sample with ten times the number density, and calculate the correlation function using equation V.1 for each density profile. Finally, we repeat these steps 1000 times, using independent realizations of the mock samples, and average the results to reduce the noise. Note that these mock samples with power-law density gradients are not meant to represent realistic Galactic models, but serve the purpose of building intuition on how density gradients can affect the derived correlation function. We study realistic Galactic models in § V.4.

Figure V.4 shows the resulting correlation functions for our adopted density gradients. The overall shape of the correlation function is quite complex, and is very sensitive to the density profile. On small scales ($\lesssim 50$ pc) the correlation function is always boosted,

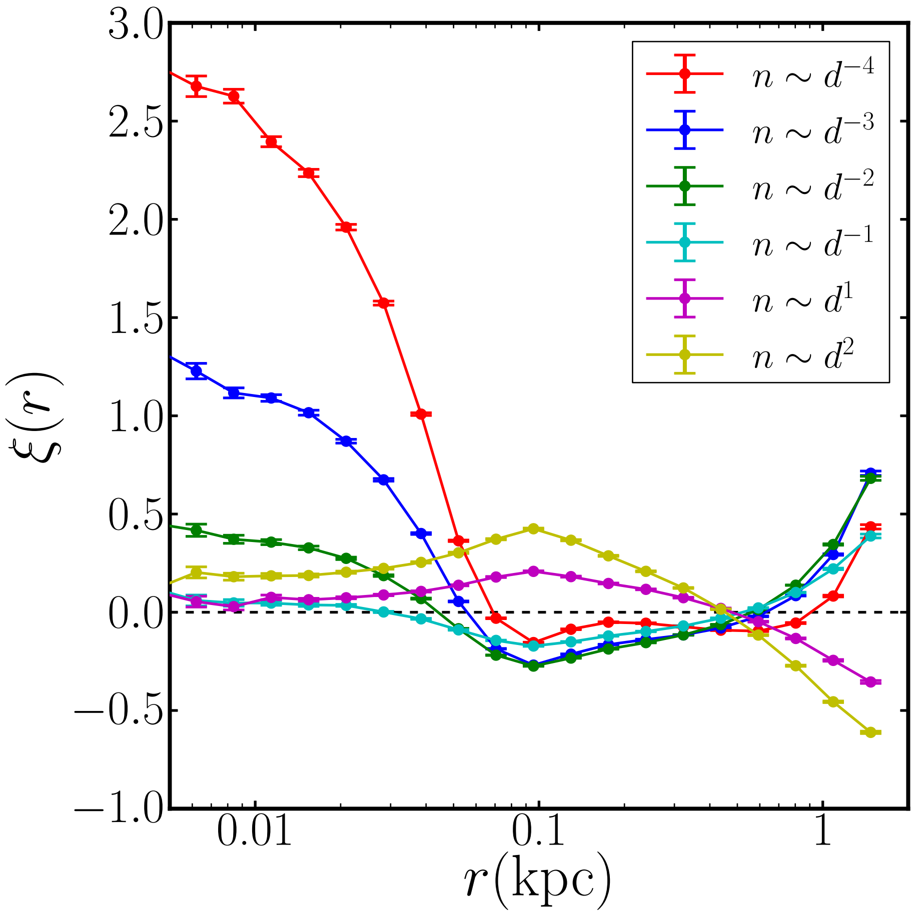

Figure V.4 Dependence of the correlation function on the underlying density gradient. The correlation functions are computed for mock star samples that all have the same pencil-beam geometry as one of our SEGUE lines-of-sight, but are designed to have different power-law stellar density profiles, as listed in the panel. Each curve is the average over 1000 mock samples containing 1000 stars each; the error bars show the uncertainty in the mean as estimated from the standard deviation among the 1000 mocks. The correlation function has a complex shape, and is highly sensitive to the stellar-density gradient, especially on small scales.

regardless of whether the underlying density gradient is positive or negative. However, on larger scales ($\sim 50-500$ pc), the clustering is depressed or boosted depending on whether the density gradient is negative or positive, respectively. Finally, on even larger scales ($\gtrsim 500$ pc) the sign of this dependence flips. There is an interesting feature at $r \sim 0.1$ kpc, where the correlation function is a minimum or maximum for negative and positive density gradients, respectively. This is approximately equal to the diameter of the pencil beam volume at its halfway point along the line-of-sight.

Next, we investigate how the survey geometry can affect the correlation function. We set the underlying density profile of our mock star samples to be $n \sim d^{-2}$, and vary the sample geometry. The geometries we test all range in distance from $1-3$ kpc, as in our SEGUE sample, but their angular size on the sky varies from the pencil beam of radius $\theta_{\mathrm{radius}} = 1.5°$ (as in SEGUE), to larger beams of radius 3°, 6°, 12°, as well as a full-sky geometry. As before, we generate 1000 independent mock samples for each geometry, and calculate their average correlation function using a uniform and dense random sample. Figure V.5 reveals a fairly simple dependence of the correlation function on survey geometry. On scales that are much smaller than the width of the pencil beam, the correlation function is unaffected by the survey geometry, as might be expected. However, the feature in the correlation function that occurs at 0.1 kpc for the SEGUE geometry shifts to progressively larger scales as the width of the pencil beam grows. In fact, the scale of the feature is always approximately equal to the diameter of the pencil-beam volume at its halfway point along the line-of-sight.

These tests demonstrate that the correlation function of stars will depend sensitively on both the underlying density gradients and the survey geometry. The resulting correlation function has a peculiar shape that is quite different from the power-law shape we are accustomed to seeing for galaxy surveys. The strong dependence on the underlying density gradients suggests that the correlation function of stars could have strong constraining power on Galactic structure models. This is especially true at the smallest scales and when

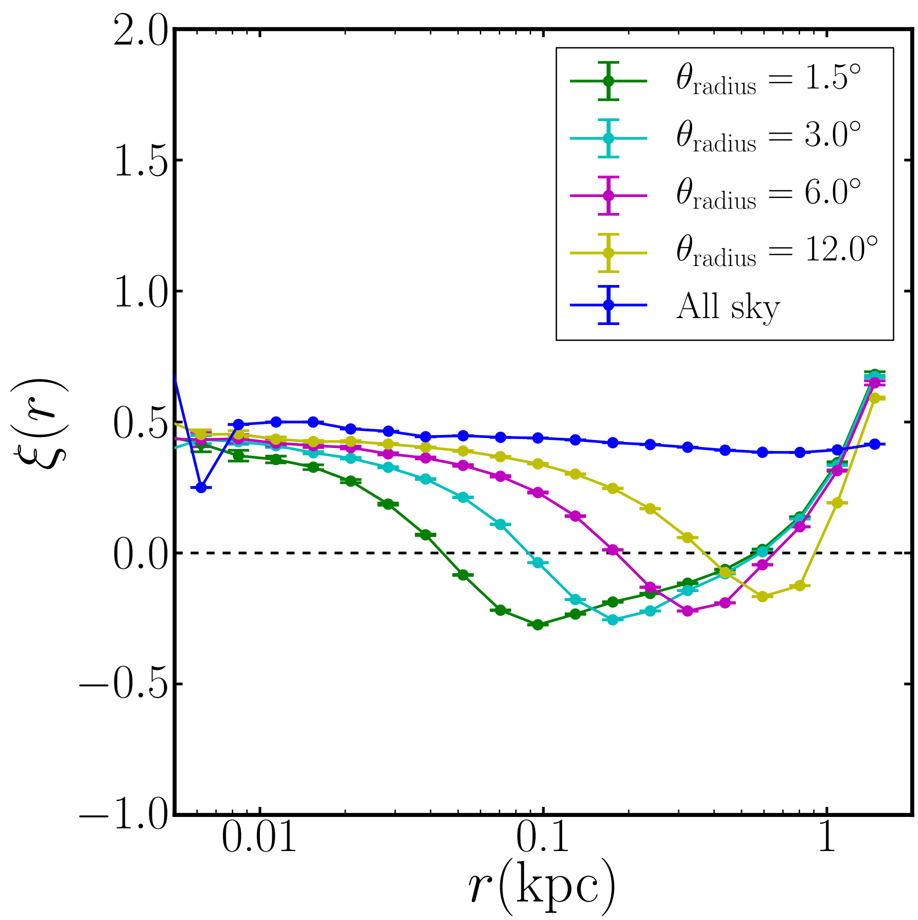

Figure V.5 Dependence of the correlation function on survey geometry. The correlation functions are computed for mock star samples that all have the same stellar-density profile of $n \sim d^{-2}$, but occupy different sample geometries. All sample geometries range in distance from $1-3$ kpc, but their angular extent on the sky varies from a circle of radius $\theta_{\mathrm{radius}} = 1.5°$, all the way up to the full sky, as listed in the panel. As in Fig. V.4, points and errors are estimated from 1000 mock samples. The correlation function is sensitive to the survey geometry, featuring a minimum at a scale approximately equal to the diameter of the pencil-beam volume at its halfway point along the line-of-sight.

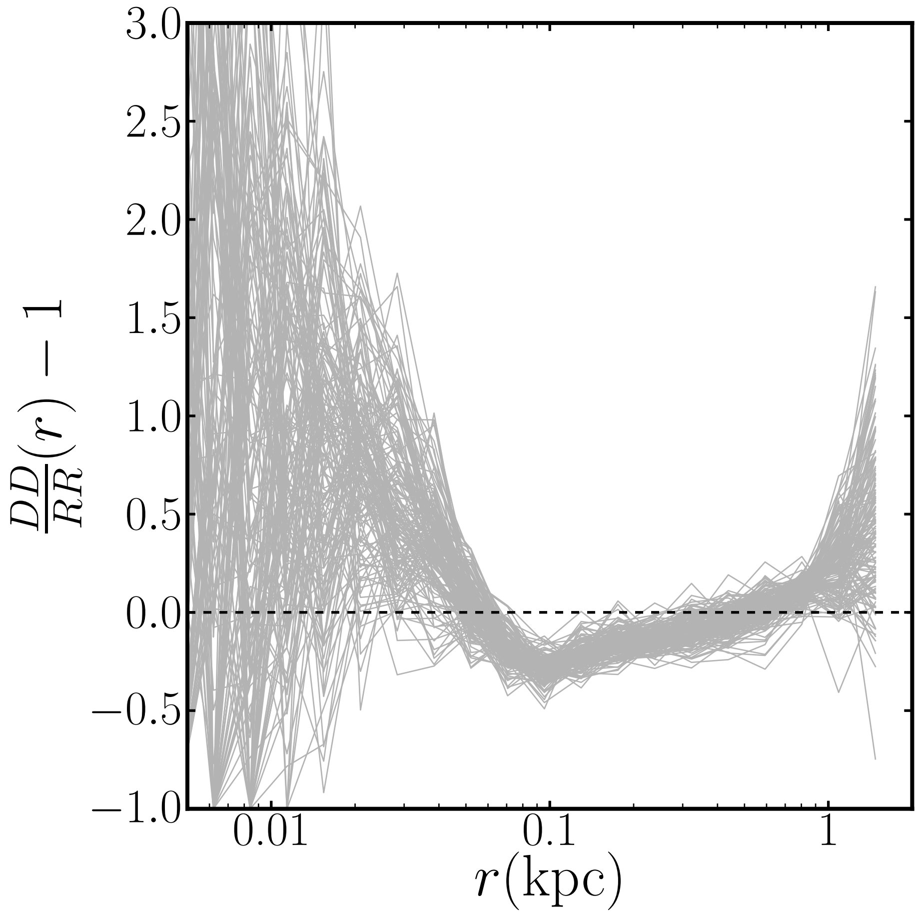

Figure V.6 The two-point correlation functions of SEGUE G-dwarf stars. Each gray line is measured from one of 152 individual SEGUE lines of sight. The shapes of the correlation functions are similar to those for the negative gradients shown in Fig. V.4.

density gradients are steep, since this is where the correlation function is most sensitive to variations in the underlying density distribution. The explanation for this is fairly straightforward. At the smallest scales we probe ($\lesssim$ 10pc), the mean separation between stars is much larger, and so there would not be many pairs if the stars were randomly distributed. If, however, there is a steep enough density gradient, the stars are redistributed so that they become sufficiently dense at either the near or far end of the survey volume (depending on whether the gradient is negative or positive), thus leading to several small-scale pairs.

To measure the correlation function of SEGUE G-dwarf stars, we first construct a random sample with the same pencil-beam geometry as our sample, and containing uniformly distributed points with 100 times higher number density than the SEGUE data. We then calculate the correlation function of each SEGUE line-of-sight independently, i.e., we only count pairs of stars that reside in the same SEGUE field. Figure V.6 shows the result, in which each gray line is the correlation function of an individual SEGUE pencil beam. The measured correlation functions have the same peculiar shape seen in the mock tests in Figure V.4. In particular, they are similar to the cases of negative density gradients, which makes perfect sense, since all SEGUE lines of sight move out of the Galactic disk.

The distances to the SEGUE stars are not known perfectly, but rather contain, on average, 12% uncertainties. It is thus important to determine how much these errors can affect the correlation function measurements. We test this issue by adding 12% Gaussian-distributed distance errors to our mock samples, and then recalculating the correlation functions. These tests demonstrate that 12% distance uncertainties have a negligible effect on the correlation function.

V.4 Fitting A Smooth Galactic Model

Since the two-point correlation function of G dwarfs is highly sensitive to stellar-density gradients, it can serve as a tool to probe the smooth density structure of the Milky Way. We approach this by replacing the uniform random sample in equation V.1 with a mock sample generated from a Milky Way model,

$$\xi'(r) = \frac{DD(r)}{MM(r)} - 1, \tag{V.2}$$

where MM are the normalized pair counts from our Milky Way model. If the model we choose truly represents the underlying stellar distribution and has the same geometry as the data, then $\xi'(r)$ should cancel on all scales and along all lines-of-sight. By searching the parameter space of a given model, we can thus place constraints on the model parameters, and determine to what extent the model can explain the observed stellar clustering.

As a proof of concept, we choose a standard thin- + thick-disk model with two exponential disk components and five parameters,

$$
\begin{aligned}
n(R,Z) \propto\ & \mathrm{sech}^2\left(\frac{Z}{2Z_{0,\mathrm{thin}}}\right)\exp\left(-\frac{R}{R_{0,\mathrm{thin}}}\right) \\
& + a\ \mathrm{sech}^2\left(\frac{Z}{2Z_{0,\mathrm{thick}}}\right)\exp\left(-\frac{R}{R_{0,\mathrm{thick}}}\right),
\end{aligned}
\tag{V.3}
$$

where $Z_{0,\mathrm{thin}}$, $Z_{0,\mathrm{thick}}$, $R_{0,\mathrm{thin}}$, $R_{0,\mathrm{thick}}$ are scale heights and scale lengths of the thin disk and the thick disk, respectively, and the fifth parameter is the ratio of the normalization factors of the thick and the thin disk, $a = n_{0,\mathrm{thick}}/n_{0,\mathrm{thin}}$. In a recent study, Bovy et al. (2012a) reported that when one separates disk populations by their chemical signatures, there is a continuous range of disk thicknesses, and there is no distinct thick disk component. Since we do not apply any additional color or metallicity cuts in the sample, for simplicity we stick to the traditional bi-modal disk model. Our model does not include a bulge or halo component because, in the restricted range of distances we probe ($1-3$ kpc), these components should contribute a negligible number of stars to our sample.

We employ a Markov-chain Monte Carlo (MCMC) method to identify the region in parameter space where $\xi'(r)$ is consistent with zero, i.e., to find the parameters that best fit the SEGUE clustering data. At every MCMC step, we need to have a mock catalog from our model that is generated from a given set of parameter values and has the same SEGUE survey geometry (all lines-of-sight). Moreover, the mock catalog should be substantially denser than the SEGUE data, so that the errors in MM are much smaller than the errors in DD. Generating new dense mock samples and finding pairs at each step of the chain can be computationally expensive. Instead, we adopt a strategy that is both accurate and more efficient. We first generate a single dense and uniformly distributed random sample with the SEGUE geometry (all lines-of-sight) and identify all the pairs of points in bins of separation. At each step in the chain we assign a new weight, w_i, to each random point according to equation V.3. We then calculate $MM(r)$ by summing the product $w_i w_j$ over all pairs with separation r. Finally, we normalize MM by the sum of $w_i w_j$ over all pairs and all scales. When normalizing, the absolute normalization of $n(R,Z)$ cancels and is thus irrelevant.

In each of our 152 pencil-beam volumes, we calculate $\xi'(r)$ in 12 logarithmic bins ranging from 5 pc to 2 kpc. Excluding any bins that have zero pair counts in DD, we have 1,777 individual measurements of $\xi_i'(r)$. We estimate the total χ^2 using

$$\chi^2 = \sum_{i,r} \frac{\xi_i'^2(r)}{\sigma_i^2(r)}, \tag{V.4}$$

which sums over all scales and all pencil beams. We use jackknife resampling to estimate the uncertainties of pair counting in both the data and the model. The final uncertainty, $\sigma_i^2(r)$, is a combination of the uncertainty in the data and the uncertainty in our model, although the pair counting in our model always has much smaller uncertainties than the data because it has a much higher number density. We treat all $\xi_i'(r)$ as independent measurements and ignore the covariances. We will investigate the covariances in a future study.

Figures V.7 and V.8 show the scale-height and scale-length distributions from our MCMC chains. After marginalizing over all other parameters, we obtain a thin-disk scale height of 233 ± 7 pc and scale length of 2.34 ± 0.48 kpc, and a thick-disk scale height of 674 ± 16 pc and scale length of 2.51 ± 0.19 kpc. While these numbers are in the same broad range as other recent measurements using SEGUE or SDSS data (e.g., Jurić et al. 2008; Carollo et al. 2010; de Jong et al. 2010; Bensby et al. 2011; Cheng et al. 2012; Bovy et al. 2012b), they are not in statistical agreement with most of these studies. Unfortunately, it is difficult to directly compare our results to other studies because the star samples differ significantly in most cases (i.e., different types of stars or different metallicity or color cuts). For example, our thick-disk scale height and length are significantly lower than those measured by Jurić et al. (2008), but that study used M stars from the SDSS. Our thick-disk scale length is significantly higher than the one measured by Cheng et al. (2012), who also used SEGUE

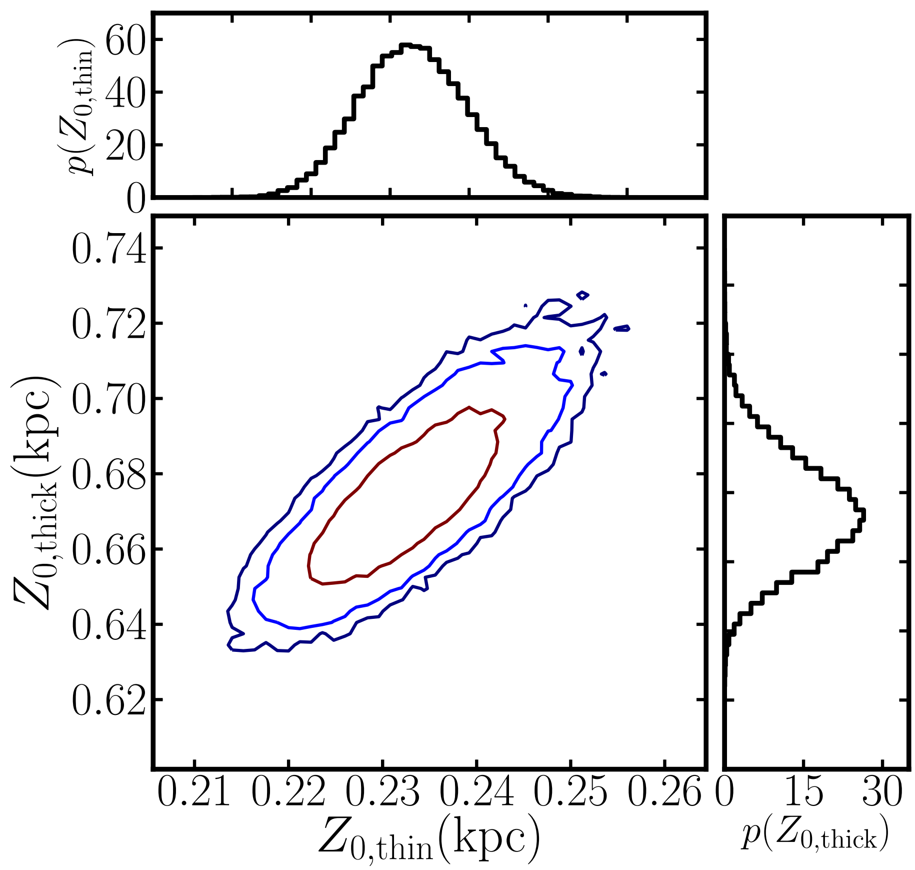

Figure V.7 The distribution of scale heights for the thin and the thick disk from the MCMC chain. The main panel shows 1-, 2-, and 3σ likelihood contours for the joint probability distribution of both scale heights, while the smaller panels on top and to the right show the individual probability distributions of each scale height, marginalized over all other parameters. The 1-σ statistical precision of these constraints is 3% and 2% for the thin- and thick-disk scale heights, respectively.

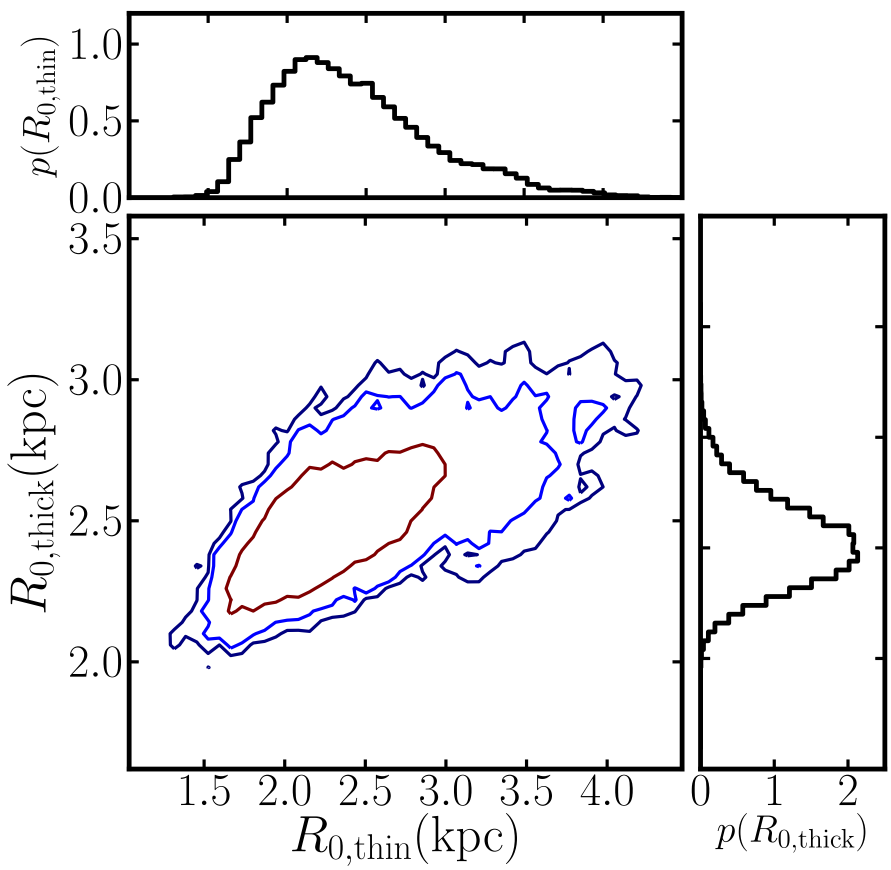

Figure V.8 The distribution of scale lengths of the thin and the thick disk from the MCMC chain. All features are similar to those in Fig. V.7. The 1-σ statistical precision of these constraints is 20% and 8% for the thin- and thick-disk scale lengths, respectively.

data, but that study focused on α-enhanced stars. Our thin-disk scale height and length are somewhat smaller than those measured by Bovy et al. (2012b), but in that study 'thin' and 'thick' disks refer to single disk fits to either α-young or α-old G-dwarf subsamples, respectively. It would be interesting to repeat our measurements on different subsets of the data, so that we may better compare our constraints to other investigations.

We check the accuracy with which our fitting methodology can recover disk parameters by creating a mock SEGUE sample from equation V.3, and then analyzing it in the same way as we have analyzed the SEGUE G-dwarf sample. Our modeling methodology successfully recovers the correct thin- and thick-disk parameters within the 1σ error bars. This exercise demonstrates that our Milky Way constraints do not contain systematic errors due to the methodology. However, there may be systematic errors in our constraints that arise from errors in the SEGUE weights we use. Although we do not expect these errors to be large given the fairly homogeneous nature of the SEGUE G-dwarf sample in the narrow distance range that we study, we cannot guarantee that these systematic errors are smaller than our statistical errors. The main point to emphasize is that the high statistical precision of our measurements (2-3% for the scale heights and 8-20% for the scale lengths) proves the constraining power of the correlation function statistic for Galactic studies. We note that our statistical precision is still considerably lower than that reported by Bovy et al. (2012b), which is three to five times higher. This is most likely due to the fact that we measure the correlation function of each SEGUE line-of-sight separately, which means that the overall variation in stellar density from one sightline to another does not contribute to our model constraints. We can improve on this by measuring a single correlation function that includes cross-sightline pairs, and we leave this to a future study.

We also investigated how well the two-disk model in Equation V.3 explains the measured clustering of SEGUE G dwarfs. The χ^2 value for our best-fit model is 2,853 for 1,772 degrees of freedom, suggesting that the model is strongly ruled out. For comparison, we tried a single exponential disk model with only two parameters. The best-fit value of

χ^2 in that case is 4,384 for 1,775 degrees of freedom. The two-disk model is thus strongly preferred over the single-disk model. However, even the two-disk model is excluded by our correlation function measurements.

V.5 Evidence of Substructure?

We next investigate the residual clustering of SEGUE stars relative to our best-fit two-disk model to see where the model fails. Figure V.9 shows $\xi'(r)$ for the best-fit model along all the lines-of-sight (gray lines), as well as the mean residuals averaged over all lines-of-sight (red points). It is clear that, although our best-fit model cancels the correlation function on most scales, there remains significant excess clustering in the SEGUE data on small scales ($\lesssim$ 50 pc) that cannot be explained by the model. This discrepancy could be due to a number of reasons. It is possible that a smooth model of the density structure of the Milky Way can in fact fully account for our clustering measurements, but we have just adopted the wrong model. The "correct" model could be a two-disk model with a different functional form than Equation V.3. Alternatively, we may be missing one or more components, such as a third disk or, more likely, a smooth sequence of disks for stars of different ages, as suggested by Bovy et al. (2012b). Subtle changes to the smooth density model can cause strong deviations in the correlation function, as demonstrated in Figure V.4. Conversely, the excess clustering that we find could be evidence of substructure in the SEGUE data that cannot be explained by any smooth density model. For example, this signal could be due to some stars living in clusters, or could be due to the presence of large localized structures such as stellar streams. If the excess clustering is produced by localized structures on the sky, we would expect that those specific SEGUE lines-of-sight are solely responsible for the failure of our two-disk model to fit the data. We investigate this possibility in Figure V.10, which displays the map of χ^2 values contributed by each SEGUE field across the sky. The map does not reveal any significant spatial structure in the χ^2 distribution, suggesting that the remaining signal is probably not caused by large localized structures such as stellar

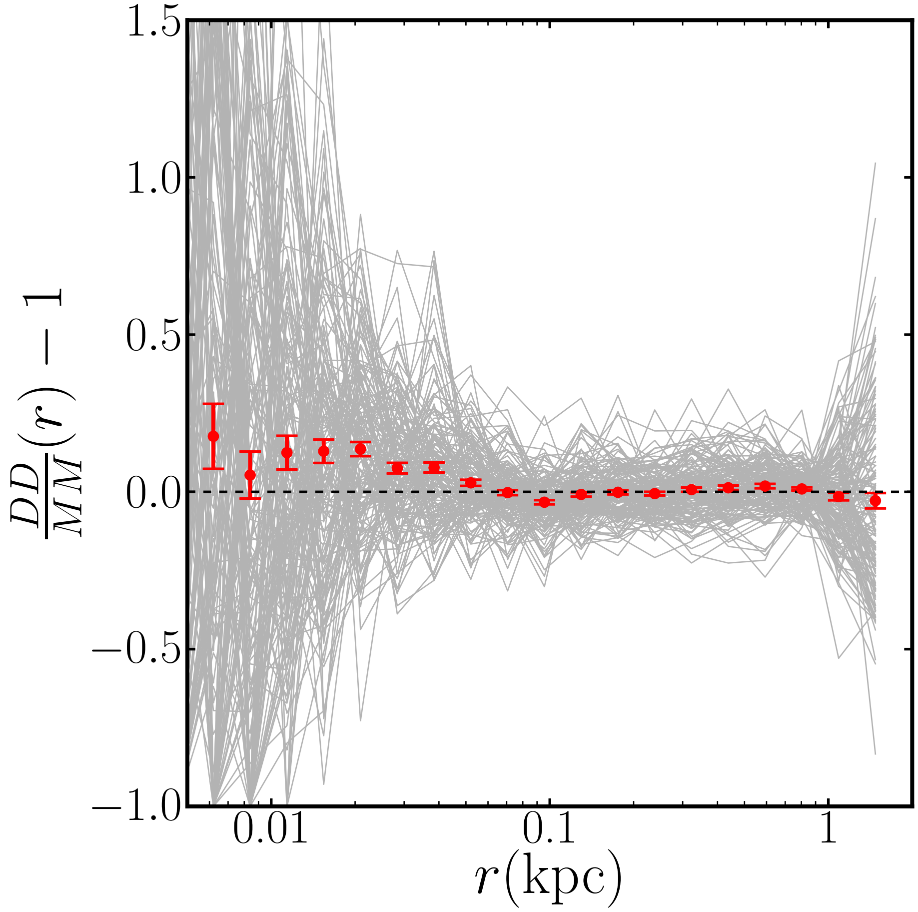

Figure V.9 Correlation function residuals of SEGUE stars relative to the best-fit two-disk model. Each gray line shows the residual pair counts for one SEGUE line-of-sight. The red points show the mean residual, and error bars show the uncertainty in the mean estimated from the dispersion among the lines-of-sight. The SEGUE data clearly shows an excess clustering at small scales ($\lesssim 50$ pc), suggesting possible substructures that are not included in our simple two-disk model.

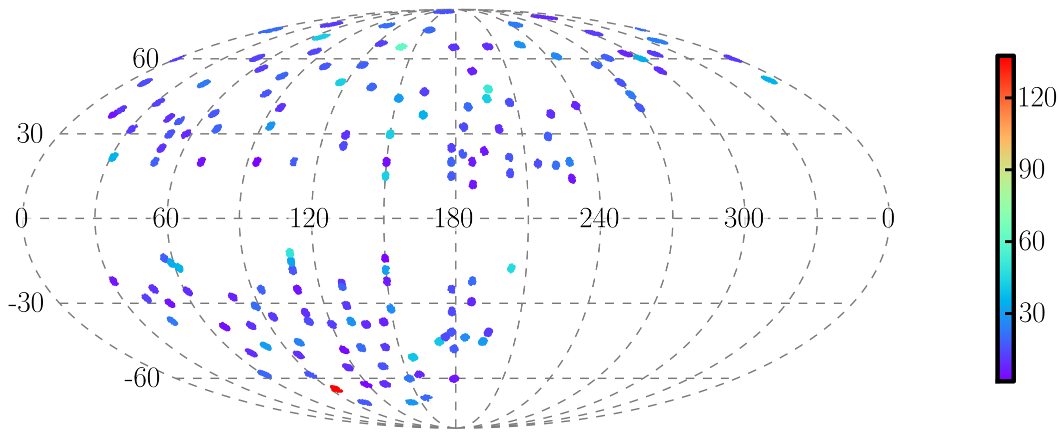

Figure V.10 Sky map of χ^2 values for the best-fit two-disk model. The color of each SEGUE field indicates the contribution to the global χ^2 coming from that particular line-of-sight. The map reveals no obvious correlation between the goodness of fit and positions on the sky, indicating that the excess signal in the correlation function is probably not caused by field-dependent structures.

streams. There is one specific SEGUE field that has an abnormally high value of χ^2: the red field at a Galactic latitude of $\approx -65°$ in Figure V.10. However, removing this line-of-sight does not resolve the discrepancy between data and model.

V.6 Summary and Discussion

In this chapter we explore applying a traditional clustering statistic, the spatial two-point correlation function, to stars in the Milky Way as a probe of Galactic structure. Tests with mock samples have shown that the shape of the correlation function is sensitive to both the stellar-density gradients in the Galaxy disk and the survey geometry. We have measured the correlation function of SDSS SEGUE G-dwarf stars, which is a large and homogenous sample with well-understood selection criteria, geometry, and distance errors. By comparing our measurements to a two-disk Galactic model, our measured correlation functions yield tight constraints on the structure of the thin and thick disk of the Milky Way. Specifically, the thin- and thick-disk scale heights are determined with a precision of 3% and 2%, respectively, while the thin- and thick-disk scale lengths are determined with a precision of 20% and 8%, respectively. This high precision is achieved with spatial information alone, and it proves the strong constraining power of the correlation function. Furthermore, we have studied the residuals of the SEGUE clustering relative to our best-fit two-disk model, and have found a small but significant excess of clustering on scales less than 50 pc in the SEGUE data relative to the smooth model. This clustering may be due to imperfections in the smooth model or it may be due to the presence of substructure in the SEGUE data that cannot be described by a smooth model. The main source of systematic error in this analysis comes from uncertainties in the weights (calculated by Schlesinger et al. 2012) that we use to account for sample incompleteness. Although we do not expect these uncertainties to be large, further work is needed to assess the extent to which they affect our model constraints.

There are several avenues for future work. First, the methodology we have used can be explored further and improved. For example, we can study the covariances between different data points and include them in the analysis. We can also probe larger scales by measuring pairs across neighboring lines-of-sight, instead of sticking to within one SEGUE field at a time. This should significantly improve the constraining power of the correlation function and it may detect the signatures of large structures such as stellar streams. Secondly, we can study subsamples of SEGUE stars, such as samples in specific metallicity ranges, in order to better compare our constraints against other works. We can also explore variants of the spatial correlation function, such as a metallicity- or age-weighted correlation function or a phase-space correlation function. Finally, we can further explore the cause of the discrepancy between the clustering of SEGUE stars and the two-disk model by exploring a larger family of smooth Galactic models.

CHAPTER VI

CONCLUSIONS

In this dissertation, I have presented several different but related analyses of structure on both extragalactic and Galactic scales.

First, I investigated whether measurements of the moments of large-scale structure can yield constraints on primordial non-Gaussianity which is a very powerful probe for constraining inflationary models in the very early universe. I used LasDamas simulations with Gaussian and three different non-Gaussian initial conditions to show that the moments of the dark matter density field differ significantly between Gaussian and non-Gaussian models. When restricted to volumes equivalent to the Sloan Digital Sky Survey II (SDSS-II) or Baryon Oscillation Spectroscopic Survey (BOSS) samples, the probability of detecting a departure from the Gaussian model is high by using measurements of the variance, but very low by using only skewness and kurtosis. I estimated that in order to detect an amount of non-Gaussianity that is consistent with recent CMB constraints using skewness or kurtosis, we would need a galaxy survey that is much larger than any planned future survey. However, future surveys should be large enough to place meaningful constraints using galaxy variance measurements.

I then turned to cosmic voids in today's large-scale structure. I applied the ZOBOV void finding algorithm to the most recent large-scale structure galaxy catalog from the Baryon Oscillation Spectroscopic Survey (BOSS), and produced a public cosmic void catalog. I also constructed mock void catalogs from 1000 mock galaxy catalogs. I measured the basic statistics of voids, such as their size and redshift distributions, and the radial density profile of the voids when stacked together. These public BOSS and mock void catalogs are useful for a number of cosmological and galaxy environment studies. Using these identified voids, I also accurately measured the shape of the stacked voids, and applied the Alcock-

Paczyński test to the stacked voids, which led to a constraint on $\Omega_{\mathrm{m}} = 0.38^{+0.18}_{-0.15}$ at 68% confidence level.

At last, I adopted the 3-D two-point correlation function statistic, which is a common tool in the field of large-scale structure but rarely used in Galactic structure study, and applied it to the SEGUE G-dwarf stars in the Milky Way. I found that the shapes of the correlation functions along individual SEGUE lines of sight depend sensitively on both the stellar density gradients and the survey geometry. By fitting mock measurements from smooth disk galaxy models to SEGUE data measurements, I was able to obtain 2-3% constraints on the thin and thick disk scales heights and 8-20% constraints on the scale lengths. Comparing the data to our best fit model shows a small but significant excess of clustering on scales less than 100 pc, which may be a hint of the existence of substructure which cannot be explained by smooth disk models.

Structure formation is a very broad research field. What I present here are some small examples of structure analysis, which can help us understand the cosmology, the formation and the evolution of the large-scale structure of the Universe, and the spatial structure and the dynamics of our Milky Way. The next generation of astronomical surveys, such as eBOSS (Dawson et al. 2015, in preparation), DESI (Levi et al. 2013), Euclid (Laureijs et al. 2011) and WFIRST (Spergel et al. 2013), will provide incredible data in the next decades. Analyzing these data will require all kinds of statistical tools and techniques, and eventually it will lead us to a more comprehensive understanding of our universe.

Appendix A

List of Cosmic Voids

We present the complete lists of cosmic voids we have identified from the BOSS galaxy catalogs. We list the void ID (col. [1]); the (J2000.0) right ascension and declination of the void weighted center (cols. [2] and [3]); the redshift of the weighted center (col. [4]); the number of galaxies in the void, N (col. [5]); the total Voronoi volume of the void V (col. [6]); the effective radius, R_{eff} (col. [7]); the number density of the minimum density Voronoi cell in the void n_{min} (col. [8]); the density contrast of the minimum density cell comparing to the mean density at that redshift δ_{min} (col. [9]); the ratio r between the minimum density particle on a ridge to the minimum density particle of the void (col. [10]); the probability that the void arises from Poisson fluctuations (col. [11]); the distance from the weighted center to the nearest survey boundary (col. [12]). The voids are ranked in decreasing order of the probability. These catalogs, along with the void catalogs from the 1,000 mock catalogs are also available for download on an external site [1].

[1] http://lss.vanderblt.edu/voids

Table A.1: List of voids in the BOSS CMASS North sample

ID	RA	DEC	z	$N_{\rm gal}$	V	$R_{\rm eff}$	$n_{\rm min}$	$\delta_{\rm min}$	r	P	$D_{boundary}$
	(deg)	(deg)			(h^{-3}Mpc^3)	(h^{-1}Mpc)	(h^3Mpc^{-3})				(h^{-1}Mpc)
(1)	(2)	(3)	(4)	(5)	(6)	(7)	(8)	(9)	(10)	(11)	(12)
60	114.782	37.641	0.648	35	1.411e+05	32.298	2.486e-05	-0.717	3.922	3.220e-14	52.504
10020	184.261	1.326	0.500	25	1.704e+04	15.964	1.364e-04	-0.652	3.441	2.200e-10	28.489
11496	124.855	3.090	0.648	117	6.052e+05	52.473	1.872e-05	-0.778	3.372	6.630e-10	54.891
15935	230.976	13.239	0.459	83	2.425e+05	38.683	3.120e-05	-0.876	3.328	1.330e-09	57.265
4407	237.406	16.985	0.463	372	1.071e+06	63.467	2.934e-05	-0.884	3.001	1.330e-07	73.644
20571	235.861	56.008	0.457	247	7.637e+05	56.705	3.015e-05	-0.854	2.981	1.730e-07	64.008
13976	131.182	28.707	0.498	101	1.043e+05	29.199	8.983e-05	-0.769	2.959	2.290e-07	38.057
2571	138.792	2.233	0.520	487	1.101e+06	64.052	4.141e-05	-0.890	2.875	6.470e-07	68.104
4535	228.210	20.057	0.591	308	1.082e+06	63.679	2.944e-05	-0.855	2.857	7.990e-07	62.597
1267	154.540	-0.619	0.459	220	2.883e+05	40.980	6.223e-05	-0.699	2.827	1.140e-06	42.569
12454	235.558	11.513	0.638	447	3.084e+06	90.295	1.578e-05	-0.849	2.811	1.380e-06	104.814
11862	176.750	5.126	0.586	443	2.164e+06	80.243	1.964e-05	-0.910	2.765	2.360e-06	100.455
5455	206.313	0.163	0.640	547	3.033e+06	89.801	1.988e-05	-0.774	2.759	2.510e-06	88.674
1005	125.041	38.447	0.460	253	6.625e+05	54.079	3.157e-05	-0.875	2.751	2.750e-06	73.005
6886	251.844	21.969	0.495	1066	2.550e+06	84.756	3.729e-05	-0.905	2.741	3.060e-06	82.966
4669	195.568	0.330	0.482	154	2.571e+05	39.445	6.605e-05	-0.819	2.736	3.250e-06	45.527
6677	255.014	24.193	0.479	60	8.690e+04	27.477	8.642e-05	-0.756	2.716	4.050e-06	41.496
2619	160.558	-0.643	0.467	243	4.095e+05	46.066	6.828e-05	-0.802	2.576	1.790e-05	53.763
21634	192.072	54.127	0.460	545	1.634e+06	73.064	2.835e-05	-0.881	2.562	2.080e-05	72.618
9173	212.982	39.695	0.487	243	5.488e+05	50.790	4.280e-05	-0.882	2.553	2.270e-05	64.971
18077	215.769	18.882	0.649	272	2.651e+06	85.851	1.299e-05	-0.852	2.529	2.870e-05	106.731
13556	220.837	36.760	0.659	98	5.652e+05	51.289	2.154e-05	-0.707	2.516	3.270e-05	75.081
17290	144.126	28.605	0.572	535	1.657e+06	73.406	3.693e-05	-0.878	2.512	3.410e-05	95.861
11581	240.589	5.557	0.454	68	1.522e+05	33.120	5.168e-05	-0.750	2.507	3.590e-05	46.209
4859	208.529	0.347	0.578	316	1.050e+06	63.044	3.141e-05	-0.858	2.498	3.910e-05	76.076
21371	163.626	49.028	0.459	397	8.503e+05	58.772	3.734e-05	-0.868	2.478	4.750e-05	71.968
17711	223.573	20.632	0.512	284	6.644e+05	54.131	4.296e-05	-0.889	2.462	5.550e-05	57.951
22524	234.611	55.462	0.644	158	1.448e+06	70.178	1.686e-05	-0.839	2.443	6.600e-05	116.371
15117	178.867	12.927	0.459	131	3.678e+05	44.445	5.588e-05	-0.779	2.443	6.650e-05	69.396
12812	256.340	31.790	0.496	200	7.303e+05	55.864	3.882e-05	-0.901	2.436	7.070e-05	61.609

Table A.1 (continued)

ID	RA (deg)	DEC (deg)	z	N_{gal}	V ($h^{-3}\mathrm{Mpc}^3$)	R_{eff} ($h^{-1}\mathrm{Mpc}$)	n_{min} ($h^3\mathrm{Mpc}^{-3}$)	δ_{min}	r	P	$D_{boundary}$ ($h^{-1}\mathrm{Mpc}$)
6729	250.690	20.509	0.549	318	1.006e+06	62.158	3.832e-05	-0.873	2.430	7.520e-05	56.055
2591	132.522	2.263	0.583	392	1.090e+06	63.848	2.988e-05	-0.864	2.403	9.660e-05	68.068
10024	183.139	1.739	0.477	39	4.074e+04	21.347	9.438e-05	-0.727	2.389	1.090e-04	28.616
4395	238.258	20.882	0.595	626	3.191e+06	91.328	2.437e-05	-0.880	2.381	1.180e-04	146.287
13669	133.778	46.359	0.583	188	9.301e+05	60.554	2.851e-05	-0.860	2.377	1.230e-04	93.960
19796	153.402	23.473	0.536	126	2.988e+05	41.471	6.445e-05	-0.812	2.364	1.380e-04	169.851
19847	167.397	25.655	0.569	334	1.154e+06	65.068	3.565e-05	-0.874	2.362	1.400e-04	172.564
19861	171.603	27.345	0.652	304	2.341e+06	82.370	1.601e-05	-0.810	2.358	1.450e-04	99.513
22129	194.166	43.544	0.466	384	1.436e+06	69.996	2.996e-05	-0.855	2.356	1.480e-04	83.651
18298	173.896	19.534	0.656	171	1.512e+06	71.203	1.536e-05	-0.817	2.349	1.580e-04	91.411
21068	171.493	59.727	0.500	264	8.638e+05	59.081	4.121e-05	-0.895	2.345	1.630e-04	164.136
17611	206.257	24.070	0.466	374	1.387e+06	69.175	3.336e-05	-0.868	2.335	1.790e-04	85.713
17222	141.005	32.063	0.470	387	1.457e+06	70.332	2.900e-05	-0.897	2.319	2.060e-04	94.546
3576	224.795	30.535	0.605	347	1.034e+06	62.732	3.190e-05	-0.843	2.305	2.320e-04	69.585
21921	229.089	46.365	0.516	328	9.404e+05	60.777	4.463e-05	-0.879	2.286	2.730e-04	132.746
22520	229.253	54.721	0.657	124	8.417e+05	58.571	2.316e-05	-0.725	2.280	2.880e-04	62.504
8794	138.556	39.662	0.514	227	9.012e+05	59.922	3.273e-05	-0.913	2.266	3.250e-04	107.118
3296	212.817	34.360	0.509	332	9.391e+05	60.750	4.224e-05	-0.891	2.263	3.330e-04	69.006
10593	182.567	3.819	0.513	196	4.149e+05	46.270	5.997e-05	-0.842	2.254	3.600e-04	57.215
5278	227.462	0.722	0.463	96	2.647e+05	39.829	5.239e-05	-0.815	2.252	3.650e-04	55.981
900	123.398	40.356	0.607	12	3.638e+04	20.556	7.528e-05	-0.586	2.250	3.720e-04	46.064
825	116.284	33.865	0.533	429	9.625e+05	61.250	4.678e-05	-0.866	2.244	3.920e-04	67.506
4866	201.439	1.388	0.532	99	1.618e+05	33.803	5.607e-05	-0.839	2.237	4.150e-04	45.109
17574	207.941	28.323	0.454	45	7.384e+04	26.026	7.599e-05	-0.633	2.230	4.430e-04	58.327
19336	202.175	30.639	0.504	56	1.225e+05	30.808	8.509e-05	-0.783	2.225	4.600e-04	55.674
15558	142.483	11.586	0.464	343	9.485e+05	60.952	5.291e-05	-0.744	2.222	4.740e-04	81.368
17812	194.466	26.258	0.654	185	1.449e+06	70.200	1.515e-05	-0.761	2.218	4.890e-04	95.028
7221	117.051	31.419	0.505	147	2.662e+05	39.906	5.975e-05	-0.846	2.215	5.010e-04	56.847
12374	225.297	6.349	0.517	361	9.040e+05	59.983	5.160e-05	-0.858	2.208	5.310e-04	73.487
16030	216.943	14.667	0.661	103	7.815e+05	57.140	2.146e-05	-0.677	2.207	5.340e-04	81.742
4403	242.153	19.984	0.489	179	5.647e+05	51.274	3.761e-05	-0.901	2.202	5.550e-04	84.109
9778	159.312	34.103	0.586	236	1.181e+06	65.572	2.656e-05	-0.889	2.199	5.690e-04	240.971

Table A.1 (continued)

ID	RA (deg)	DEC (deg)	z	N_{gal}	V (h^{-3}Mpc^3)	R_{eff} (h^{-1}Mpc)	n_{min} (h^3Mpc^{-3})	δ_{min}	r	P	$D_{boundary}$ (h^{-1}Mpc)
2211	139.595	-0.905	0.533	26	3.488e+04	20.269	1.156e-04	-0.664	2.193	5.980e-04	44.851
4457	226.458	19.415	0.537	395	9.696e+05	61.399	4.801e-05	-0.851	2.180	6.690e-04	70.821
20012	169.425	31.849	0.460	434	1.442e+06	70.088	3.408e-05	-0.857	2.177	6.850e-04	71.693
21786	208.130	58.841	0.452	61	1.774e+05	34.858	6.201e-05	-0.700	2.175	6.950e-04	54.426
14752	217.584	7.100	0.465	136	3.478e+05	43.625	7.594e-05	-0.754	2.171	7.140e-04	82.068
12573	202.708	6.481	0.469	254	7.216e+05	55.642	4.156e-05	-0.880	2.168	7.350e-04	74.997
2596	137.224	2.700	0.654	121	7.560e+05	56.514	2.026e-05	-0.725	2.168	7.360e-04	67.803
17603	214.937	26.553	0.632	240	1.722e+06	74.358	1.790e-05	-0.829	2.156	8.100e-04	76.508
15033	177.622	13.683	0.503	288	8.484e+05	58.728	4.163e-05	-0.893	2.149	8.540e-04	120.477
14779	184.296	7.955	0.503	309	7.142e+05	55.452	7.102e-05	-0.819	2.149	8.560e-04	94.083
4637	200.281	0.600	0.663	125	7.280e+05	55.805	2.671e-05	-0.637	2.148	8.620e-04	77.203
13023	231.044	34.237	0.557	321	1.222e+06	66.314	3.389e-05	-0.890	2.147	8.690e-04	75.110
2629	163.369	-0.928	0.488	200	2.534e+05	39.254	7.150e-05	-0.804	2.139	9.300e-04	51.756
17502	218.398	25.559	0.502	98	3.296e+05	42.851	4.935e-05	-0.874	2.138	9.350e-04	77.960
8793	137.445	39.999	0.464	291	1.086e+06	63.756	3.824e-05	-0.849	2.131	9.840e-04	81.220
9009	160.818	42.484	0.646	140	1.198e+06	65.887	1.879e-05	-0.802	2.129	1.000e-03	112.036
16640	135.877	48.592	0.455	66	1.889e+05	35.594	5.944e-05	-0.713	2.124	1.040e-03	60.247
17126	134.607	24.456	0.491	178	3.045e+05	41.736	7.064e-05	-0.805	2.119	1.090e-03	68.255
6592	252.685	22.767	0.639	429	3.099e+06	90.445	1.629e-05	-0.865	2.110	1.160e-03	119.765
183	124.736	50.678	0.541	135	3.623e+05	44.222	6.285e-05	-0.817	2.109	1.180e-03	86.592
11120	148.954	3.777	0.549	351	1.038e+06	62.812	4.245e-05	-0.862	2.107	1.190e-03	76.127
11874	216.047	5.596	0.485	132	3.352e+05	43.094	5.432e-05	-0.851	2.104	1.220e-03	54.245
15443	229.500	8.740	0.501	408	9.464e+05	60.907	4.977e-05	-0.873	2.099	1.270e-03	70.081
22068	201.862	42.563	0.493	431	1.267e+06	67.133	3.564e-05	-0.909	2.097	1.290e-03	61.824
8549	116.446	32.966	0.463	56	1.583e+05	33.558	5.657e-05	-0.763	2.095	1.310e-03	58.475
15007	130.000	8.477	0.656	283	1.662e+06	73.483	1.657e-05	-0.775	2.090	1.360e-03	71.010
19657	165.409	27.681	0.510	274	8.027e+05	57.652	3.867e-05	-0.901	2.081	1.460e-03	187.075
14029	133.266	27.948	0.581	317	1.077e+06	63.583	3.900e-05	-0.837	2.079	1.490e-03	62.542
14952	156.026	10.620	0.594	238	1.091e+06	63.855	3.650e-05	-0.834	2.070	1.590e-03	196.756
12141	135.558	7.161	0.502	141	2.277e+05	37.879	9.487e-05	-0.756	2.070	1.590e-03	48.598
19858	161.724	27.140	0.613	180	8.934e+05	59.747	3.049e-05	-0.824	2.061	1.700e-03	181.932
12888	258.606	26.804	0.501	269	4.299e+05	46.818	7.225e-05	-0.816	2.059	1.730e-03	62.103

Table A.1 (continued)

ID	RA (deg)	DEC (deg)	z	N_{gal}	V (h^{-3}Mpc^3)	R_{eff} (h^{-1}Mpc)	n_{min} (h^3Mpc^{-3})	δ_{min}	r	P	$D_{boundary}$ (h^{-1}Mpc)
9889	145.501	37.344	0.518	162	4.242e+05	46.611	7.401e-05	-0.803	2.053	1.810e-03	206.161
1303	138.030	0.668	0.629	259	1.320e+06	68.053	2.171e-05	-0.742	2.052	1.820e-03	70.668
1047	129.253	39.992	0.538	64	1.328e+05	31.650	7.194e-05	-0.794	2.049	1.870e-03	42.985
4726	224.168	0.044	0.452	95	2.014e+05	36.362	4.835e-05	-0.766	2.038	2.020e-03	53.593
22164	202.995	49.504	0.540	522	1.823e+06	75.776	3.622e-05	-0.894	2.037	2.040e-03	178.101
8608	119.234	18.416	0.458	149	4.740e+05	48.369	3.886e-05	-0.772	2.035	2.070e-03	67.780
11043	157.531	6.621	0.482	605	2.165e+06	80.250	3.650e-05	-0.899	2.030	2.160e-03	98.718
7585	125.859	26.988	0.492	423	1.261e+06	67.013	3.834e-05	-0.899	2.025	2.230e-03	86.585
20037	209.130	40.286	0.489	73	1.358e+05	31.885	8.052e-05	-0.780	2.021	2.300e-03	55.424
11474	233.432	5.898	0.638	115	7.288e+05	55.827	2.925e-05	-0.757	2.021	2.300e-03	77.843
17643	218.915	25.226	0.462	285	7.577e+05	56.555	4.561e-05	-0.839	2.013	2.430e-03	72.215
276	118.041	47.108	0.489	330	7.076e+05	55.279	5.405e-05	-0.852	2.013	2.440e-03	67.544
16215	182.411	9.682	0.461	187	5.170e+05	49.788	5.366e-05	-0.826	2.012	2.460e-03	41.339
148	121.032	47.634	0.654	229	1.753e+06	74.792	1.746e-05	-0.816	2.012	2.460e-03	96.742
1364	173.770	1.587	0.497	506	1.646e+06	73.250	3.052e-05	-0.922	2.011	2.470e-03	57.659
16381	121.228	7.337	0.499	37	3.200e+04	19.696	1.609e-04	-0.556	2.008	2.540e-03	29.920
17291	145.586	29.082	0.541	247	5.933e+05	52.127	4.828e-05	-0.850	2.008	2.540e-03	116.262
18352	198.503	18.908	0.469	448	1.481e+06	70.718	3.808e-05	-0.890	2.005	2.590e-03	92.264
6272	247.836	14.921	0.600	597	2.491e+06	84.092	2.639e-05	-0.848	2.001	2.660e-03	93.325
19141	207.905	28.920	0.475	125	2.051e+05	36.586	7.372e-05	-0.791	2.000	2.680e-03	49.306
16374	120.862	9.312	0.480	51	4.044e+04	21.293	1.604e-04	-0.558	1.997	2.740e-03	31.704
9662	197.892	38.623	0.460	320	9.193e+05	60.320	3.741e-05	-0.843	1.997	2.750e-03	71.043
15329	219.240	9.030	0.571	510	2.159e+06	80.181	2.780e-05	-0.902	1.995	2.780e-03	146.058
12335	232.324	7.633	0.457	350	9.796e+05	61.610	4.059e-05	-0.839	1.995	2.790e-03	64.613
16079	215.096	16.044	0.475	82	2.496e+05	39.061	5.981e-05	-0.831	1.994	2.810e-03	106.728
21913	200.263	54.657	0.649	251	2.025e+06	78.480	1.872e-05	-0.778	1.991	2.870e-03	106.286
5989	217.773	-0.965	0.537	156	2.148e+05	37.154	7.105e-05	-0.793	1.988	2.930e-03	54.347
22124	178.895	44.425	0.655	173	1.340e+06	68.394	2.157e-05	-0.773	1.986	2.970e-03	92.981
11881	140.807	5.285	0.638	339	2.199e+06	80.672	1.922e-05	-0.816	1.982	3.070e-03	64.739
19612	201.267	28.931	0.644	354	2.766e+06	87.078	1.535e-05	-0.818	1.981	3.080e-03	106.863
21507	150.881	57.130	0.540	1216	4.839e+06	104.931	2.381e-05	-0.930	1.980	3.110e-03	142.341
14622	241.838	10.411	0.477	135	2.116e+05	36.965	7.119e-05	-0.805	1.976	3.200e-03	46.383

Table A.1 (continued)

ID	RA (deg)	DEC (deg)	z	$N_{\rm gal}$	V (h^{-3}Mpc^3)	$R_{\rm eff}$ (h^{-1}Mpc)	$n_{\rm min}$ (h^3Mpc^{-3})	$\delta_{\rm min}$	r	P	$D_{boundary}$ (h^{-1}Mpc)
14901	144.727	8.356	0.638	390	3.187e+06	91.289	1.262e-05	-0.850	1.975	3.230e-03	129.808
19724	149.915	27.741	0.647	411	3.296e+06	92.325	1.665e-05	-0.774	1.973	3.280e-03	109.252
12909	230.188	37.032	0.497	119	4.252e+05	46.648	4.377e-05	-0.888	1.962	3.540e-03	69.098
19870	183.948	28.562	0.659	242	1.322e+06	68.091	2.670e-05	-0.745	1.961	3.560e-03	84.463
4687	206.793	-0.875	0.463	153	3.597e+05	44.120	5.044e-05	-0.800	1.961	3.560e-03	56.926
15591	194.637	15.129	0.463	307	9.213e+05	60.362	3.845e-05	-0.814	1.961	3.570e-03	78.569
21215	155.067	54.273	0.656	79	7.326e+05	55.923	1.902e-05	-0.714	1.959	3.630e-03	92.648
881	117.451	34.652	0.648	142	1.004e+06	62.119	2.344e-05	-0.733	1.958	3.650e-03	74.056
20222	213.085	62.581	0.461	227	5.866e+05	51.930	3.456e-05	-0.863	1.953	3.770e-03	62.248
899	123.446	39.072	0.574	226	8.711e+05	59.246	4.384e-05	-0.802	1.953	3.770e-03	69.931
19635	162.166	26.751	0.670	33	1.546e+05	33.293	3.138e-05	-0.528	1.953	3.780e-03	63.218
4738	216.995	0.186	0.645	242	1.163e+06	65.242	2.227e-05	-0.735	1.952	3.810e-03	84.342
9956	246.080	22.071	0.490	50	4.656e+04	22.317	1.324e-04	-0.635	1.948	3.920e-03	32.000
18662	240.112	42.180	0.505	563	1.672e+06	73.631	3.954e-05	-0.893	1.947	3.940e-03	175.398
141	125.875	51.482	0.497	345	9.727e+05	61.465	5.038e-05	-0.867	1.940	4.130e-03	61.187
18756	250.239	47.198	0.622	299	1.970e+06	77.773	2.235e-05	-0.871	1.940	4.160e-03	100.469
7200	118.085	32.017	0.658	107	8.069e+05	57.753	1.657e-05	-0.775	1.939	4.170e-03	86.681
21349	153.861	50.583	0.510	379	9.239e+05	60.419	5.693e-05	-0.854	1.939	4.170e-03	187.238
9094	188.246	43.770	0.566	215	6.911e+05	54.846	5.074e-05	-0.801	1.939	4.180e-03	64.462
22148	199.378	44.418	0.643	471	3.553e+06	94.659	1.443e-05	-0.828	1.934	4.320e-03	100.054
4680	230.790	1.045	0.658	55	2.609e+05	39.641	3.098e-05	-0.534	1.930	4.440e-03	65.485
3442	193.617	39.620	0.507	494	1.213e+06	66.153	5.465e-05	-0.860	1.930	4.440e-03	41.942
11658	241.691	5.032	0.480	44	4.521e+04	22.100	9.971e-05	-0.718	1.930	4.450e-03	38.947
18175	204.721	23.855	0.582	242	1.184e+06	65.620	3.590e-05	-0.852	1.930	4.450e-03	158.787
21959	225.251	51.287	0.475	247	7.217e+05	55.644	5.476e-05	-0.845	1.925	4.620e-03	61.442
21565	186.051	60.474	0.511	267	6.925e+05	54.885	4.743e-05	-0.875	1.924	4.630e-03	186.490
11396	197.761	5.660	0.610	89	4.480e+05	47.469	2.821e-05	-0.854	1.924	4.640e-03	72.392
21119	190.904	62.443	0.657	104	8.416e+05	58.569	1.761e-05	-0.791	1.922	4.710e-03	89.383
16630	138.344	48.675	0.574	172	6.789e+05	54.522	4.081e-05	-0.856	1.921	4.730e-03	130.941
11786	191.598	4.738	0.568	550	2.000e+06	78.156	3.546e-05	-0.875	1.921	4.740e-03	75.763
4678	226.974	0.355	0.605	328	1.295e+06	67.616	2.920e-05	-0.839	1.919	4.810e-03	75.464
21463	200.545	49.878	0.499	250	6.783e+05	54.507	5.212e-05	-0.867	1.918	4.850e-03	161.627

Table A.1 (continued)

ID	RA (deg)	DEC (deg)	z	N_{gal}	V ($h^{-3}\mathrm{Mpc}^3$)	R_{eff} ($h^{-1}\mathrm{Mpc}$)	$n_{\min}$ ($h^3\mathrm{Mpc}^{-3}$)	$\delta_{\min}$	r	P	$D_{boundary}$ ($h^{-1}\mathrm{Mpc}$)
17833	203.226	26.146	0.522	149	4.859e+05	48.770	5.057e-05	-0.865	1.917	4.880e-03	144.001
15445	193.085	14.756	0.518	378	1.074e+06	63.520	4.725e-05	-0.872	1.917	4.880e-03	205.867
16196	138.686	11.982	0.653	193	1.686e+06	73.840	1.946e-05	-0.693	1.914	4.970e-03	97.522
4270	243.816	19.008	0.459	269	9.080e+05	60.072	4.168e-05	-0.825	1.913	5.020e-03	69.427
3441	193.925	39.112	0.568	67	1.910e+05	35.724	5.428e-05	-0.788	1.913	5.030e-03	45.332
19601	199.232	30.437	0.461	84	2.176e+05	37.315	4.633e-05	-0.836	1.912	5.060e-03	51.503
13703	227.372	37.616	0.573	219	6.222e+05	52.960	4.451e-05	-0.826	1.905	5.300e-03	80.852
4262	231.521	26.472	0.515	470	1.046e+06	62.968	6.231e-05	-0.834	1.905	5.320e-03	64.438
2634	165.797	-0.817	0.454	83	1.209e+05	30.679	7.180e-05	-0.653	1.904	5.360e-03	48.958
1236	186.739	-0.544	0.649	212	7.737e+05	56.950	2.973e-05	-0.687	1.903	5.370e-03	58.490
12591	243.297	26.857	0.561	403	7.965e+05	57.503	6.174e-05	-0.782	1.902	5.420e-03	57.640
2536	152.573	-0.563	0.540	130	2.854e+05	40.844	7.263e-05	-0.789	1.900	5.480e-03	53.983
8911	147.256	37.828	0.595	164	8.603e+05	59.000	4.003e-05	-0.818	1.896	5.650e-03	221.500
2235	147.461	-0.633	0.495	150	3.195e+05	42.408	5.280e-05	-0.854	1.895	5.670e-03	49.969
16693	140.364	49.459	0.470	249	7.268e+05	55.774	4.027e-05	-0.883	1.892	5.830e-03	94.283
12105	223.133	6.344	0.469	266	6.477e+05	53.674	4.211e-05	-0.864	1.882	6.230e-03	69.434
887	121.662	37.898	0.483	152	2.941e+05	41.254	6.922e-05	-0.811	1.880	6.310e-03	49.460
12778	258.511	26.950	0.477	89	2.033e+05	36.479	6.377e-05	-0.815	1.880	6.320e-03	45.761
16311	201.662	7.986	0.511	67	1.529e+05	33.173	7.515e-05	-0.807	1.879	6.380e-03	111.338
22602	226.184	57.685	0.648	220	1.758e+06	74.874	2.400e-05	-0.639	1.878	6.380e-03	108.138
14960	156.786	11.099	0.554	239	8.491e+05	58.744	4.021e-05	-0.867	1.877	6.430e-03	201.946
11374	187.134	4.371	0.659	132	9.529e+05	61.046	2.897e-05	-0.606	1.877	6.430e-03	88.201
20199	224.958	58.712	0.532	95	2.916e+05	41.139	5.024e-05	-0.853	1.877	6.460e-03	81.574
11752	179.681	3.292	0.457	81	2.080e+05	36.753	7.584e-05	-0.700	1.874	6.570e-03	48.942
5285	227.787	0.513	0.653	66	2.974e+05	41.409	3.177e-05	-0.568	1.871	6.730e-03	68.770
15562	167.948	15.084	0.663	85	4.825e+05	48.656	2.289e-05	-0.656	1.869	6.820e-03	76.807
15417	205.911	9.249	0.452	59	1.533e+05	33.199	6.422e-05	-0.690	1.868	6.870e-03	53.289
21616	176.092	54.264	0.651	189	1.912e+06	76.990	1.523e-05	-0.819	1.862	7.150e-03	101.268
21937	224.392	50.225	0.615	43	1.961e+05	36.040	5.579e-05	-0.659	1.858	7.360e-03	119.485
14673	171.889	9.053	0.632	524	4.153e+06	99.712	1.977e-05	-0.825	1.857	7.390e-03	142.031
3559	217.570	32.725	0.656	157	1.016e+06	62.371	2.532e-05	-0.699	1.856	7.420e-03	92.379
15046	169.489	15.168	0.463	274	9.270e+05	60.487	3.612e-05	-0.872	1.856	7.420e-03	79.464

Table A.1 (continued)

ID	RA (deg)	DEC (deg)	z	$N_{\rm gal}$	V (h^{-3}Mpc^3)	$R_{\rm eff}$ (h^{-1}Mpc)	$n_{\rm min}$ (h^3Mpc^{-3})	$\delta_{\rm min}$	r	P	$D_{boundary}$ (h^{-1}Mpc)
4350	237.349	19.950	0.545	380	1.396e+06	69.340	3.613e-05	-0.897	1.854	7.520e-03	138.503
11495	124.772	3.454	0.485	117	1.683e+05	34.251	1.209e-04	-0.681	1.852	7.640e-03	43.153
9813	175.455	34.044	0.458	113	3.360e+05	43.129	6.087e-05	-0.759	1.849	7.810e-03	67.246
1211	153.712	-0.750	0.512	52	8.298e+04	27.058	9.369e-05	-0.754	1.847	7.900e-03	47.384
1255	141.550	-0.561	0.573	139	2.889e+05	41.007	6.545e-05	-0.769	1.847	7.930e-03	50.766
15511	215.893	13.208	0.525	262	7.506e+05	56.378	5.584e-05	-0.851	1.845	8.040e-03	220.234
5072	219.904	0.762	0.605	219	7.861e+05	57.254	3.241e-05	-0.822	1.844	8.070e-03	68.010
14252	244.999	33.785	0.588	240	1.234e+06	66.547	3.276e-05	-0.831	1.842	8.200e-03	82.064
17794	141.138	24.900	0.475	340	1.330e+06	68.221	3.531e-05	-0.875	1.842	8.210e-03	67.778
1357	164.070	-0.819	0.583	208	5.112e+05	49.603	5.594e-05	-0.747	1.841	8.250e-03	59.132
3524	205.064	35.822	0.539	408	1.071e+06	63.473	5.263e-05	-0.855	1.840	8.270e-03	76.669
11216	200.286	4.999	0.517	97	1.908e+05	35.714	9.350e-05	-0.751	1.840	8.280e-03	45.882
19841	150.344	22.694	0.576	306	1.549e+06	71.770	2.695e-05	-0.861	1.839	8.340e-03	177.898
21589	174.212	49.094	0.538	269	1.098e+06	64.003	4.161e-05	-0.885	1.839	8.370e-03	250.440
16911	129.404	59.382	0.478	38	5.668e+04	23.830	1.442e-04	-0.605	1.837	8.460e-03	43.681
15951	152.581	14.419	0.641	423	3.404e+06	93.318	1.585e-05	-0.820	1.837	8.480e-03	124.004
17737	135.006	22.627	0.518	163	4.550e+05	47.714	4.939e-05	-0.866	1.836	8.550e-03	68.175
22586	230.790	58.336	0.559	263	8.773e+05	59.387	3.904e-05	-0.871	1.834	8.630e-03	59.317
4204	235.911	25.675	0.512	339	6.738e+05	54.384	6.614e-05	-0.826	1.833	8.690e-03	60.365
12126	133.333	6.939	0.626	46	1.662e+05	34.104	3.784e-05	-0.714	1.833	8.690e-03	48.614
15737	132.568	17.375	0.509	180	2.850e+05	40.824	8.691e-05	-0.776	1.828	8.980e-03	52.731
21432	173.998	48.315	0.463	235	8.189e+05	58.039	4.706e-05	-0.833	1.828	9.020e-03	77.722
10757	181.156	2.828	0.490	49	9.265e+04	28.071	1.031e-04	-0.716	1.827	9.030e-03	52.012
14253	239.285	37.744	0.493	88	3.250e+05	42.652	6.203e-05	-0.830	1.827	9.040e-03	148.755
12768	259.361	26.162	0.620	58	2.786e+05	40.514	3.162e-05	-0.768	1.826	9.110e-03	61.323
17188	140.297	33.357	0.541	411	1.588e+06	72.382	3.013e-05	-0.900	1.823	9.320e-03	175.256
8529	115.287	32.789	0.498	78	1.417e+05	32.342	7.745e-05	-0.796	1.821	9.460e-03	47.405
18319	167.005	20.388	0.485	433	1.623e+06	72.904	3.892e-05	-0.887	1.818	9.620e-03	129.076
20890	171.703	62.088	0.640	346	2.895e+06	88.410	1.896e-05	-0.861	1.817	9.660e-03	124.019
18716	230.402	43.550	0.451	22	6.152e+04	24.489	8.227e-05	-0.655	1.817	9.680e-03	52.091
16296	160.265	11.249	0.530	710	2.940e+06	88.867	3.246e-05	-0.907	1.817	9.680e-03	231.685
16260	157.278	16.169	0.532	260	8.949e+05	59.781	4.447e-05	-0.871	1.816	9.730e-03	164.979

Table A.1 (continued)

ID	RA (deg)	DEC (deg)	z	$N_{\rm gal}$	V (h^{-3}Mpc^3)	$R_{\rm eff}$ (h^{-1}Mpc)	$n_{\rm min}$ (h^3Mpc^{-3})	$\delta_{\rm min}$	r	P	$D_{boundary}$ (h^{-1}Mpc)
14689	232.097	12.725	0.648	171	9.365e+05	60.694	2.409e-05	-0.714	1.816	9.750e-03	80.493
9026	165.215	43.530	0.555	137	4.518e+05	47.602	5.672e-05	-0.812	1.815	9.810e-03	288.917
21843	174.657	56.341	0.519	226	5.142e+05	49.700	7.457e-05	-0.794	1.813	9.950e-03	208.540
16192	148.407	14.246	0.533	189	7.470e+05	56.286	4.554e-05	-0.867	1.810	1.010e-02	137.831
16268	161.036	16.922	0.505	186	5.329e+05	50.295	5.319e-05	-0.863	1.808	1.030e-02	176.928
19273	164.037	33.231	0.512	108	2.887e+05	40.999	6.217e-05	-0.837	1.806	1.040e-02	192.527
19904	178.868	25.340	0.605	257	1.229e+06	66.447	2.976e-05	-0.801	1.803	1.060e-02	134.398
1395	184.962	-0.390	0.534	56	6.872e+04	25.410	1.211e-04	-0.653	1.799	1.090e-02	39.201
6764	250.989	25.945	0.543	211	5.461e+05	50.707	6.131e-05	-0.822	1.799	1.090e-02	64.048
18632	242.368	42.636	0.459	251	6.481e+05	53.686	3.997e-05	-0.832	1.798	1.100e-02	69.606
1270	155.970	-0.875	0.537	171	2.986e+05	41.462	6.712e-05	-0.808	1.797	1.110e-02	50.334
890	119.454	35.191	0.579	158	6.299e+05	53.178	4.901e-05	-0.795	1.796	1.110e-02	73.119
21120	191.681	62.314	0.616	237	1.528e+06	71.451	2.705e-05	-0.819	1.796	1.120e-02	160.751
18411	191.773	16.916	0.479	209	5.496e+05	50.815	4.822e-05	-0.868	1.794	1.130e-02	116.007
6678	256.588	22.216	0.628	40	6.440e+04	24.866	5.473e-05	-0.634	1.790	1.160e-02	45.964
15010	133.225	7.341	0.513	149	2.258e+05	37.777	8.976e-05	-0.761	1.790	1.160e-02	45.389
8101	121.871	15.451	0.478	129	5.394e+05	50.498	5.836e-05	-0.840	1.790	1.160e-02	110.350
19989	177.092	26.006	0.456	203	5.673e+05	51.355	5.084e-05	-0.787	1.789	1.170e-02	63.162
9847	180.403	32.860	0.461	144	4.112e+05	46.131	5.515e-05	-0.782	1.788	1.170e-02	59.886
5990	217.981	-0.365	0.508	311	6.816e+05	54.595	5.547e-05	-0.857	1.787	1.180e-02	65.302
19957	169.103	20.977	0.576	133	3.641e+05	44.299	5.447e-05	-0.776	1.787	1.180e-02	134.327
19613	188.006	29.521	0.538	300	9.738e+05	61.489	4.563e-05	-0.874	1.787	1.180e-02	89.388
17328	220.054	26.920	0.499	36	4.660e+04	22.323	1.064e-04	-0.729	1.786	1.190e-02	37.037
12747	254.916	30.779	0.541	249	7.122e+05	55.399	4.928e-05	-0.857	1.783	1.210e-02	60.226
12360	226.578	6.060	0.458	105	2.536e+05	39.265	4.810e-05	-0.810	1.783	1.220e-02	59.346
10833	158.003	2.862	0.616	18	6.605e+04	25.076	4.789e-05	-0.724	1.782	1.220e-02	42.913
19839	164.666	25.125	0.624	148	9.602e+05	61.201	2.863e-05	-0.783	1.782	1.220e-02	158.898
13929	132.276	30.919	0.526	158	1.721e+05	34.505	8.648e-05	-0.762	1.781	1.230e-02	44.107
13931	133.575	31.836	0.572	260	7.330e+05	55.933	5.077e-05	-0.801	1.781	1.230e-02	64.225
12135	129.854	5.672	0.488	33	4.539e+04	22.129	1.219e-04	-0.664	1.781	1.230e-02	31.128
11861	208.226	5.310	0.577	109	3.349e+05	43.079	5.617e-05	-0.744	1.780	1.240e-02	54.868
4282	230.240	22.849	0.553	228	6.473e+05	53.662	3.345e-05	-0.889	1.779	1.250e-02	69.561

Table A.1 (continued)

ID	RA (deg)	DEC (deg)	z	$N_{\rm gal}$	V (h^{-3}Mpc^3)	$R_{\rm eff}$ (h^{-1}Mpc)	$n_{\rm min}$ (h^3Mpc^{-3})	$\delta_{\rm min}$	r	P	$D_{boundary}$ (h^{-1}Mpc)
21985	204.181	55.706	0.456	152	3.465e+05	43.573	6.195e-05	-0.740	1.778	1.250e-02	65.062
11128	166.289	4.245	0.579	58	3.068e+05	41.839	3.874e-05	-0.838	1.777	1.260e-02	70.208
14984	150.589	10.021	0.471	307	1.071e+06	63.479	3.650e-05	-0.882	1.777	1.270e-02	97.808
14345	247.612	39.902	0.477	531	1.811e+06	75.612	3.928e-05	-0.886	1.777	1.270e-02	111.223
15232	217.846	10.671	0.488	121	2.412e+05	38.616	7.694e-05	-0.789	1.776	1.270e-02	137.524
3606	206.866	36.398	0.605	219	8.595e+05	58.982	3.139e-05	-0.819	1.776	1.270e-02	69.746
16553	136.335	58.610	0.469	536	1.603e+06	72.599	4.537e-05	-0.853	1.775	1.280e-02	94.872
17861	144.877	22.537	0.661	46	3.431e+05	43.431	2.299e-05	-0.637	1.774	1.290e-02	81.241
4661	231.953	0.944	0.465	95	2.164e+05	37.244	6.055e-05	-0.786	1.771	1.310e-02	50.957
898	122.236	38.802	0.520	221	4.431e+05	47.296	6.027e-05	-0.834	1.770	1.320e-02	49.228
19781	187.454	31.370	0.559	36	8.123e+04	26.866	9.086e-05	-0.698	1.766	1.360e-02	42.054
15595	197.773	12.503	0.663	121	9.826e+05	61.674	2.713e-05	-0.592	1.763	1.380e-02	77.915
734	111.200	40.586	0.553	23	1.756e+04	16.123	1.365e-04	-0.556	1.763	1.380e-02	33.238
8772	151.594	44.012	0.507	272	6.335e+05	53.279	6.868e-05	-0.814	1.762	1.390e-02	179.649
14854	193.314	10.844	0.511	264	9.064e+05	60.035	4.151e-05	-0.894	1.762	1.390e-02	183.253
14307	250.395	30.901	0.500	211	5.640e+05	51.255	5.548e-05	-0.854	1.762	1.400e-02	58.127
17894	183.438	24.447	0.552	362	1.184e+06	65.635	3.739e-05	-0.891	1.761	1.400e-02	181.004
17822	201.289	26.094	0.461	153	6.063e+05	52.504	4.037e-05	-0.805	1.761	1.400e-02	75.978
15251	196.406	11.659	0.563	445	2.178e+06	80.408	2.698e-05	-0.889	1.759	1.420e-02	216.406
22048	185.406	47.883	0.552	131	4.809e+05	48.601	5.218e-05	-0.838	1.759	1.420e-02	164.127
9931	231.362	27.930	0.463	222	4.726e+05	48.322	4.622e-05	-0.836	1.758	1.430e-02	54.917
3491	197.682	35.898	0.649	29	2.127e+05	37.032	3.393e-05	-0.675	1.757	1.440e-02	56.018
906	122.250	39.925	0.471	63	6.592e+04	25.060	1.303e-04	-0.623	1.756	1.440e-02	38.307
353	122.482	52.167	0.617	188	1.016e+06	62.370	1.904e-05	-0.860	1.756	1.450e-02	82.050
19789	157.330	30.931	0.453	196	5.923e+05	52.098	5.208e-05	-0.781	1.755	1.460e-02	56.441
13055	236.789	33.413	0.652	235	1.969e+06	77.758	1.704e-05	-0.798	1.754	1.470e-02	99.985
773	119.151	37.103	0.548	63	1.237e+05	30.914	8.686e-05	-0.717	1.754	1.470e-02	46.178
21833	208.156	48.005	0.572	490	1.931e+06	77.245	3.868e-05	-0.825	1.754	1.470e-02	227.385
139	119.043	43.931	0.531	376	8.605e+05	59.004	5.156e-05	-0.850	1.752	1.480e-02	60.509
4653	202.753	-0.070	0.464	280	6.405e+05	53.474	4.715e-05	-0.813	1.751	1.500e-02	73.730
13608	128.501	53.710	0.525	249	7.578e+05	56.558	5.359e-05	-0.859	1.749	1.510e-02	54.951
14443	232.562	8.220	0.541	130	4.419e+05	47.250	4.850e-05	-0.850	1.749	1.520e-02	71.904

Table A.1 (continued)

ID	RA (deg)	DEC (deg)	z	N_{gal}	V ($h^{-3}\mathrm{Mpc}^3$)	R_{eff} ($h^{-1}\mathrm{Mpc}$)	n_{min} ($h^3\mathrm{Mpc}^{-3}$)	δ_{min}	r	P	$D_{boundary}$ ($h^{-1}\mathrm{Mpc}$)
9816	180.997	34.628	0.660	149	7.787e+05	57.073	2.772e-05	-0.562	1.747	1.540e-02	82.384
4241	234.264	23.718	0.660	153	1.174e+06	65.442	2.442e-05	-0.614	1.746	1.540e-02	84.003
18590	224.647	42.725	0.659	37	3.305e+05	42.889	2.192e-05	-0.670	1.746	1.540e-02	84.200
19825	176.624	29.067	0.509	405	1.198e+06	65.890	4.738e-05	-0.878	1.745	1.560e-02	152.787
21396	157.354	48.857	0.559	416	1.717e+06	74.281	2.941e-05	-0.896	1.744	1.570e-02	297.452
4335	229.988	20.961	0.459	398	9.995e+05	62.025	3.827e-05	-0.839	1.743	1.570e-02	70.864
20968	197.323	65.043	0.514	333	7.606e+05	56.628	6.374e-05	-0.832	1.743	1.580e-02	55.943
7658	118.432	19.562	0.585	146	8.128e+05	57.894	3.788e-05	-0.829	1.742	1.590e-02	104.638
15070	180.852	15.020	0.561	111	1.790e+05	34.963	1.061e-04	-0.648	1.741	1.590e-02	137.228
21562	182.443	59.499	0.557	221	7.353e+05	55.993	4.686e-05	-0.845	1.741	1.590e-02	223.728
16153	155.696	16.937	0.655	197	1.757e+06	74.853	1.313e-05	-0.844	1.739	1.610e-02	93.518
4156	241.870	25.035	0.465	63	1.519e+05	33.097	6.005e-05	-0.762	1.738	1.620e-02	45.759
18618	234.961	42.790	0.597	468	2.388e+06	82.918	3.314e-05	-0.829	1.738	1.620e-02	133.310
16507	145.298	46.406	0.672	39	2.931e+05	41.209	2.482e-05	-0.608	1.738	1.630e-02	60.136
2607	134.689	2.610	0.471	206	4.749e+05	48.400	6.618e-05	-0.819	1.738	1.630e-02	52.691
15616	198.151	14.281	0.600	100	5.861e+05	51.914	3.092e-05	-0.840	1.737	1.630e-02	211.241
12543	179.496	5.525	0.500	259	6.145e+05	52.739	6.994e-05	-0.821	1.736	1.640e-02	94.286
16497	135.713	52.541	0.478	138	4.831e+05	48.677	4.846e-05	-0.867	1.736	1.650e-02	93.885
12263	200.632	6.304	0.656	150	1.037e+06	62.799	2.212e-05	-0.737	1.736	1.650e-02	89.666
7610	124.101	26.647	0.576	258	1.271e+06	67.201	4.480e-05	-0.825	1.735	1.650e-02	114.591
13615	128.868	55.329	0.565	109	4.234e+05	46.581	4.498e-05	-0.841	1.735	1.650e-02	50.999
21161	231.672	51.066	0.487	57	9.376e+04	28.183	1.140e-04	-0.688	1.735	1.650e-02	48.630
17190	148.483	32.669	0.473	125	4.758e+05	48.430	4.736e-05	-0.863	1.735	1.660e-02	101.929
4681	196.911	0.437	0.547	291	7.201e+05	55.604	4.499e-05	-0.851	1.734	1.660e-02	56.137
3697	194.365	33.643	0.641	235	1.351e+06	68.586	2.316e-05	-0.685	1.734	1.670e-02	59.720
4362	231.828	18.899	0.662	39	1.983e+05	36.175	3.664e-05	-0.502	1.734	1.670e-02	71.343
3521	197.980	37.565	0.506	170	4.754e+05	48.418	7.428e-05	-0.802	1.733	1.680e-02	85.258
6772	250.287	26.285	0.593	195	6.208e+05	52.919	4.002e-05	-0.819	1.732	1.680e-02	53.667
17772	145.850	22.558	0.462	140	3.982e+05	45.640	5.907e-05	-0.766	1.729	1.720e-02	77.264
16610	136.324	49.187	0.655	163	1.485e+06	70.769	1.773e-05	-0.789	1.729	1.720e-02	93.692
7635	123.577	26.117	0.460	184	6.247e+05	53.031	4.353e-05	-0.846	1.727	1.740e-02	71.483
15596	201.813	13.668	0.463	194	6.354e+05	53.332	4.841e-05	-0.843	1.726	1.750e-02	77.850

Table A.1 (continued)

ID	RA (deg)	DEC (deg)	z	$N_{\rm gal}$	V (h^{-3}Mpc^3)	$R_{\rm eff}$ (h^{-1}Mpc)	$n_{\rm min}$ (h^3Mpc^{-3})	$\delta_{\rm min}$	r	P	$D_{boundary}$ (h^{-1}Mpc)
21868	172.937	46.448	0.650	271	2.248e+06	81.266	2.347e-05	-0.681	1.725	1.770e-02	104.089
15240	165.230	12.657	0.640	122	8.373e+05	58.470	3.366e-05	-0.678	1.725	1.770e-02	125.285
18106	200.485	22.071	0.460	255	9.758e+05	61.530	4.183e-05	-0.852	1.724	1.780e-02	72.651
6161	248.666	17.316	0.643	242	1.691e+06	73.905	2.005e-05	-0.762	1.723	1.790e-02	94.330
12467	240.019	11.599	0.496	100	1.713e+05	34.452	9.463e-05	-0.759	1.720	1.820e-02	42.840
12777	259.303	26.513	0.593	97	3.093e+05	41.955	3.899e-05	-0.808	1.719	1.830e-02	47.881
6214	241.971	19.115	0.645	232	2.307e+06	81.969	1.785e-05	-0.788	1.718	1.850e-02	113.471
21258	168.998	54.523	0.522	196	5.653e+05	51.295	6.239e-05	-0.831	1.717	1.860e-02	214.095
16016	225.843	12.934	0.595	105	6.954e+05	54.961	3.118e-05	-0.847	1.717	1.860e-02	120.235
8978	149.234	35.676	0.455	137	4.803e+05	48.582	4.668e-05	-0.804	1.716	1.870e-02	61.385
2628	161.019	-0.288	0.662	50	3.364e+05	43.145	2.739e-05	-0.568	1.716	1.870e-02	78.918
16300	199.556	11.447	0.623	46	2.972e+05	41.397	4.415e-05	-0.676	1.714	1.890e-02	161.372
7685	116.682	19.581	0.560	150	4.029e+05	45.819	4.672e-05	-0.835	1.714	1.890e-02	61.083
5079	224.651	0.487	0.651	173	8.347e+05	58.408	2.760e-05	-0.709	1.713	1.900e-02	81.704
17908	193.443	25.632	0.529	238	7.186e+05	55.564	3.695e-05	-0.898	1.713	1.910e-02	190.998
13604	131.281	52.186	0.658	33	2.546e+05	39.316	2.888e-05	-0.607	1.713	1.910e-02	73.191
14869	188.578	9.854	0.531	578	1.972e+06	77.786	3.722e-05	-0.897	1.712	1.910e-02	193.071
20938	216.743	61.153	0.493	322	8.491e+05	58.744	4.676e-05	-0.871	1.712	1.920e-02	75.229
14851	176.530	10.947	0.487	319	8.270e+05	58.230	4.999e-05	-0.862	1.711	1.920e-02	94.400
19902	169.850	23.788	0.550	124	3.864e+05	45.184	5.461e-05	-0.831	1.710	1.940e-02	104.445
310	115.895	43.002	0.496	290	5.656e+05	51.302	6.317e-05	-0.826	1.710	1.940e-02	70.109
3298	214.769	34.420	0.539	101	1.802e+05	35.036	9.758e-05	-0.721	1.710	1.940e-02	57.672
17314	136.628	25.141	0.580	255	8.817e+05	59.485	3.587e-05	-0.837	1.709	1.950e-02	128.720
21443	180.971	49.733	0.545	284	1.003e+06	62.104	4.478e-05	-0.870	1.709	1.960e-02	231.206
21788	224.759	54.917	0.482	174	5.057e+05	49.425	6.991e-05	-0.809	1.708	1.960e-02	79.347
4620	197.550	-0.076	0.489	78	1.311e+05	31.513	9.708e-05	-0.732	1.708	1.960e-02	48.300
15466	211.661	12.467	0.595	44	1.939e+05	35.907	4.820e-05	-0.763	1.708	1.970e-02	205.081
2236	149.677	-0.704	0.460	161	2.782e+05	40.499	6.271e-05	-0.697	1.706	2.000e-02	51.867
18030	196.331	22.504	0.635	258	1.944e+06	77.419	2.010e-05	-0.833	1.705	2.000e-02	135.783
46	115.372	38.180	0.468	133	2.000e+05	36.280	7.842e-05	-0.746	1.705	2.010e-02	36.385
9757	168.878	37.382	0.510	207	5.904e+05	52.042	6.841e-05	-0.824	1.704	2.020e-02	187.762
14993	152.599	10.728	0.606	71	3.344e+05	43.059	4.635e-05	-0.760	1.703	2.020e-02	196.893

Table A.1 (continued)

ID	RA (deg)	DEC (deg)	z	$N_{\rm gal}$	V (h^{-3}Mpc^3)	$R_{\rm eff}$ (h^{-1}Mpc)	$n_{\rm min}$ (h^3Mpc^{-3})	$\delta_{\rm min}$	r	P	$D_{boundary}$ (h^{-1}Mpc)
17178	146.106	34.085	0.568	253	9.594e+05	61.185	3.933e-05	-0.846	1.703	2.020e-02	240.847
15273	178.527	7.178	0.543	262	8.756e+05	59.347	4.999e-05	-0.857	1.703	2.030e-02	74.740
13551	216.867	38.744	0.628	139	6.739e+05	54.388	3.730e-05	-0.726	1.703	2.030e-02	57.862
22014	194.521	46.938	0.548	362	1.120e+06	64.425	4.739e-05	-0.843	1.701	2.050e-02	156.174
18624	237.101	46.479	0.610	233	1.260e+06	67.001	2.897e-05	-0.823	1.701	2.050e-02	187.784
17698	213.157	22.945	0.662	107	8.773e+05	59.386	2.126e-05	-0.680	1.701	2.060e-02	78.712
21112	209.444	58.943	0.564	313	1.289e+06	67.514	4.570e-05	-0.839	1.699	2.080e-02	159.155
17146	164.278	17.209	0.496	120	2.940e+05	41.248	8.056e-05	-0.794	1.699	2.080e-02	154.478
13605	134.625	54.780	0.589	261	1.362e+06	68.757	3.306e-05	-0.837	1.698	2.090e-02	140.080
15191	159.806	10.148	0.642	303	2.699e+06	86.374	2.097e-05	-0.715	1.698	2.090e-02	120.588
8920	144.585	36.365	0.658	164	1.465e+06	70.463	2.126e-05	-0.711	1.698	2.090e-02	86.956
11196	124.929	3.452	0.559	165	3.522e+05	43.811	8.485e-05	-0.724	1.697	2.100e-02	46.377
6231	245.490	15.726	0.533	375	1.120e+06	64.422	5.035e-05	-0.861	1.697	2.100e-02	93.822
13181	246.227	30.633	0.563	153	5.077e+05	49.488	5.208e-05	-0.827	1.696	2.120e-02	94.451
1253	139.555	-0.047	0.596	115	3.800e+05	44.935	4.691e-05	-0.769	1.695	2.130e-02	58.529
21702	206.853	53.332	0.648	136	1.273e+06	67.235	2.095e-05	-0.715	1.695	2.140e-02	107.774
16506	150.807	45.755	0.643	181	1.404e+06	69.465	2.538e-05	-0.698	1.693	2.160e-02	119.072
7409	126.976	30.477	0.663	32	1.853e+05	35.366	3.614e-05	-0.509	1.692	2.170e-02	69.100
15953	146.057	14.934	0.478	68	2.150e+05	37.162	6.116e-05	-0.833	1.692	2.170e-02	113.530
1171	194.260	-0.370	0.517	73	1.324e+05	31.619	9.064e-05	-0.758	1.692	2.180e-02	45.837
14212	133.415	20.232	0.500	160	2.954e+05	41.315	6.861e-05	-0.825	1.691	2.190e-02	51.700
21437	195.593	49.658	0.468	155	4.356e+05	47.026	6.358e-05	-0.775	1.691	2.190e-02	91.713
12627	243.745	27.586	0.458	60	1.293e+05	31.373	7.133e-05	-0.701	1.691	2.190e-02	56.348
22230	212.257	48.531	0.512	185	4.529e+05	47.640	6.039e-05	-0.845	1.691	2.190e-02	191.360
20209	240.059	50.762	0.638	505	4.729e+06	104.126	1.747e-05	-0.801	1.691	2.190e-02	129.557
7075	117.213	27.956	0.564	120	4.369e+05	47.071	5.336e-05	-0.823	1.690	2.200e-02	65.820
19903	176.098	24.120	0.593	112	4.270e+05	46.713	4.302e-05	-0.804	1.689	2.210e-02	64.668
2616	153.316	-0.499	0.576	77	2.282e+05	37.911	5.180e-05	-0.797	1.689	2.210e-02	49.766
283	121.960	52.621	0.470	147	2.823e+05	40.695	7.584e-05	-0.755	1.689	2.220e-02	53.385
21819	198.978	47.591	0.577	265	9.357e+05	60.675	4.513e-05	-0.814	1.688	2.220e-02	181.295
19995	170.921	24.414	0.618	284	1.257e+06	66.953	3.770e-05	-0.748	1.688	2.220e-02	87.805
12018	160.435	6.858	0.602	359	2.166e+06	80.260	2.186e-05	-0.866	1.688	2.230e-02	156.908

Table A.1 (continued)

ID	RA (deg)	DEC (deg)	z	$N_{\rm gal}$	V (h^{-3}Mpc^3)	$R_{\rm eff}$ (h^{-1}Mpc)	$n_{\rm min}$ (h^3Mpc^{-3})	$\delta_{\rm min}$	r	P	$D_{boundary}$ (h^{-1}Mpc)
14367	238.579	38.824	0.617	236	1.629e+06	72.994	2.557e-05	-0.812	1.688	2.230e-02	173.775
17851	138.765	19.200	0.655	142	1.156e+06	65.102	1.706e-05	-0.768	1.687	2.240e-02	93.909
6576	253.727	19.974	0.600	83	1.988e+05	36.208	8.379e-05	-0.588	1.687	2.250e-02	44.133
15190	224.135	9.150	0.511	237	6.171e+05	52.815	6.754e-05	-0.820	1.687	2.250e-02	136.473
21899	192.242	46.368	0.629	187	1.288e+06	67.491	2.965e-05	-0.802	1.685	2.280e-02	147.796
14868	188.216	11.150	0.486	313	7.151e+05	55.475	6.374e-05	-0.832	1.685	2.280e-02	133.019
21759	222.427	52.381	0.522	221	6.560e+05	53.902	6.020e-05	-0.834	1.685	2.280e-02	96.862
11147	152.082	3.954	0.517	89	1.679e+05	34.223	8.168e-05	-0.785	1.682	2.310e-02	48.550
17114	227.154	20.985	0.515	55	5.894e+04	24.142	1.601e-04	-0.573	1.682	2.320e-02	36.022
17405	219.666	25.442	0.648	129	7.972e+05	57.522	2.864e-05	-0.726	1.682	2.320e-02	72.362
11926	202.269	6.054	0.537	158	3.704e+05	44.551	6.150e-05	-0.824	1.681	2.330e-02	67.856
9689	169.700	37.607	0.653	143	1.145e+06	64.906	2.099e-05	-0.761	1.681	2.330e-02	97.035
4723	212.033	-0.205	0.614	260	1.066e+06	63.380	3.466e-05	-0.800	1.680	2.350e-02	86.196
970	119.926	33.766	0.481	300	9.454e+05	60.886	4.144e-05	-0.866	1.679	2.350e-02	91.128
18083	159.972	20.424	0.651	151	1.301e+06	67.720	2.197e-05	-0.670	1.679	2.360e-02	102.097
4860	195.859	0.982	0.458	39	5.737e+04	23.926	1.025e-04	-0.570	1.676	2.410e-02	43.089
17072	174.069	16.212	0.575	50	1.318e+05	31.574	8.617e-05	-0.645	1.674	2.430e-02	180.650
17847	138.767	18.837	0.546	194	6.290e+05	53.152	4.818e-05	-0.859	1.671	2.470e-02	181.955
4875	230.211	1.084	0.533	111	2.814e+05	40.654	6.787e-05	-0.816	1.671	2.480e-02	53.356
1219	163.835	-0.736	0.651	114	5.622e+05	51.200	2.822e-05	-0.665	1.669	2.510e-02	67.018
15447	197.691	13.927	0.523	283	1.006e+06	62.156	4.324e-05	-0.881	1.669	2.510e-02	213.511
7993	126.592	19.814	0.634	72	6.674e+05	54.212	2.098e-05	-0.826	1.669	2.510e-02	86.429
14866	176.591	10.650	0.547	344	1.322e+06	68.091	4.928e-05	-0.837	1.667	2.540e-02	100.172
21397	160.444	50.191	0.490	114	2.317e+05	38.101	7.645e-05	-0.805	1.667	2.540e-02	142.654
14840	190.703	8.529	0.655	106	8.773e+05	59.386	2.371e-05	-0.718	1.666	2.550e-02	93.051
13598	134.997	52.925	0.628	81	6.162e+05	52.788	2.861e-05	-0.809	1.666	2.550e-02	119.472
20250	168.175	66.050	0.515	97	1.014e+05	28.928	1.026e-04	-0.730	1.665	2.570e-02	43.261
14368	250.219	30.571	0.644	75	4.705e+05	48.248	3.095e-05	-0.704	1.665	2.580e-02	66.187
16021	225.870	12.870	0.462	298	1.106e+06	64.148	3.370e-05	-0.837	1.664	2.590e-02	75.383
9724	173.990	41.386	0.459	291	8.673e+05	59.161	4.773e-05	-0.800	1.663	2.600e-02	69.653
18739	249.353	50.312	0.659	158	1.062e+06	63.290	2.006e-05	-0.727	1.662	2.620e-02	84.815
22100	206.034	42.797	0.565	580	2.334e+06	82.288	2.861e-05	-0.905	1.661	2.630e-02	91.937

Table A.1 (continued)

ID	RA (deg)	DEC (deg)	z	N_{gal}	V ($h^{-3}\mathrm{Mpc}^3$)	R_{eff} ($h^{-1}\mathrm{Mpc}$)	n_{min} ($h^3\mathrm{Mpc}^{-3}$)	δ_{min}	r	P	$D_{boundary}$ ($h^{-1}\mathrm{Mpc}$)
7247	122.775	30.055	0.514	127	2.964e+05	41.362	6.836e-05	-0.820	1.661	2.630e-02	42.368
19828	155.780	22.979	0.566	82	2.730e+05	40.242	7.122e-05	-0.749	1.661	2.640e-02	226.960
6575	249.798	24.984	0.507	162	3.375e+05	43.190	7.170e-05	-0.809	1.660	2.650e-02	49.388
19174	155.192	32.921	0.579	151	6.785e+05	54.512	3.911e-05	-0.822	1.660	2.660e-02	255.298
12019	160.116	6.762	0.551	109	3.775e+05	44.835	5.707e-05	-0.823	1.659	2.670e-02	143.031
11872	213.914	5.726	0.552	181	3.908e+05	45.356	5.043e-05	-0.836	1.659	2.680e-02	62.786
7976	119.149	14.631	0.579	300	9.803e+05	61.624	3.850e-05	-0.825	1.659	2.680e-02	62.240
12804	258.376	29.798	0.465	96	2.523e+05	39.198	4.013e-05	-0.858	1.658	2.690e-02	56.349
9083	189.842	41.991	0.506	27	3.171e+04	19.635	1.781e-04	-0.545	1.657	2.700e-02	37.417
9168	192.466	42.309	0.635	138	6.922e+05	54.875	2.826e-05	-0.749	1.656	2.720e-02	61.475
21422	182.891	49.671	0.580	137	5.776e+05	51.662	4.755e-05	-0.804	1.654	2.760e-02	227.991
1943	173.050	-0.759	0.564	231	7.035e+05	55.174	4.787e-05	-0.844	1.653	2.780e-02	58.348
3302	225.891	30.137	0.654	135	6.289e+05	53.148	2.720e-05	-0.677	1.653	2.780e-02	72.577
9052	230.231	35.119	0.464	229	7.409e+05	56.135	4.007e-05	-0.870	1.652	2.780e-02	74.032
8992	149.089	37.630	0.559	192	7.613e+05	56.644	4.896e-05	-0.827	1.651	2.800e-02	297.216
19817	165.583	26.646	0.644	97	6.363e+05	53.356	2.941e-05	-0.739	1.651	2.800e-02	115.792
7404	126.305	29.961	0.571	211	6.561e+05	53.905	4.763e-05	-0.814	1.651	2.810e-02	75.864
11932	170.961	6.642	0.520	176	3.682e+05	44.464	5.936e-05	-0.842	1.651	2.810e-02	99.634
17793	148.408	26.246	0.528	225	5.324e+05	50.278	5.872e-05	-0.829	1.651	2.810e-02	117.651
22741	177.811	46.224	0.497	163	5.264e+05	50.090	4.893e-05	-0.871	1.649	2.840e-02	157.066
14385	241.929	7.448	0.492	65	1.777e+05	34.876	7.388e-05	-0.805	1.649	2.840e-02	58.264
16512	131.716	59.330	0.661	64	4.629e+05	47.990	2.788e-05	-0.581	1.648	2.850e-02	75.133
16031	218.348	14.376	0.461	121	4.440e+05	47.325	4.956e-05	-0.804	1.648	2.850e-02	73.723
10595	188.053	3.454	0.516	411	9.663e+05	61.329	6.037e-05	-0.841	1.648	2.860e-02	61.992
22188	219.178	48.130	0.468	190	6.082e+05	52.561	4.246e-05	-0.863	1.648	2.860e-02	90.159
18504	246.460	45.917	0.654	109	9.342e+05	60.644	2.200e-05	-0.653	1.647	2.870e-02	94.905
19161	169.499	21.085	0.457	160	5.563e+05	51.020	5.098e-05	-0.820	1.647	2.880e-02	64.533
17926	190.881	25.504	0.621	136	7.986e+05	57.554	3.588e-05	-0.736	1.646	2.890e-02	164.938
19434	207.992	29.093	0.501	184	2.781e+05	40.494	8.559e-05	-0.781	1.646	2.900e-02	49.443
21271	158.851	52.871	0.476	203	3.727e+05	44.645	9.269e-05	-0.746	1.644	2.920e-02	108.783
10550	187.358	1.551	0.588	46	1.069e+05	29.444	9.160e-05	-0.583	1.643	2.950e-02	35.837
15116	174.515	12.515	0.519	168	4.839e+05	48.703	5.030e-05	-0.864	1.643	2.950e-02	162.381

Table A.1 (continued)

ID	RA (deg)	DEC (deg)	z	$N_{\rm gal}$	V (h^{-3}Mpc^3)	$R_{\rm eff}$ (h^{-1}Mpc)	$n_{\rm min}$ (h^3Mpc^{-3})	$\delta_{\rm min}$	r	P	$D_{boundary}$ (h^{-1}Mpc)
21527	196.371	58.983	0.573	51	1.886e+05	35.578	7.047e-05	-0.710	1.643	2.950e-02	218.588
21677	195.560	55.059	0.552	163	6.074e+05	52.537	5.790e-05	-0.830	1.643	2.950e-02	281.609
7231	128.672	34.895	0.532	104	1.246e+05	30.984	8.698e-05	-0.747	1.642	2.960e-02	39.213
15569	163.038	16.286	0.647	317	2.669e+06	86.047	1.929e-05	-0.797	1.642	2.970e-02	110.424
12784	258.398	29.297	0.635	101	7.486e+05	56.327	3.422e-05	-0.697	1.641	2.980e-02	72.754
991	127.151	38.742	0.521	182	4.631e+05	47.993	8.082e-05	-0.777	1.641	2.980e-02	68.344
14660	195.635	8.386	0.485	361	1.027e+06	62.582	4.436e-05	-0.878	1.641	2.990e-02	116.763
19826	176.846	28.830	0.472	303	9.764e+05	61.544	5.040e-05	-0.854	1.640	3.000e-02	99.808
4007	212.461	31.449	0.489	211	4.613e+05	47.934	5.165e-05	-0.859	1.640	3.010e-02	42.900
17692	220.177	20.306	0.481	202	6.503e+05	53.746	4.674e-05	-0.871	1.639	3.020e-02	120.520
16643	146.326	53.865	0.635	333	2.432e+06	83.422	1.982e-05	-0.810	1.638	3.040e-02	135.138
19814	177.889	26.032	0.526	245	7.245e+05	55.716	6.074e-05	-0.826	1.637	3.050e-02	106.825
10596	191.065	4.105	0.459	212	6.041e+05	52.442	4.714e-05	-0.802	1.637	3.050e-02	62.506
17689	207.853	22.768	0.565	67	2.319e+05	38.111	5.661e-05	-0.812	1.637	3.060e-02	128.640
5074	221.008	1.004	0.467	241	5.721e+05	51.497	4.211e-05	-0.864	1.637	3.060e-02	48.680
17264	147.092	32.487	0.654	137	1.166e+06	65.292	2.426e-05	-0.712	1.637	3.060e-02	94.955
18592	218.729	43.834	0.573	375	1.962e+06	77.666	3.934e-05	-0.861	1.637	3.060e-02	185.350
20075	180.187	41.529	0.545	134	3.212e+05	42.486	6.288e-05	-0.817	1.636	3.080e-02	111.305
21754	207.477	56.464	0.472	245	5.885e+05	51.987	6.985e-05	-0.774	1.635	3.090e-02	101.164
15280	176.394	8.144	0.510	117	2.574e+05	39.461	7.202e-05	-0.815	1.635	3.090e-02	107.740
17623	210.629	26.267	0.460	137	4.350e+05	47.004	5.635e-05	-0.764	1.635	3.090e-02	72.065
17327	219.011	25.233	0.568	584	2.128e+06	79.790	2.803e-05	-0.885	1.635	3.090e-02	82.612
16321	181.249	9.926	0.518	155	3.131e+05	42.124	8.656e-05	-0.769	1.633	3.140e-02	39.674
20249	166.778	65.573	0.575	96	1.993e+05	36.238	6.297e-05	-0.736	1.632	3.150e-02	46.244
19423	164.352	30.684	0.467	167	4.874e+05	48.820	4.845e-05	-0.860	1.631	3.160e-02	87.092
17901	185.373	26.397	0.464	323	9.307e+05	60.569	5.494e-05	-0.806	1.631	3.170e-02	83.132
11055	144.837	3.636	0.543	219	5.945e+05	52.161	5.418e-05	-0.841	1.630	3.190e-02	58.333
15536	149.662	11.747	0.583	82	4.035e+05	45.839	4.497e-05	-0.812	1.630	3.190e-02	246.589
7759	121.629	20.919	0.660	79	6.904e+05	54.829	2.268e-05	-0.692	1.629	3.200e-02	83.103
12708	258.287	32.441	0.455	77	2.246e+05	37.711	4.788e-05	-0.769	1.629	3.210e-02	43.209
12173	125.781	6.439	0.486	108	1.196e+05	30.568	1.567e-04	-0.568	1.628	3.230e-02	24.218
17750	136.408	22.542	0.656	251	1.975e+06	77.837	1.769e-05	-0.799	1.627	3.240e-02	91.057

Table A.1 (continued)

ID	RA (deg)	DEC (deg)	z	N_{gal}	V ($h^{-3}\mathrm{Mpc}^3$)	R_{eff} ($h^{-1}\mathrm{Mpc}$)	$n_{\min}$ ($h^3\mathrm{Mpc}^{-3}$)	$\delta_{\min}$	r	P	$D_{boundary}$ ($h^{-1}\mathrm{Mpc}$)
1168	192.608	-0.836	0.561	214	4.579e+05	47.814	3.401e-05	-0.887	1.627	3.240e-02	57.182
15533	226.580	12.714	0.549	192	7.495e+05	56.350	4.237e-05	-0.862	1.626	3.260e-02	105.611
14435	241.372	9.020	0.462	224	5.890e+05	52.000	5.556e-05	-0.803	1.626	3.270e-02	73.808
9095	164.411	40.471	0.452	34	8.502e+04	27.278	1.003e-04	-0.579	1.625	3.300e-02	52.469
13394	256.029	28.817	0.592	25	7.556e+04	26.226	5.324e-05	-0.738	1.624	3.320e-02	55.879
16505	147.605	44.832	0.461	364	1.063e+06	63.315	4.912e-05	-0.763	1.624	3.320e-02	74.352
15353	205.673	9.479	0.530	207	5.920e+05	52.089	6.489e-05	-0.810	1.621	3.370e-02	155.335
12341	233.721	6.476	0.484	274	9.033e+05	59.968	5.085e-05	-0.853	1.620	3.380e-02	72.655
16580	135.279	59.568	0.515	279	7.084e+05	55.300	6.069e-05	-0.844	1.620	3.380e-02	80.301
14809	177.050	9.084	0.611	342	1.983e+06	77.932	3.184e-05	-0.816	1.620	3.400e-02	95.718
18198	211.973	22.518	0.570	365	1.355e+06	68.642	3.751e-05	-0.876	1.619	3.410e-02	181.816
21108	180.162	61.338	0.465	142	6.691e+05	54.259	4.668e-05	-0.849	1.619	3.420e-02	83.495
17756	139.875	25.126	0.555	146	3.368e+05	43.160	9.171e-05	-0.701	1.618	3.420e-02	78.080
22196	182.705	42.833	0.457	217	5.246e+05	50.033	7.377e-05	-0.690	1.618	3.430e-02	66.370
14972	138.876	9.140	0.573	842	3.237e+06	91.767	3.199e-05	-0.854	1.617	3.450e-02	105.836
1176	184.764	-0.018	0.553	16	2.113e+04	17.151	1.053e-04	-0.657	1.617	3.460e-02	38.203
17708	217.248	22.238	0.457	45	1.206e+05	30.653	6.592e-05	-0.723	1.616	3.480e-02	66.254
8779	145.716	42.200	0.528	326	9.040e+05	59.982	4.501e-05	-0.871	1.615	3.490e-02	228.312
11210	187.364	4.395	0.461	125	3.493e+05	43.689	4.995e-05	-0.759	1.615	3.500e-02	68.290
18751	255.410	42.768	0.522	153	4.695e+05	48.215	3.750e-05	-0.897	1.614	3.510e-02	63.624
22307	243.455	56.236	0.462	176	4.084e+05	46.026	6.450e-05	-0.729	1.614	3.530e-02	53.623
12080	144.709	7.787	0.587	132	6.511e+05	53.767	3.911e-05	-0.808	1.613	3.530e-02	172.577
10838	164.036	2.997	0.572	17	5.277e+04	23.268	6.648e-05	-0.766	1.613	3.530e-02	46.033
18371	181.486	16.577	0.511	157	3.870e+05	45.207	5.291e-05	-0.864	1.613	3.530e-02	171.717
11892	128.453	5.776	0.519	301	7.457e+05	56.254	4.892e-05	-0.868	1.612	3.560e-02	59.484
12841	258.721	32.779	0.594	333	1.625e+06	72.932	3.025e-05	-0.862	1.611	3.570e-02	65.427
3520	194.391	37.550	0.657	135	9.515e+05	61.016	2.167e-05	-0.743	1.611	3.580e-02	83.850
21053	180.940	60.654	0.648	194	1.742e+06	74.638	2.015e-05	-0.726	1.611	3.590e-02	107.391
16741	139.260	63.851	0.567	46	6.525e+04	24.974	9.639e-05	-0.660	1.610	3.600e-02	42.510
16366	128.503	9.726	0.526	58	1.558e+05	33.381	7.560e-05	-0.795	1.610	3.600e-02	40.215
7668	126.520	24.389	0.515	117	2.870e+05	40.919	7.630e-05	-0.799	1.609	3.630e-02	63.321
13763	130.036	58.136	0.550	317	8.846e+05	59.551	4.782e-05	-0.841	1.608	3.660e-02	65.874

Table A.1 (continued)

ID	RA (deg)	DEC (deg)	z	N_{gal}	V (h^{-3}Mpc^3)	R_{eff} (h^{-1}Mpc)	n_{min} (h^3Mpc^{-3})	δ_{min}	r	P	$D_{boundary}$ (h^{-1}Mpc)
14846	164.160	9.002	0.553	219	8.893e+05	59.656	5.290e-05	-0.828	1.607	3.660e-02	188.464
13129	242.744	35.793	0.510	262	7.796e+05	57.094	7.891e-05	-0.786	1.606	3.680e-02	79.599
12867	255.314	30.800	0.613	197	1.020e+06	62.437	4.271e-05	-0.739	1.606	3.680e-02	71.657
1275	169.465	-0.837	0.636	96	5.143e+05	49.701	1.871e-05	-0.845	1.605	3.700e-02	58.542
11400	202.163	4.579	0.503	39	7.541e+04	26.209	9.996e-05	-0.745	1.605	3.700e-02	32.299
11588	220.555	5.490	0.625	90	4.480e+05	47.468	2.923e-05	-0.779	1.605	3.700e-02	65.579
3707	204.088	35.090	0.657	70	4.112e+05	46.129	3.435e-05	-0.592	1.604	3.730e-02	77.730
4920	208.191	1.575	0.500	98	1.659e+05	34.089	1.068e-04	-0.727	1.604	3.740e-02	41.921
1361	167.325	-0.829	0.479	331	4.998e+05	49.231	9.142e-05	-0.735	1.604	3.740e-02	49.779
21698	212.438	51.004	0.578	188	6.837e+05	54.650	5.234e-05	-0.784	1.604	3.740e-02	256.761
13028	240.773	29.796	0.574	286	8.938e+05	59.756	3.986e-05	-0.844	1.604	3.740e-02	75.667
12396	243.627	8.154	0.505	49	1.119e+05	29.896	7.866e-05	-0.798	1.603	3.750e-02	44.648
1223	168.368	-1.147	0.548	75	1.179e+05	30.422	9.611e-05	-0.687	1.602	3.780e-02	49.705
1338	188.935	0.290	0.534	263	8.033e+05	57.668	3.522e-05	-0.898	1.601	3.800e-02	29.815
18663	210.096	42.993	0.656	83	9.018e+05	59.934	2.391e-05	-0.716	1.601	3.800e-02	91.513
12145	127.075	6.025	0.579	189	5.896e+05	52.017	5.701e-05	-0.740	1.601	3.810e-02	68.850
7639	127.272	27.412	0.603	132	6.012e+05	52.358	4.323e-05	-0.762	1.601	3.810e-02	69.635
15430	224.599	8.206	0.456	79	2.506e+05	39.112	4.951e-05	-0.792	1.600	3.820e-02	63.262
4293	231.249	24.906	0.613	211	1.238e+06	66.615	2.947e-05	-0.803	1.599	3.840e-02	81.174
13679	129.205	44.964	0.492	150	2.834e+05	40.746	7.251e-05	-0.800	1.599	3.840e-02	54.233
3421	226.200	29.496	0.533	247	4.676e+05	48.149	7.813e-05	-0.785	1.599	3.840e-02	57.977
7232	127.643	34.488	0.582	136	3.600e+05	44.130	4.063e-05	-0.816	1.599	3.850e-02	63.274
1070	119.365	30.082	0.506	41	1.223e+05	30.791	8.719e-05	-0.777	1.599	3.850e-02	56.289
8589	125.631	19.249	0.462	334	8.025e+05	57.647	4.283e-05	-0.830	1.598	3.870e-02	77.577
22165	213.522	46.849	0.585	192	8.692e+05	59.203	4.085e-05	-0.832	1.597	3.890e-02	228.926
8258	127.318	14.711	0.509	153	4.191e+05	46.423	5.267e-05	-0.864	1.596	3.920e-02	48.105
21141	167.675	63.669	0.480	578	1.924e+06	77.157	4.254e-05	-0.884	1.596	3.920e-02	80.447
1256	142.942	-0.480	0.545	143	3.095e+05	41.963	6.575e-05	-0.809	1.595	3.930e-02	50.038
13097	237.467	35.332	0.499	130	4.314e+05	46.875	6.442e-05	-0.830	1.595	3.940e-02	140.309
12079	144.385	7.108	0.527	76	2.871e+05	40.925	5.546e-05	-0.852	1.595	3.950e-02	137.984
7854	123.036	20.546	0.491	149	6.239e+05	53.009	4.791e-05	-0.869	1.594	3.960e-02	143.407
8172	119.897	11.439	0.597	95	2.111e+05	36.937	8.252e-05	-0.594	1.593	3.990e-02	59.718

Table A.1 (continued)

ID	RA (deg)	DEC (deg)	z	N_{gal}	V (h^{-3}Mpc^3)	R_{eff} (h^{-1}Mpc)	n_{min} (h^3Mpc^{-3})	δ_{min}	r	P	$D_{boundary}$ (h^{-1}Mpc)
14740	196.283	8.525	0.648	248	2.035e+06	78.610	2.481e-05	-0.718	1.593	3.990e-02	108.303
17058	200.611	17.196	0.514	296	9.198e+05	60.329	6.159e-05	-0.833	1.592	4.020e-02	122.212
6216	245.277	18.120	0.503	304	7.853e+05	57.234	5.370e-05	-0.863	1.592	4.020e-02	88.429
2592	132.083	2.837	0.647	81	4.505e+05	47.556	3.423e-05	-0.611	1.592	4.020e-02	62.702
9172	211.306	39.676	0.515	48	7.919e+04	26.639	1.092e-04	-0.713	1.591	4.040e-02	53.500
19726	159.495	27.284	0.529	142	5.028e+05	49.330	5.393e-05	-0.846	1.591	4.040e-02	229.854
14690	231.145	13.853	0.498	131	2.114e+05	36.955	7.346e-05	-0.813	1.590	4.050e-02	43.978
6319	244.037	13.098	0.515	40	3.814e+04	20.881	1.349e-04	-0.653	1.590	4.060e-02	28.433
14346	247.958	38.967	0.603	41	2.378e+05	38.434	5.192e-05	-0.714	1.589	4.080e-02	74.362
16129	202.466	15.629	0.541	202	6.078e+05	52.548	5.063e-05	-0.852	1.589	4.100e-02	105.301
19414	197.341	30.480	0.502	195	4.881e+05	48.842	5.749e-05	-0.852	1.588	4.100e-02	50.641
4025	193.747	33.642	0.471	118	3.521e+05	43.803	5.006e-05	-0.858	1.588	4.110e-02	43.869
21032	175.455	58.036	0.658	103	9.011e+05	59.918	2.344e-05	-0.681	1.587	4.130e-02	87.456
17079	133.577	33.512	0.539	105	1.709e+05	34.426	1.013e-04	-0.703	1.587	4.140e-02	48.174
17938	156.870	21.594	0.526	96	2.484e+05	38.999	7.985e-05	-0.780	1.586	4.150e-02	167.910
18003	182.096	23.429	0.461	144	4.319e+05	46.891	6.408e-05	-0.746	1.586	4.160e-02	74.995
826	116.367	34.758	0.490	167	3.449e+05	43.503	6.924e-05	-0.823	1.585	4.180e-02	51.205
11732	139.572	2.901	0.569	251	6.415e+05	53.501	5.526e-05	-0.817	1.585	4.190e-02	47.380
17935	145.862	19.930	0.579	197	1.009e+06	62.221	3.646e-05	-0.847	1.584	4.200e-02	146.218
17563	203.888	28.367	0.558	274	1.014e+06	62.324	4.370e-05	-0.855	1.582	4.270e-02	97.545
19865	175.592	27.445	0.581	299	1.204e+06	66.002	4.304e-05	-0.820	1.582	4.270e-02	117.688
19123	150.624	29.795	0.557	232	6.088e+05	52.578	4.788e-05	-0.841	1.581	4.280e-02	203.500
11148	158.044	3.712	0.565	303	8.383e+05	58.494	3.656e-05	-0.849	1.580	4.310e-02	63.306
21904	198.553	45.675	0.523	199	5.637e+05	51.245	5.742e-05	-0.845	1.579	4.330e-02	75.628
11544	128.331	5.428	0.630	118	5.525e+05	50.905	3.092e-05	-0.766	1.578	4.360e-02	58.459
21820	199.321	48.127	0.610	136	5.714e+05	51.479	3.065e-05	-0.823	1.578	4.360e-02	188.790
3706	197.746	35.718	0.569	116	4.420e+05	47.256	4.726e-05	-0.843	1.578	4.380e-02	44.438
2567	134.088	1.446	0.535	194	4.132e+05	46.205	6.347e-05	-0.818	1.577	4.380e-02	63.536
21240	155.984	51.273	0.632	313	2.204e+06	80.728	2.711e-05	-0.775	1.577	4.390e-02	142.398
22199	185.003	43.557	0.484	210	4.240e+05	46.603	9.679e-05	-0.726	1.577	4.400e-02	56.377
9466	224.743	35.679	0.583	50	9.114e+04	27.918	1.057e-04	-0.565	1.576	4.410e-02	42.570
21582	179.074	48.823	0.454	72	2.439e+05	38.761	4.689e-05	-0.773	1.576	4.420e-02	57.794

Table A.1 (continued)

ID	RA (deg)	DEC (deg)	z	N_{gal}	V (h^{-3}Mpc^3)	R_{eff} (h^{-1}Mpc)	n_{min} (h^3Mpc^{-3})	δ_{min}	r	P	$D_{boundary}$ (h^{-1}Mpc)
4604	214.315	-0.243	0.487	392	8.832e+05	59.519	4.731e-05	-0.871	1.575	4.430e-02	66.422
15274	183.822	7.210	0.650	207	1.712e+06	74.208	1.919e-05	-0.711	1.575	4.450e-02	103.812
16656	145.690	48.279	0.616	93	5.733e+05	51.533	3.809e-05	-0.780	1.574	4.480e-02	175.105
18616	238.289	41.291	0.454	51	1.596e+05	33.648	6.829e-05	-0.599	1.574	4.480e-02	57.529
22748	231.324	57.066	0.473	284	7.672e+05	56.789	4.726e-05	-0.863	1.573	4.480e-02	82.124
7249	125.594	35.303	0.656	159	1.277e+06	67.305	2.261e-05	-0.731	1.573	4.490e-02	90.539
13052	245.487	27.363	0.538	96	1.249e+05	31.007	1.178e-04	-0.675	1.573	4.490e-02	44.936
18749	253.558	44.778	0.460	103	2.378e+05	38.435	7.890e-05	-0.669	1.573	4.490e-02	65.811
21847	181.857	58.055	0.518	176	5.698e+05	51.430	7.514e-05	-0.807	1.572	4.530e-02	205.412
12469	233.716	13.545	0.565	116	3.580e+05	44.049	5.390e-05	-0.821	1.571	4.540e-02	54.923

Table A.2: List of voids in the BOSS CMASS South sample

ID	RA (deg)	DEC (deg)	z	$N_{\rm gal}$	V (h^{-3}Mpc^3)	$R_{\rm eff}$ (h^{-1}Mpc)	$n_{\rm min}$ (h^3Mpc^{-3})	$\delta_{\rm min}$	r	P	$D_{boundary}$ (h^{-1}Mpc)
(1)	(2)	(3)	(4)	(5)	(6)	(7)	(8)	(9)	(10)	(11)	(12)
9561	45.047	-8.258	0.596	20	8.179e+04	26.928	3.104e-05	-0.844	6.122	1.400e-45	85.130
5227	329.982	26.290	0.514	270	8.236e+05	58.149	3.238e-05	-0.903	3.058	6.350e-08	80.784
7087	0.581	21.615	0.644	365	3.549e+06	94.622	1.016e-05	-0.875	2.740	3.120e-06	115.519
3478	32.189	-6.105	0.571	448	1.638e+06	73.126	2.546e-05	-0.899	2.654	7.970e-06	93.793
7225	347.344	21.352	0.598	1047	9.776e+06	132.644	8.540e-06	-0.928	2.622	1.110e-05	215.422
6622	14.735	33.167	0.504	277	6.061e+05	52.500	5.061e-05	-0.861	2.524	3.030e-05	62.562
7103	8.903	24.567	0.653	247	1.956e+06	77.588	1.429e-05	-0.796	2.467	5.300e-05	97.881
1029	15.076	-0.284	0.597	150	7.396e+05	56.102	2.606e-05	-0.869	2.426	7.770e-05	69.769
4240	334.702	12.750	0.640	618	5.583e+06	110.053	1.321e-05	-0.852	2.420	8.200e-05	125.732
3940	341.634	-1.311	0.661	38	1.772e+05	34.845	2.921e-05	-0.626	2.419	8.300e-05	64.477
1971	20.702	4.570	0.653	154	1.321e+06	68.072	1.446e-05	-0.822	2.417	8.450e-05	98.020
6977	1.322	12.599	0.505	323	8.474e+05	58.704	2.847e-05	-0.921	2.410	9.000e-05	60.541
2119	31.066	3.695	0.532	303	8.144e+05	57.932	4.034e-05	-0.865	2.290	2.650e-04	77.725
3345	39.037	-1.761	0.580	271	8.145e+05	57.933	4.660e-05	-0.789	2.290	2.650e-04	63.933
5079	14.705	20.643	0.494	864	3.460e+06	93.826	2.731e-05	-0.929	2.280	2.900e-04	150.220
1671	42.675	1.861	0.515	95	2.320e+05	38.120	4.571e-05	-0.863	2.265	3.270e-04	53.895
7580	359.764	29.760	0.463	407	1.503e+06	71.064	2.877e-05	-0.884	2.230	4.430e-04	79.631
8549	26.138	-6.288	0.477	330	7.320e+05	55.909	4.041e-05	-0.876	2.222	4.720e-04	49.747
8776	0.100	-7.353	0.498	346	6.453e+05	53.606	5.164e-05	-0.865	2.217	4.900e-04	62.779
5009	329.282	21.418	0.449	26	3.616e+04	20.514	9.173e-05	-0.557	2.209	5.260e-04	44.072
1851	30.896	2.125	0.488	247	6.522e+05	53.798	4.440e-05	-0.884	2.203	5.520e-04	50.848
7526	342.261	30.710	0.524	282	8.260e+05	58.206	5.580e-05	-0.840	2.199	5.690e-04	79.026
6630	27.546	31.032	0.513	150	3.960e+05	45.557	6.437e-05	-0.815	2.181	6.620e-04	55.594
7490	31.204	29.711	0.660	99	4.604e+05	47.903	3.560e-05	-0.544	2.163	7.670e-04	66.930
7189	24.447	26.191	0.522	452	1.607e+06	72.657	3.972e-05	-0.881	2.133	9.750e-04	172.199
289	322.004	5.724	0.653	201	1.510e+06	71.175	1.760e-05	-0.803	2.128	1.010e-03	94.160
2543	22.993	2.278	0.468	344	9.083e+05	60.078	4.229e-05	-0.857	2.127	1.020e-03	44.181
4325	341.580	15.528	0.479	85	2.916e+05	41.139	5.675e-05	-0.826	2.125	1.030e-03	114.509
643	336.658	-0.176	0.578	219	7.595e+05	56.600	3.017e-05	-0.864	2.113	1.140e-03	45.995
7437	14.683	32.568	0.630	461	2.625e+06	85.577	1.992e-05	-0.873	2.111	1.150e-03	90.875

Table A.2 (continued)

ID	RA (deg)	DEC (deg)	z	$N_{\rm gal}$	V (h^{-3}Mpc^3)	$R_{\rm eff}$ (h^{-1}Mpc)	$n_{\rm min}$ (h^3Mpc^{-3})	$\delta_{\rm min}$	r	P	$D_{boundary}$ (h^{-1}Mpc)
9591	39.947	-6.188	0.519	263	7.554e+05	56.498	3.584e-05	-0.897	2.104	1.220e-03	68.925
794	320.476	0.941	0.570	315	1.006e+06	62.152	4.108e-05	-0.854	2.079	1.480e-03	74.901
6069	342.919	24.735	0.511	156	6.246e+05	53.027	3.066e-05	-0.912	2.068	1.610e-03	190.082
2124	37.399	3.740	0.500	150	1.417e+05	32.345	1.390e-04	-0.619	2.064	1.660e-03	36.724
3181	26.874	-2.882	0.473	314	6.810e+05	54.579	5.140e-05	-0.843	2.063	1.680e-03	47.274
7557	7.426	29.591	0.467	645	1.840e+06	76.012	3.672e-05	-0.876	2.059	1.720e-03	81.308
4211	333.512	11.836	0.459	359	1.040e+06	62.852	3.628e-05	-0.825	2.059	1.720e-03	69.771
9567	44.270	-7.368	0.472	41	1.140e+05	30.076	4.664e-05	-0.851	2.057	1.750e-03	58.585
3243	29.965	-2.866	0.518	212	5.726e+05	51.513	4.979e-05	-0.851	2.033	2.100e-03	46.729
8115	4.237	-3.729	0.564	209	6.181e+05	52.843	5.738e-05	-0.794	2.030	2.150e-03	77.488
8157	7.493	-4.147	0.654	122	7.444e+05	56.221	2.976e-05	-0.619	2.011	2.470e-03	68.890
1677	42.192	2.216	0.578	168	4.396e+05	47.168	3.332e-05	-0.868	2.010	2.500e-03	43.432
4518	333.451	16.358	0.502	245	9.180e+05	60.291	3.838e-05	-0.900	1.992	2.840e-03	100.180
7411	16.149	30.842	0.546	277	8.817e+05	59.486	5.204e-05	-0.831	1.972	3.290e-03	50.792
1682	35.205	2.643	0.641	517	3.141e+06	90.852	2.137e-05	-0.788	1.959	3.610e-03	78.951
7470	24.754	30.953	0.647	269	1.678e+06	73.719	1.926e-05	-0.763	1.937	4.240e-03	101.956
9545	44.740	-7.076	0.607	12	3.131e+04	19.553	8.332e-05	-0.534	1.936	4.260e-03	59.275
8349	0.252	-4.946	0.575	183	3.698e+05	44.526	6.272e-05	-0.775	1.933	4.360e-03	46.547
8960	5.995	-6.421	0.568	79	1.854e+05	35.375	6.056e-05	-0.783	1.922	4.700e-03	53.899
7488	26.764	30.774	0.462	231	5.798e+05	51.729	4.341e-05	-0.853	1.911	5.080e-03	63.537
6564	358.852	12.119	0.571	151	7.605e+05	56.625	3.623e-05	-0.845	1.910	5.120e-03	52.828
687	327.904	-0.199	0.561	300	7.930e+05	57.420	5.503e-05	-0.802	1.899	5.520e-03	83.200
905	20.396	-1.370	0.638	205	1.140e+06	64.805	1.817e-05	-0.872	1.896	5.640e-03	69.190
6364	8.282	16.103	0.509	370	1.135e+06	64.706	3.953e-05	-0.886	1.896	5.670e-03	184.345
673	27.580	0.029	0.542	50	7.456e+04	26.110	7.776e-05	-0.741	1.893	5.780e-03	39.912
1800	346.754	0.316	0.482	194	4.470e+05	47.431	6.138e-05	-0.817	1.892	5.810e-03	62.444
5685	10.833	15.160	0.634	389	2.829e+06	87.737	1.813e-05	-0.777	1.892	5.820e-03	137.559
3920	331.133	-1.181	0.505	166	3.458e+05	43.544	5.667e-05	-0.845	1.890	5.870e-03	54.599
1944	26.733	3.167	0.552	162	5.516e+05	50.876	5.224e-05	-0.831	1.889	5.940e-03	53.256
5050	332.678	22.127	0.461	281	1.163e+06	65.232	2.735e-05	-0.901	1.885	6.090e-03	74.194
1483	10.375	7.083	0.650	284	2.369e+06	82.699	1.515e-05	-0.784	1.876	6.510e-03	104.532
1788	12.986	0.928	0.454	140	3.128e+05	42.112	5.253e-05	-0.788	1.875	6.540e-03	43.512

Table A.2 (continued)

ID	RA (deg)	DEC (deg)	z	N_{gal}	V (h^{-3}Mpc^3)	R_{eff} (h^{-1}Mpc)	$n_{\min}$ (h^3Mpc^{-3})	$\delta_{\min}$	r	P	$D_{boundary}$ (h^{-1}Mpc)
1047	355.208	-1.102	0.603	194	6.902e+05	54.822	3.498e-05	-0.800	1.863	7.080e-03	65.585
239	323.953	5.365	0.474	547	1.708e+06	74.148	3.494e-05	-0.903	1.862	7.150e-03	101.168
6402	17.002	28.276	0.605	197	1.278e+06	67.312	3.177e-05	-0.822	1.862	7.160e-03	175.363
1521	28.674	5.777	0.563	132	4.230e+05	46.567	4.020e-05	-0.855	1.847	7.890e-03	70.434
6641	13.925	33.383	0.551	64	2.050e+05	36.576	5.393e-05	-0.825	1.844	8.060e-03	59.873
4991	29.685	24.915	0.627	136	8.334e+05	58.379	2.118e-05	-0.865	1.836	8.500e-03	67.170
3235	10.316	-3.029	0.637	135	7.508e+05	56.382	3.548e-05	-0.720	1.829	8.930e-03	64.684
4638	18.354	14.830	0.590	183	7.884e+05	57.309	3.219e-05	-0.838	1.828	8.970e-03	231.393
315	318.861	6.651	0.457	46	6.866e+04	25.403	1.018e-04	-0.633	1.826	9.120e-03	46.138
6958	358.797	10.019	0.542	285	1.257e+06	66.947	3.233e-05	-0.894	1.824	9.250e-03	98.998
974	18.149	-0.483	0.480	108	3.822e+05	45.020	5.019e-05	-0.850	1.823	9.280e-03	71.886
1911	6.680	2.989	0.456	141	3.310e+05	42.910	5.214e-05	-0.748	1.822	9.370e-03	61.765
6582	358.776	12.427	0.460	402	1.085e+06	63.747	3.973e-05	-0.808	1.820	9.460e-03	35.011
169	321.955	6.812	0.605	71	2.711e+05	40.150	6.140e-05	-0.636	1.818	9.610e-03	61.319
1907	359.140	2.845	0.505	121	3.603e+05	44.144	6.766e-05	-0.815	1.806	1.040e-02	152.500
6142	347.124	21.461	0.471	756	3.118e+06	90.625	1.771e-05	-0.953	1.804	1.060e-02	98.172
4591	331.572	20.141	0.624	405	2.599e+06	85.286	2.907e-05	-0.795	1.801	1.080e-02	107.281
3589	36.576	-6.087	0.540	429	1.159e+06	65.156	3.881e-05	-0.880	1.793	1.140e-02	86.993
5640	349.879	13.804	0.455	121	2.385e+05	38.473	4.939e-05	-0.720	1.791	1.150e-02	59.507
168	319.996	6.365	0.487	180	3.957e+05	45.545	5.421e-05	-0.855	1.791	1.150e-02	55.886
6347	9.272	16.973	0.462	454	1.482e+06	70.728	3.473e-05	-0.832	1.788	1.170e-02	77.609
1031	19.200	0.510	0.602	63	2.206e+05	37.485	4.359e-05	-0.751	1.784	1.210e-02	58.710
1836	10.374	2.849	0.580	333	1.530e+06	71.477	3.014e-05	-0.880	1.782	1.220e-02	90.903
7275	353.433	27.263	0.647	393	4.448e+06	102.018	1.325e-05	-0.837	1.775	1.270e-02	108.836
9559	43.905	-8.029	0.584	25	9.456e+04	28.262	4.606e-05	-0.803	1.775	1.280e-02	58.462
7631	14.729	33.034	0.472	136	2.767e+05	40.422	7.924e-05	-0.748	1.768	1.340e-02	61.758
2349	27.654	9.211	0.516	139	3.315e+05	42.935	6.383e-05	-0.816	1.767	1.350e-02	50.559
7242	27.784	28.196	0.538	169	5.515e+05	50.874	5.306e-05	-0.823	1.761	1.400e-02	122.174
1925	41.796	2.096	0.615	326	1.153e+06	65.043	2.297e-05	-0.854	1.757	1.440e-02	66.779
9632	40.884	-6.149	0.467	167	3.803e+05	44.947	6.408e-05	-0.804	1.754	1.460e-02	65.213
6313	357.920	25.424	0.526	125	4.423e+05	47.266	5.251e-05	-0.838	1.754	1.460e-02	224.131
9635	42.814	-7.057	0.563	81	2.449e+05	38.813	5.891e-05	-0.790	1.750	1.500e-02	59.068

Table A.2 (continued)

ID	RA (deg)	DEC (deg)	z	N_{gal}	V ($h^{-3}\mathrm{Mpc}^3$)	R_{eff} ($h^{-1}\mathrm{Mpc}$)	n_{min} ($h^3\mathrm{Mpc}^{-3}$)	δ_{min}	r	P	$D_{boundary}$ ($h^{-1}\mathrm{Mpc}$)
7011	355.588	7.723	0.636	469	3.365e+06	92.959	1.961e-05	-0.749	1.749	1.510e-02	132.898
915	351.643	-0.731	0.640	70	5.477e+05	50.757	2.523e-05	-0.768	1.748	1.520e-02	78.894
6377	3.276	17.428	0.529	181	4.983e+05	49.181	5.300e-05	-0.836	1.748	1.520e-02	118.896
5298	331.108	28.764	0.559	26	8.684e+04	27.472	6.884e-05	-0.778	1.745	1.550e-02	52.764
3492	41.081	-1.799	0.657	182	1.112e+06	64.263	2.341e-05	-0.712	1.743	1.580e-02	73.890
3328	352.721	-1.917	0.553	121	1.853e+05	35.364	7.697e-05	-0.723	1.741	1.590e-02	40.353
8868	0.689	-8.310	0.633	217	7.885e+05	57.310	3.712e-05	-0.688	1.738	1.620e-02	76.561
754	352.525	-0.844	0.488	167	2.899e+05	41.059	9.389e-05	-0.740	1.737	1.630e-02	61.031
8241	21.186	-4.226	0.590	25	5.356e+04	23.384	8.804e-05	-0.618	1.733	1.680e-02	40.581
5660	352.546	16.304	0.514	511	1.688e+06	73.861	3.855e-05	-0.881	1.730	1.710e-02	156.280
1943	27.200	3.789	0.506	141	3.673e+05	44.428	6.719e-05	-0.816	1.728	1.740e-02	61.599
5842	358.114	33.232	0.450	25	4.448e+04	21.980	9.030e-05	-0.564	1.716	1.870e-02	48.496
930	29.745	-0.799	0.573	425	1.193e+06	65.797	3.963e-05	-0.858	1.715	1.880e-02	60.831
1830	351.746	1.790	0.575	495	1.705e+06	74.106	4.868e-05	-0.807	1.713	1.900e-02	89.343
5582	4.016	8.804	0.624	935	7.635e+06	122.153	1.345e-05	-0.828	1.710	1.940e-02	158.528
2241	24.004	8.571	0.668	28	2.461e+05	38.875	2.946e-05	-0.580	1.704	2.020e-02	66.927
4907	26.234	21.391	0.534	759	3.007e+06	89.544	2.676e-05	-0.911	1.704	2.020e-02	130.306
2100	12.935	4.709	0.515	336	1.029e+06	62.621	4.727e-05	-0.858	1.703	2.030e-02	82.540
2317	21.169	12.876	0.454	168	4.274e+05	46.730	6.154e-05	-0.751	1.702	2.040e-02	57.778
7081	6.428	23.126	0.589	409	2.111e+06	79.575	2.429e-05	-0.890	1.701	2.060e-02	234.405
7459	20.312	30.406	0.587	396	1.892e+06	76.727	2.982e-05	-0.865	1.696	2.120e-02	107.377
5264	334.597	28.274	0.470	445	1.378e+06	69.032	5.823e-05	-0.803	1.696	2.120e-02	78.852
4643	18.474	14.354	0.478	197	4.719e+05	48.296	6.185e-05	-0.815	1.696	2.130e-02	114.473
7403	353.110	28.761	0.476	582	1.642e+06	73.191	4.061e-05	-0.862	1.691	2.180e-02	108.519
8103	9.773	-3.361	0.549	103	2.142e+05	37.117	6.984e-05	-0.768	1.690	2.210e-02	62.006
1850	29.324	2.974	0.455	187	4.489e+05	47.498	6.422e-05	-0.690	1.689	2.220e-02	58.251
656	350.769	-0.805	0.534	257	6.679e+05	54.226	4.535e-05	-0.860	1.688	2.230e-02	66.184
135	324.671	5.414	0.520	163	4.903e+05	48.916	5.193e-05	-0.844	1.685	2.270e-02	120.937
8713	6.455	-6.097	0.601	40	1.164e+05	30.286	5.859e-05	-0.705	1.681	2.330e-02	55.208
5059	333.198	21.922	0.538	117	6.121e+05	52.672	5.532e-05	-0.819	1.679	2.350e-02	136.182
8543	28.531	-7.246	0.638	139	7.126e+05	55.409	4.174e-05	-0.616	1.679	2.360e-02	84.011
3550	4.764	-2.887	0.651	174	1.319e+06	68.026	2.499e-05	-0.734	1.674	2.430e-02	100.470

Table A.2 (continued)

ID	RA (deg)	DEC (deg)	z	$N_{\rm gal}$	V (h^{-3}Mpc^3)	$R_{\rm eff}$ (h^{-1}Mpc)	$n_{\rm min}$ (h^3Mpc^{-3})	$\delta_{\rm min}$	r	P	$D_{boundary}$ (h^{-1}Mpc)
7528	343.409	31.812	0.558	107	2.848e+05	40.814	7.043e-05	-0.773	1.673	2.450e-02	51.651
7525	337.222	30.089	0.633	224	1.437e+06	69.996	1.663e-05	-0.835	1.671	2.490e-02	68.915
199	320.725	1.330	0.493	313	7.145e+05	55.458	5.812e-05	-0.848	1.671	2.490e-02	67.796
7344	351.651	20.992	0.487	91	2.921e+05	41.159	5.829e-05	-0.839	1.670	2.500e-02	132.882
5524	336.666	24.501	0.518	230	8.936e+05	59.752	4.952e-05	-0.850	1.666	2.550e-02	185.496
1940	21.433	2.706	0.615	218	1.274e+06	67.246	2.750e-05	-0.843	1.665	2.580e-02	86.882
270	322.813	6.959	0.541	219	7.661e+05	56.762	3.250e-05	-0.892	1.664	2.580e-02	65.162
2246	27.581	9.817	0.459	180	3.324e+05	42.973	5.626e-05	-0.773	1.664	2.590e-02	47.289
637	331.935	0.060	0.462	166	3.545e+05	43.903	6.973e-05	-0.764	1.662	2.620e-02	67.870
5613	13.867	22.865	0.598	175	8.320e+05	58.346	4.390e-05	-0.755	1.658	2.690e-02	213.936
6018	18.122	30.013	0.457	239	5.432e+05	50.618	4.497e-05	-0.818	1.655	2.740e-02	63.505
7935	348.590	32.782	0.625	17	8.422e+04	27.193	6.296e-05	-0.503	1.654	2.760e-02	52.001
8547	29.422	-6.342	0.530	449	1.053e+06	63.104	5.346e-05	-0.825	1.653	2.760e-02	91.341
4992	18.984	25.096	0.503	208	8.317e+05	58.339	3.706e-05	-0.899	1.651	2.810e-02	169.922
1741	9.809	3.174	0.488	239	6.185e+05	52.856	6.557e-05	-0.821	1.650	2.820e-02	83.528
7643	339.384	30.812	0.511	88	1.783e+05	34.915	7.482e-05	-0.792	1.650	2.830e-02	51.483
1438	14.948	8.080	0.491	159	4.232e+05	46.576	6.673e-05	-0.821	1.649	2.840e-02	143.840
5547	345.176	8.459	0.658	87	7.419e+05	56.160	2.555e-05	-0.673	1.649	2.850e-02	88.645
1891	39.805	2.040	0.573	287	6.435e+05	53.558	4.655e-05	-0.833	1.648	2.860e-02	49.460
819	340.804	-0.379	0.574	114	3.588e+05	44.081	5.256e-05	-0.775	1.644	2.930e-02	57.000
6647	22.294	32.703	0.540	22	4.184e+04	21.535	9.952e-05	-0.674	1.644	2.940e-02	51.387
1450	337.526	5.474	0.543	514	1.758e+06	74.870	3.615e-05	-0.870	1.642	2.970e-02	107.296
300	320.030	6.435	0.520	59	1.556e+05	33.365	7.212e-05	-0.784	1.640	3.000e-02	58.054
3454	27.337	-1.941	0.602	142	5.932e+05	52.123	5.348e-05	-0.701	1.639	3.020e-02	64.024
3395	35.949	-3.309	0.590	151	5.133e+05	49.670	5.134e-05	-0.758	1.638	3.040e-02	58.610
1779	2.627	3.778	0.456	101	3.488e+05	43.669	5.619e-05	-0.773	1.637	3.050e-02	62.798
8525	28.596	-7.698	0.554	195	4.931e+05	49.010	5.749e-05	-0.814	1.637	3.070e-02	67.532
7263	29.461	28.712	0.505	81	2.155e+05	37.191	8.713e-05	-0.761	1.636	3.070e-02	85.996
8458	2.334	-6.297	0.652	39	3.457e+05	43.540	2.921e-05	-0.673	1.635	3.100e-02	81.328
763	349.116	1.179	0.638	266	1.915e+06	77.033	2.254e-05	-0.793	1.633	3.130e-02	77.613
2202	332.639	5.233	0.512	290	7.020e+05	55.133	6.835e-05	-0.810	1.632	3.150e-02	62.729
692	12.345	-0.682	0.523	135	3.167e+05	42.283	6.131e-05	-0.824	1.632	3.150e-02	52.612

Table A.2 (continued)

ID	RA (deg)	DEC (deg)	z	$N_{\rm gal}$	V (h^{-3}Mpc^3)	$R_{\rm eff}$ (h^{-1}Mpc)	$n_{\rm min}$ (h^3Mpc^{-3})	$\delta_{\rm min}$	r	P	$D_{boundary}$ (h^{-1}Mpc)
3392	34.570	-3.651	0.469	263	7.756e+05	56.996	4.553e-05	-0.855	1.629	3.210e-02	64.231
2377	20.223	10.695	0.589	149	6.846e+05	54.675	4.771e-05	-0.793	1.628	3.220e-02	233.170
6330	342.722	24.996	0.654	108	1.176e+06	65.488	2.014e-05	-0.753	1.624	3.310e-02	94.184
5526	336.424	21.146	0.601	188	1.304e+06	67.772	2.461e-05	-0.859	1.623	3.340e-02	207.660
5746	4.144	33.366	0.487	91	2.133e+05	37.063	6.824e-05	-0.817	1.617	3.450e-02	55.379
1070	39.278	0.245	0.479	307	1.042e+06	62.898	4.272e-05	-0.869	1.613	3.530e-02	76.698
5217	330.137	24.942	0.635	341	2.920e+06	88.670	2.236e-05	-0.762	1.613	3.530e-02	104.413
8234	18.607	-4.247	0.567	44	1.035e+05	29.130	7.499e-05	-0.730	1.613	3.540e-02	45.376
5000	14.221	14.531	0.663	49	4.407e+05	47.209	2.518e-05	-0.678	1.612	3.550e-02	77.536
5718	3.273	14.500	0.458	63	1.294e+05	31.377	8.870e-05	-0.641	1.612	3.570e-02	66.154
4363	337.811	16.468	0.478	199	7.213e+05	55.635	4.019e-05	-0.877	1.612	3.570e-02	113.977
9564	43.784	-6.938	0.498	88	2.403e+05	38.566	5.145e-05	-0.852	1.611	3.570e-02	56.294
4639	17.397	14.248	0.453	14	3.636e+04	20.551	9.922e-05	-0.599	1.611	3.580e-02	57.318
3947	32.531	-2.457	0.646	37	2.237e+05	37.660	4.873e-05	-0.552	1.607	3.660e-02	65.631
897	337.133	1.000	0.612	91	3.862e+05	45.176	4.330e-05	-0.743	1.604	3.730e-02	56.193
2150	5.016	5.179	0.558	235	1.054e+06	63.135	3.498e-05	-0.875	1.604	3.740e-02	166.958
7521	337.549	30.381	0.552	121	2.764e+05	40.409	6.806e-05	-0.780	1.602	3.780e-02	55.576
883	340.292	0.221	0.498	82	1.987e+05	36.201	7.014e-05	-0.817	1.601	3.790e-02	64.484
248	325.767	7.014	0.457	21	6.672e+04	25.161	9.712e-05	-0.671	1.600	3.820e-02	64.057
7000	348.791	9.751	0.656	96	8.229e+05	58.133	2.648e-05	-0.661	1.591	4.040e-02	91.709
1382	344.625	5.843	0.611	46	3.211e+05	42.481	3.996e-05	-0.777	1.589	4.080e-02	130.583
2121	33.606	3.613	0.487	87	1.740e+05	34.634	6.693e-05	-0.821	1.589	4.090e-02	55.331
4604	330.399	18.021	0.591	63	2.224e+05	37.583	7.482e-05	-0.662	1.587	4.140e-02	62.228
4387	338.928	10.601	0.488	259	1.080e+06	63.653	3.951e-05	-0.892	1.585	4.180e-02	135.545
1302	27.813	7.844	0.490	103	2.404e+05	38.574	7.132e-05	-0.814	1.582	4.270e-02	55.760
788	324.320	-0.918	0.487	167	3.295e+05	42.845	7.376e-05	-0.802	1.581	4.280e-02	58.574
3909	345.961	-1.909	0.571	114	1.852e+05	35.359	6.909e-05	-0.726	1.581	4.280e-02	41.412
1574	22.558	8.110	0.590	162	5.800e+05	51.735	5.092e-05	-0.770	1.576	4.430e-02	193.197
3338	21.089	-2.013	0.578	57	1.241e+05	30.947	8.048e-05	-0.711	1.574	4.460e-02	40.989
925	19.699	-0.394	0.546	324	9.092e+05	60.098	4.783e-05	-0.843	1.573	4.500e-02	74.880
1030	15.901	0.135	0.541	93	3.627e+05	44.241	5.225e-05	-0.826	1.573	4.510e-02	51.602
4965	27.052	20.911	0.463	477	1.654e+06	73.360	3.397e-05	-0.863	1.572	4.530e-02	78.984

Table A.3: List of voids in the BOSS LOWZ North sample

ID	RA	DEC	z	N_{gal}	V	R_{eff}	n_{min}	δ_{min}	r	P	$D_{boundary}$
	(deg)	(deg)			(h^{-3}Mpc^3)	(h^{-1}Mpc)	(h^3Mpc^{-3})				(h^{-1}Mpc)
(1)	(2)	(3)	(4)	(5)	(6)	(7)	(8)	(9)	(10)	(11)	(12)
13788	184.439	37.133	0.292	109066	3.887e+08	452.732	2.068e-05	-0.918	4.377	1.010e-18	7.255
998	213.379	-0.158	0.327	281	4.997e+05	49.227	2.955e-05	-0.914	4.089	9.150e-16	50.606
11176	237.907	8.246	0.384	1394	3.572e+06	94.826	2.479e-05	-0.872	3.859	1.150e-13	99.872
11431	205.520	8.443	0.361	1377	4.834e+06	104.894	2.469e-05	-0.884	3.677	3.730e-12	90.113
4739	203.474	50.656	0.342	24983	9.501e+07	283.073	2.156e-05	-0.883	3.617	1.100e-11	135.103
14307	244.113	52.377	0.401	170	5.971e+05	52.239	2.392e-05	-0.859	3.517	6.220e-11	71.522
13222	147.338	43.824	0.327	13420	5.258e+07	232.397	2.280e-05	-0.891	3.453	1.830e-10	190.372
11627	167.872	18.274	0.326	18256	6.947e+07	255.013	2.434e-05	-0.874	3.331	1.270e-09	118.648
3294	121.868	21.044	0.363	3351	1.055e+07	136.068	2.785e-05	-0.849	3.286	2.500e-09	126.800
11134	248.111	38.157	0.234	1418	3.665e+06	95.646	2.773e-05	-0.927	3.269	3.240e-09	60.334
11375	237.146	9.245	0.266	551	1.070e+06	63.442	3.033e-05	-0.891	3.050	7.080e-08	63.306
4402	122.937	16.086	0.274	1855	3.820e+06	96.976	3.505e-05	-0.879	2.990	1.540e-07	77.763
16634	218.128	50.843	0.349	18707	7.048e+07	256.241	2.586e-05	-0.870	2.985	1.650e-07	118.364
5734	166.960	45.271	0.384	590	2.649e+06	85.837	2.220e-05	-0.879	2.962	2.210e-07	110.799
8541	196.822	17.742	0.294	3171	1.167e+07	140.721	2.764e-05	-0.900	2.904	4.570e-07	126.609
14348	225.014	48.016	0.343	8601	3.148e+07	195.881	2.609e-05	-0.839	2.876	6.400e-07	85.765
11918	140.498	15.689	0.360	4419	1.502e+07	153.077	3.199e-05	-0.871	2.870	6.860e-07	157.620
16394	152.100	47.928	0.286	2836	1.230e+07	143.208	2.498e-05	-0.914	2.853	8.460e-07	193.666
6177	174.869	30.699	0.387	1925	7.430e+06	121.053	2.556e-05	-0.861	2.852	8.500e-07	104.910
8656	157.222	9.377	0.386	1540	5.794e+06	111.418	2.633e-05	-0.857	2.845	9.240e-07	107.860
1077	201.227	0.278	0.243	108	1.147e+05	30.145	7.926e-05	-0.735	2.814	1.340e-06	37.784
5692	142.345	44.537	0.370	3554	1.438e+07	150.861	2.524e-05	-0.851	2.695	5.100e-06	146.047
1625	248.149	15.665	0.397	203	4.798e+05	48.564	3.841e-05	-0.791	2.695	5.130e-06	67.943
16341	167.505	52.932	0.264	743	3.378e+06	93.079	2.798e-05	-0.904	2.693	5.230e-06	155.248
14778	168.356	33.312	0.343	1915	6.690e+06	116.890	2.927e-05	-0.892	2.692	5.300e-06	187.232
75	201.565	-0.062	0.392	269	8.408e+05	58.550	3.524e-05	-0.832	2.690	5.380e-06	58.793
2151	252.039	23.261	0.307	607	1.162e+06	65.225	3.683e-05	-0.866	2.687	5.550e-06	64.299
3404	121.724	19.611	0.354	2524	8.089e+06	124.530	3.119e-05	-0.838	2.684	5.790e-06	116.834
11530	153.070	10.043	0.340	868	3.016e+06	89.634	3.443e-05	-0.890	2.648	8.510e-06	110.908
32	213.163	0.265	0.251	127	1.281e+05	31.272	6.661e-05	-0.777	2.639	9.320e-06	34.440

Table A.3 (continued)

ID	RA (deg)	DEC (deg)	z	N_{gal}	V (h^{-3}Mpc^3)	R_{eff} (h^{-1}Mpc)	n_{min} (h^3Mpc^{-3})	δ_{min}	r	P	$D_{boundary}$ (h^{-1}Mpc)
13721	201.523	19.370	0.367	4938	1.982e+07	167.884	2.464e-05	-0.884	2.634	9.820e-06	76.970
12090	137.080	18.098	0.258	1478	3.952e+06	98.083	3.638e-05	-0.882	2.624	1.100e-05	76.784
16283	167.099	61.705	0.381	692	2.180e+06	80.443	3.084e-05	-0.855	2.596	1.460e-05	96.582
1557	246.566	16.463	0.229	196	2.439e+05	38.760	6.740e-05	-0.819	2.589	1.570e-05	51.852
11446	209.670	14.923	0.272	3799	1.272e+07	144.821	3.341e-05	-0.878	2.572	1.870e-05	60.886
17482	159.774	49.555	0.346	479	1.342e+06	68.431	3.054e-05	-0.907	2.541	2.540e-05	204.890
16633	191.266	58.545	0.306	1419	4.590e+06	103.094	3.547e-05	-0.887	2.531	2.820e-05	139.601
8913	237.810	7.279	0.298	372	9.048e+05	59.999	3.844e-05	-0.853	2.529	2.870e-05	68.952
12071	143.357	12.234	0.399	474	1.702e+06	74.066	3.227e-05	-0.809	2.523	3.060e-05	74.959
4477	122.231	20.813	0.226	580	9.472e+05	60.923	3.582e-05	-0.892	2.503	3.710e-05	72.346
7629	124.326	2.426	0.340	45	4.162e+04	21.499	1.269e-04	-0.629	2.477	4.790e-05	35.525
10199	238.037	44.638	0.287	2377	7.257e+06	120.106	3.596e-05	-0.879	2.476	4.830e-05	67.261
4880	179.349	38.639	0.279	154	5.032e+05	49.342	4.295e-05	-0.841	2.466	5.310e-05	61.529
15600	151.298	22.383	0.396	1412	5.498e+06	109.486	3.260e-05	-0.808	2.459	5.720e-05	82.921
11954	220.420	15.921	0.369	2430	8.554e+06	126.872	2.886e-05	-0.862	2.459	5.720e-05	91.205
16286	181.844	60.800	0.224	339	7.328e+05	55.929	4.824e-05	-0.854	2.446	6.410e-05	65.389
15671	208.169	41.235	0.354	50	8.468e+04	27.241	8.904e-05	-0.711	2.435	7.140e-05	47.220
11600	206.089	12.105	0.343	151	5.871e+05	51.945	3.730e-05	-0.886	2.434	7.200e-05	97.544
10510	134.590	44.169	0.365	1074	3.400e+06	93.277	2.777e-05	-0.836	2.428	7.600e-05	78.151
12092	148.959	12.436	0.271	3482	1.069e+07	136.661	3.578e-05	-0.867	2.425	7.830e-05	80.183
12488	152.612	17.334	0.343	557	1.876e+06	76.514	3.816e-05	-0.861	2.400	9.940e-05	84.277
15370	152.645	34.533	0.354	1395	5.231e+06	107.691	2.887e-05	-0.904	2.388	1.110e-04	185.206
31	210.920	0.082	0.382	1078	2.430e+06	83.402	3.942e-05	-0.843	2.377	1.220e-04	57.089
5442	164.220	39.175	0.240	675	2.275e+06	81.587	3.289e-05	-0.890	2.344	1.650e-04	109.059
3577	124.570	14.605	0.388	486	1.511e+06	71.190	3.540e-05	-0.791	2.328	1.900e-04	81.642
15734	212.238	45.510	0.328	3496	1.248e+07	143.897	3.008e-05	-0.891	2.307	2.280e-04	113.966
14361	242.219	35.403	0.320	1251	4.318e+06	101.017	3.892e-05	-0.886	2.256	3.540e-04	129.138
9523	256.739	30.809	0.364	366	9.040e+05	59.983	3.971e-05	-0.840	2.249	3.770e-04	62.089
1000	223.838	0.114	0.217	32	2.669e+04	18.539	1.597e-04	-0.518	2.208	5.290e-04	32.524
7907	192.121	5.028	0.401	147	3.211e+05	42.478	5.464e-05	-0.703	2.206	5.400e-04	54.081
2148	251.780	23.339	0.392	379	8.717e+05	59.261	4.983e-05	-0.742	2.205	5.430e-04	80.277
15774	238.930	53.523	0.262	645	1.739e+06	74.606	4.145e-05	-0.860	2.201	5.630e-04	75.490

Table A.3 (continued)

ID	RA (deg)	DEC (deg)	z	$N_{\rm gal}$	V (h^{-3}Mpc^3)	$R_{\rm eff}$ (h^{-1}Mpc)	$n_{\rm min}$ (h^3Mpc^{-3})	$\delta_{\rm min}$	r	P	$D_{boundary}$ (h^{-1}Mpc)
13793	189.456	24.139	0.323	332	1.406e+06	69.503	2.904e-05	-0.906	2.193	6.000e-04	141.434
14775	159.759	22.776	0.268	2488	9.226e+06	130.108	3.080e-05	-0.889	2.192	6.040e-04	127.564
15788	161.012	63.790	0.365	89	1.924e+05	35.814	5.419e-05	-0.782	2.191	6.110e-04	50.138
17555	215.738	52.236	0.392	712	3.253e+06	91.919	3.257e-05	-0.823	2.177	6.840e-04	91.665
13145	174.125	17.556	0.389	1042	5.355e+06	108.531	2.505e-05	-0.864	2.174	7.000e-04	99.947
7411	125.616	3.859	0.312	138	1.264e+05	31.130	9.719e-05	-0.690	2.168	7.350e-04	30.505
5425	179.143	35.948	0.369	541	1.654e+06	73.362	3.153e-05	-0.873	2.164	7.600e-04	85.486
13894	136.452	34.071	0.402	126	3.987e+05	45.659	3.907e-05	-0.760	2.159	7.930e-04	68.965
11588	168.093	11.202	0.306	1131	4.002e+06	98.487	3.407e-05	-0.883	2.157	8.040e-04	144.502
11539	155.168	10.466	0.250	1718	4.671e+06	103.696	3.683e-05	-0.889	2.153	8.310e-04	87.568
15786	237.310	47.275	0.298	1773	5.765e+06	111.234	3.833e-05	-0.868	2.148	8.620e-04	46.570
76	208.356	0.290	0.312	107	2.268e+05	37.830	4.444e-05	-0.847	2.131	9.900e-04	45.957
16573	171.845	46.286	0.373	290	1.185e+06	65.654	2.917e-05	-0.884	2.128	1.010e-03	139.326
8920	230.405	6.565	0.334	132	2.619e+05	39.689	4.342e-05	-0.873	2.127	1.020e-03	52.178
15	206.464	-0.296	0.341	119	2.149e+05	37.158	6.596e-05	-0.786	2.119	1.080e-03	53.532
16334	157.270	54.716	0.367	154	6.126e+05	52.685	3.625e-05	-0.847	2.115	1.120e-03	140.271
16320	222.239	55.753	0.222	225	4.542e+05	47.685	4.453e-05	-0.866	2.093	1.330e-03	55.863
10254	246.299	34.927	0.381	2415	9.043e+06	129.242	3.605e-05	-0.813	2.092	1.340e-03	119.643
5720	151.546	37.209	0.231	429	1.069e+06	63.422	4.914e-05	-0.853	2.082	1.440e-03	83.671
16258	171.112	60.186	0.317	278	1.081e+06	63.670	4.112e-05	-0.867	2.082	1.450e-03	110.573
11089	249.664	32.616	0.266	106	3.029e+05	41.662	4.908e-05	-0.826	2.070	1.580e-03	58.219
103	226.001	0.132	0.390	127	2.558e+05	39.381	6.510e-05	-0.673	2.069	1.590e-03	51.045
8908	230.779	8.895	0.355	496	1.231e+06	66.490	4.477e-05	-0.837	2.063	1.670e-03	63.310
13716	153.984	24.079	0.278	1351	5.086e+06	106.683	3.267e-05	-0.879	2.056	1.760e-03	91.517
11593	163.879	13.021	0.359	356	1.498e+06	70.976	3.229e-05	-0.883	2.045	1.910e-03	172.563
3099	118.816	24.081	0.364	364	1.001e+06	62.051	4.009e-05	-0.853	2.045	1.920e-03	79.751
12977	141.480	54.740	0.395	216	9.461e+05	60.900	3.462e-05	-0.837	2.025	2.230e-03	85.088
13650	199.893	21.312	0.318	1490	5.775e+06	111.297	3.738e-05	-0.864	2.019	2.330e-03	105.329
15678	153.707	55.128	0.397	768	2.910e+06	88.565	3.690e-05	-0.815	2.010	2.490e-03	79.324
12698	143.945	60.364	0.279	210	4.706e+05	48.253	5.209e-05	-0.807	2.007	2.560e-03	61.538
14805	177.178	18.264	0.268	762	2.839e+06	87.840	3.671e-05	-0.876	2.005	2.590e-03	73.710
12327	204.704	14.609	0.366	158	4.803e+05	48.582	5.870e-05	-0.784	2.004	2.610e-03	63.946

Table A.3 (continued)

ID	RA (deg)	DEC (deg)	z	$N_{\rm gal}$	V (h^{-3}Mpc^3)	$R_{\rm eff}$ (h^{-1}Mpc)	$n_{\rm min}$ (h^3Mpc^{-3})	$\delta_{\rm min}$	r	P	$D_{boundary}$ (h^{-1}Mpc)
12778	137.940	61.345	0.401	155	3.614e+05	44.187	5.215e-05	-0.692	2.002	2.650e-03	64.576
11396	222.719	8.049	0.256	52	1.297e+05	31.398	7.174e-05	-0.740	2.001	2.660e-03	53.469
10263	243.328	32.844	0.316	944	2.953e+06	88.998	4.120e-05	-0.858	2.001	2.660e-03	103.650
13189	141.666	32.043	0.408	72	2.563e+05	39.405	4.188e-05	-0.753	2.001	2.660e-03	53.622
14303	251.939	44.934	0.327	317	8.367e+05	58.456	3.778e-05	-0.878	2.000	2.690e-03	60.185
15235	167.729	30.186	0.286	601	2.727e+06	86.672	3.571e-05	-0.868	1.998	2.720e-03	137.291
1643	246.005	16.577	0.370	472	9.919e+05	61.867	4.831e-05	-0.808	1.994	2.810e-03	70.522
14329	250.228	37.311	0.289	604	2.051e+06	78.816	4.445e-05	-0.838	1.988	2.940e-03	99.570
11538	148.655	10.001	0.339	338	1.019e+06	62.426	4.527e-05	-0.868	1.987	2.940e-03	139.536
17014	157.621	60.424	0.306	928	3.245e+06	91.845	3.848e-05	-0.860	1.987	2.950e-03	71.792
11499	188.258	11.518	0.382	208	8.851e+05	59.561	3.401e-05	-0.856	1.987	2.960e-03	116.551
1859	247.553	17.689	0.243	40	5.305e+04	23.309	9.684e-05	-0.686	1.987	2.960e-03	43.579
16444	178.224	56.450	0.381	1185	4.729e+06	104.125	3.392e-05	-0.830	1.986	2.970e-03	118.680
13568	211.248	17.481	0.268	2655	8.987e+06	128.977	4.203e-05	-0.858	1.985	2.990e-03	65.498
16302	215.884	58.535	0.393	574	2.318e+06	82.097	3.769e-05	-0.795	1.983	3.050e-03	91.175
17559	228.771	55.693	0.370	894	3.457e+06	93.797	3.371e-05	-0.864	1.981	3.090e-03	55.495
13750	182.593	21.721	0.346	779	2.760e+06	87.016	4.539e-05	-0.833	1.978	3.160e-03	135.836
977	223.621	0.277	0.358	163	3.660e+05	44.373	5.729e-05	-0.792	1.977	3.170e-03	49.947
13784	214.500	22.751	0.223	576	9.746e+05	61.506	6.226e-05	-0.836	1.977	3.180e-03	61.926
8606	176.481	6.246	0.259	321	8.676e+05	59.168	4.237e-05	-0.857	1.974	3.240e-03	61.796
10149	259.790	33.233	0.401	99	2.087e+05	36.797	5.914e-05	-0.694	1.965	3.460e-03	37.273
4608	134.362	44.955	0.341	603	1.947e+06	77.459	3.218e-05	-0.883	1.958	3.640e-03	78.557
10524	218.028	39.670	0.396	429	1.108e+06	64.194	4.158e-05	-0.801	1.952	3.810e-03	63.531
4335	126.486	22.455	0.348	144	3.173e+05	42.311	4.881e-05	-0.839	1.951	3.820e-03	54.899
11153	235.682	10.828	0.333	140	2.345e+05	38.255	1.011e-04	-0.674	1.945	4.010e-03	60.246
13580	222.327	20.649	0.404	124	4.213e+05	46.505	4.373e-05	-0.742	1.944	4.040e-03	62.985
33	217.293	-0.037	0.271	137	1.694e+05	34.326	8.928e-05	-0.684	1.942	4.090e-03	42.623
13586	138.091	21.378	0.309	854	2.566e+06	84.926	3.837e-05	-0.876	1.939	4.190e-03	88.342
12003	226.555	11.408	0.261	415	1.105e+06	64.132	4.918e-05	-0.832	1.930	4.440e-03	44.287
14333	243.816	46.729	0.373	1300	5.490e+06	109.434	2.928e-05	-0.876	1.926	4.570e-03	133.755
14304	249.815	45.525	0.217	57	6.492e+04	24.932	1.074e-04	-0.682	1.926	4.590e-03	48.422
7758	125.730	5.239	0.260	111	9.868e+04	28.667	9.597e-05	-0.671	1.922	4.710e-03	39.944

Table A.3 (continued)

ID	RA (deg)	DEC (deg)	z	$N_{\rm gal}$	V (h^{-3}Mpc^3)	$R_{\rm eff}$ (h^{-1}Mpc)	$n_{\rm min}$ (h^3Mpc^{-3})	$\delta_{\rm min}$	r	P	$D_{boundary}$ (h^{-1}Mpc)
12062	141.818	12.303	0.313	878	3.078e+06	90.239	4.365e-05	-0.850	1.918	4.830e-03	120.744
4281	123.624	26.430	0.254	171	2.834e+05	40.749	6.871e-05	-0.768	1.911	5.080e-03	50.584
13679	148.631	20.221	0.231	299	6.942e+05	54.928	6.073e-05	-0.837	1.910	5.130e-03	84.843
13743	216.364	14.359	0.285	1653	5.703e+06	110.835	4.304e-05	-0.844	1.908	5.190e-03	131.246
12064	150.950	16.709	0.399	466	1.667e+06	73.555	3.593e-05	-0.779	1.908	5.210e-03	60.201
13177	202.153	15.377	0.225	279	5.168e+05	49.781	4.515e-05	-0.881	1.906	5.270e-03	52.330
11662	171.606	7.872	0.377	897	3.783e+06	96.663	2.871e-05	-0.856	1.905	5.320e-03	115.289
14091	209.218	23.976	0.331	173	5.724e+05	51.506	4.525e-05	-0.856	1.905	5.320e-03	105.303
16422	158.470	50.565	0.315	466	1.948e+06	77.480	2.591e-05	-0.917	1.903	5.380e-03	193.422
35	225.204	-0.099	0.231	50	3.327e+04	19.952	1.846e-04	-0.506	1.903	5.400e-03	32.028
10385	130.162	55.666	0.309	144	1.868e+05	35.463	9.777e-05	-0.663	1.901	5.460e-03	41.907
2082	252.433	23.290	0.222	229	1.978e+05	36.146	1.196e-04	-0.680	1.892	5.830e-03	48.483
16628	216.657	53.152	0.305	287	9.680e+05	61.366	4.266e-05	-0.853	1.889	5.920e-03	111.845
16377	180.765	50.635	0.314	606	2.207e+06	80.763	4.964e-05	-0.840	1.888	5.980e-03	153.797
15127	174.941	36.198	0.325	739	2.451e+06	83.640	4.173e-05	-0.867	1.887	6.020e-03	127.100
14106	145.078	25.080	0.230	135	3.397e+05	43.286	5.059e-05	-0.858	1.887	6.030e-03	56.018
11070	255.112	36.443	0.376	547	2.154e+06	80.111	3.647e-05	-0.811	1.886	6.060e-03	90.948
5432	169.238	38.263	0.398	176	8.487e+05	58.735	3.494e-05	-0.819	1.886	6.070e-03	76.438
15325	156.694	21.820	0.360	421	1.630e+06	73.009	4.762e-05	-0.825	1.881	6.280e-03	120.623
13823	166.286	19.892	0.345	635	2.598e+06	85.286	3.480e-05	-0.887	1.879	6.340e-03	134.545
5553	175.939	30.706	0.349	391	1.257e+06	66.948	4.642e-05	-0.831	1.879	6.360e-03	105.780
12280	210.795	8.924	0.350	489	1.645e+06	73.233	4.712e-05	-0.844	1.878	6.410e-03	96.929
12727	139.016	57.568	0.326	603	1.710e+06	74.187	4.610e-05	-0.851	1.873	6.640e-03	95.982
16321	235.452	50.935	0.411	42	1.214e+05	30.715	5.648e-05	-0.652	1.871	6.740e-03	47.216
15631	173.776	25.748	0.336	800	2.354e+06	82.524	4.870e-05	-0.842	1.865	7.020e-03	45.218
16733	181.921	42.467	0.388	635	2.014e+06	78.343	3.796e-05	-0.810	1.864	7.070e-03	62.577
16323	183.578	62.614	0.355	271	9.486e+05	60.954	3.972e-05	-0.869	1.863	7.090e-03	101.386
5557	178.193	32.055	0.272	176	5.841e+05	51.857	4.035e-05	-0.850	1.857	7.400e-03	59.034
13113	202.433	16.774	0.277	145	4.662e+05	48.103	5.059e-05	-0.807	1.856	7.460e-03	50.733
10515	223.997	39.073	0.320	373	7.766e+05	57.022	5.255e-05	-0.831	1.852	7.660e-03	64.594
16653	187.249	47.983	0.342	346	1.181e+06	65.580	4.469e-05	-0.864	1.850	7.730e-03	108.090
10864	134.257	29.278	0.348	76	2.201e+05	37.456	6.026e-05	-0.801	1.846	7.940e-03	64.193

Table A.3 (continued)

ID	RA (deg)	DEC (deg)	z	$N_{\rm gal}$	V (h^{-3}Mpc^3)	$R_{\rm eff}$ (h^{-1}Mpc)	$n_{\rm min}$ (h^3Mpc^{-3})	$\delta_{\rm min}$	r	P	$D_{boundary}$ (h^{-1}Mpc)
15591	186.142	28.890	0.401	214	7.557e+05	56.506	3.736e-05	-0.806	1.845	8.000e-03	69.418
9800	239.100	30.941	0.364	116	2.508e+05	39.122	5.644e-05	-0.792	1.842	8.200e-03	55.407
13877	138.152	33.076	0.295	418	1.159e+06	65.171	4.832e-05	-0.833	1.840	8.320e-03	78.240
11636	183.122	13.864	0.304	110	3.162e+05	42.263	7.689e-05	-0.735	1.838	8.390e-03	72.918
13483	213.332	25.608	0.309	157	4.547e+05	47.703	5.395e-05	-0.815	1.837	8.470e-03	63.306
12815	140.367	61.990	0.264	43	6.298e+04	24.681	1.095e-04	-0.625	1.832	8.740e-03	42.794
8791	127.026	7.646	0.404	50	1.060e+05	29.357	8.215e-05	-0.515	1.832	8.750e-03	40.695
13444	148.075	26.586	0.325	69	1.632e+05	33.903	8.207e-05	-0.735	1.832	8.780e-03	73.450
7643	142.387	5.638	0.396	216	5.374e+05	50.436	4.532e-05	-0.721	1.831	8.800e-03	63.937
15125	164.754	32.928	0.394	298	1.135e+06	64.703	3.598e-05	-0.779	1.831	8.820e-03	86.625
15197	160.101	30.157	0.402	94	3.280e+05	42.784	4.678e-05	-0.724	1.829	8.930e-03	68.297
17438	196.553	60.554	0.292	465	1.513e+06	71.219	4.236e-05	-0.839	1.824	9.220e-03	98.583
12976	142.230	53.504	0.214	129	1.075e+05	29.496	1.271e-04	-0.624	1.824	9.270e-03	37.974
2029	253.291	22.320	0.349	231	4.414e+05	47.233	5.459e-05	-0.823	1.813	9.940e-03	64.287
12965	144.513	61.392	0.370	190	5.693e+05	51.414	5.665e-05	-0.772	1.813	9.970e-03	62.982
16431	197.126	49.464	0.326	318	9.432e+05	60.838	4.685e-05	-0.848	1.810	1.020e-02	120.399
13210	148.042	31.981	0.380	350	1.320e+06	68.057	4.075e-05	-0.828	1.809	1.020e-02	122.203
16282	160.284	59.982	0.345	204	5.556e+05	50.999	5.665e-05	-0.835	1.804	1.050e-02	65.264
14277	156.260	18.601	0.223	279	6.854e+05	54.696	4.905e-05	-0.852	1.801	1.080e-02	63.386
8865	184.833	6.823	0.390	423	1.599e+06	72.547	3.190e-05	-0.840	1.801	1.080e-02	93.184
16380	188.231	53.323	0.370	484	2.036e+06	78.623	3.431e-05	-0.855	1.797	1.110e-02	145.912
17622	225.146	48.889	0.331	746	2.798e+06	87.418	3.890e-05	-0.859	1.795	1.120e-02	79.536
12455	230.221	12.590	0.381	334	7.804e+05	57.114	5.181e-05	-0.794	1.794	1.130e-02	62.123
13752	203.972	21.965	0.324	610	2.229e+06	81.035	3.971e-05	-0.869	1.791	1.150e-02	68.026
8535	168.329	5.733	0.395	72	3.248e+05	42.645	4.624e-05	-0.749	1.789	1.170e-02	81.475
1027	198.083	0.297	0.362	103	1.424e+05	32.392	6.221e-05	-0.749	1.786	1.190e-02	43.443
8619	217.624	7.048	0.329	382	9.001e+05	59.897	6.304e-05	-0.797	1.784	1.200e-02	59.978
12177	146.516	8.856	0.363	124	3.528e+05	43.836	7.511e-05	-0.724	1.784	1.200e-02	128.346
8918	219.362	6.543	0.385	101	3.192e+05	42.398	4.426e-05	-0.792	1.784	1.210e-02	59.538
12010	229.261	11.860	0.310	477	9.297e+05	60.546	6.100e-05	-0.778	1.782	1.220e-02	61.575
254	232.596	0.990	0.322	121	1.003e+05	28.823	1.464e-04	-0.525	1.781	1.230e-02	34.802
14767	193.507	27.325	0.220	101	1.791e+05	34.965	1.124e-04	-0.661	1.780	1.240e-02	54.887

Table A.3 (continued)

ID	RA (deg)	DEC (deg)	z	N_{gal}	V (h^{-3}Mpc^3)	R_{eff} (h^{-1}Mpc)	n_{min} (h^3Mpc^{-3})	δ_{min}	r	P	$D_{boundary}$ (h^{-1}Mpc)
12098	134.782	10.919	0.321	436	9.235e+05	60.412	5.225e-05	-0.833	1.780	1.240e-02	59.836
12219	186.736	12.092	0.326	506	1.648e+06	73.280	4.938e-05	-0.840	1.779	1.250e-02	104.807
15292	168.821	27.207	0.392	476	2.038e+06	78.646	3.735e-05	-0.813	1.778	1.250e-02	93.078
16696	193.474	44.310	0.349	259	6.421e+05	53.518	5.307e-05	-0.838	1.777	1.260e-02	65.943
3257	125.791	27.498	0.268	156	1.946e+05	35.948	8.757e-05	-0.684	1.775	1.280e-02	51.740
14097	138.654	20.509	0.301	586	1.826e+06	75.820	4.008e-05	-0.854	1.774	1.280e-02	88.272
14780	158.725	34.197	0.407	59	1.347e+05	31.802	5.718e-05	-0.662	1.774	1.280e-02	57.565
17705	223.611	56.323	0.242	91	2.399e+05	38.548	5.260e-05	-0.829	1.772	1.300e-02	61.480
10400	131.636	54.547	0.370	105	1.710e+05	34.432	1.007e-04	-0.575	1.768	1.340e-02	45.835
12493	143.528	13.307	0.348	172	4.634e+05	48.005	6.155e-05	-0.800	1.765	1.360e-02	158.186
10173	258.022	30.071	0.243	114	1.733e+05	34.589	6.125e-05	-0.801	1.764	1.370e-02	36.325
11392	194.129	6.789	0.376	129	4.016e+05	45.769	5.691e-05	-0.760	1.764	1.370e-02	64.143
3828	119.898	20.972	0.320	1115	3.304e+06	92.396	4.443e-05	-0.856	1.762	1.390e-02	86.102
11410	155.659	7.973	0.396	192	9.114e+05	60.146	2.797e-05	-0.828	1.762	1.390e-02	81.938
16693	196.785	46.319	0.291	377	9.065e+05	60.039	5.356e-05	-0.815	1.761	1.400e-02	87.268
9716	247.518	32.792	0.390	720	2.554e+06	84.799	3.698e-05	-0.823	1.761	1.400e-02	90.991
12761	144.184	48.910	0.371	1518	6.436e+06	115.395	3.831e-05	-0.808	1.759	1.420e-02	143.368
9487	256.620	36.080	0.317	226	6.831e+05	54.635	5.435e-05	-0.824	1.757	1.440e-02	70.604
16391	166.353	47.518	0.257	269	1.188e+06	65.697	4.267e-05	-0.845	1.756	1.450e-02	152.340
3124	126.963	31.185	0.340	18	1.226e+04	14.303	1.293e-04	-0.622	1.753	1.470e-02	35.056
14070	219.789	23.701	0.373	266	8.982e+05	59.855	3.791e-05	-0.847	1.750	1.500e-02	68.065
11993	211.491	13.936	0.383	701	3.178e+06	91.207	3.111e-05	-0.844	1.749	1.510e-02	113.759
12484	134.959	12.221	0.286	249	7.133e+05	55.428	4.606e-05	-0.829	1.745	1.550e-02	58.809
7410	162.941	6.187	0.216	91	9.473e+04	28.279	9.119e-05	-0.730	1.744	1.560e-02	44.904
8630	165.795	6.683	0.400	191	7.231e+05	55.680	5.108e-05	-0.698	1.744	1.570e-02	73.109
495	229.374	0.885	0.379	62	1.267e+05	31.161	7.415e-05	-0.651	1.742	1.580e-02	37.766
1895	247.842	16.137	0.337	340	6.443e+05	53.580	7.562e-05	-0.779	1.742	1.580e-02	63.416
17694	223.290	45.646	0.216	115	2.222e+05	37.576	6.156e-05	-0.814	1.742	1.580e-02	45.005
11078	240.641	39.128	0.264	279	1.065e+06	63.356	4.542e-05	-0.844	1.740	1.600e-02	69.259
5735	161.940	42.263	0.363	330	1.220e+06	66.283	3.638e-05	-0.866	1.737	1.640e-02	163.628
16555	220.702	55.901	0.270	182	5.377e+05	50.444	5.685e-05	-0.795	1.734	1.670e-02	79.074
15199	150.638	28.543	0.308	266	8.048e+05	57.703	5.400e-05	-0.803	1.730	1.710e-02	112.981

Table A.3 (continued)

ID	RA (deg)	DEC (deg)	z	N_{gal}	V ($h^{-3}\mathrm{Mpc}^3$)	R_{eff} ($h^{-1}\mathrm{Mpc}$)	n_{min} ($h^3\mathrm{Mpc}^{-3}$)	δ_{min}	r	P	$D_{boundary}$ ($h^{-1}\mathrm{Mpc}$)
13132	144.480	33.909	0.230	247	6.611e+05	54.042	5.549e-05	-0.851	1.729	1.720e-02	46.757
87	221.960	0.289	0.391	162	3.826e+05	45.034	5.765e-05	-0.687	1.728	1.730e-02	54.668
12674	130.262	57.878	0.393	257	5.628e+05	51.218	5.542e-05	-0.722	1.728	1.740e-02	56.510
11423	194.570	7.831	0.238	174	3.752e+05	44.743	5.115e-05	-0.834	1.727	1.750e-02	59.999
16260	159.768	53.098	0.224	729	1.728e+06	74.446	4.933e-05	-0.870	1.718	1.850e-02	66.866
13653	180.390	24.866	0.398	206	8.058e+05	57.727	4.122e-05	-0.776	1.715	1.880e-02	78.331
14423	251.775	43.335	0.393	579	1.863e+06	76.329	4.567e-05	-0.719	1.714	1.890e-02	89.554
12236	195.005	12.221	0.279	278	1.207e+06	66.044	4.117e-05	-0.848	1.714	1.900e-02	121.922
1019	217.658	0.282	0.384	280	6.184e+05	52.852	5.142e-05	-0.754	1.713	1.910e-02	53.619
11544	137.673	10.483	0.374	633	2.130e+06	79.817	4.472e-05	-0.822	1.710	1.940e-02	87.901
11934	138.349	22.948	0.257	828	2.089e+06	79.302	4.603e-05	-0.877	1.708	1.960e-02	63.450
14261	178.128	18.823	0.221	193	4.761e+05	48.441	5.650e-05	-0.829	1.707	1.980e-02	57.846
11454	135.017	17.891	0.382	149	5.540e+05	50.950	4.384e-05	-0.793	1.706	1.990e-02	79.263
3315	124.389	27.477	0.324	492	1.007e+06	62.187	6.087e-05	-0.803	1.704	2.010e-02	58.929
4516	123.037	19.734	0.377	325	1.414e+06	69.635	4.391e-05	-0.780	1.701	2.050e-02	109.601
15335	172.931	24.955	0.280	145	4.349e+05	47.000	5.645e-05	-0.785	1.701	2.050e-02	54.510
13550	217.349	24.791	0.404	113	3.077e+05	41.880	6.101e-05	-0.640	1.701	2.060e-02	62.022
5431	159.050	34.462	0.303	741	2.628e+06	85.609	4.414e-05	-0.848	1.700	2.060e-02	243.337
8584	150.578	7.102	0.377	368	1.009e+06	62.216	4.217e-05	-0.801	1.700	2.070e-02	93.226
15699	163.496	44.157	0.335	376	1.174e+06	65.435	6.190e-05	-0.811	1.700	2.070e-02	232.647
13645	204.842	26.447	0.363	388	1.663e+06	73.492	2.796e-05	-0.908	1.700	2.070e-02	89.234
16715	214.721	45.896	0.353	1283	5.277e+06	108.001	3.604e-05	-0.848	1.699	2.080e-02	144.676
14726	239.170	45.232	0.245	180	4.435e+05	47.308	5.244e-05	-0.830	1.699	2.080e-02	60.263
14711	237.005	44.174	0.302	765	2.647e+06	85.816	4.465e-05	-0.834	1.699	2.080e-02	68.482
11748	218.577	11.434	0.284	1088	3.492e+06	94.114	4.817e-05	-0.822	1.699	2.080e-02	113.897
16529	217.196	56.575	0.332	306	8.619e+05	59.036	5.640e-05	-0.817	1.697	2.100e-02	98.573
12752	142.731	47.498	0.325	157	5.834e+05	51.836	5.583e-05	-0.822	1.697	2.110e-02	127.848
99	207.623	0.114	0.228	134	1.400e+05	32.214	1.019e-04	-0.692	1.694	2.150e-02	36.794
7571	184.189	6.288	0.317	172	4.401e+05	47.186	5.986e-05	-0.794	1.689	2.220e-02	74.358
16710	188.760	45.811	0.289	372	9.585e+05	61.165	6.449e-05	-0.762	1.686	2.260e-02	64.074
12522	128.469	8.501	0.278	123	1.758e+05	34.753	6.921e-05	-0.736	1.685	2.270e-02	39.889
8579	225.511	5.833	0.301	80	7.944e+04	26.668	1.259e-04	-0.542	1.685	2.270e-02	35.891

Table A.3 (continued)

ID	RA (deg)	DEC (deg)	z	$N_{\rm gal}$	V (h^{-3}Mpc^3)	$R_{\rm eff}$ (h^{-1}Mpc)	$n_{\rm min}$ (h^3Mpc^{-3})	$\delta_{\rm min}$	r	P	$D_{boundary}$ (h^{-1}Mpc)
11122	239.777	37.537	0.357	80	2.789e+05	40.532	6.620e-05	-0.759	1.685	2.270e-02	143.830
17626	210.006	56.134	0.277	337	1.103e+06	64.101	5.607e-05	-0.792	1.683	2.310e-02	126.258
13007	137.157	47.861	0.220	76	1.640e+05	33.956	5.385e-05	-0.837	1.681	2.330e-02	49.596
14143	197.603	24.040	0.250	682	2.104e+06	79.491	4.621e-05	-0.846	1.679	2.350e-02	103.587
11659	197.255	7.450	0.403	180	5.833e+05	51.833	5.589e-05	-0.670	1.679	2.360e-02	65.371
7316	151.529	5.290	0.407	40	1.150e+05	30.166	6.067e-05	-0.627	1.678	2.370e-02	56.158
17437	169.517	62.176	0.347	187	5.352e+05	50.367	6.476e-05	-0.802	1.676	2.400e-02	87.503
15739	208.099	44.381	0.393	590	2.064e+06	78.978	3.987e-05	-0.812	1.675	2.420e-02	90.724
13869	177.712	17.914	0.329	127	3.979e+05	45.629	5.397e-05	-0.828	1.674	2.440e-02	98.741
13611	136.325	21.053	0.390	36	1.256e+05	31.067	6.752e-05	-0.661	1.671	2.480e-02	83.044
4373	123.645	16.664	0.246	210	5.662e+05	51.320	5.198e-05	-0.826	1.670	2.490e-02	61.750
5639	136.204	40.926	0.398	193	6.473e+05	53.662	3.637e-05	-0.785	1.664	2.590e-02	63.462
11970	216.866	17.064	0.407	106	4.047e+05	45.885	4.155e-05	-0.729	1.662	2.620e-02	57.298
4810	170.611	40.463	0.315	214	6.419e+05	53.512	5.023e-05	-0.840	1.662	2.620e-02	168.066
16675	179.276	44.534	0.260	326	7.924e+05	57.405	7.066e-05	-0.750	1.658	2.680e-02	79.492
14289	218.456	40.365	0.375	141	4.616e+05	47.942	5.367e-05	-0.747	1.657	2.710e-02	73.589
12701	138.019	58.596	0.393	101	4.160e+05	46.308	5.259e-05	-0.736	1.653	2.770e-02	89.424
10318	217.105	40.107	0.257	97	1.627e+05	33.863	8.497e-05	-0.692	1.651	2.810e-02	44.968
13156	192.860	16.207	0.289	284	9.814e+05	61.648	4.609e-05	-0.824	1.649	2.830e-02	179.484
13665	140.677	19.264	0.406	155	4.878e+05	48.834	5.672e-05	-0.651	1.649	2.840e-02	59.296
14050	214.181	26.475	0.366	96	2.821e+05	40.687	7.101e-05	-0.717	1.644	2.920e-02	55.955
15239	154.565	27.681	0.344	210	6.980e+05	55.028	5.306e-05	-0.838	1.643	2.960e-02	172.075
17628	196.573	55.274	0.225	522	1.130e+06	64.612	6.694e-05	-0.802	1.641	2.980e-02	67.578
5426	173.730	37.075	0.284	114	3.559e+05	43.961	7.588e-05	-0.724	1.640	3.000e-02	124.446
14029	208.569	25.861	0.274	265	9.042e+05	59.986	5.383e-05	-0.795	1.632	3.150e-02	70.406
5678	140.270	40.265	0.346	351	1.444e+06	70.117	4.245e-05	-0.862	1.632	3.150e-02	99.723
4404	120.876	12.306	0.403	63	1.518e+05	33.094	6.220e-05	-0.662	1.630	3.190e-02	52.195
11651	181.172	6.556	0.287	334	8.078e+05	57.776	5.461e-05	-0.792	1.630	3.190e-02	40.752
13224	137.873	28.228	0.260	143	4.573e+05	47.794	5.863e-05	-0.799	1.629	3.210e-02	76.356
13133	143.639	35.969	0.349	271	1.159e+06	65.171	3.873e-05	-0.887	1.625	3.300e-02	151.041
13551	218.792	22.848	0.270	298	7.469e+05	56.285	5.851e-05	-0.793	1.620	3.390e-02	67.431
12665	133.965	57.582	0.258	416	5.139e+05	49.688	7.645e-05	-0.738	1.619	3.410e-02	58.778

Table A.3 (continued)

ID	RA (deg)	DEC (deg)	z	$N_{\rm gal}$	V (h^{-3}Mpc^3)	$R_{\rm eff}$ (h^{-1}Mpc)	$n_{\rm min}$ (h^3Mpc^{-3})	$\delta_{\rm min}$	r	P	$D_{boundary}$ (h^{-1}Mpc)
12061	140.402	11.131	0.275	93	3.495e+05	43.697	4.549e-05	-0.836	1.617	3.450e-02	84.951
13206	137.221	31.471	0.371	455	1.722e+06	74.357	3.605e-05	-0.857	1.616	3.460e-02	97.082
13857	181.437	23.156	0.295	511	1.678e+06	73.722	4.693e-05	-0.829	1.616	3.480e-02	102.576
9280	210.314	6.534	0.361	173	5.950e+05	52.176	4.843e-05	-0.840	1.615	3.490e-02	55.746
14400	226.595	44.810	0.391	299	1.428e+06	69.863	3.073e-05	-0.846	1.612	3.550e-02	91.731
13795	197.831	23.658	0.332	250	1.110e+06	64.233	3.809e-05	-0.877	1.612	3.560e-02	141.570
11140	252.025	36.608	0.330	188	6.442e+05	53.577	5.924e-05	-0.811	1.612	3.570e-02	111.159
8373	147.947	6.242	0.273	215	4.928e+05	48.999	5.632e-05	-0.791	1.609	3.630e-02	65.641
16563	233.805	51.121	0.338	56	1.378e+05	32.043	7.205e-05	-0.780	1.608	3.650e-02	52.877
16256	199.062	56.900	0.292	165	5.333e+05	50.306	4.663e-05	-0.831	1.606	3.690e-02	148.217
12422	223.130	16.029	0.354	176	5.200e+05	49.887	3.992e-05	-0.855	1.604	3.730e-02	48.907
11697	194.181	10.841	0.325	222	7.259e+05	55.752	4.287e-05	-0.862	1.603	3.750e-02	121.843
11543	129.652	8.961	0.312	82	1.045e+05	29.216	1.216e-04	-0.582	1.603	3.760e-02	43.559
4332	118.762	20.092	0.249	88	1.873e+05	35.495	6.707e-05	-0.776	1.600	3.830e-02	53.470
12675	135.233	56.697	0.217	81	9.082e+04	27.885	1.356e-04	-0.598	1.599	3.840e-02	46.255
12277	215.808	8.023	0.394	150	6.836e+05	54.649	4.008e-05	-0.799	1.599	3.860e-02	85.898
15406	151.578	29.911	0.221	171	3.614e+05	44.189	8.201e-05	-0.757	1.596	3.910e-02	58.293
8521	142.837	6.434	0.287	277	6.067e+05	52.516	5.564e-05	-0.794	1.595	3.950e-02	58.370
17554	221.134	50.217	0.278	158	4.429e+05	47.288	5.038e-05	-0.818	1.593	3.980e-02	76.015
16378	191.584	55.193	0.261	573	1.761e+06	74.916	5.134e-05	-0.814	1.592	4.010e-02	159.610
15601	167.767	29.365	0.352	49	1.377e+05	32.034	5.340e-05	-0.806	1.592	4.010e-02	149.118
14280	224.445	40.211	0.359	323	8.148e+05	57.942	4.605e-05	-0.848	1.592	4.020e-02	65.580
17486	158.403	47.792	0.396	322	1.165e+06	65.267	4.145e-05	-0.745	1.591	4.040e-02	82.411
16667	186.941	44.707	0.389	144	4.843e+05	48.717	4.200e-05	-0.802	1.591	4.040e-02	60.714
15784	233.718	56.893	0.277	232	4.461e+05	47.400	5.782e-05	-0.786	1.590	4.060e-02	54.922
16589	199.729	50.309	0.392	474	2.070e+06	79.064	3.760e-05	-0.805	1.588	4.100e-02	92.760
11479	169.047	9.652	0.238	634	1.552e+06	71.817	5.288e-05	-0.828	1.580	4.300e-02	96.397
4900	154.247	36.129	0.262	53	1.911e+05	35.733	6.804e-05	-0.767	1.579	4.340e-02	165.068
15224	197.478	28.365	0.365	649	2.242e+06	81.198	3.521e-05	-0.834	1.577	4.400e-02	74.437
12705	137.440	59.530	0.327	417	1.117e+06	64.360	5.394e-05	-0.825	1.575	4.430e-02	65.017
1095	204.447	2.828	0.221	99	1.244e+05	30.967	1.096e-04	-0.675	1.574	4.480e-02	28.987
5514	182.304	35.755	0.389	38	6.719e+04	25.219	8.541e-05	-0.572	1.573	4.510e-02	44.419

Table A.3 (continued)

ID	RA (deg)	DEC (deg)	z	N_{gal}	V ($h^{-3}\mathrm{Mpc}^3$)	R_{eff} ($h^{-1}\mathrm{Mpc}$)	n_{min} ($h^3\mathrm{Mpc}^{-3}$)	δ_{min}	r	P	$D_{boundary}$ ($h^{-1}\mathrm{Mpc}$)
7877	179.211	4.616	0.336	94	1.875e+05	35.504	7.385e-05	-0.784	1.572	4.520e-02	51.950

Table A.4: List of voids in the BOSS LOWZ South sample

ID	RA	DEC	z	$N_{\rm gal}$	V	$R_{\rm eff}$	$n_{\rm min}$	$\delta_{\rm min}$	r	P	$D_{boundary}$
	(deg)	(deg)			(h^{-3}Mpc^3)	(h^{-1}Mpc)	(h^3Mpc^{-3})				(h^{-1}Mpc)
(1)	(2)	(3)	(4)	(5)	(6)	(7)	(8)	(9)	(10)	(11)	(12)
4653	350.894	21.568	0.342	16524	6.306e+07	246.915	1.589e-05	-0.934	4.510	3.180e-20	173.682
3284	332.562	21.087	0.381	1107	3.954e+06	98.092	2.151e-05	-0.890	3.240	4.930e-09	88.241
5589	2.482	23.356	0.351	5371	2.067e+07	170.261	2.036e-05	-0.940	3.150	1.810e-08	158.719
5789	5.575	29.235	0.292	636	2.057e+06	78.899	2.330e-05	-0.917	3.042	7.830e-08	65.494
4501	346.370	14.684	0.315	326	9.163e+05	60.254	3.326e-05	-0.885	2.830	1.100e-06	186.512
3362	337.565	10.019	0.362	1324	5.388e+06	108.757	2.422e-05	-0.920	2.701	4.760e-06	138.634
5686	349.211	21.548	0.222	376	1.010e+06	62.238	2.653e-05	-0.922	2.604	1.340e-05	59.909
6581	31.601	-4.318	0.387	1396	4.586e+06	103.063	2.858e-05	-0.854	2.517	3.240e-05	67.373
5547	11.133	19.696	0.337	1917	7.213e+06	119.861	2.535e-05	-0.922	2.458	5.720e-05	201.142
7599	321.468	2.116	0.379	103	3.110e+05	42.028	3.866e-05	-0.856	2.450	6.210e-05	59.634
4325	359.116	6.182	0.386	1978	7.846e+06	123.270	3.020e-05	-0.851	2.449	6.290e-05	105.450
3713	24.360	21.240	0.368	2031	7.895e+06	123.523	3.062e-05	-0.844	2.407	9.270e-05	123.320
4775	7.187	10.434	0.276	3269	1.099e+07	137.903	3.094e-05	-0.903	2.378	1.210e-04	115.654
1998	15.754	-2.615	0.334	111	2.318e+05	38.110	5.784e-05	-0.830	2.337	1.750e-04	54.255
3372	338.238	9.336	0.400	68	1.656e+05	34.064	5.044e-05	-0.728	2.336	1.770e-04	73.151
4803	351.496	15.226	0.244	239	7.874e+05	57.284	4.005e-05	-0.876	2.298	2.480e-04	89.385
7545	40.640	-4.855	0.263	203	3.077e+05	41.881	7.364e-05	-0.759	2.285	2.760e-04	52.660
5820	349.816	32.205	0.402	58	1.322e+05	31.604	3.741e-05	-0.798	2.282	2.840e-04	50.380
7505	44.120	-7.483	0.293	37	5.135e+04	23.058	1.022e-04	-0.633	2.281	2.860e-04	38.367
5548	28.001	28.905	0.396	229	8.167e+05	57.987	3.364e-05	-0.818	2.258	3.480e-04	79.934
2628	16.985	-2.106	0.361	222	5.522e+05	50.895	4.079e-05	-0.846	2.232	4.330e-04	52.097
4766	338.501	21.713	0.348	627	2.600e+06	85.302	3.032e-05	-0.897	2.222	4.700e-04	173.261
5815	344.587	29.799	0.397	318	1.023e+06	62.515	3.177e-05	-0.838	2.200	5.650e-04	75.746
2591	36.102	-4.351	0.390	631	2.348e+06	82.449	3.115e-05	-0.841	2.186	6.370e-04	57.833
1731	25.177	11.349	0.252	90	1.593e+05	33.628	7.973e-05	-0.776	2.146	8.780e-04	56.913
590	326.176	1.035	0.252	174	2.970e+05	41.388	5.353e-05	-0.833	2.100	1.260e-03	52.888
789	33.205	0.699	0.328	136	2.822e+05	40.689	5.116e-05	-0.830	2.099	1.270e-03	43.265
5735	17.570	33.091	0.406	41	6.444e+04	24.871	6.766e-05	-0.590	2.085	1.420e-03	46.260
7563	43.330	-7.013	0.409	25	6.198e+04	24.550	7.898e-05	-0.573	2.070	1.590e-03	48.610
3747	22.992	20.236	0.299	698	2.673e+06	86.092	3.820e-05	-0.878	2.069	1.590e-03	118.326

Table A.4 (continued)

ID	RA (deg)	DEC (deg)	z	$N_{\rm gal}$	V (h^{-3}Mpc^3)	$R_{\rm eff}$ (h^{-1}Mpc)	$n_{\rm min}$ (h^3Mpc^{-3})	$\delta_{\rm min}$	r	P	$D_{boundary}$ (h^{-1}Mpc)
1268	339.772	4.107	0.220	285	4.741e+05	48.373	7.055e-05	-0.802	2.060	1.720e-03	55.770
5746	22.803	29.092	0.317	326	9.629e+05	61.258	4.099e-05	-0.863	2.057	1.750e-03	86.307
5639	10.978	27.261	0.389	406	1.566e+06	72.040	3.520e-05	-0.848	2.055	1.770e-03	100.158
6334	8.797	11.149	0.279	2701	9.155e+06	129.776	3.423e-05	-0.877	2.049	1.860e-03	133.230
6347	347.522	13.714	0.383	997	4.608e+06	103.227	2.860e-05	-0.846	2.033	2.100e-03	113.960
490	344.624	0.948	0.410	33	5.561e+04	23.679	7.765e-05	-0.530	2.026	2.210e-03	42.765
573	342.839	-0.346	0.235	42	3.918e+04	21.070	1.196e-04	-0.698	2.024	2.240e-03	37.068
6407	5.678	-2.705	0.240	289	4.842e+05	48.713	4.746e-05	-0.853	2.005	2.600e-03	50.846
3858	333.850	23.415	0.277	793	2.465e+06	83.802	3.596e-05	-0.889	1.996	2.760e-03	89.115
5752	28.668	29.458	0.270	111	2.483e+05	38.989	5.289e-05	-0.828	1.992	2.850e-03	48.566
1286	0.836	1.905	0.224	336	5.496e+05	50.813	5.978e-05	-0.842	1.988	2.920e-03	42.506
1710	25.084	11.225	0.373	663	1.908e+06	76.942	3.857e-05	-0.810	1.965	3.480e-03	83.745
1750	18.959	11.754	0.390	1224	4.767e+06	104.401	3.736e-05	-0.809	1.953	3.780e-03	96.125
3821	14.996	18.816	0.392	243	9.142e+05	60.208	3.890e-05	-0.832	1.945	4.000e-03	92.668
1465	25.873	5.274	0.223	199	2.489e+05	39.024	7.316e-05	-0.795	1.942	4.100e-03	48.794
1995	16.408	-1.955	0.220	154	1.769e+05	34.822	8.848e-05	-0.752	1.938	4.220e-03	36.835
2508	19.258	-2.183	0.285	73	1.285e+05	31.307	7.394e-05	-0.736	1.934	4.320e-03	33.891
5763	343.329	29.510	0.283	311	9.875e+05	61.776	4.111e-05	-0.869	1.929	4.480e-03	60.148
5825	13.681	31.598	0.217	52	4.443e+04	21.972	1.367e-04	-0.642	1.920	4.770e-03	41.657
3331	332.353	8.544	0.407	65	1.410e+05	32.286	5.528e-05	-0.665	1.911	5.110e-03	54.870
1031	333.450	5.807	0.223	70	6.910e+04	25.456	1.404e-04	-0.629	1.902	5.440e-03	40.822
1241	353.267	1.914	0.322	698	2.040e+06	78.671	4.014e-05	-0.866	1.888	5.960e-03	82.534
5745	23.280	30.523	0.377	163	5.519e+05	50.884	4.475e-05	-0.820	1.887	6.010e-03	76.066
1688	26.609	8.221	0.348	60	1.352e+05	31.843	7.457e-05	-0.747	1.885	6.090e-03	58.414
736	2.347	-1.604	0.267	190	4.310e+05	46.859	5.058e-05	-0.830	1.881	6.280e-03	43.244
4789	346.427	9.893	0.285	674	1.945e+06	77.435	4.271e-05	-0.847	1.878	6.400e-03	124.295
1186	10.099	3.790	0.222	286	4.815e+05	48.622	7.401e-05	-0.805	1.877	6.460e-03	56.722
1867	35.008	3.095	0.269	25	2.673e+04	18.548	1.310e-04	-0.527	1.867	6.920e-03	26.322
500	320.712	0.536	0.400	113	2.727e+05	40.230	5.457e-05	-0.705	1.864	7.060e-03	49.811
5531	359.391	20.783	0.230	321	8.792e+05	59.429	4.497e-05	-0.878	1.857	7.390e-03	73.267
5642	4.634	29.387	0.385	376	1.474e+06	70.600	3.667e-05	-0.778	1.847	7.930e-03	97.151
5726	15.366	31.820	0.312	299	5.448e+05	50.667	6.263e-05	-0.791	1.843	8.160e-03	60.221

Table A.4 (continued)

ID	RA (deg)	DEC (deg)	z	$N_{\rm gal}$	V (h^{-3}Mpc^3)	$R_{\rm eff}$ (h^{-1}Mpc)	$n_{\rm min}$ (h^3Mpc^{-3})	$\delta_{\rm min}$	r	P	$D_{boundary}$ (h^{-1}Mpc)
4632	19.047	27.520	0.356	283	8.029e+05	57.657	5.035e-05	-0.829	1.840	8.310e-03	120.485
5803	356.368	28.460	0.399	461	2.009e+06	78.277	3.006e-05	-0.838	1.832	8.780e-03	74.956
7066	1.409	-6.506	0.393	248	5.483e+05	50.775	4.665e-05	-0.762	1.822	9.360e-03	58.862
756	13.760	1.256	0.232	135	3.297e+05	42.855	7.633e-05	-0.798	1.820	9.500e-03	52.186
4022	331.042	26.621	0.329	117	3.542e+05	43.892	4.849e-05	-0.851	1.819	9.530e-03	58.248
6470	24.032	-3.070	0.244	165	3.136e+05	42.146	7.323e-05	-0.778	1.803	1.060e-02	50.765
675	349.657	-0.096	0.402	76	2.103e+05	36.891	6.018e-05	-0.692	1.800	1.080e-02	48.156
5635	352.582	27.111	0.266	228	6.648e+05	54.141	5.036e-05	-0.835	1.799	1.090e-02	95.988
1709	23.852	12.174	0.222	244	4.365e+05	47.058	5.630e-05	-0.835	1.788	1.170e-02	60.223
5806	16.735	30.934	0.274	205	4.547e+05	47.702	5.113e-05	-0.833	1.788	1.180e-02	60.567
123	325.867	2.067	0.393	253	8.160e+05	57.971	4.516e-05	-0.756	1.786	1.190e-02	65.127
6465	23.606	-4.958	0.217	22	2.022e+04	16.901	1.550e-04	-0.594	1.780	1.240e-02	37.507
1554	27.264	4.604	0.390	236	7.562e+05	56.518	4.353e-05	-0.785	1.775	1.280e-02	67.219
7575	322.382	1.700	0.277	154	3.999e+05	45.704	5.837e-05	-0.789	1.769	1.330e-02	58.892
3803	16.113	23.619	0.401	215	7.379e+05	56.057	4.253e-05	-0.782	1.765	1.360e-02	70.547
6322	351.520	29.575	0.376	208	9.161e+05	60.250	3.106e-05	-0.884	1.762	1.390e-02	88.658
1548	1.540	4.460	0.358	295	1.015e+06	62.348	4.327e-05	-0.848	1.761	1.400e-02	71.792
4942	6.704	18.309	0.249	201	7.584e+05	56.573	3.805e-05	-0.882	1.753	1.480e-02	100.760
4956	20.994	26.242	0.285	444	1.431e+06	69.901	5.086e-05	-0.817	1.753	1.480e-02	114.516
1464	22.576	4.991	0.348	123	3.166e+05	42.282	6.305e-05	-0.762	1.752	1.480e-02	86.198
1630	344.372	4.748	0.250	396	1.108e+06	64.190	5.469e-05	-0.846	1.748	1.520e-02	61.933
1628	340.512	4.679	0.399	677	2.469e+06	83.843	4.410e-05	-0.783	1.732	1.690e-02	75.675
5157	353.079	13.201	0.280	252	7.565e+05	56.524	4.944e-05	-0.839	1.722	1.790e-02	81.618
5714	4.098	32.335	0.333	149	2.238e+05	37.663	8.478e-05	-0.758	1.714	1.890e-02	55.618
7077	0.365	-7.075	0.331	74	9.259e+04	28.064	1.059e-04	-0.675	1.711	1.930e-02	43.830
1236	346.048	1.049	0.301	218	3.590e+05	44.088	6.138e-05	-0.811	1.711	1.930e-02	53.552
1254	352.299	2.304	0.387	537	2.214e+06	80.859	4.166e-05	-0.828	1.702	2.040e-02	104.551
181	324.995	5.796	0.226	205	2.546e+05	39.318	7.877e-05	-0.769	1.697	2.110e-02	53.300
5631	2.798	28.843	0.229	503	1.104e+06	64.123	4.973e-05	-0.869	1.693	2.170e-02	76.609
512	333.808	0.624	0.294	203	2.987e+05	41.469	9.122e-05	-0.709	1.689	2.220e-02	51.893
6641	0.360	-7.435	0.364	129	2.317e+05	38.103	6.417e-05	-0.787	1.678	2.370e-02	49.175
3188	340.795	14.305	0.306	162	4.796e+05	48.560	6.523e-05	-0.804	1.676	2.400e-02	163.573

Table A.4 (continued)

ID	RA (deg)	DEC (deg)	z	N_{gal}	V ($h^{-3}\mathrm{Mpc}^3$)	R_{eff} ($h^{-1}\mathrm{Mpc}$)	n_{min} ($h^3\mathrm{Mpc}^{-3}$)	δ_{min}	r	P	$D_{boundary}$ ($h^{-1}\mathrm{Mpc}$)
4464	354.513	13.604	0.407	76	2.321e+05	38.122	5.019e-05	-0.729	1.673	2.450e-02	55.506
3366	334.743	8.976	0.401	111	3.022e+05	41.630	7.139e-05	-0.635	1.668	2.520e-02	71.308
2665	38.315	-6.265	0.308	117	1.631e+05	33.897	1.358e-04	-0.548	1.668	2.530e-02	47.300
1847	10.396	7.284	0.294	1604	5.274e+06	107.984	4.115e-05	-0.873	1.662	2.610e-02	92.724
4886	5.949	33.673	0.367	18	2.319e+04	17.690	1.384e-04	-0.501	1.653	2.770e-02	43.794
5405	351.334	9.087	0.312	208	4.777e+05	48.495	6.298e-05	-0.790	1.648	2.850e-02	136.940
218	326.740	6.513	0.404	144	3.313e+05	42.926	5.484e-05	-0.668	1.648	2.850e-02	60.559
1888	22.823	2.209	0.261	37	7.536e+04	26.203	1.093e-04	-0.642	1.648	2.850e-02	44.505
2319	13.657	-3.014	0.400	84	1.932e+05	35.863	5.994e-05	-0.693	1.647	2.870e-02	50.921
6595	6.820	-4.378	0.359	129	2.926e+05	41.185	6.942e-05	-0.756	1.641	2.990e-02	45.366
881	24.040	14.453	0.298	84	2.718e+05	40.182	6.056e-05	-0.807	1.640	3.000e-02	86.321
4388	5.881	10.440	0.332	109	4.676e+05	48.151	4.858e-05	-0.861	1.639	3.020e-02	120.036
3685	24.427	17.205	0.344	526	1.699e+06	74.022	3.890e-05	-0.868	1.629	3.210e-02	101.829
5776	11.199	28.998	0.249	466	1.082e+06	63.688	5.616e-05	-0.811	1.628	3.240e-02	59.801
5754	30.781	30.305	0.357	61	5.576e+04	23.699	1.111e-04	-0.610	1.627	3.250e-02	44.876
3399	340.154	16.017	0.382	35	2.122e+05	36.999	5.379e-05	-0.784	1.625	3.280e-02	115.976
215	326.317	6.929	0.351	316	7.813e+05	57.136	5.316e-05	-0.839	1.625	3.290e-02	61.019
2505	2.733	-0.614	0.375	144	4.007e+05	45.736	6.033e-05	-0.757	1.621	3.370e-02	32.156
3395	336.518	15.153	0.265	161	6.629e+05	54.091	4.056e-05	-0.864	1.621	3.370e-02	90.801
5404	2.186	7.968	0.331	306	9.246e+05	60.435	4.901e-05	-0.860	1.619	3.410e-02	107.532
5410	354.641	10.304	0.365	91	3.663e+05	44.385	5.078e-05	-0.822	1.617	3.460e-02	99.483
4773	352.929	7.204	0.346	556	1.929e+06	77.225	4.585e-05	-0.848	1.615	3.500e-02	140.776
1881	22.034	4.186	0.397	199	6.377e+05	53.395	4.581e-05	-0.766	1.612	3.560e-02	61.403
214	323.571	6.129	0.288	290	4.866e+05	48.793	8.114e-05	-0.708	1.612	3.560e-02	53.801
784	26.531	-0.098	0.232	72	7.944e+04	26.668	1.211e-04	-0.671	1.608	3.650e-02	34.017
4927	1.202	17.694	0.393	569	2.015e+06	78.360	4.063e-05	-0.837	1.607	3.660e-02	68.901
3357	340.594	9.982	0.261	72	2.823e+05	40.694	6.162e-05	-0.808	1.605	3.710e-02	118.515
4861	5.640	33.577	0.323	32	3.288e+04	19.873	1.286e-04	-0.572	1.603	3.750e-02	40.093
3532	337.196	12.899	0.396	161	6.899e+05	54.816	5.347e-05	-0.736	1.602	3.770e-02	82.640
912	18.013	10.979	0.354	385	1.049e+06	63.026	6.071e-05	-0.787	1.602	3.780e-02	167.820
4328	342.856	18.545	0.395	172	7.629e+05	56.684	3.441e-05	-0.824	1.600	3.830e-02	85.262
2000	17.943	-2.547	0.397	49	9.796e+04	28.597	6.106e-05	-0.688	1.597	3.900e-02	43.435

Table A.4 (continued)

ID	RA (deg)	DEC (deg)	z	N_{gal}	V ($h^{-3}\mathrm{Mpc}^3$)	R_{eff} ($h^{-1}\mathrm{Mpc}$)	n_{min} ($h^3\mathrm{Mpc}^{-3}$)	δ_{min}	r	P	$D_{boundary}$ ($h^{-1}\mathrm{Mpc}$)
4461	11.084	17.978	0.342	1398	5.323e+06	108.318	3.827e-05	-0.866	1.596	3.930e-02	194.505
2595	38.258	-4.182	0.343	170	2.884e+05	40.987	7.790e-05	-0.707	1.593	4.000e-02	51.716
1758	20.479	9.388	0.237	109	3.238e+05	42.598	6.243e-05	-0.843	1.589	4.090e-02	99.388
1897	22.472	2.483	0.233	52	1.033e+05	29.103	8.956e-05	-0.757	1.586	4.160e-02	35.996
1297	344.903	0.155	0.326	252	4.293e+05	46.798	6.006e-05	-0.816	1.584	4.220e-02	52.979
708	323.714	-0.573	0.343	55	1.060e+05	29.356	7.397e-05	-0.749	1.581	4.290e-02	48.575
69	322.872	4.201	0.347	196	6.335e+05	53.279	5.131e-05	-0.807	1.579	4.340e-02	78.259
1181	12.548	5.708	0.377	331	8.641e+05	59.086	5.472e-05	-0.774	1.577	4.380e-02	86.464
1272	352.981	1.356	0.236	288	6.221e+05	52.957	5.944e-05	-0.839	1.575	4.450e-02	56.455

REFERENCES

Abazajian, K. N., et al. 2009, ApJS, 182, 543

Afshordi, N., & Tolley, A. J. 2008, Phys. Rev. D, 78, 123507

Ahn, C. P., et al. 2012, ApJS, 203, 21

Alam, S., et al. 2015

Alcock, C., & Paczynski, B. 1979, Nature, 281, 358

An, D., et al. 2009, ApJ, 700, 523

Anderson, L., et al. 2014, MNRAS, 441, 24

Babich, D., Creminelli, P., & Zaldarriaga, M. 2004, J. Cosmol. Astropart. Phys., 8, 9

Baldauf, T., Seljak, U., & Senatore, L. 2011, J. Cosmol. Astropart. Phys., 4, 6

Bartolo, N., Komatsu, E., Matarrese, S., & Riotto, A. 2004, Phys. Rep., 402, 103

Belokurov, V., et al. 2006, ApJ, 642, L137

Bennett, C. L., et al. 2013, ApJS, 208, 20

Benoist, C., Cappi, A., da Costa, L. N., Maurogordato, S., Bouchet, F. R., & Schaeffer, R. 1999, ApJ, 514, 563

Bensby, T., Alves-Brito, A., Oey, M. S., Yong, D., & Meléndez, J. 2011, ApJ, 735, L46

Berlind, A. A., & Weinberg, D. H. 2002, ApJ, 575, 587

Berlind, A. A., et al. 2003, ApJ, 593, 1

Bernardeau, F. 1992, ApJ, 392, 1

—. 1994, ApJ, 433, 1

Bernardeau, F., Colombi, S., Gaztañaga, E., & Scoccimarro, R. 2002, Phys. Rep., 367, 1

Biswas, R., Alizadeh, E., & Wandelt, B. D. 2010, Phys. Rev. D, 82, 23002

Bolton, A. S., et al. 2012, AJ, 144, 144

Bond, J. R., Kofman, L., & Pogosyan, D. 1996, Nature, 380, 603

Bos, E. G. P., van de Weygaert, R., Dolag, K., & Pettorino, V. 2012, MNRAS, 426, 440

Bouchet, F. R., Juszkiewicz, R., Colombi, S., & Pellat, R. 1992, ApJ, 394, L5

Bouchet, F. R., Strauss, M. A., Davis, M., Fisher, K. B., Yahil, A., & Huchra, J. P. 1993, ApJ, 417, 36

Bovy, J., Rix, H.-W., & Hogg, D. W. 2012a, ApJ, 751, 131

Bovy, J., Rix, H.-W., Liu, C., Hogg, D. W., Beers, T. C., & Lee, Y. S. 2012b, ApJ, 753, 148

Carollo, D., et al. 2010, ApJ, 712, 692

Ceccarelli, L., Paz, D., Lares, M., Padilla, N., & Lambas, D. G. 2013, MNRAS, 434, 1435

Chen, X. 2010, Advances in Astronomy, 2010

Cheng, J. Y., et al. 2012, ApJ, 752, 51

Chodorowski, M. J., & Bouchet, F. R. 1996, MNRAS, 279, 557

Clampitt, J., Cai, Y.-C., & Li, B. 2013, MNRAS, 431, 749

Colberg, J. M., et al. 2008, MNRAS, 387, 933

Coles, P., & Frenk, C. S. 1991, MNRAS, 253, 727

Coles, P., Moscardini, L., Lucchin, F., Matarrese, S., & Messina, A. 1993, MNRAS, 264, 749

Colless, M., et al. 2001, MNRAS, 328, 1039

Cooper, A. P., Cole, S., Frenk, C. S., & Helmi, A. 2011, MNRAS, 417, 2206

Creminelli, P., Nicolis, A., Senatore, L., Tegmark, M., & Zaldarriaga, M. 2006, J. Cosmol. Astropart. Phys., 5, 4

Crocce, M., Pueblas, S., & Scoccimarro, R. 2006, MNRAS, 373, 369

Croton, D. J., et al. 2004, MNRAS, 352, 1232

Dalal, N., Doré, O., Huterer, D., & Shirokov, A. 2008, Phys. Rev. D, 77, 123514

Davis, M., Efstathiou, G., Frenk, C. S., & White, S. D. M. 1985, ApJ, 292, 371

Dawson, K. S., et al. 2013, AJ, 145, 10

de Jong, J. T. A., Yanny, B., Rix, H.-W., Dolphin, A. E., Martin, N. F., & Beers, T. C. 2010, ApJ, 714, 663

de Lapparent, V., Geller, M. J., & Huchra, J. P. 1986, ApJ, 302, L1

De Propris, R., Harrison, C. D., & Mares, P. J. 2010, ApJ, 719, 1582

Doinidis, S. P., & Beers, T. C. 1989, ApJ, 340, L57

Eisenstein, D. J., et al. 2001, AJ, 122, 2267

—. 2011, AJ, 142, 72

Falk, T., Rangarajan, R., & Srednicki, M. 1993, ApJ, 403, L1

Fosalba, P., & Gaztanaga, E. 1998, MNRAS, 301, 503

Freeman, K., & Bland-Hawthorn, J. 2002, ARA&A, 40, 487

Friedman, A. 1922, Zeitschrift fur Physik, 10, 377

Frieman, J. A., & Gaztanaga, E. 1994, ApJ, 425, 392

Fry, J. N. 1985, ApJ, 289, 10

Fry, J. N., & Gaztanaga, E. 1993, ApJ, 413, 447

—. 1994, ApJ, 425, 1

Fry, J. N., & Scherrer, R. J. 1994, ApJ, 429, 36

Fukugita, M., Ichikawa, T., Gunn, J. E., Doi, M., Shimasaku, K., & Schneider, D. P. 1996, AJ, 111, 1748

Gangui, A., Lucchin, F., Matarrese, S., & Mollerach, S. 1994, ApJ, 430, 447

Gaztanaga, E. 1992, ApJ, 398, L17

Geller, M. J., & Huchra, J. P. 1989, Science, 246, 897

Ghigna, S., Bonometto, S. A., Guzzo, L., Giovanelli, R., Haynes, M. P., Klypin, A., & Primack, J. R. 1996, ApJ, 463, 395

Giannantonio, T., & Porciani, C. 2010, Phys. Rev. D, 81, 063530

Giannantonio, T., Porciani, C., Carron, J., Amara, A., & Pillepich, A. 2012, MNRAS, 422, 2854

Giannantonio, T., Ross, A. J., Percival, W. J., Crittenden, R., Bacher, D., Kilbinger, M., Nichol, R., & Weller, J. 2014, Phys. Rev. D, 89, 023511

Goldberg, D. M., & Vogeley, M. S. 2004, ApJ, 605, 1

Gottlöber, S., Łokas, E. L., Klypin, A., & Hoffman, Y. 2003, MNRAS, 344, 715

Granett, B. R., Neyrinck, M. C., & Szapudi, I. 2008, ApJ, 683, L99

Gregory, S. A., & Thompson, L. A. 1978, ApJ, 222, 784

Gunn, J. E., et al. 2006, AJ, 131, 2332

Guo, H., et al. 2013, ApJ, 767, 122

Guth, A. H. 1981, Phys. Rev. D, 23, 347

—. 1997, The inflationary universe, ed. A. H. Guth

Hamaus, N., Seljak, U., & Desjacques, V. 2011, Phys. Rev. D, 84, 083509

Hamaus, N., Sutter, P. M., & Wandelt, B. D. 2014, Physical Review Letters, 112, 251302

Hamilton, A. J. S. 1997, ”The Evolving Universe”, 231, 185

Hogg, D. W. 1999, ArXiv Astrophysics e-prints

Hoyle, F., Rojas, R. R., Vogeley, M. S., & Brinkmann, J. 2005, ApJ, 620, 618

Hoyle, F., Szapudi, I., & Baugh, C. M. 2000, MNRAS, 317, L51

Hoyle, F., Vogeley, M. S., & Pan, D. 2012, MNRAS, 426, 3041

Hubble, E. 1929, Proceedings of the National Academy of Science, 15, 168

Hui, L., & Gaztañaga, E. 1999, ApJ, 519, 622

Ivezić, Ž., Beers, T. C., & Jurić, M. 2012, ARA&A, 50, 251

Jennings, E., Baugh, C. M., & Pascoli, S. 2012, MNRAS, 420, 1079

Jennings, E., Li, Y., & Hu, W. 2013, MNRAS, 434, 2167

Jurić, M., et al. 2008, ApJ, 673, 864

Juszkiewicz, R., & Bouchet, F. R. 1992, in Distribution of Matter in the Universe, ed. G. A. M. . D. Gerbal, 301–310

Juszkiewicz, R., Bouchet, F. R., & Colombi, S. 1993, ApJ, 412, L9

Kazin, E. A., et al. 2010, ApJ, 710, 1444

Kim, R. S., & Strauss, M. A. 1998, ApJ, 493, 39

Kirshner, R. P., Oemler, Jr., A., Schechter, P. L., & Shectman, S. A. 1981, ApJ, 248, L57

Komatsu, E., & Spergel, D. N. 2001, Phys. Rev. D, 63, 063002

Kordopatis, G., et al. 2013, AJ, 146, 134

Kroupa, P. 2001, MNRAS, 322, 231

Lahav, O., Itoh, M., Inagaki, S., & Suto, Y. 1993, ApJ, 402, 387

Lam, T. Y., & Sheth, R. K. 2009, MNRAS, 395, 1743

Lam, T. Y., Sheth, R. K., & Desjacques, V. 2009, MNRAS, 399, 1482

Laureijs, R., et al. 2011, ArXiv e-prints

Lavaux, G., & Wandelt, B. D. 2012, ApJ, 754, 109

Lee, J., & Park, D. 2009, ApJ, 696, L10

Levi, M., et al. 2013, ArXiv e-prints

Li, B., Zhao, G.-B., & Koyama, K. 2012, MNRAS, 421, 3481

Liddle, A. R., & Lyth, D. H. 2000, Cosmological Inflation and Large-Scale Structure, ed. D. H. Liddle, A. R. & Lyth

Longhitano, M., & Binggeli, B. 2010, A&A, 509, A46

Lopez-Corredoira, M., Garzon, F., Hammersley, P. L., & Mahoney, T. J. 1998, MNRAS, 301, 289

Lucchin, F., Matarrese, S., Melott, A. L., & Moscardini, L. 1994, ApJ, 422, 430

Luo, X., & Schramm, D. N. 1993, ApJ, 408, 33

Maldacena, J. 2003, Journal of High Energy Physics, 5, 13

Manera, M., & Gaztañaga, E. 2011, MNRAS, 415, 383

Mao, Q., Berlind, A. A., Scherrer, R. J., Scoccimarro, R., Tinker, J. L., McBride, C. K., & Neyrinck, M. C. 2015, in prep.

Maraston, C., et al. 2013, MNRAS, 435, 2764

Marín, F. 2011, ApJ, 737, 97

Marinoni, C., & Buzzi, A. 2010, Nature, 468, 539

Marinoni, C., et al. 2005, A&A, 442, 801

McBride, C., Berlind, A., Scoccimarro, R., Wechsler, R., Busha, M., Gardner, J., & van den Bosch, F. 2009, in Bulletin of the American Astronomical Society, Vol. 41, American Astronomical Society Meeting Abstracts #213, 425.06

McBride, C., et al. 2011, in American Astronomical Society Meeting Abstracts, Vol. 217, American Astronomical Society Meeting Abstracts, 249.07

Morrison, H. L., Mateo, M., Olszewski, E. W., Harding, P., Dohm-Palmer, R. C., Freeman, K. C., Norris, J. E., & Morita, M. 2000, AJ, 119, 2254

Neyrinck, M. C. 2008, MNRAS, 386, 2101

Nuza, S. E., et al. 2013, MNRAS, 432, 743

Pan, D. C., Vogeley, M. S., Hoyle, F., Choi, Y.-Y., & Park, C. 2012, MNRAS, 421, 926

Pápai, P., & Szapudi, I. 2010, ApJ, 725, 2078

Parejko, J. K., et al. 2013, MNRAS, 429, 98

Peebles, P. J. E. 1973, ApJ, 185, 413

Peebles, P. J. E. 1980, The large-scale structure of the universe, ed. P. J. E. Peebles

Peebles, P. J. E. 1993, Principles of physical cosmology, ed. P. J. E. Peebles

—. 2001, ApJ, 557, 495

Perlmutter, S., et al. 1999, ApJ, 517, 565

Planck Collaboration et al. 2013, arXiv:1303.5084

—. 2014, A&A, 571, A19

—. 2015, ArXiv e-prints

Platen, E., van de Weygaert, R., & Jones, B. J. T. 2007, MNRAS, 380, 551

Reid, B., et al. in prep.

Riess, A. G., et al. 1998, AJ, 116, 1009

Rix, H.-W., & Bovy, J. 2013, A&A Rev., 21, 61

Rockosi, C., Beers, T. C., Majewski, S., Schiavon, R., & Eisenstein, D. 2009, in Astronomy, Vol. 2010, astro2010: The Astronomy and Astrophysics Decadal Survey, 14

Rojas, R. R., Vogeley, M. S., Hoyle, F., & Brinkmann, J. 2004, ApJ, 617, 50

—. 2005, ApJ, 624, 571

Ross, A. J., Brunner, R. J., & Myers, A. D. 2008, ApJ, 682, 737

Ross, A. J., et al. 2013, MNRAS, 428, 1116

Ryden, B. S. 1995, ApJ, 452, 25

Salopek, D. S., & Bond, J. R. 1990, Phys. Rev. D, 42, 3936

Salpeter, E. E. 1955, ApJ, 121, 161

Saunders, W., Frenk, C., Rowan-Robinson, M., Lawrence, A., & Efstathiou, G. 1991, Nature, 349, 32

Scherrer, R. J., & Schaefer, R. K. 1995, ApJ, 446, 44

Schlegel, D. J., Finkbeiner, D. P., & Davis, M. 1998, ApJ, 500, 525

Schlesinger, K. J., et al. 2012, ApJ, 761, 160

Scoccimarro, R. 1998, MNRAS, 299, 1097

Scoccimarro, R., & Frieman, J. 1996, ApJS, 105, 37

Scoccimarro, R., Hui, L., Manera, M., & Chan, K. C. 2012, Phys. Rev. D, 85, 083002

Scoccimarro, R., Sefusatti, E., & Zaldarriaga, M. 2004, Phys.Rev. D, 69, 103513

Sefusatti, E. 2009, Phys. Rev. D, 80, 123002

Sefusatti, E., Crocce, M., Pueblas, S., & Scoccimarro, R. 2006, Phys. Rev. D, 74, 023522

Sefusatti, E., & Komatsu, E. 2007, Phys. Rev. D, 76, 083004

Seljak, U. 2009, Physical Review Letters, 102, 021302

Seljak, U., & Zaldarriaga, M. 1996, ApJ, 469, 437

Senatore, L., Smith, K. M., & Zaldarriaga, M. 2010, J. Cosmol. Astropart. Phys., 1, 28, original template of orthogonal shape non-Gaussianity

Shectman, S. A., Landy, S. D., Oemler, A., Tucker, D. L., Lin, H., Kirshner, R. P., & Schechter, P. L. 1996, ApJ, 470, 172

Skrutskie, M. F., et al. 2006, AJ, 131, 1163

Slosar, A., Hirata, C., Seljak, U., Ho, S., & Padmanabhan, N. 2008, J. Cosmol. Astropart. Phys., 8, 31

Smee, S. A., et al. 2013, AJ, 146, 32

Spergel, D., et al. 2013, ArXiv e-prints

Spolyar, D., Sahlén, M., & Silk, J. 2013, Physical Review Letters, 111, 241103

Springel, V. 2005, MNRAS, 364, 1105

Springel, V., Frenk, C. S., & White, S. D. M. 2006, Nature, 440, 1137

Starkenburg, E., et al. 2009, ApJ, 698, 567

Strauss, M. A., et al. 2002, AJ, 124, 1810

Sutter, P. M., Lavaux, G., Wandelt, B. D., & Weinberg, D. H. 2012a, ApJ, 761, 187

—. 2012b, ApJ, 761, 44

Sutter, P. M., Lavaux, G., Wandelt, B. D., Weinberg, D. H., Warren, M. S., & Pisani, A. 2014, MNRAS, 442, 3127

Swanson, M. E. C., Tegmark, M., Hamilton, A. J. S., & Hill, J. C. 2008, MNRAS, 387, 1391

Szapudi, I., Branchini, E., Frenk, C. S., Maddox, S., & Saunders, W. 2000, MNRAS, 318, L45

Szapudi, I., et al. 2002, ApJ, 570, 75

Thompson, K. L., & Vishniac, E. T. 1987, ApJ, 313, 517

Verde, L., Jimenez, R., Kamionkowski, M., & Matarrese, S. 2001, MNRAS, 325, 412

Verde, L., Wang, L., Heavens, A. F., & Kamionkowski, M. 2000, MNRAS, 313, 141

Weinberg, D. H., & Cole, S. 1992, MNRAS, 259, 652

Weinberg, D. H., Mortonson, M. J., Eisenstein, D. J., Hirata, C., Riess, A. G., & Rozo, E. 2013, Phys. Rep., 530, 87

White, M., Tinker, J. L., & McBride, C. K. 2014, MNRAS, 437, 2594

Xue, X.-X., et al. 2011, ApJ, 738, 79

Yanny, B., et al. 2009, AJ, 137, 4377

York, D. G., et al. 2000, AJ, 120, 1579

Zehavi, I., et al. 2005, ApJ, 621, 22

Zivick, P., Sutter, P. M., Wandelt, B. D., Li, B., & Lam, T. Y. 2014, ArXiv e-prints